

Integrating Rotordynamic and Electromagnetic Dynamic Models for Flexible-Rotor Electrical Machines

Karuna Kalita, BE, MTech

**GEORGE GREEN LIBRARY OF
SCIENCE AND ENGINEERING**

Thesis submitted to the University of Nottingham for the degree of
Doctor of Philosophy

March 2007

This thesis is dedicated to my parents, Mrs Parbati Kalita and Late Harendra Chandra Kalita and my uncle, Late Jogendra Chandra Kalita for their countless sacrifices

Contents

Abstract	x
Acknowledgement	xi
Nomenclature	xii
List of Figures	xviii
List of Tables	xxv
1 Introduction	1
1.1 General.	1
1.2 Eccentricity in an electrical machine.	1
1.3 Motivation.	3
1.4 Aim of the research.	4
1.5 Organisation of the thesis.	4
2 Literature Review	9
2.1 Introduction.	9
2.2 General observations about the origin of UMP and its effect.	10
2.3 Airgap permeance.	11
2.4 Conformal transformation technique.	11
2.5 Analytical methods of calculating UMP.	12
2.6 Numerical methods for the solution of static magnetic fields.	16
2.7 Integration of electromagnetic model and mechanical model.	20
2.8 Numerical methods for the computation of magnetically-oriented forces.	24

2.8.1	Lorentz force.	25
2.8.2	Virtual work.	25
2.8.3	Maxwell stress tensor.	25
2.9	Experimental findings of UMP.	28
2.10	Summary of the literature review.	29
3	2-D Finite Element Modelling of Electric Machines	35
3.1	Introduction.	35
3.2	Basic equations of the electromagnetic field.	36
3.3	Finite element formulation.	39
3.3.1	Shape functions.	40
3.3.1.1	4-Noded quadrilateral element.	41
3.3.1.2	8-Noded quadrilateral element.	41
3.3.1.3	3-Noded triangular element.	41
3.3.1.4	6-Noded triangular element.	42
3.3.2	The magnetic stiffness matrix.	42
3.3.3	Conduction modelling.	45
3.3.4	Calculation of the magnetomotive forces.	48
3.3.4.1	MMF from current carrying coils.	48
3.3.4.2	Magnetomotive force of permanent magnets. .	48
3.3.5	Calculation of magnetic flux density.	49
3.4	Material properties.	50
3.5	Non-linear finite element analysis.	50
3.6	Computer code for finite element analysis of electromagnetic.	52
3.6.1	Pre-processor.	53
3.6.2	Solver.	54

3.6.3	Post-processor.	55
3.7	Case studies for static Unbalance Magnetic Pull (UMP)	55
3.7.1	Case study I: Unbalanced magnetic pull of an induction machine.	56
3.7.2	Case study II: Unbalanced magnetic pull of a high speed permanent magnet alternator (PMA)	57
3.7.2.1	Reduction of critical speed due to negative stiffness.	57
3.7.3	Case study III: Investigation of tooth passing spatial harmonics (FPF) with non-magnetic and magnetic slot wedges.	59
3.8	Magnetic Pull (UMP) for overhung machine.	60
3.9	Summary of the chapter.	60
4	Co-ordinate Transformations Used in the Magnetic FEA	83
4.1	Introduction.	83
4.2	General principles of the coordinate transformations.	85
4.3	Transformations of the stator currents.	88
4.3.1	Transformation of the full set of nodal currents in the stator to the nodal currents corresponds to the conducting regions in the stator (Stage I)	89
4.3.2	Transformation of the nodal currents corresponds to the conducting regions to the coil side currents in the stator (Stage II)	90
4.3.3	Transformation of the coil side currents to the full coil currents in the stator (Stage III)	92
4.3.4	Transformation of the full coil currents to the coil group currents in the stator (Stage IV)	93
4.3.5	Transformation of the coil group currents to the terminal currents (Stage V)	94
4.3.6	Transformation of the coil group currents according to the bridge windings.	95

4.4	Transformations of the rotor bar currents.	97
4.4.1	Transformation of the full set of nodal currents in the rotor to the nodal currents corresponds to the conducting regions (Stage I)	98
4.4.2	Transformation of the nodal currents corresponds to the conducting regions in the rotor to the set of currents based on the “modes” of conduction (Stage II)	99
4.4.3	Transformation of the set of currents based on the “modes” of conduction to the set of nodal currents from the Fourier transform (stage III)	102
4.4.4	Transformation of the set of nodal currents from the Fourier transform (stage IV)	103
4.5	Transformations of the magnetic potentials.	103
4.5.1	Transformation of the set of nodal potentials in the stator to apply that tangential-flux conditions.	104
4.5.2	Transformation of the set of nodal potentials of a hollow rotor to apply the equal-flux conditions.	105
4.6	Conclusions.	105
5	Modelling of Electro-Magneto-Mechanical Devices	116
5.1	Introduction.	116
5.2	Calculation of resistance matrix from finite element method.	117
5.3	Resistance of the end-windings.	118
5.4	Coupled electromagnetic model for an EMM device with changeable geometry	121
5.5	Modelling of an induction machine.	125
5.6	Conclusions.	128
6	Time-marching Simulations of Rotating Electric Machinery	131
6.1	Introduction.	131
6.2	Accommodating movement in rotating electric machine modelling.	132

6.2.1	Established approaches for accommodating movement in FE models.	132
6.2.2	Approaches used in this thesis for accommodating movement.	134
6.3	Some general features of machine modelling.	135
6.3.1	Revisit of the electro-magneto-mechanical model.	135
6.3.2	Definition and calculation of marginal inductance and its derivative.	137
6.4	Airgap stitching method.	139
6.4.1	Marginal inductance and its rate of change using airgap stitching method from non-linear FEA.	139
6.4.2	Marginal inductance and its rate of change using airgap stitching method from linear FEA.	140
6.5	The central circle (CC) method.	144
6.5.1	Formulation of the rotor.	145
6.5.2	Formulation of the stator.	147
6.5.3	Coupling the rotor and stator models.	149
6.5.4	Marginal inductance and its rate of change from non-linear finite element analysis with geometry change.	150
6.5.5	Marginal inductance and its rate of change from linear finite element analysis with geometry change.	151
6.6	Case studies.	153
6.7	Conclusions.	155
7	Methods of Calculating Steady State Solutions for Induction Machines	162
7.1	Introduction.	162
7.2	Available approaches to calculate steady state solution.	163
7.3	Central circle method with non-linear model reduction.	164
7.3.1	Formulation for the rotor.	165

7.3.2	Formulation for the stator.	167
7.3.3	Coupling the rotor and stator models and accounting for the non-linearity.	170
7.3.3.1	Method I of accounting for non-linearity.	172
7.3.3.2	Method I of accounting for non-linearity.	174
7.3.3.3	The method of calculation of the nonlinear coefficients of the power series.	175
7.4	Case studies.	175
7.4.1	Case study I: Sinusoidal voltage with lower level of saturation.	177
7.4.2	Case study II: Sinusoidal voltage with higher level of saturation.	177
7.5	Conclusions.	178
8	Unified Electromagnetic Dynamic and Rotordynamics Model	184
8.1	Introduction.	184
8.2	Electro-magneto-mechanical model.	186
8.3	Mechanical model.	187
8.4	Coupled linearised model.	189
8.5	Reference electromagnetic solution.	192
8.6	The Time period of an electrical machine.	193
8.7	Case study of the coupled electrical and mechanics dynamics of an induction machine.	194
8.7.1	Finite element model of the flexible rotor.	195
8.7.2	Equalising currents for an eccentric rotor.	195
8.7.3	Minimum time period of the machine.	196
8.7.4	Preparing the state transition matrix for the coupled model.	196
8.7.5	Stability of the system.	197

8.7.6	Energy transfer while closing the bridge.	197
8.8	Conclusions.	198
9	Method of Reducing Unbalanced Magnetic Pull	208
9.1	Introduction.	208
9.2	Reduction of UMP in an induction machine using bridge windings.	209
9.3	Conclusions.	210
10	Experimental Validation	212
10.1	Introduction.	212
10.2	Design of the test rig.	213
10.2.1	Motor electrical design.	213
10.2.1.1	Winding scheme.	213
10.2.1.2	Full pitch and fractional pitch.	213
10.2.1.3	Number of turns in each coil.	214
10.2.2	Drive system for the motor and electrical sensors.	215
10.2.2.1	Drive system for the motor.	215
10.2.2.2	Current transducers.	216
10.2.2.3	Voltage transducers.	216
10.2.3	Mechanical design of the system.	216
10.2.4	Other transducers.	217
10.2.5	Data acquisition.	218
10.3	Numerical model verification with experimental results.	218
10.3.1	Mechanical model.	219
10.3.2	Electrical model.	220
10.3.2.1	No-load test.	221
10.3.2.2	Locked-rotor test.	222

10.4	Results for the modified motor.	222
10.4.1	Bridge currents and voltages.	223
10.4.2	Reduction of UMP.	224
10.5	Conclusions.	225
11	Conclusions and Future Work	241
11.1	Conclusions.	241
11.2	Future work.	244
11.2.1	Application to other electrical machines.	244
11.2.2	Three dimensional analysis.	244
11.2.3	Detailed study of the approximate method.	244
11.2.4	Optimum scaling in the approximate method.	245
11.2.5	Extending the central circle method for accommodating eccentricity	246
11.2.6	Automatic differentiation of the inductance with respect to position.	246
11.2.7	Time dependent transformations.	247
11.2.8	Passive components in the parallel paths.	248
11.2.9	Inclusion of torsional dynamics in the coupled model . . .	248
11.2.10	Incorporation of the effect of base plate in the mechanical model	248
	References	249
	Appendix A	I
	Appendix B	XIV

Abstract

The magnetic field within electrical machines causes an interaction between the electrical and mechanical dynamics of the system. In the simplest cases, when the rotor mean position is central in the stator, the interaction manifests itself mainly as a negative stiffness between the rotor and the stator. When the rotor mean position is offset relative to the stator, then components of force arise whose frequency in the stationary frame is twice the electrical frequency of the supply.

For induction machines in particular, both the electrical system and the mechanical system may be quite complex dynamically in the sense that over the range of frequencies of interest, it is necessary to consider a number of degrees of freedom in both the electrical part of the model and the mechanical part.

This work sets out a structured and formal approach to the preparation of such models. Each different combination of voltage and slip is examined separately. In each case, the first step is to compute the steady-state *reference solution* for machine currents as a function of time. Then, the electro-magnetic behaviour of the electrical machine is linearised around that reference solution. The result is a linear time-dependent model for the electromagnetic behaviour which is then easily coupled with a linear model for the mechanical dynamics. The mechanical dynamics are usually stationary. Floquet methods can then be applied to determine whether the system is stable and the response of the system to mechanical or electrical perturbations can be computed quickly.

The analysis method is applied to a particular three-phase induction machine which has parallel paths integrated into its winding structure in the sense that each of the phases is split into a “Wheatstone-bridge” arrangement following. Currents passing diametrically through a phase in the *vertical* direction account for the main torque-producing components of stator field. Currents passing diametrically through the phase in the *horizontal* direction account for transverse forces. The parallel paths can

be switched to open-circuit or closed-circuit without affecting the torque-producing function of the machine and all of the stator conductors contribute to torque-production. For a number of combinations of voltage and slip, the machine is stable irrespective of whether the parallel paths are open-circuit or not but the effective damping of the machine for synchronous vibration is shown to be much higher with the parallel paths in closed-circuit.

Acknowledgements

I express my profound gratitude to my supervisor, Professor Seamus Garvey, for his valuable help, advice, encouragement and fruitful thoughts. My special thanks are also extended to the University of Nottingham for providing me with the financial support.

I am thankful to all my previous teachers who have helped me at different stages of my education. Thanks to all my colleagues and researchers who have greatly contributed to my research, especially Dr. W. K. S. Khoo.

I wish to express my special thanks to my parents for their unwavering support throughout my life. I would also like to thank Dr. Kamini Arandhara and Mrs. Gabrielle Arandhara for their help and advice.

Nomenclature

$\{ \}$	Vector symbol
$[\]$	Matrix symbol
\mathbf{A}	Magnetic vector potential which is function of spatial co-ordinates
$\{\mathbf{A}\}$	Magnetic vector potential vector
$\{\mathbf{A}\}$	Magnetic vector potential vector which is function of spatial co-ordinates
$\{\mathbf{A}_R\}$	Nodal potential vector of the rotor
$\{\mathbf{A}_{red}\}$	Reduced vector of magnetic potentials
$\{\mathbf{A}_S\}$	Nodal potential vector of the stator
b	Number of nodes in a single rotor bar
$\{\mathbf{b}_R\}$	Nodal free MMF vector in the rotor
$\{\mathbf{b}_S\}$	Nodal free MMF vector in the stator
$\{\mathbf{b}_z\}$	Free MMF vector
$\{\mathbf{b}_z\}$	Free MMF vector which is function of spatial co-ordinates
B	Magnetic flux density
\mathbf{B}	Magnetic flux density which is function of spatial co-ordinates
\mathbf{B}_0	Remanent flux density which is function of spatial co-ordinates
$\{\mathbf{B}\}$	Magnetic flux density vector
$\{\mathbf{B}\}$	Magnetic flux density vector which is function of spatial co-ordinates

$\{\mathbf{B}_0\}$	Remanent flux density vector which is function of spatial co-ordinates
$[\mathbf{D}]$	Damping matrix
e_z	Unit vector along z-direction
\mathbf{E}	Electric field strength which is a function of spatial coordinates
$\{\mathbf{E}\}$	Electric field strength vector
$\{\mathbf{E}\}$	Electric field strength vector which is a function of spatial coordinates
$\{\mathbf{f}\}$	External forces
$\{\mathbf{f}_E\}$	Electromagnetic force vector
$\{\mathbf{f}_M\}$	Mechanical force vector
$[\mathbf{F}]$	Internal rotor damping matrix
$[\mathbf{G}]$	Gyroscopic matrix
\mathbf{H}	Field intensity which is function of spatial co-ordinates
$\{\mathbf{H}\}$	Field intensity vector
$[\mathbf{H}]$	Sensitivity matrix
$\{\mathbf{H}\}$	Field intensity vector which is function of spatial co-ordinates
i_{Alev}, i_{Blev} and i_{Clev}	Three levitation currents in the bridge
$i_{Aph}, i_{Bph}, i_{Cph}$	Three terminal currents
i_k	Nodal currents corresponding to node k
$\{\mathbf{I}\}$	Nodal current vector
$\{\mathbf{I}_e\}$	Eddy currents vector
$\{\mathbf{I}_{ER}\}$	Full vector of currents in the end-ring links

$\{I_m\}$	Equivalent nodal current vector for permanent magnet
$\{I_R\}$	Reduced current vector corresponding to the rotor bar
$\{I_S\}$	Reduced current vector corresponding to the stator phase currents
$[J]$	Jacobian matrix
J_0	Current density
$\{J_0\}$	Current density vector
k	Number of rotor bars
$[K]$	Magnetic stiffness matrix
$[K_{mar}]$	Marginal magnetic stiffness matrix
$[K_{mech}]$	Mechanical stiffness matrix
$[K_R]$	Stiffness matrix of the rotor
$[K_S]$	Stiffness matrix of the stator
l	Axial length of the machine
$[L]$	Inductance
m	Mass
$[M]$	Mass matrix
N	Shape function
$\{N\}$	Shape function vector
p	Pole pairs
p_k	Nodal potentials
P_D	Total power dissipated over an element
P_I	Instantaneous electrical power

$[P]$	Matrix which dictates how the individual flux quantities in $\{\Phi\}$ are coupled to the current variables
$\{q\}$	Displacement vector
$[R]$	Resistance matrix
r	Radius of the rotor
$[R_E]$	Diagonal matrix of the link resistances for the end-ring
$[R_{nc}]$	Resistance matrix associated with the nodal currents
$[R_R]$	Resistance matrix associated with the reduced number of rotor bar currents
$[R_S]$	Resistance related to the stator
s	Slip
$[S]$	Selection matrix
t	Time
t_1	Thickness of the end-ring
$[T]$	Transformation matrix
T_m	Mean torque
T_p	Time period of the coupled system
u	Horizontal position of the rotor centre
$[U]$	Transformation matrix
v	Vertical position of the rotor
w_1	Width of the area associated with a end-ring link
W_D	Work done by a current distribution
$\{V\}$	Externally-applied voltages vector

$\{x\}$	Instantaneous geometry of the system
$[Z]$	State transition matrix

Greek symbols

α	Relaxation factor
η	Local coordinate
θ	Angle of turn of the rotor
$[\Theta(.,.)]$	Matrix function
μ	Permeability
μ_{xx}	Permeability along x -direction
μ_{yy}	Permeability along y -direction
$[\mu]$	Permeability tensor
ν	Susceptibility
ξ	Local coordinate
ρ	Resistivity
σ	Conductivity
τ	Time
ϕ	Phase angle
$\{\Phi\}$	Magnetic flux vector
ω	Angular frequency
ω_c	Critical speed
ω_e	Electrical frequency
Ω_{mech}	Constant mechanical speed of the rotor

Ω Mean rotational speed

$\{\mathfrak{R}\}$ Residue vector

List of figures

1.1	An electrical machine.	7
1.2	A concentric rotor ('O' is the centre of the axis of rotation).	8
1.3	An eccentric rotor with static eccentricity ('P' is the centre of the axis of rotation).	8
2.1	UMP from static eccentricity.	31
2.2	UMP from dynamic eccentricity.	31
2.3	Airgap of an electric machine with an eccentric rotor.	31
2.4	Z-plane.	32
2.5	T-plane.	32
2.6	The radial and tangential components of magnetic flux density in the airgap (Binns and Dye, 1973).	32
2.7	Numerical field computation methods (Hameyer and Belmans, 1999).	33
2.8	Frequency response functions at no load condition. In the figure thick line represents the radial and the dashed line represents the tangential components (Tenhunen, 2003).	33
2.9	The normal and tangential components of magnetic flux density. . . .	34
2.10	The radial strain for different supply voltages: (a) Series pattern of stator coils, (b) Equalizing pattern of stator coils (Berman, 1993). .	34
3.1	Master element.	61
3.2	Isoparametric element.	61
3.3	Node point ordering of a 4-noded quadrilateral element.	61
3.4	Node point ordering of a 8-noded quadrilateral element.	62
3.5	Node point ordering of a 3-noded triangular element.	62

3.6	Node point ordering of a 6-noded triangular element.	63
3.7	$B(H)$ curves for some permanent magnet (Bastos and Sadowski, 2003).	63
3.8	Magnetisation curve for a permanent magnet.	64
3.9	Magnetization characteristics in $B(H)$ -form of a typical electrical steel.	64
3.10	Schematic representation of solution procedure of non-linear static electromagnetic problem.	65
3.11	FE mesh of the induction motor considered for case study I.	66
3.12	Contour of magnetic vector potential when a sinusoidal current when 3-phase current with a peak of 200 Amps (per slot) is applied.	66
3.13	Normal component of flux density in the middle of the airgap when 3-phase current with a peak of 200 Amps (per slot) is applied.	67
3.14	Tangential component of flux density in the middle of the airgap when 3-phase currents with a peak of 200 (per slot) Amps is applied	67
3.15	Normal stress at the middle of the airgap when a sinusoidal current when 3-phase current with a peak of 200 Amps (per slot) is applied.	68
3.16	Shear stress at the middle of the airgap when a sinusoidal current when 3-phase current with a peak of 200 Amps (per slot) is applied.	68
3.17	Horizontal and vertical force versus eccentricity for the induction machine considered for Case Study I when 3-phase currents with a peak of 200 Amps (per slot) is applied.	69
3.18	Horizontal and vertical forces for 3-phase currents with different peaks (per slot) in the stator for the induction motor considered for case study I.	69
3.19	FE mesh of permanent magnet alternator (PMA).	70
3.20	Contour plot of magnetic vector potentials of the PMA considering permanent magnet excitation only.	71
3.21	Normal component of flux density in the middle of the airgap of the PMA.	71
3.22	Tangential component of flux density in the middle of the airgap of the PMA (when the rotor is concentric with the stator).	72

3.23	Normal stress in the middle of the airgap of the PMA (when the rotor is concentric with the stator).	72
3.24	Shear stress in the middle of the airgap of the PMA (when the rotor is concentric with the stator).	73
3.25	Forces on the rotor along x-direction versus eccentricity for the PMA.	73
3.26	True critical speed when negative stiffness due to UMP is also considered along with mechanical stiffness versus predicted critical speed of the PMA.	74
3.27	Dimension of the slot.	75
3.28	A FE mesh.	76
3.29	A FE mesh.	76
3.30	Flux contour with non-magnetic slot wedge with current density of 15 A/mm ²	77
3.31	Flux contour with magnetic slot wedge with current density of 15 A/mm ²	77
3.32	Normal component of flux density in the airgap with current density of 15 A/mm ² for non-magnetic slot wedge.	78
3.33	Normal component of flux density in the airgap with current density of 15 A/mm ² for magnetic slot wedge.	78
3.34	Tangential component of flux density in the airgap with current density of 15 A/mm ² for non-magnetic slot wedge.	79
3.35	Tangential component of flux density in the airgap with current density of 15 A/mm ² for magnetic slot wedge.	79
3.36	Normal stress in the airgap with current density of 15 A/mm ² for non-magnetic slot wedge.	80
3.37	Normal stress in the airgap with current density of 15 A/mm ² for magnetic slot wedge.	80
3.38	Schematic view of an electrical machine with an overhung rotor. . . .	82
3.39	Equivalent system.	82
4.1	An electric circuit (for illustration purpose only).	107

4.2	Flow diagram showing the different transformations of stator currents.	108
4.3	Stator of an induction machine showing the winding connection. Red, blue and yellow colours show the three different phases.	109
4.4	Winding connection of a 4-pole, 3-phase Induction Motor.	109
4.5	Part of the stator core discretised with three 4-noded elements.	110
4.6	Stator slot with two sets of coil 1 and 2.	110
4.7	One Stator slot shown in Figure (4.6) showing the finite element nodes when discretized with two elements.	111
4.8	4-pole, 3-phase Induction Motor with a Bridge Configured Windings.	111
4.9	Rotor of an induction machine with 32 bars.	112
4.10	Flow diagram showing the different transformation of rotor.	113
4.11	First three modes of conduction of a typical rotor bar.	114
4.12	A notional stator of an electrical machine.	115
4.13	A notional rotor of an electrical machine.	115
5.1	Cross section of rotor end-rings.	129
5.2	Cross section of rotor end-rings with seven links (three along the circumferential and four along the radial direction).	129
5.3	Stator, rotor and airgap of an electric machine.	130
6.1	Rotor movement modeling by airgap stitching method.	157
6.2	Rotor movement modeling by central circle method.	157
6.3	One quarter of an electric machine discretized with 4-noded quadrilateral and 3-noded triangular finite elements.	158
6.4	Rotor and stator with common central circle.	158
6.5	Stator currents of an induction machine by airgap stitching method when slip = 10% and supply voltage = 20V.	160
6.6	Rotor currents of an induction machine by airgap stitching method when slip = 10% and supply voltage = 20V.	160

6.7	Stator currents of an induction machine by central circle method when slip = 10% and supply voltage = 20V.	161
6.8	Rotor currents of an induction machine by central circle method when slip = 10% and supply voltage = 20V.	161
7.1	A simple electromagnetic device.	179
7.2	FE Mesh of the model (region A and region B).	179
7.3	Contour plot of magnetic potentials.	180
7.4	Currents in the region A, i_a from linear, approximateI and full non-linear methods for case study I.	180
7.5	Currents in the region B, i_b from linear, approximateI and full non-linear methods for case study I.	181
7.6	Currents in the region A, i_a from linear, approximateI and full non-linear methods for case study II.	181
7.7	Currents in the region B, i_b from linear, approximateI and full non-linear methods for case study II.	182
7.8	Currents in the region A, i_a from approximateI, approximateII and full non-linear methods for case study II.	182
7.9	Currents in the region B, i_b from approximateI, approximateII and full non-linear methods for case study II.	183
8.1	Schematic diagram of an induction machine.	199
8.2	Finite element model of the induction machine.	200
8.3	Natural speed versus rotor speed.	201
8.4	First four modes of the system.	201
8.5	Equalising current per meter of axial length in phase A bridge for an eccentricity of 2% of the airgap and when supply frequency is 25 Hz and slip is 2%.	202
8.6	Equalising current per meter of axial length in phase B bridge for an eccentricity of 2% of the airgap and when supply frequency is 25 Hz and slip is 2%.	202
8.7	Equalising current per meter of axial length in phase C bridge for an eccentricity of 2% of the airgap and when supply frequency is 25 Hz and slip is 2%.	203

8.8	Equalising current per meter of axial length in phase A bridge for an eccentricity of 10% of the airgap and when supply frequency is 25 Hz and slip is 2%.	203
8.9	Equalising current per meter of axial length in phase B bridge for an eccentricity of 10% of the airgap and when supply frequency is 25 Hz and slip is 2%.	204
8.10	Equalising current per meter of axial length in phase C bridge for an eccentricity of 10% of the airgap and when supply frequency is 25 Hz and slip is 2%.	204
8.11	Energy transfer to the electrical system from the mechanical motion due to forward whirling.	207
8.12	Energy transfer to the electrical system from the mechanical motion due to backward whirling.	207
9.1	Stator of an electrical machine showing the winding connection. Red, blue and yellow colours show the three different phases.	211
9.2	4-pole, 3-phase induction motor with a bridge configured windings.	211
10.1	Experimental setup.	226
10.2	MMF harmonics with fractional pitch - $\frac{6}{9}$ of the stator windings.	227
10.3	A simply supported beam with a concentrated load.	227
10.4	Test setup of impact hammer excitation experiment.	228
10.5	Experimental setup showing the stator with the strain gauges.	229
10.6	Output voltage of the strain gauge amplifier when the load is applied along x-direction.	229
10.7	Output voltage of the strain gauge amplifier when the load is applied along y-direction.	230
10.8	A schematic diagram of the experimental rig (all dimensions are in mm).	230
10.9a	Excitation points on the base of the experimental rig.	231
10.9b	Excitation points on the shaft of the experimental rig.	231
10.10	Frequency responses from the strain gauge in dB (V/V) for non-rotating shaft.	232

10.11	Mode shape at 1.35 Hz. 'Cyan' and 'red' colours show the un-deflected and deflected rotor respectively. 'Green' and 'blue' colours show the un-deflected and deflected base respectively.	233
10.12	Mode shape at 58.61 Hz. 'Cyan' and 'red' colours show the un-deflected and deflected rotor respectively. 'Green' and 'blue' colours show the un-deflected and deflected base respectively.	233
10.13	Mode shape at 65.78 Hz. 'Cyan' and 'red' colours show the un-deflected and deflected rotor respectively. 'Green' and 'blue' colours show the un-deflected and deflected base respectively.	234
10.14	Mode shape at 72.39 Hz. 'Cyan' and 'red' colours show the un-deflected and deflected rotor respectively. 'Green' and 'blue' colours show the un-deflected and deflected base respectively.	234
10.15	Noload supply voltages from numerical model as well experiments when supply frequency is 20 Hz.	235
10.16	Noload stator currents from numerical model as well experiments when supply frequency is 20 Hz.	235
10.17	Noload supply voltages from numerical model as well experiments when supply frequency is 25 Hz.	236
10.18	Noload stator currents from numerical model as well experiments when supply frequency is 25 Hz.	236
10.19	Supply voltages for locked rotor test from numerical model and experiments.	237
10.20	Stator currents from numerical and experiments for locked rotor test.	237
10.21	Equalising voltages from experiments when supply frequency is 20 Hz.	238
10.22	Equalising currents from experiments when supply frequency is 20 Hz.	238
10.23	Equalising voltages from experiments when supply frequency is 25 Hz.	239
10.24	Equalising currents from experiments when supply frequency is 25 Hz.	239
10.25	Frequency response when the supply frequency is 25 Hz with OPEN bridge (blue) and CLOSED bridge (red).	240
10.26	Rotor centre orbit with OPEN and CLOSED bridge when the supply frequency is 25 Hz.	240

List of tables

3.1	Parameters of the 2 kW induction motor	65
3.2	Parameters of the permanent magnet alternator	70
3.3	Parameters of the 2-pole generator	75
3.4	Fourier coefficients of normal stress in the airgap for different levels of currents in the rotor slot	81
6.1	Main electromagnetic parameters of the machine	159
8.1	Main electromagnetic parameters of the machine	199
8.2	Coefficients of the bearing	200
8.3	The minimum periods of a machine with parameters given in Table (8.1) for different slips	205
8.4	Stability chart of the machine at different slips for different voltage levels	205
8.5	Time constants with the parallel paths closed for five different slips in case of forward whirling	206
8.6	Time constants with the parallel paths closed for five different slips in case of backward whirling	206
10.1	MMF harmonics with different slot combinations	226

Chapter One

Introduction

1.1 General

Rotating electrical machines play a very important role in industry. Electric motors consume something in the order of two-thirds of all electrical power used in industry. Therefore, the efficiency of these motors is also a major environmental factor. Besides, there is also a strong industrial demand for reliable and safe operation of rotating machines (Devanneaux, *et al.*, 2003).

Most of the electrical machines comprise two parts: the cylindrical rotating member called the rotor and the annular stationary member called the stator. Figure (1.1) shows an electrical machine showing the stator and the rotor. The rotor has an axial shaft which is carried on bearings at each end. The rotor core and stator core are both constructed from a stack of sheet steel laminations. The constructional and certain other distinguishing features separate electrical machine into different categories. Among these machines, the induction machine is by far the most common because of its relatively simple, robust construction and low price.

1.2 Eccentricity in an electrical machine

Eccentricity refers to an offset between the centre of the rotor core and the centre of the stator core at any given axial position along the motor length. Clearly, eccentricity can vary along the length. In this thesis, we are concerned only with machines in which the stator core is rigidly fixed and the rotor core is relatively short and rigid. Such rotor cores can translate in directions normal to the axis of rotation and they can also rotate about axes normal to the rotation axis. In this thesis, we restrict attention to

pure translation for reasons which are well-founded. These reasons are exposed further in a chapter about rotordynamic modelling. Eccentricity is described as being either static or dynamic depending on whether the offset between the core centres is constant or whether it is moving (usually in an orbit of some description). Static eccentricity occurs when the axis of the rotor is not being aligned with that of the stator although it still rotates about its own axis. This can occur for example simply due to manufacturing tolerances. Excessive static eccentricity can also occur when the bearings are incorrectly positioned or become worn. Figures (1.2) and (1.3) show concentric and eccentric rotor respectively. Dynamic eccentricity is caused by the centre of rotation of the rotor not being aligned with the rotor axis. The usual causes of dynamic eccentricity are also manufacturing tolerances, wear and incorrect manufacture. Rotor ‘whirl’ near critical speed is another source of dynamic eccentricity and is an important consideration in large, flexible-shaft machine.

One result of eccentricity is that an uneven distribution of electromagnetic field is produced in the airgap of an electrical machine. These uneven electromagnetic fields in the air gap gives rise to electromagnetic forces between the rotor and stator and termed as Unbalance Magnetic Pull (UMP). The net magnetic forces may often be significant and the direction of these net forces is often such that they tend to pull the rotor away from the centre position. In other words the magnetic field within every rotating electrical machine creates a coupling between the eccentricity of the rotor relative to the stator and the net magnetic force. This “coupling” behaves like a bearing with very complicated (speed, frequency and load dependent) properties that is not fully understood. The effect of UMP on the dynamics of a machine is often equivalent to a strong negative stiffness between rotor and stator. In extreme cases, if the mechanical stiffness of the rotor and its support is not sufficiently high, the rotor of the machine may even pull over and knock the stator when the machine is energized. In less severe cases, the first critical speed of a motor may be reduced by a significant amount.

To study the dynamic behaviour of an electric machine there is a need for an accurate UMP model integrated with an accurate rotordynamic model. The UMP modifies the dynamics of the machine by introducing additional damping and stiffness terms into the mechanical system equations forming a coupling between the mechanical and

electrical behaviour of the machine. Previous works on the study of coupled (mechanical and electromagnetic) behaviour of electric machines have reduced either the electrical or mechanical behaviours to a very simple form.

Understanding the characteristics of the dynamic performance of induction machines is of fundamental importance to design engineers. The present research represents a challenging problem to a dynamicist since a proper design involves a melding of electromagnetic theory, electrical systems and rotordynamics. The existing literature does not provide a general solution. A fuller discussion of the literature is given in the next chapter.

1.3 Motivation

The objectives of this work relate centrally to the *More Electric Engine* movement. Inevitably, engines will have shaft-mounted electromagnetic machines integrated into their structure. Engine design is already critically limited by rotordynamic concerns and the incorporation of electrical machines into engines will have very substantial rotordynamic implications. Work to date on the modelling of UMP in machines has been limited in two main respects:

- Attention has previously been focused almost exclusively on magnetic normal stress at the airgaps as the primary cause of UMP in machines. This focus is now dated – especially where permanent magnet machines are concerned since in these machines, the magnetic normal stress at the airgap is extremely insensitive to electrical or mechanical eccentricity (lack of symmetry) and magnetic shear stresses can dominate the production of UMP.
- Attention has previously been focused on modelling the electromagnetic behaviour separately from the mechanical - allowing only very simple (low-dimensional) models for the mechanical dynamics involved. In an aero-engine context, the mechanical dynamics are relatively high dimensional (i.e. a significant number of resonance frequencies contribute to the relative movements of the rotor and stator) and for this reason, it is necessary to provide for the development of rotordynamic models without limitations on either the mechanical or electromagnetic complexity.

1.4 Aim of the research

The objectives of this research can be summarized as follows

- To develop a coupled model combining the electromagnetic dynamics and rotordynamics of an electrical machine to study the electromechanical interaction. This model should be able to examine some low-cost passive and semi-active provisions for the adjustment of UMP. This outcome will be very worthwhile gains in cost effectiveness and efficiency of a number of classes of system powered by electrical machine.
- To construct an experimental rig and demonstrate how UMP can be reduced. The results from the coupled model will be compared with that from the experimental rig.

1.5 Organisation of the thesis

This thesis is organised in the following chapters.

Chapter 1 introduces eccentricity and unbalanced magnetic pull of an electric machine.

In **Chapter 2** the literature review of analytical and numerical calculation of unbalanced magnetic pull is described. Methods of reducing unbalanced magnetic pull are also discussed in this chapter.

Chapter 3 is concerned with the development of a 2D electromagnetic finite element modelling to analyse any electromagnetic or magnetic devices including the electrical machines. A finite element code is developed in MATLAB environment. This FE code comprises a pre-processor, postprocessor and a solver. The solver is capable of solving linear as well as non-linear electromagnetic problem. The efficiency of this code is verified with the results of commercial software developed by the Department of Electrical Engineering of the University of Bath, UK. Some case studies have been performed using this code, where the static eccentricity of two different electrical

machines is calculated and the performance of an electrical generator with and without magnetic slot wedge in the slots is compared.

The electromagnetic finite element model developed in Chapter 3 is generic and not restricted to electrical machines. In general electrical machines are voltage fed, so this model needs some special treatment to handle it. Different transformation methods are discussed in **Chapter 4** with special reference to induction machines.

Chapter 5 discusses the modelling of an electro-magneto-mechanical device. The circuit equation of an electro-magneto-mechanical device is coupled to its field equation incorporating geometry change and magnetic non-linearity in the modelling.

Chapter 6 describes the time-marching simulations of rotating electric machinery. This chapter also discusses two methods to accommodate the movement of the rotor during the time domain simulation. The merits and demerits of these two methods are explained.

Chapter 7 describes methods for calculating steady state currents of induction machine for a concentric as well as an eccentric rotor. This chapter also unveils a novel method called “central circle method” for calculating steady state currents of induction machine with a concentric rotor. One of the main attractions of “central circle method” is the non-linear model reduction. Non-linear model reduction is attempted for a simple static electromagnetic problem.

Chapter 8 discuss the electromagnetic dynamics and mechanical dynamics in its full glory. An integrated model of electromagnetic dynamics and mechanical dynamics is proposed. The stability of the coupled system is studied. A 3-phase induction motor is chosen as an example.

Chapter 9 discusses a passive method for reducing UMP in an electrical machine and its effectiveness is verified with an experimental setup. The working principle of this method is explained in this chapter.

In **Chapter 10** details about the experimental rig are described. The steady state currents from the numerical methods are verified with experimental results. A 3 phase, 2 kW induction motor with a flexible shaft is commissioned for this purpose. The efficiency of the proposed method for reducing UMP is examined.

Chapter 11 concludes the thesis and proposes future work to be undertaken. The present study presents some interesting possibilities for further investigations.

Appendices A and B supplement the thesis with basic electromagnetic formulation, additional formulae and results.

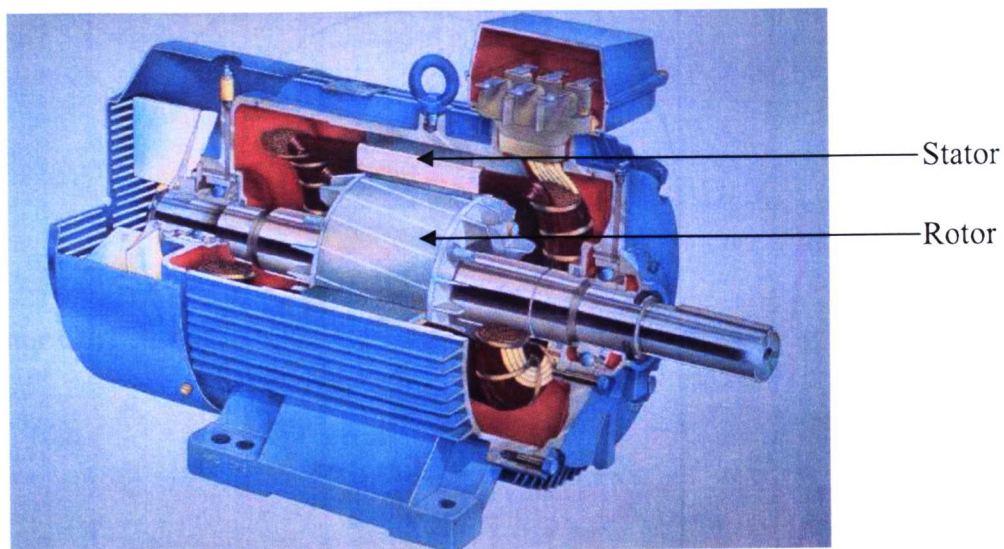


Figure (1.1): An electrical machine

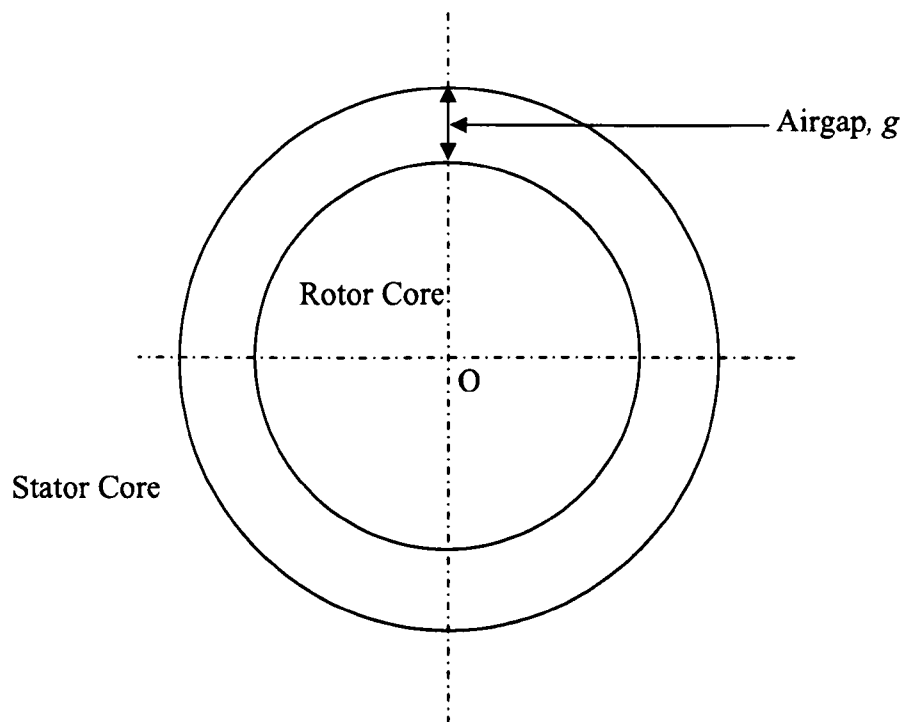


Figure (1.2): A concentric rotor. 'O' is the centre of the axis of rotation

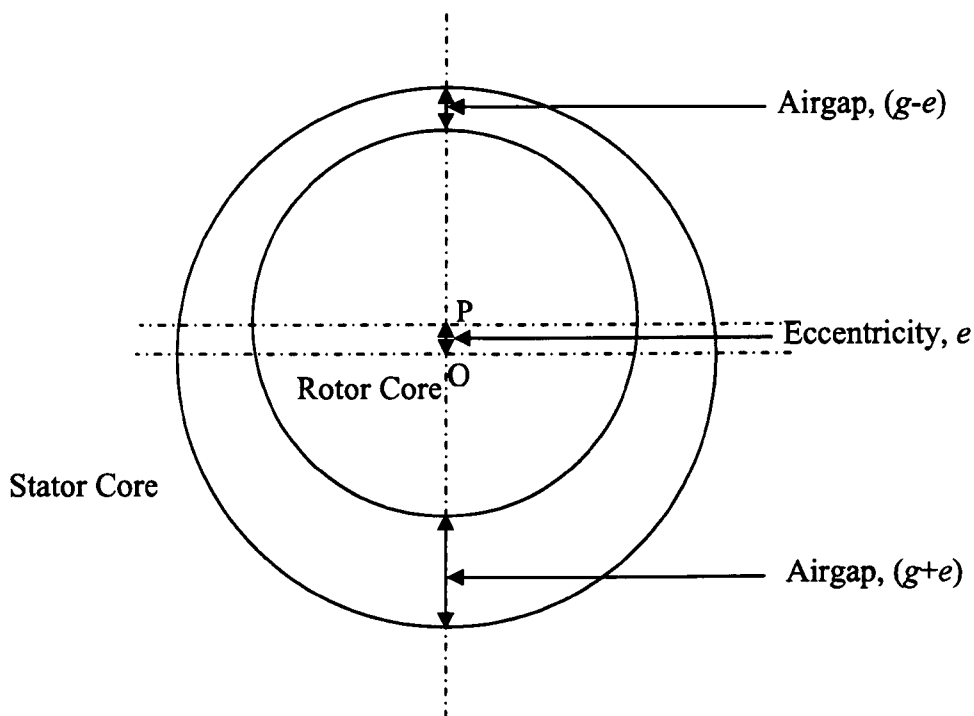


Figure (1.3): An eccentric rotor with static eccentricity. 'P' is the centre of the axis of rotation

Chapter Two

Literature Review

2.1 Introduction

This chapter presents the literature review of unbalanced magnetic pull (UMP) and its interaction on the mechanical dynamics. The calculation of UMP in electrical machines, the examination of practical means of reducing this pull, and its effects on the dynamics of the machine are subjects which have received considerable attention over the last 50 years. The unbalanced force necessitates an increase in shaft diameter and bearings size and has the effect of reducing critical speed, and the practical importance of its accurate prediction is beyond question (Binns and Dye, 1973). There are noticeable differences among the published papers in the method of UMP calculation and also in the method of integrating UMP with the mechanical dynamics model.

In 1963 Kaehne (1963) presented a detailed literature review on UMP in electrical machines. Two recent literature reviews in this topic are done by Tenhunen (2003) and Dorrell (1993). It is not immediately obvious how the various published work on UMP should be classified. Mainly based on the method of calculation the review of the published works is classified into following five main categories and they are discussed individually:

1. Analytical methods of calculating UMP
2. Numerical methods for the solution of static magnetic fields
3. Numerical methods for the computation of magnetic forces from fields
4. Integration of electromagnetic and mechanical model
5. Experimental findings of UMP

Before discussing the above points it will be wise to introduce the general observations about the origin of UMP and its effects. A few analytical methods which are commonly used while calculating UMP are also discussed.

2.2 General observations about the origin of UMP and its effect

An electrical machine consists of two parts: a rotating part which is called the rotor and a stationary part called the stator. The UMP may be defined as a net force between the rotor and the stator of an electric machine, which results from a difference in the airgap flux densities on opposite sides of the machine. It can be said that UMP comes to exist because of a lack of symmetry in the magnetic field linking the rotor and the stator. This lack of symmetry can arise because of various reasons, for example the effects of slots, non-symmetrical stator windings, saturation phenomena and eccentric rotor in a stator bore. Although the UMP arising from all sources is considered in this study emphases on the UMP generated from the eccentricity of the rotor. Because of the eccentricity in the airgap of an electric machine, in addition to the main field two additional fields also occurs i.e. $p \pm 1$. Here p is the number of pole pairs. The main field produces the torque and these two additional fields gives rise to the UMP. A general view on this is given later in this study. An eccentric machine having pole-pairs of higher than one will have always these additional two fields. For a 2 pole machine only one additional field is present since the other field changes into homopolar.

The UMP from the static eccentricity is stationary with respect to the stator frame of reference and tends to act in the direction of the smallest airgap and the UMP from the dynamic eccentricity has a rotating component with respect to the stator frame of reference. Figures (2.1) and (2.2) show the static UMP and the dynamic UMP respectively.

The UMP modifies the dynamics of the system by introducing additional terms in the damping and stiffness matrices of the equation of motion. Apart from that the UMP also introduces an additional forcing term in the right hand side of the equation of motion.

2.3 Airgap permeance

The basic theory of the airgap permeance harmonics is more than 50 years old. The airgap permeance is the inverse of its reluctance. Figure (2.3) shows an eccentric rotor. If the airgap happens to be very small compared to the outer radius of the rotor and the airgap with respect to the stator reference frame can be approximated as

$$\delta(\alpha, t) \approx \delta_m [1 - \varepsilon \cos(\alpha - \omega_\varepsilon t - \varphi_\varepsilon)] \quad (2.1)$$

with the relative eccentricity, $\varepsilon = \frac{e}{\delta_m}$. Here δ_m , is average airgap length, φ_ε , is the phase angle and ω_ε is the whirling frequency. In case of static eccentricity $\omega_\varepsilon = 0$.

The airgap permeance varies inversely with its length. Inverting airgap length and resolving into an airgap permeance Fourier series produces

$$\Lambda(\alpha) = \frac{\mu_0}{\delta(\alpha, t)} = \sum_{n=0}^{\infty} \Lambda_n \cos n(\alpha - \omega_\varepsilon t - \varphi_\varepsilon) \quad (2.2)$$

The Fourier coefficients Λ_n are

$$\Lambda_n = \begin{cases} \frac{\mu_0}{\delta_m} \frac{1}{\sqrt{1-\varepsilon^2}} & (n=0) \\ \frac{2\mu_0}{\delta_m} \frac{1}{\sqrt{1-\varepsilon^2}} \left(\frac{1-\sqrt{1-\varepsilon^2}}{\varepsilon} \right)^n & (n>0) \end{cases} \quad (2.3)$$

2.4 Conformal transformation technique

Another analytical method called the conformal transformation technique is also used sometimes to calculate UMP in an eccentric rotor. In the airgap permeance method the expression for the airgap MMF is usually assumed to be sinusoidal of known amplitude. This usual assumption of sinusoidal MMF is a poor approximation

especially if there are parallel stator paths with a non-uniform airgap. The conformal transformation technique has an edge over the airgap permeance on this point and can be used to study different combination of windings. A detailed explanation of conformal transformation techniques is given by Dorrell and Smith (1994). This technique transforms the machine from being magnetically asymmetric to one which is magnetically symmetric but electrically asymmetric, i.e. to a machine which has a uniform airgap but non-uniform winding distribution.

The conformal transformation of two eccentric circles to two concentric circles is achieved by utilizing a simple inversion as

$$\bar{z} = \frac{1}{t} \quad (2.4)$$

By finding a proper value of d in Z-plane and c in T-plane, the eccentric rotor machine as represented by circles 1 and 2 shown in Figure (2.4) can be mapped on the T-plane as two concentric circles shown in Figure (2.5). The transformation results in an irregular slot pattern in the T-plane and hence any method based upon this technique must be capable of accommodating general asymmetrical windings. The flux density distribution round the stator surface is different in the Z- and T-planes but related by a transformation matrix. The machine represented in the T-plane can be used to find an impedance matrix linking the stator currents and the terminal voltages.

2.5 Analytical methods of calculating UMP

Until recently, the analytical methods for calculating the electromagnetic forces have been the most widely used. Most of the early works of the unbalanced magnetic pull is analytical and the most favourite method is the airgap permeance method. According to Dorrell (1994) the theory of the rotating fields in the airgap i.e. airgap permeance method is the most common analytical method to calculate the forces acting between the rotor and the stator and is widely used in the studies of the noise and vibrations in electrical machines. Based on this theory, Freise and Jordan (1962) derived the equations for the forces caused by the eccentricity of asynchronous and synchronous machines for symmetrical winding conditions. In these equations

they used damping factors for taking into account the force reduction caused by the equalizing currents. They also noticed that these currents change the direction of the force from the direction of the shortest airgap. In addition, they discussed the effect of eccentricity forces on the critical speed of a rotor.

Smith and Dorrell (1996) developed an analytical model for cage induction motors considering the static eccentricity of the rotor based on the airgap permeance approach including the stator and the rotor MMF harmonics. Unlike the method proposed by Freise and Jordan (1962) this method can accommodate different series/parallel winding connections and this is achieved by resolving the stator windings into harmonic conductor density distribution. The saturation and slotting effects are not considered in their calculation. It is also mentioned that the parallel winding connections can lead to the localised saturation of the leakage paths around the coils carrying the largest currents and the series winding connections can lead to the localised saturation of the main magnetising paths around the area corresponding to the shortest airgap. The horizontal and the vertical components of UMP by the stator and the rotor airgap field components are given by

$$f_h = \frac{w\pi d}{4\mu_0} \text{Re} \left\{ \left(\bar{B}_s^n \bar{B}_R^{*(n-1)} + \bar{B}_s^n \bar{B}_R^{*(n+1)} \right) + \left(\bar{B}_s^n \bar{B}_R^{-(n-1)} + \bar{B}_s^n \bar{B}_R^{-(n+1)} \right) e^{j2\alpha} \right\} \quad (2.5)$$

$$f_v = \frac{w\pi d}{4\mu_0} \text{Im} \left\{ \left(\bar{B}_s^n \bar{B}_R^{*(n-1)} + \bar{B}_s^n \bar{B}_R^{*(n+1)} \right) + \left(\bar{B}_s^n \bar{B}_R^{-(n-1)} + \bar{B}_s^n \bar{B}_R^{-(n+1)} \right) e^{j2\alpha} \right\} \quad (2.6)$$

Here w is the machine effective stack length, d is the mean airgap diameter, \bar{B}_s and \bar{B}_R are the amplitudes of the stator and rotor flux density, n is the stator winding harmonics, ω is the supply frequency, μ_0 is the permeability of free space and $*$ represents the complex conjugate.

It is clear from the UMP expressions that generally two force components are present, a constant force and an oscillating component at twice the line frequency. It is also evident that the force components are produced by the interaction of the two fields whose pole pair differs by one i.e. n and $n+1$ or n or $n-1$. It is concluded from the

analytical study that in a series-connected winding the flux density distribution is non-sinusoidal with the flux concentrating around the narrowest airgap, hence UMP is significant whereas in a parallel-connected windings the flux density distribution is much more sinusoidal and hence the UMP levels are greatly reduced. It is also shown by Smith and Dorrell (1994) that the direction of the UMP deviates slightly from the narrowest airgap.

Using the airgap permeance method Schuisky (1971) developed the expressions for the UMP and studied different kinds of machine i.e. synchronous, asynchronous and dc machine under the static as well as the dynamic eccentricity. He also incorporated the different winding connections and saturation effect in his analytical method. The occurrence and magnitude of damping of UMP are dependent first and foremost on the type and connections of winding. The homopolar flux is not considered in his expression and he stated that it has no influence on the UMP. Later Belmans *et al.* (1987) showed that the homopolar flux does contribute to the UMP.

The practical significance of unbalanced magnetic pull is explained in details by Frohne (1967). He also used the airgap permeance method to calculate the UMP and mentioned that UMP always acts in the direction of the shortest airgap. It is shown by other researchers that there is a slight deviation from the direction of the shortest airgap. For the static eccentricity the UMP is constant. The dynamic eccentricity gives rise to a rotating component. The dynamic UMP exhibits effects that are similar to mechanical unbalance. These are often referred to as magnetic unbalance. According to him, among the practical effects of UMP, attention must be also paid to the following:

1. The increase in the static shaft deflection.
2. The reduction of the critical speed of the rotor

He also showed that UMP is generated by the interaction of two fields with a pole-pair difference of one. The influence of UMP on the deflection and hence the critical speed of the shaft is demonstrated. In a simplified method in which the saturation of the iron is ignored, a rather high value of UMP is obtained and this might lead to an uneconomic machine design and particularly to erroneous assessment of vibrational behaviour. He proposed one method in which the magnitude of UMP can be calculated taking into account the saturation and damping.

Berman (1993) presented a detailed analytical expression of UMP incorporating the effect of the stator winding with the equalising connections.

Belmans *et al.* (1987) used the airgap permeance method to calculate UMP in a two-pole induction machine for the static eccentricity. He also established a relationship between the UMP and the homopolar flux which is ignored by previous researchers in their study. He also showed that the direction of UMP differs from the direction of the shortest airgap. According to him $p+1$ components of UMP in the case of a two-pole machine are damped by the equalising currents but the vibratory components with twice the supply frequency, which occur due to the homopolar flux are not influenced by the equalising currents and therefore, do not depend upon the machine load. Here p is the pole pair of the machine.

Freise and Jordan (1962) showed that two-pole machines are special cases where the eccentricity of the rotor tends to cause the homopolar fluxes. This flux crosses the air gap only once and returns via the shaft and casing. The theory of the rotating field shows that the homopolar flux can exist in any machine but it is most likely to be significant in two-pole machine (Kovacs, 1977).

Haase *et al.* (1972), Fruchtenicht *et al.* (1982), Holopainen *et al.* (2005), Guo *et al.* (2002), Joksimović (2005) are a few of the researchers who used the airgap permeance method to calculate the UMP in the study of noise and vibration calculation of electrical machines.

Binns and Dye (1973) determined the relationship between the UMP and the static eccentricity of a cage rotor through measurements of the electromagnetic field at the rotor surface, and the significance of the tangential-flux component in the machine airgap is assessed. Figure (2.6) shows the radial and tangential components of magnetic flux density in the airgap of an electrical machine. It is mentioned in their work that the UMP can be related to the unbalance and slip frequency flux components by using the surface-integral methods of force evaluation, through the simple equation

$$P = \frac{B_{\sigma} B_u S}{2\mu_o} \quad (2.7)$$

where B_{σ} is slip-frequency component of flux density (peak), B_u is unbalanced component of flux density (peak), S is surface area of surface of integration and μ_o is the permeability in free space.

According to Binns and Dye (1973), the measurement of the tangential-flux components shows that these can be neglected in any further work on UMP.

Another method for UMP calculation is the conformal transformation technique which is not as popular as the airgap permeance method. Swann (1963) put forwarded a method to calculate UMP upon the conformal transformation technique because of its capability of modelling different winding connections. Later Dorrell and Smith (1994) developed this method and coupled to a winding impedance approach to demonstrate the reduction of the static UMP of a typical stator winding with the parallel paths together with the unbalanced winding currents.

Though quite a large amount of work has been done to calculate unbalanced magnetic pull using analytical methods, many still suffer from some drawbacks. One of the main drawbacks of the analytical methods is that the magnetic saturation of the iron is not incorporated in the analytical formulation. Frohne (1967) and Schuiskey (1971) have incorporated the magnetic saturation in the analytical UMP calculation but these are over simplified. Most of the induction machines are skewed but none of the researchers has incorporated this design in their analytical model.

2.6 Numerical methods for the solution of the static magnetic field

The relationship between the magnetic field intensity, $\{\mathbf{H}\}$ and the magnetic flux density, $\{\mathbf{B}\}$ is a property of the material in which the field exists, thus

$$\{\mathbf{B}\} = \mu\{\mathbf{H}\} \quad (2.8)$$

where μ is the permeability. $\{\mathbf{H}\}$ is determined by a combination of permanent magnet distribution and distribution of currents. Currents are induced by changing $\{\mathbf{B}\}$ but this issue can be considered separately. The problem of computing $\{\mathbf{B}\}$ for given $\{\mathbf{H}\}$ is a static magnetic field problem. To solve a static magnetic field problem numerically, an appropriate method has to be chosen. The most important methods prescribed by Hameyer and Belmans (1999) are listed below:

1. Finite Element Method (FEM)
2. Finite Difference Method (FDM)
3. Boundary Element Method (BEM)
4. Magnetic Equivalent Circuit (MEC)
5. Point Mirroring Method (PMM).

The advantages and disadvantages of the above methods are given in Figure (2.7). The FEM is widely used in any engineering analysis and extensively used in the analyses of structures, solids, electromagnetics, heat transfers and fluids. The phenomenal success of the FEM is mostly related to the development of computational power. The FEM is a technique for solving partial differential equations of a continuum domain. The continuum is discretised into a finite number of parts known as the elements, the behaviour of which is specified by approximate functions. The solution of this discrete problem is similar to the standard discrete problem. Details about the FEM is widely discussed by Zienkiewicz and Taylor (1989), Bathe (1996), Sylvester and Ferrari (1996).

Nowadays the FEM is widely used for the analysis of electromagnetic field problems because of its flexibility. Bastos and Sadowski (2003) gave a detailed explanation about the electromagnetic modelling by the FEM in his book. Williamson *et al.* (1990) described two methods for predicting the performance of cage induction motors using the FEM. The first method was used for the steady state analysis of an induction motor. The parameters of the equivalent circuit model were calculated using the FEM. The second method is suitable for the transient analysis and uses a time-stepped coupled circuit model for the machine together with the magneto-static FE field solutions that are used to update the circuit parameters.

The FE analysis of induction machines needs further attention than the other electrical machines because finite element should be capable of handling induced currents in the rotor. The field of an induction motor must be solved with a method that takes the time-dependence into account.

Perhaps the difficulties associated with the solution of time-dependent nonlinear fields have hindered the progress of the numerical analysis of induction motors. The first publication dealing with this problem appeared at the beginning of the 1980's (Arkkio, 1987). The basic theory of the finite element method and the use of it to analyse electrical machines is presented in details by Arkkio (1987), Hameyer and Belmans (1999) and Silvester and Ferrari (1996).

Attention has moved towards the time-stepping finite element analysis of electrical machines because of the rapidly developing power and speed of computers. For most types of electrical machines the modelling is of a two-dimensional (Williamson, 1994). Williamson (1994) mentioned that although three-dimensional modelling gives more accurate results than two-dimensional, its associated high computational cost means it is still beyond the bounds of economic viability.

Most published finite-element based analyses of cage motors employ an eddy current formulation for the rotor (Williamson *et al.*, 1990), i.e., the current density in a rotor bar is computed from the local rate of change magnetic vector potential (Arkkio, 1987), (Ho, *et al.*, 1999) and (Ho, *et al.*, 2000). Effects due to the three-dimensional nature of the rotor, such as the end-ring resistance, are taken into account by modifying the rotor conductivity or by combining the rotor loop voltage equations with the time stepped field equation. Such methods are both elegant and powerful but suffer from two distinct disadvantages. Firstly, no satisfactory technique appears to have been found for dealing with machines with skewed rotors, and secondly the nonlinear field solution must itself be time-stepped, so a very long solution time is required. The coupled-circuit method presented by Williamson *et al.* (1990) is capable analysing the machines with skewed rotors and is believed to have features to reduce the solution time required.

A suitable finite-element software package can be used to study UMP in detail taking into account the full magnetic circuit and eccentric airgap, and the influence of saturation. This was done by Benaragama (1982) although without the influence of the rotor eddy currents. Here is an example mentioned in Stoll (1997): a typical 500 MW generator on open circuit with a 10% static eccentricity was found to produce a force per unit rotor length of 23.4kN when the direct axis of the rotor is towards the small airgap. In this static finite element calculation, the damping effect of eddy currents is excluded.

The use of the parallel windings reduces the net UMP by allowing different amplitude currents to flow in the parallel branches. Salon *et al.* (1990) and DeBortoli *et al.* (1993) used a time-stepping finite element method for studying the equalizing currents setup by an eccentric rotor in the parallel circuits of the stator windings. The FEM is used to compute the eccentricity induced harmonics of airgap flux density and UMP acting on the rotor. Different stator winding schemes such as series, series/parallel, and parallel were investigated.

The calculation of force using numerical methods has been a popular research topic during the last few decades, but the numerical field computation methods have only been rarely used for analysing eccentric rotors (Tenhunen, 2003). It is shown that there is a significant tangential force that exists in the airgap because of the eccentricity which was neglected in most of the analytical calculations. Figure 2.8 shows the frequency response function at no load condition showing the radial and tangential components of the force.

Arkkio *et al.* (2000) presented a simple parametric force model for the electromagnetic forces acting between the rotor and the stator when the rotor is in whirling motion. The model parameters of an electric motor were determined by numerical simulations including the non-linear saturation of the magnetic materials. The numerical results were validated by extensive measurements.

Amirulddin *et al.* (2005) presented a simulation model capable of investigating the effect of induction-machine design on the generation and control of the radial forces. They investigated the radial force production in both cage and wound rotor machines,

and introduced a mixed field orientation method for the decoupled control of the torque and radial forces.

From the above it has been observed that there is a strong need for a coupled numerical model where the UMP is calculated and then combined with the mechanical model to study the behaviours of the coupled system. To the knowledge of the author there is no published literature available on the effect of parallel windings on rotordynamics model.

2.7 Integration of electromagnetic model and mechanical model

If the time constants of electrical and mechanical dynamics happen to be at the same range then the UMP may be large enough to couple both systems. The literatures that have been reviewed in the earlier sections indicate that there has been intensive study on the methods of calculating UMP, but due to rotor eccentricity, there are several other aspects of the UMP which are still unclear. Many authors have tried to obtain the analytical expression of the UMP for any pole-pair induction machine, and only a few authors have studied the vibratory characteristics of the rotor system coupling the UMP with the mechanical model. These are Früchtenicht *et al.* (1982), Belmans *et al.* (1987), Salon *et al.* (1999), Holopainen *et al.* (2002a), Guo *et al.* (2002) and Pennacchi and Frosini (2005).

Früchtenicht *et al.* (1982a) developed an analytic model for the electromechanical forces between the rotor and the stator, when the rotor is in circular whirling motion. The electromagnetic force parameters of this model are determined from the analytical solutions. Using this model together with a simple mechanical rotor model they studied the effects of the electromechanical interaction in a cage induction motor. They also mentioned that total unbalanced force acting on the rotor consists of two rectangular components:

- The first component is the well known unbalanced force which always tends to pull the rotor in the direction of the shortest airgap length and thus being related to the electromagnetic spring constant

- The second component is a force where its line of action always perpendicular to the first component. The second force component acts like an external mechanical damping.

The analytical formula for the stiffness coefficient derived as

$$k_e = -\frac{\pi B_p^2}{4\mu_0} \left[\frac{2R}{\delta_e} - \frac{s_{p+1}^2}{s_{p+1}^2 + \beta_{p+1}^2} \cdot \frac{\xi_{p+1}^2 \cdot \xi_{\text{Schr}, p+1}^2}{1 + \sigma_{gR, p+1}} \cdot \left(\frac{R}{\delta_e} - p - 1 \right) + \right. \\ \left. - \frac{s_{p-1}^2}{s_{p-1}^2 + \beta_{p-1}^2} \cdot \frac{\xi_{p-1}^2 \cdot \xi_{\text{Schr}, p-1}^2}{1 + \sigma_{gR, p-1}} \cdot \left(\frac{R}{\delta_e} + p - 1 \right) \right] \quad (2.9)$$

and the formula for the damping coefficient derived as

$$d_e = -\frac{\pi B_p^2}{4\mu_0 \Omega_m} \left[\frac{s_{p+1} \cdot \beta_{p+1}}{s_{p+1}^2 + \beta_{p+1}^2} \cdot \frac{\xi_{p+1}^2 \cdot \xi_{\text{Schr}, p+1}^2}{1 + \sigma_{gR, p+1}} \cdot \left(\frac{R}{\delta_e} - p - 1 \right) + \right. \\ \left. - \frac{s_{p-1} \cdot \beta_{p-1}}{s_{p-1}^2 + \beta_{p-1}^2} \cdot \frac{\xi_{p-1}^2 \cdot \xi_{\text{Schr}, p-1}^2}{1 + \sigma_{gR, p-1}} \cdot \left(\frac{R}{\delta_e} + p - 1 \right) \right] \quad (2.10)$$

where $s_{p\pm 1}$ are the slips of the rotor with respect to the eccentricity harmonic fields, β_{p+1} is the resistance-reactance ratios of the rotor mesh, $\xi_{p\pm 1}$ is the winding factors of the eccentricity harmonics, $\xi_{\text{Schr}, p\pm 1}$ is the skew factors of the eccentricity harmonics, and $\sigma_{gR, p\pm 1}$ is the geometrical leakage coefficients of the eccentricity harmonics. Using these coefficients, together with the Jeffcott rotor model including the contributions of the external and internal damping, Früchtenticht *et al.* (1982b) developed an electromechanical model to study the effects of electromechanical interaction on the rotordynamic stability.

Belmans *et al.* (1987a) developed an analytical model to calculate the electro magnetically generated forces due to the eccentric rotor of a two-pole induction motor with a flexible shaft. They derived an analytical expression for electro magnetically induced spring constant and also for damping coefficient. These expressions includes the contribution from the homopolar flux exist in the machine. It is shown that due to

electromagnetically induced forces the critical speed of the machine is reduced. The natural frequency of a coupled electro-mechanical model

$$\omega_c = \sqrt{\left(\frac{K_{mech} - K_{mag}}{m} \right)} \quad (2.11)$$

where K_{mech} is the mechanical spring constant and K_{mag} is the electromagnetically induced spring constant. The electromagnetically induced damping ratio is

$$\xi_c = \frac{C_{mech} - C_{mag}}{2\omega_c m} \quad (2.12)$$

where C_{mech} is the mechanical damping coefficient and C_{mag} is the electromagnetically induced damping coefficients. The rotor is assumed to be a Laval rotor for the machine considered. It is concluded that if the electro magnetically induced damping coefficient is larger than the mechanical damping coefficient, instability will occur.

The previous research on the coupling of electromagnetic model with the mechanical model has not been conclusive, in part because it has generally been based on the assumption of synchronous whirling motion (Früchtennicht *et al.*, 1982 and Belmans *et al.*, 1987) and in part because the effects of the saturation of magnetic materials are not included in the analytical force models (Früchtennicht *et al.*, 1982 and Belmans *et al.*, 1987).

Guo *et al.* (2002) studied the non-linear vibratory responses of a Jeffcott rotor excited by the UMP and the eccentric force using a numerical method. The analytical expression of UMP in a three-phase electric machine with any pole-pairs caused by the static and the dynamic eccentricity is derived based on the idea of modulating the fundamental MMF wave by airgap permeance expressed as Fourier series. The conclusions of their study are

- The UMP includes constant and oscillatory components. The frequency of the oscillatory component is twice the supply frequency. If the pole-pair number is larger than three, only the constant component of unbalanced magnetic pull

remains. When the eccentricity is large, the magnitude of the UMP is non-linear.

- Due to the UMP, the natural frequency of the rotor system will be reduced and the magnitude of vibration will become larger. When the relative eccentricity is small, the UMP is constant and the orbits of the rotor centre are axisymmetric.
- When the relative eccentricity is large, the centre orbits are not axisymmetric due to the non-linear UMP. If $p = 1$, the components of UMP are ω_p , $(2\omega_e - \omega_p)$ and $2\omega_e$.

Holopainen *et al.* (2002a) studied the electromechanical interaction between the rotor and the stator and developed an analytical model to study this interaction and the stability of the machine. A lower order linear model, developed by Arkkio (2000), is used for the electromagnetic forces between the rotor and the stator. The parametric force model which includes only two cage-current harmonics and one equation for the total electromagnetic force, can be written in the rotor reference frame as

$$\hat{\underline{i}}_{p-1,t}^r + \tau_{p-1}^{-1} \hat{\underline{i}}_{p-1}^r + a_{p-1} (\underline{p}_{c,t}^r)^* + js\omega_s (\underline{p}_c^r)^* e^{j(S\omega_s t + \vartheta_{b0})} = 0 \quad (2.13)$$

$$\hat{\underline{i}}_{p+1,t}^r + \tau_{p+1}^{-1} \hat{\underline{i}}_{p+1}^r + a_{p+1} (\underline{p}_{c,t}^r + js\omega_s \underline{p}_c^r) e^{j(S\omega_s t + \vartheta_{b0})} = 0 \quad (2.14)$$

$$\underline{F}_e^r(t) = k_e \underline{p}_c^r + c_{p-1} (\hat{\underline{i}}_{p-1}^r)^* e^{j(S\omega_s t + \vartheta_{b0})} + c_{p+1} (\hat{\underline{i}}_{p+1}^r)^* e^{-j(S\omega_s t + \vartheta_{b0})} \quad (2.15)$$

where $\hat{\underline{i}}_{p-1}^r$ and $\hat{\underline{i}}_{p+1}^r$ are the space vectors of the harmonic components $p \pm 1$ of the cage currents, the circumflex above a symbol refers to the space-vector character, p is the number of pole pairs, the asterisk (*) denotes the complex conjugate, ω_s is the electrical supply frequency, s is the slip of the rotor with respect to the fundamental component of the stator field, ϑ is the phase angle of the magnetic-flux-density space-vector at $t = 0$, \underline{F}_e^r is the total electromagnetic force exerted on the rotor, and finally $a_{p \pm 1}$, $\tau_{p \pm 1}$, $c_{p \pm 1}$ and k_e are the system parameters. These parameters are estimated from the numerical simulations. To reveal the relation of these parameters

to the machine and operation characteristics, the analytical formulae can be written using several simplifying assumptions which are given in Holopainen, *et al.* (2005).

$$a_{p\pm 1} = \frac{Lk_{p\pm 1}}{2\mu_0 L_{p\pm 1}} \hat{B}_p, \quad c_{p\pm 1} = \frac{\pi d_r l_e k_{p\pm 1}}{4\delta} \hat{B}_p,$$

$$k_e = \frac{\pi d_r l_e}{2\mu_0 \delta_0} (\hat{B}_p^2 + \hat{B}_h^2), \quad \tau_{p\pm 1} = \frac{L_{p\pm 1}}{R_{p\pm 1}}$$

where μ_0 is the permeability in free space, d_r is the outer diameter of the rotor core, l_e is the equivalent core length, δ_e is the equivalent airgap length including slotting, L is the self-inductance of one mesh of the rotor cage, $k_{p\pm 1}$ is the coupling factors due to the leakage flux and the saturation, $k_{p\pm 1}$, $R_{p\pm 1}$, and $L_{p\pm 1}$ are the time constants, the resistances, and the total inductances of the rotor cage determined separately for the harmonic components $p \pm 1$ respectively, \hat{B}_p is the amplitude of the fundamental component of the magnetic flux density in the air gap, and \hat{B}_h is the effective amplitude of all the high-order harmonics. In steady-state operation \hat{B}_p and \hat{B}_h and thus the analytical parameters are constant.

Holopainen *et al.* (2002a) modelled the rotor as a Jeffcott rotor and combined this mechanical model with above mentioned parametric force model. By applying this model the electromechanical interaction are studied. It is concluded from the numerical results that the electromagnetic fields and rotor vibrations may interact strongly. If the new electromagnetic variables are interpreted as ‘quasi-displacements’, the interaction turns up in the equations of motion as additional damping, stiffness and circulatory terms. The circulatory terms, i.e. cross-coupled stiffness terms, are a major source of instability in rotating machines.

2.8 Numerical methods for the computation of magnetically-oriented forces

The calculation of the electromagnetic forces has been a very popular research topic during the recent decades. Three such methods used to calculate the forces acting between the rotor and the stator are discussed here in separate subsections.

2.8.1 Lorentz force

A problem frequently encountered is that of a current-carrying conductor in an external magnetic field. The differential force equation may be written:

$$\delta F = I (\delta \times B) \quad (2.16)$$

where δ is the elementary length in the direction of the current I . Equation (2.16) is derived from the fundamental force relationship between two moving charges. It represents the magnetic part of the Lorentz force.

If the conductor is straight and the field is constant along its length, the differential force may be integrated. In a two dimensional magnetostatic finite element model, the field components are located in the plane, where the current is oriented perpendicularly to it. In this case Equation (2.16) can be simplified to the following expression for the conductor length l :

$$F = BIl \quad (2.17)$$

These equations are theoretically valid only for a conductor in a magnetic field. However, in practice it might be used even for the calculation of force in electrical machines with many slots containing current, provided that B is the average value of the magnetic flux density in the airgap. This simplification already indicates a loss of accuracy, as the local information about the field is not taken into account. This

approach combines the analytical and the numerical field analysis at a rather simplified level.

2.8.2 Virtual work

Coulomb (1983) presented a method, based on the principle of virtual work for calculating magnetically oriented forces from a finite element solution. In this method, the force is calculated as a partial derivative of the co-energy functional with respect to the virtual movement. The co-energy is defined by the integral

$$W_{\text{co}} = \int_V \left(\int_0^H \{\mathbf{B}\}^T \cdot d\{\mathbf{H}\} \right) dV \quad (2.18)$$

The component of the force F_s in the direction of the displacement s is

$$F_s = \frac{\partial W_{\text{co}}}{\partial s} \approx \frac{dW_{\text{co}}}{ds} \quad (2.19)$$

where W_{co} is the co-energy functional. The force in the direction of s is calculated as follows

$$F_s = \sum_e \int_{V_e} \left[-\{\mathbf{B}\}^T [\mathbf{J}]^{-1} \frac{\partial [\mathbf{J}]}{\partial s} \{\mathbf{H}\} + \int_0^H \{\mathbf{B}\}^T \cdot d\{\mathbf{H}\} |\mathbf{J}|^{-1} \frac{\partial |\mathbf{J}|}{\partial s} \right] dV \quad (2.20)$$

where summation may be restricted to the subset of virtually distorted finite elements (area contained between the movable and stationary parts). When applying this method to electrical machines, the summation is over the airgap elements (Antila *et al.*, 1998). $[\mathbf{J}]$ is the Jacobian matrix, which couples the local coordinates to the global ones.

2.8.3 Maxwell stress tensor

Methods based on the Maxwell stress tensor are commonly used in the calculation of forces and torques in the finite element analysis of electric devices (Reichert, Freundl and Vogt, 1976). Belmans *et al.* (1987), use this method to calculate UMP in the airgap.

The electromagnetic force on a three-dimensional object is obtained as a surface integral

$$F = \oint_S \sigma \, ds \quad (2.21)$$

$$F = \oint_S \left[\frac{1}{\mu_o} (B \cdot n) B - \frac{1}{2\mu_o} B^2 n \right] ds \quad (2.22)$$

where σ is the Maxwell stress tensor, n is the unit normal vector of the integration surface S and B is magnetic flux density. In a two-dimensional model, the surface integral is reduced to a line integral along the air gap.

The normal, σ_{nn} and tangential, τ_{tt} components of the Maxwell stress are

$$\sigma_{nn} = \frac{(B_n^2 - B_t^2)}{2\mu_o} \quad (2.23)$$

$$\tau_{tt} = \frac{2B_n B_t}{2\mu_o} \quad (2.24)$$

where B_n and B_t are the normal and tangential components of flux density respectively. If a circle of radius r is taken as the integration path as shown Figure (2.9), the normal and tangential components of the force are

$$F_x = l \int_0^{2\pi} (\sigma_{nn} \cos \theta - \tau_{tt} \sin \theta) r d\theta \quad (2.25)$$

$$F_y = l \int_0^{2\pi} (\sigma_{nn} \sin \theta + \tau_{tt} \cos \theta) r d\theta \quad (2.26)$$

Here l is the axial length of the machine. If the solution were exact, the force would be independent on the integration radius r when r varies within the air gap. However, the calculated force depends greatly on the choice of the integration radius. A modified method based on the Maxwell stress is also put forward by Arkkio (1987).

Methods based on the Maxwell's stress are commonly used on analytical studies with some simplifications. Supposing that the permeability of the core material is infinite, the flux lines enter and leave the stator and rotor surfaces perpendicularly. Maxwell's stress tensor $\sigma(x, t)$ is then calculated from the radial component of the flux density distribution in the air gap $B_r(x, t)$ (Fruchtenicht *et al.*, 1982)

$$\sigma(x, t) = \frac{1}{2\mu_0} (B_r(x, t))^2 \quad (2.27)$$

The flux density distribution can be solved by harmonic analysis of the airgap fields or by using the conformal transformation technique. The force is then obtained by integrating the Maxwell's stress tensor around the rotor (Fruchtenicht *et al.*, 1982).

2.9 Experimental findings of UMP

Not much work has been reported on the experimental findings of UMP in literature because of the obvious difficulties. The parallel windings on either the stator or rotor damp UMP (Dorell, 1999). Dorrell and Smith (1993) have shown that the parallel stator windings can also be used to reduce UMP but this is not very effective for a cage rotor since the rotor already have many more parallel paths. Dorrell and Smith (1996a) developed an analytical model to investigate the effectiveness of series and parallel connections of stator coils. They (Dorrell and Smith, 1996b) also verified the

results from this analytical model with the experimental results. They mentioned that for a static eccentric rotor, any eccentric field component will cause vibrating UMP at twice-supply-frequency.

Berman (1993) theoretically proved and also experimentally verified the substantial reduction in UMP due to the parallel windings with equalizing branches. He measured the radial forces on an experimental setup. His experimental setup consists of two induction motors with a common shaft which capable of permitting a variety of connection patterns for the stator coils. Forces are calculated in two mutually perpendicular directions with the help of the strain gauges serving as branches in differential bridges. His experimental findings confirmed that using the equalising connections, up to 25 times reduction in UMP can be achieved. Figure (2.10) shows the radial strain for different supply voltages with series and equalizing pattern of stator coils.

The relationship between the UMP and the homopolar flux is derived by Belmans *et al.* (Belmans *et al.*, 1987). The stability of the radial vibration behaviour of induction motors also depends upon the electro magnetically generated forces due to the eccentric rotor position. The homopolar flux generated by the eccentric rotor position clearly influences the unbalanced magnetic pull in 2-pole induction motors, not only by altering the value of the constant component of the pull, but also generating a pull component with a frequency double that of slip (Belmans *et al.*, 1987).

2.10 Summary of the review

The unbalanced magnetic pull of an electric machine can be calculated analytically as well as numerically. An electric machine is a complex electromagnetic device. Analytical methods can calculate the electromagnetic forces between the stator and the rotor very quickly but certain aspects of an electric machine such as magnetic saturation, skew effect, effect of slots, uneven distribution of field is difficult to incorporate in the model. Numerical methods can calculate UMP taking these effects in consideration. This chapter reviewed the literature related to analytical and numerical methods for calculating UMP in an electrical machine.

Clearly a substantial amount of work has already been carried out to calculate the UMP and its effect in the stability of an electrical machine using analytical model. There are still gaps to be filled in these analytical models. Improvements can be made of these analytical models by incorporating magnetic saturation, effect of skew, effect of slots, effects of uneven distribution of magnetic field into these models.

It is also found that there is a strong need for a coupled numerical model which can integrate the electrical dynamics with a detailed mechanical dynamics. This will allow us to investigate the electromechanical interaction in electrical machines. This is the main aim of this study.

The results of the numerical models are incomplete without experimental verifications. There is not much literature published on the experimental findings of the UMP and the electromechanical interaction because of the obvious difficulty. An attempt has been made in this thesis for experimental investigation of electromechanical interaction in an induction machine.

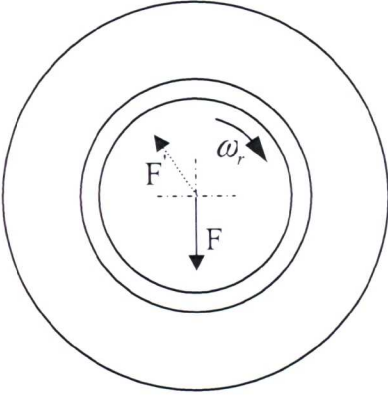


Figure (2.1): UMP from static eccentricity

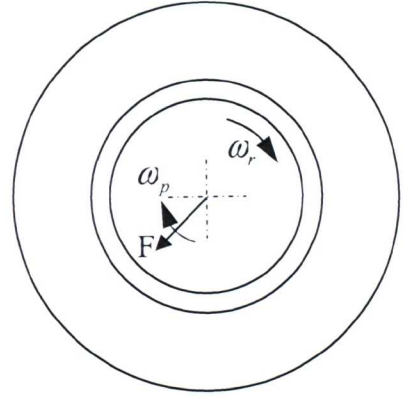


Figure (2.2): UMP from dynamic eccentricity

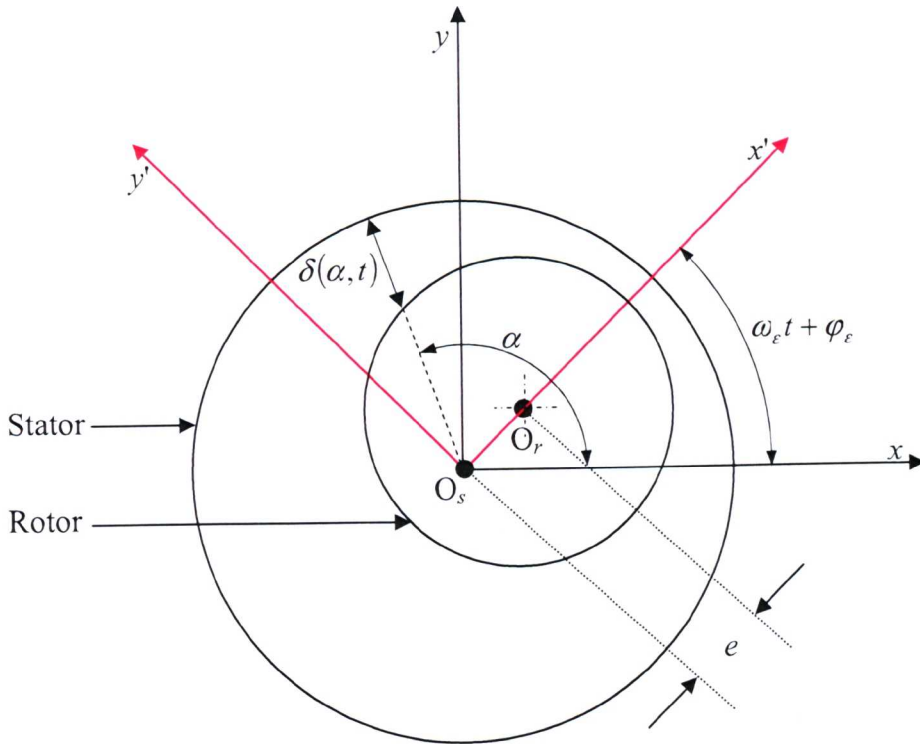


Figure (2.3): Airgap of an electric machine with an eccentric rotor

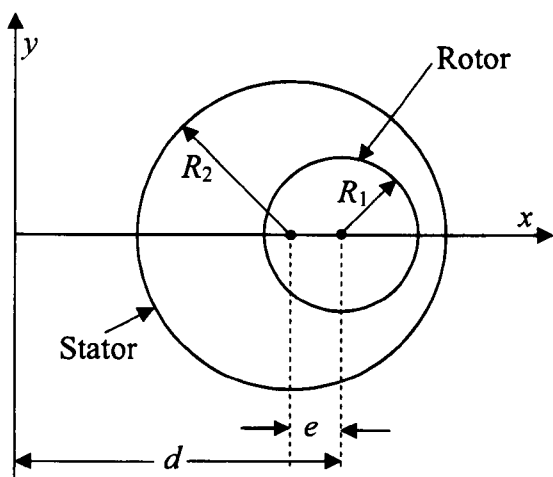


Figure (2.4): Z-Plane

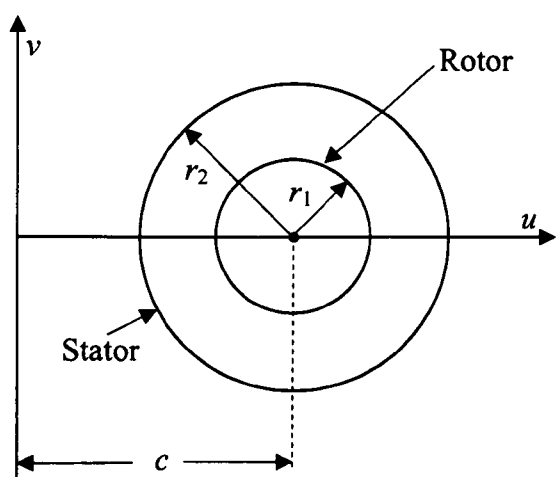


Figure (2.5): T-Plane

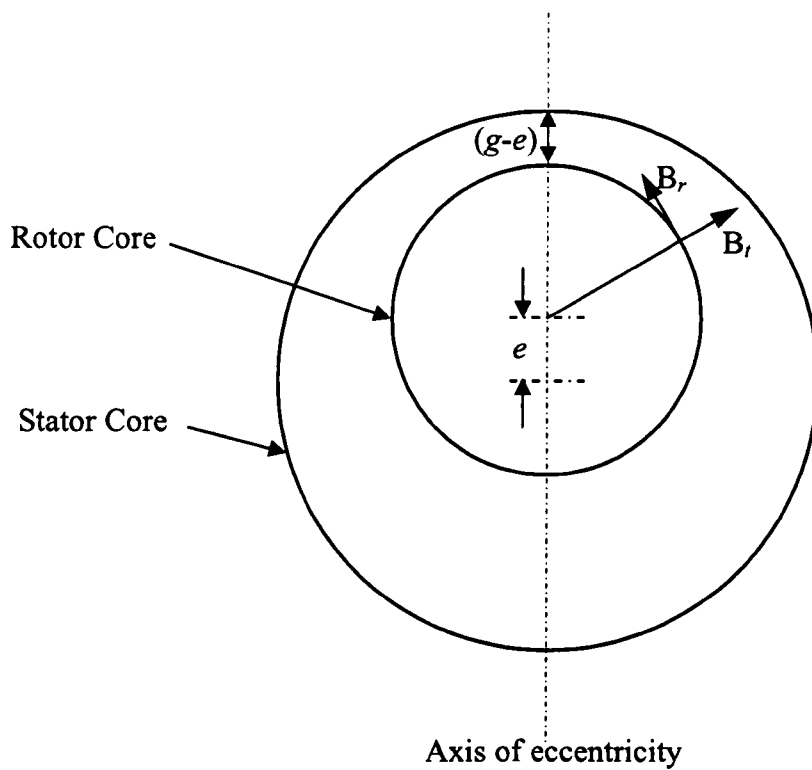


Figure (2.6): The radial and tangential components of magnetic flux density in the airgap. (Binns and Dye, 1973)


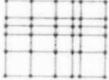

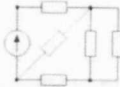
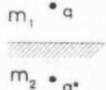
method	principle of discretisation	geometry approximation	non-linearities	computational costs
FEM		extremely flexible	possible	high
FDM		inflexible	possible	high
BEM		extremely flexible	troublesome	high
MEC		specific geometries	possible	very low
PMM		simple geometries	by constant factors	low

Figure (2.7): Numerical field computation methods (Hameyer and Belmans, 1999)

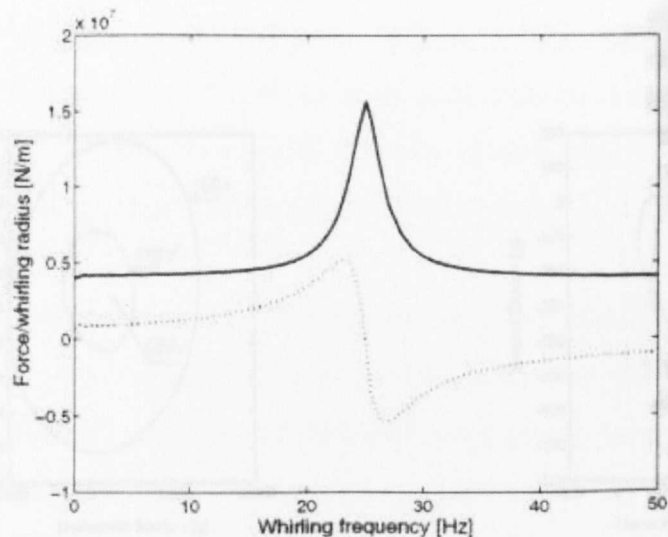


Figure (2.8): Frequency response functions at no load condition. In the figure thick line represents the radial and the dashed line represents the tangential components. (Tenhunen, 2003)

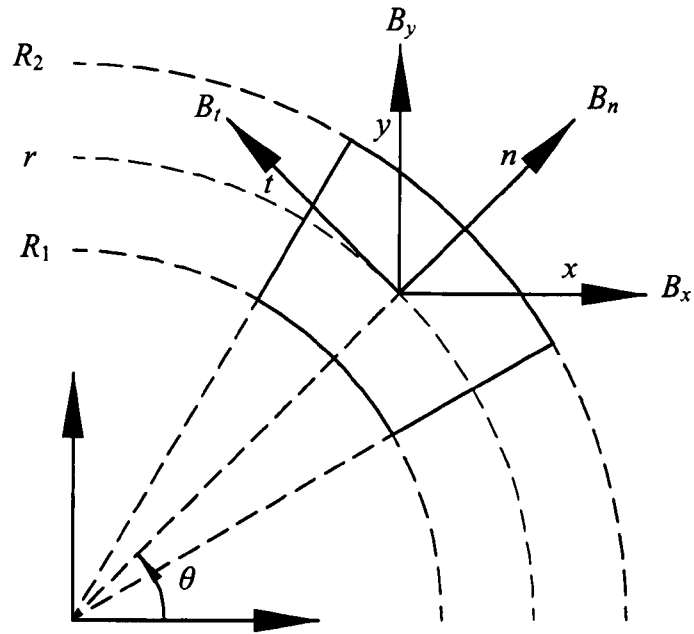
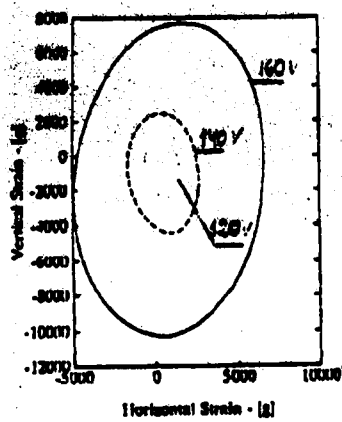
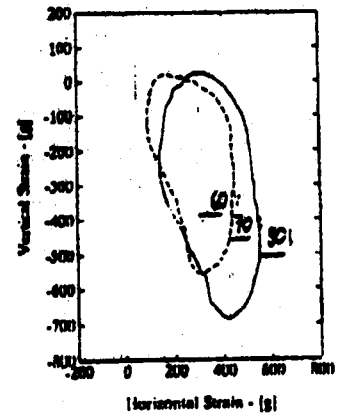


Figure (2.9): The normal and tangential components of magnetic flux density



(a)



(b)

Figure (2.10): The radial strain for different supply voltages: (a) series pattern of stator coils, (b) equalizing pattern of stator coils (Berman, 1993)

Chapter Three

2-D Finite Element Modelling of Electric Machines

3.1 Introduction

During the past few decades, the numerical computation of magnetic fields has gradually become a standard in electrical machine design. The finite element method (FEM) currently represents the state-of-the-art in the numerical magnetic field computation relating to electrical machines [Bastos and Sadowski (2003), Hameyer and Belmans (1999)].

In the scope of this thesis, a typical motor or generator can be modelled with high accuracy by two-dimensional FEM, which is coupled with the circuit equations for the windings. The FEM for electromagnetic analysis is well established but it will be appropriate to introduce the procedure adopted in this study.

In this chapter, the basic equations of the electromagnetic field are presented along with a systematic procedure of finite element formulation for electromagnetic study. The relationships between currents and flux, and subsequently between flux and force are described. It is assumed here that currents are known and they are calculated from the given current densities in the current-carrying regions. The modelling of eddy-currents additionally using magnetic vector potential is dealt with shortly. The presence of ferromagnetic materials makes the relationship between current and flux non-linear. At first formulations are derived for linear FE analysis and subsequently material nonlinearity is incorporated in the model. The treatment of time-varying geometry is deferred to Chapter 6.

The procedure presented here is general in nature and can be applicable to any electrical device; but specific emphasis is placed on electrical machines. A non-linear finite element computer code has been developed. Using the procedure developed three electrical machines have been studied.

3.2 Basic equations of the electromagnetic field

In this section the differential equations of the magnetic vector potentials are derived from Maxwell's equations. The aim is to give the basic field theoretical material for the next sections that contain the discretization of the field equation by the finite element method. Details about the field potentials and its formulations are given by (Hameyer and Belmans, 1999)

In three-dimensional magneto-static analysis magnetic flux density is derived as the curl of magnetic vector potential

$$\{\mathbf{B}\}(x, y, z) = \nabla \times \{\mathbf{A}\}(x, y, z) \quad (3.1)$$

where

$\{\mathbf{B}\}(x, y, z)$ is the vector magnetic flux density

$\{\mathbf{A}\}(x, y, z)$ is the vector magnetic vector potential

A static magnetic field in an electrical machine is governed by Maxwell's equations

$$\nabla \times \{\mathbf{H}\}(x, y, z) = \{\mathbf{J}_0\}(x, y, z) \quad (3.2)$$

where

$\{\mathbf{H}\}(x, y, z)$ is the magnetic field intensity vector

$\{\mathbf{J}_0\}(x, y, z)$ is the current density vector

The integral of magnetic flux density over any closed surface is zero and in differential form

$$\nabla \cdot \{\mathbf{B}\}(x, y, z) = 0 \quad (3.3)$$

Using the permeability tensor, $[\mu]$ we have the material equation

$$\{\mathbf{B}\}(x, y, z) = [\mu]\{\mathbf{H}\}(x, y, z) \quad (3.4)$$

where $[\mu]$ is a material-dependent and possibly nonlinear function of the magnetic field. In this study, nonlinearity is dealt with using a local linearization. For an isotropic material $[\mu]$ is a scalar and is denoted by μ , and if the material is not an isotropic, tensor $[\mu]$ is a 3×3 matrix, which takes into account the effect of the magnetizing directions. The 2D field equation for an orthotropic material is shown in Appendix A. Using the magnetic vector potential $\{\mathbf{A}\}(x, y, z)$, the system of differential equations is reduced to

$$\nabla \times (\nabla \times \{\mathbf{A}\}(x, y, z)) = [\mu]\{\mathbf{J}_0\}(x, y, z) \quad (3.5)$$

Applying vector calculus $\nabla \times (\nabla \times \{\mathbf{A}\}(x, y, z)) = \nabla(\nabla \cdot \{\mathbf{A}\}(x, y, z)) - \nabla^2 \{\mathbf{A}\}(x, y, z)$ to Equation (3.5) yields

$$\nabla(\nabla \cdot \{\mathbf{A}\}(x, y, z)) - \nabla^2 \{\mathbf{A}\}(x, y, z) = [\mu]\{\mathbf{J}_0\}(x, y, z) \quad (3.6)$$

With $\nabla \cdot \{\mathbf{A}\} = 0$ and by assuming a constant permeability, μ , leads to the A -formulation of a magnetic-static field, a Poisson's equation:

$$\nabla^2 \{\mathbf{A}\}(x, y, z) = -\mu\{\mathbf{J}_0\}(x, y, z) \quad (3.7)$$

To consider quasi-stationary fields, for example necessary for eddy current calculations, the magneto-dynamic formulation must be employed. In addition to Ampere's law, Faraday law has to be considered to evaluate the conduction to the field by the eddy currents:

$$\nabla \times \{\mathbf{E}\}(x, y, z) = -\frac{\partial}{\partial t} \{\mathbf{B}\}(x, y, z) = -\frac{\partial}{\partial t} (\nabla \times \{\mathbf{A}\}(x, y, z)) \quad (3.8)$$

Now Ohm's law is employed to calculate the eddy currents, $\{\mathbf{I}_e\}(x, y, z)$

$$\{J_e\}(x, y, z) = -\sigma \frac{\partial}{\partial t} \{\mathbf{A}\}(x, y, z) \quad (3.9)$$

where σ is the conductivity of the material. Ampere's law can now be rewritten, yielding the A -formulation for the quasi-stationary magnetic field in the time domain:

$$\nabla \times \left[\frac{1}{\mu} \nabla \times \{\mathbf{A}\}(x, y, z) \right] + \sigma \frac{\partial}{\partial t} \{\mathbf{A}\}(x, y, z) = \{\mathbf{J}_0\}(x, y, z) \quad (3.10)$$

Substituting again $\nabla \times (\nabla \times \{\mathbf{A}\}(x, y, z)) = \nabla(\nabla \cdot \{\mathbf{A}\}(x, y, z)) - \nabla^2 \{\mathbf{A}\}(x, y, z)$ and assuming $\nabla \cdot \{\mathbf{A}\}(x, y, z) = 0$, results in a similar A -formulation the time domain for the transient magnetic field:

$$\nabla^2 \{\mathbf{A}\}(x, y, z) - \mu\sigma \frac{\partial}{\partial t} \{\mathbf{A}\}(x, y, z) = -\mu \{\mathbf{J}_0\}(x, y, z) \quad (3.11)$$

Assuming sinusoidal excitation currents with an angular frequency, ω and thus substituting

$$\frac{\partial}{\partial t} \{\mathbf{A}\}(x, y, z) = j\omega \{\mathbf{A}\}(x, y, z) \quad (3.12)$$

yields the A -formulation in the frequency domain to solve eddy current problem.

$$\nabla^2 \{\mathbf{A}\}(x, y, z) - j\omega\mu\sigma \{\mathbf{A}\}(x, y, z) = -\mu \{\mathbf{J}_0\}(x, y, z) \quad (3.13)$$

This equation is the A -formulation to describe time-harmonic problems. The time-dependent components of the vector potential $\{\mathbf{A}\}(t) = \{\hat{\mathbf{A}}\} \cdot \cos(\omega t + \phi)$ are expressed as

$$\{\mathbf{A}\}(t) = \{\hat{\mathbf{A}}\} \cdot e^{j(\omega t + \phi)} \quad (3.14)$$

Employing a true eddy-current model would require that all magnetic potential variables were state-variables which had to be integrated for applications other than where pure sinusoidal variations were encountered. The standard magnetic FEA packages use this procedure. The model presented in this study will represent induced circulating currents using discrete current variables. Inductances are calculated once these currents are known and hence the back EMFs. This is one of the reasons why we can not use these standard packages for this study. The equations described above are for three dimensional magneto-static problems. From this point onwards we will confine our study on two-dimensional magneto-static analysis. The two-dimensional model is based on the assumption that the magnetic vector potential and current density have only z -axis components and their values are determined in the xy -plane

$$\mathbf{A}_z = \mathbf{A}(x, y) \hat{k} \quad (3.15)$$

$$\mathbf{J}_z = \mathbf{J}(x, y) \hat{k} \quad (3.16)$$

where \hat{k} denotes the unit vector in the z -axis direction.

3.3 Finite element formulation

For a magnetically linear material, the electromagnetic energy inner product is

$$[\mathbf{A}, \mathbf{A}]_j = \int_{\mathcal{V}_j} \left[\begin{pmatrix} \frac{\partial \mathbf{A}}{\partial x} \\ \frac{\partial \mathbf{A}}{\partial y} \end{pmatrix} \right]^T \begin{bmatrix} \frac{1}{\mu_{yy}} & 0 \\ 0 & \frac{1}{\mu_{xx}} \end{bmatrix} \begin{bmatrix} \frac{\partial \mathbf{A}}{\partial x} \\ \frac{\partial \mathbf{A}}{\partial y} \end{bmatrix} d\mathcal{V}_j \quad (3.17)$$

where Ψ_j is the area of the j th element, \mathbf{A} is the magnetic vector potential which is a function of position and μ_{xx} and μ_{yy} are the permeabilities along x and y respectively where these are the principle axes of the magnetic material.

3.3.1 Shape functions

To facilitate the definition of various finite elements, we introduce the idea of a “reference” or “local” element and the reference or local system of coordinates. Figures (3.1) and (3.2) show the node ordering chosen in the reference and actual Cartesian coordinates. The various relations needed to define an element are generated in the local system of coordinates because it is easier to do so. In order to represent the magnetic field within one element using finite number of variables, we need a coordinate transformation between a space of infinite dimension and a finite number of coordinates. This transformation is accomplished by shape functions.

The coordinate transformation

$$x = x(\xi, \eta) \quad (3.18)$$

$$\text{And} \quad y = y(\xi, \eta) \quad (3.19)$$

represents a mapping of the points (ξ, η) in the ξ, η -plane onto points (x, y) in the x, y -plane. Figure (3.1) shows a rectangular element in the ξ, η -plane and Figure (3.2) shows a curved element in x, y -plane. The element in the ξ, η -plane is referred as the master element and the element in the x, y -plane is described as an isoparametric element. A finite element is called “isoparametric” when the same functions are used for mapping element coordinates as are used for the shape-functions. Isoparametric elements are the commonly used elements in FE codes. In electromagnetic finite element analysis magnetic potentials are approximated by piecewise polynomials that can be used for mapping one element onto another. Shape functions are derived for 4-noded quadrilateral element, 8-noded quadrilateral element, 3-node triangular element and 6-noded triangular element and they are explained in the following subsections.

3.3.1.1 4-Noded quadrilateral element

Figure (3.3) shows the node ordering chosen for the 4-noded quadrilateral element.

The four shape functions can be written as

$$\left. \begin{aligned} N_1(\xi, \eta) &= \frac{1}{4}(1 - \xi)(1 - \eta) \\ N_2(\xi, \eta) &= \frac{1}{4}(1 - \xi)(1 + \eta) \\ N_3(\xi, \eta) &= \frac{1}{4}(1 + \xi)(1 + \eta) \\ N_4(\xi, \eta) &= \frac{1}{4}(1 + \xi)(1 - \eta) \end{aligned} \right\} \quad (3.20)$$

3.3.1.2 8-Noded quadrilateral element

Figure (3.4) shows the node ordering chosen for the 8-noded quadrilateral element.

The eight shape functions can be written as

$$\left. \begin{aligned} N_1(\xi, \eta) &= \frac{1}{4}(1 - \xi)(1 - \eta)(-1 - \xi - \eta) \\ N_2(\xi, \eta) &= \frac{1}{4}(1 - \xi)(1 + \eta)(-1 - \xi + \eta) \\ N_3(\xi, \eta) &= \frac{1}{4}(1 + \xi)(1 + \eta)(-1 + \xi + \eta) \\ N_4(\xi, \eta) &= \frac{1}{4}(1 + \xi)(1 - \eta)(-1 + \xi - \eta) \\ N_5(\xi, \eta) &= \frac{1}{2}(1 - \xi^2)(1 - \eta^2) \\ N_6(\xi, \eta) &= \frac{1}{2}(1 - \xi^2)(1 + \eta) \\ N_7(\xi, \eta) &= \frac{1}{2}(1 + \xi^2)(1 - \eta^2) \\ N_8(\xi, \eta) &= \frac{1}{2}(1 - \xi^2)(1 - \eta) \end{aligned} \right\} \quad (3.21)$$

3.3.1.3 3-Noded triangular element

Figure (3.5) shows the node ordering chosen for the 3-noded triangular element. The three shape functions can be written as

$$\left. \begin{aligned} N_1(\xi, \eta) &= (1 - \xi - \eta) \\ N_2(\xi, \eta) &= \eta \\ N_3(\xi, \eta) &= \xi \end{aligned} \right\} \quad (3.22)$$

3.3.1.4 6-Noded triangular element

Figure (3.6) shows the node ordering chosen for the 6-noded triangular element. The six shape functions can be written as

$$\left. \begin{aligned} N_1(\xi, \eta) &= 2(\xi + \eta - 1) \left(\xi + \eta - \frac{1}{2} \right) \\ N_2(\xi, \eta) &= \eta(2\eta - 1) \\ N_3(\xi, \eta) &= \xi(2\xi - 1) \\ N_4(\xi, \eta) &= -4\eta(\xi + \eta - 1) \\ N_5(\xi, \eta) &= 4\xi\eta \\ N_6(\xi, \eta) &= -4\xi(\xi + \eta - 1) \end{aligned} \right\} \quad (3.23)$$

3.3.2 The magnetic stiffness matrix

We assume that the finite element approximation of the magnetic vector potential, A over a given element with n nodes has the form

$$A(x, y) = \{N(\xi, \eta)\}^T \{A\} = \sum_{j=1}^n N_j A_j \quad (3.24)$$

where $\{N(\xi, \eta)\}$ is an n -vector of interpolation functions (shape functions) and $\{A\}$ an n -vector of nodal magnetic vector potential. The (ξ, η) is omitted from $\{N(\xi, \eta)\}$ hereafter for the sake of brevity. Moreover, the mapping of (ξ, η) onto (x, y) is given by

$$x = \sum_{i=1}^n N_i x_i = \{N\}^T \{x\} \quad (3.25)$$

$$y = \sum_{i=1}^n N_i y_i = \{N\}^T \{y\} \quad (3.26)$$

in which $\{x\} = [x_1, x_2, \dots, x_n]$ and $\{y\} = [y_1, y_2, \dots, y_n]$ are n -vectors with entries equal to the x - and y - components, respectively, of the nodal points (x_j, y_j) .

The stiffness matrix involves the partial derivatives $\partial \mathbf{A} / \partial x$ and $\partial \mathbf{A} / \partial y$ and to find these quantities, it is necessary to have expressions for the partial derivatives of the shape functions with respect to x and y .

$$\begin{Bmatrix} \frac{\partial \{\mathbf{N}\}^T}{\partial \xi} \\ \frac{\partial \{\mathbf{N}\}^T}{\partial \eta} \end{Bmatrix} = \begin{bmatrix} \frac{\partial x}{\partial \xi} & \frac{\partial y}{\partial \xi} \\ \frac{\partial x}{\partial \eta} & \frac{\partial y}{\partial \eta} \end{bmatrix} \begin{Bmatrix} \frac{\partial \{\mathbf{N}\}^T}{\partial x} \\ \frac{\partial \{\mathbf{N}\}^T}{\partial y} \end{Bmatrix} \quad (3.27)$$

$$\begin{Bmatrix} \frac{\partial \{\mathbf{N}\}^T}{\partial x} \\ \frac{\partial \{\mathbf{N}\}^T}{\partial y} \end{Bmatrix} = [\mathbf{J}]^{-1} \begin{Bmatrix} \frac{\partial \{\mathbf{N}\}^T}{\partial \xi} \\ \frac{\partial \{\mathbf{N}\}^T}{\partial \eta} \end{Bmatrix} \quad (3.28)$$

where $[\mathbf{J}]$ is called the Jacobian. Again

$$\frac{\partial x}{\partial \xi} = \sum_{i=1}^n x_i \frac{\partial N_i}{\partial \xi} \quad \text{and} \quad \frac{\partial x}{\partial \eta} = \sum_{i=1}^n x_i \frac{\partial N_i}{\partial \eta} \quad (3.29) \text{ and } (3.30)$$

$$\frac{\partial y}{\partial \xi} = \sum_{i=1}^n y_i \frac{\partial N_i}{\partial \xi} \quad \text{and} \quad \frac{\partial y}{\partial \eta} = \sum_{i=1}^n y_i \frac{\partial N_i}{\partial \eta} \quad (3.31) \text{ and } (3.32)$$

Now the Jacobian is calculated as

$$[\mathbf{J}] = \begin{bmatrix} \frac{\partial x}{\partial \xi} & \frac{\partial y}{\partial \xi} \\ \frac{\partial x}{\partial \eta} & \frac{\partial y}{\partial \eta} \end{bmatrix} = \begin{bmatrix} \frac{\partial N_1}{\partial \xi} & \dots & \frac{\partial N_n}{\partial \xi} \\ \frac{\partial N_1}{\partial \eta} & \dots & \frac{\partial N_n}{\partial \eta} \end{bmatrix} \begin{bmatrix} x_1 & y_1 \\ \vdots & \vdots \\ x_n & y_n \end{bmatrix} \quad (3.33)$$

Finally for the j th element

$$\begin{Bmatrix} \frac{\partial \mathbf{A}}{\partial x} \\ \frac{\partial \mathbf{A}}{\partial y} \end{Bmatrix} = \begin{Bmatrix} \frac{\partial \{\mathbf{N}\}^T}{\partial x} \\ \frac{\partial \{\mathbf{N}\}^T}{\partial y} \end{Bmatrix} \{\mathbf{A}_j\} = [\mathbf{J}]^{-1} \begin{Bmatrix} \frac{\partial \{\mathbf{N}\}^T}{\partial \xi} \\ \frac{\partial \{\mathbf{N}\}^T}{\partial \eta} \end{Bmatrix} \{\mathbf{A}_j\} \quad (3.34)$$

The differential element of an area can be shown to transform according to

$$dxdy = |\mathbf{J}| d\xi d\eta \quad (3.35)$$

Now we can write the expressions for the isoparametric element stiffness matrix. Inserting Equations (3.34) and (3.35) into Equation (3.17) we obtain

$$[\mathbf{A}, \mathbf{A}]_j = \int_{\Psi_j} \{\mathbf{A}_j\}^T \begin{Bmatrix} \left(\frac{\partial \{\mathbf{N}\}}{\partial \xi} \right)^T \\ \left(\frac{\partial \{\mathbf{N}\}}{\partial \eta} \right)^T \end{Bmatrix} [\mathbf{J}]^{-T} \begin{bmatrix} 1 & 0 \\ \mu_{yy} & 1 \\ 0 & \mu_{xx} \end{bmatrix} [\mathbf{J}]^{-1} \begin{Bmatrix} \left(\frac{\partial \{\mathbf{N}\}}{\partial \xi} \right) \\ \left(\frac{\partial \{\mathbf{N}\}}{\partial \eta} \right) \end{Bmatrix} \{\mathbf{A}_j\} d\Psi_j \quad (3.36)$$

$$[\mathbf{A}, \mathbf{A}]_j = \int_{\eta_1}^{\eta_2} \int_{\xi_1}^{\xi_2} \{\mathbf{A}_j\}^T \begin{Bmatrix} \left(\frac{\partial \{\mathbf{N}\}}{\partial \xi} \right)^T \\ \left(\frac{\partial \{\mathbf{N}\}}{\partial \eta} \right)^T \end{Bmatrix} [\mathbf{J}]^{-T} \begin{bmatrix} 1 & 0 \\ \mu_{yy} & 1 \\ 0 & \mu_{xx} \end{bmatrix} [\mathbf{J}]^{-1} \begin{Bmatrix} \left(\frac{\partial \{\mathbf{N}\}}{\partial \xi} \right) \\ \left(\frac{\partial \{\mathbf{N}\}}{\partial \eta} \right) \end{Bmatrix} \{\mathbf{A}_j\} |\mathbf{J}| d\xi d\eta \quad (3.37)$$

$$[\mathbf{A}, \mathbf{A}]_j = \{\mathbf{A}_j\}^T [\mathbf{K}_j] \{\mathbf{A}_j\} \quad (3.38)$$

where $[\mathbf{K}_j]$ is the stiffness matrix for the j th element. Here ξ_1 and ξ_2 are the integration limits for ξ ; similarly η_1 and η_2 are the integration limits for η . For a quadrilateral element ξ_1 and ξ_2 are -1 and 1 respectively and η_1 and η_2 are also -1 and 1 respectively. The stiffness matrix for the whole domain, which is known as the global stiffness matrix, is obtained by assembling the individual stiffness matrices.

3.3.3 Conduction modelling

The electrostatic constitutive relationship is

$$\mathbf{E}(x, y) = \boldsymbol{\rho}(x, y) \mathbf{J}(x, y) \quad (3.39)$$

where $\mathbf{J}(x, y)$, $\mathbf{E}(x, y)$ and $\boldsymbol{\rho}(x, y)$ are continuous current density, local electrical field strength (V/m) and local resistivity respectively. Total power (per unit length) being dissipated over a domain Ψ is

$$\int_{\Psi} \mathbf{E} \mathbf{J} d\Psi = \int_{\Psi} \mathbf{J}^T \boldsymbol{\rho} d\Psi \quad (3.40)$$

Now $\mathbf{J}(x, y)$ for a single “element” will be approximated as

$$\mathbf{J}(x, y) = \sum_{k=1}^n N_k(x, y) j_k \quad (3.41)$$

where k is the index of “nodes” on the element and where $N_k(x, y)$ is a “shape function” which is unity at the k -th node but zero at all others. Total power being dissipated P_D over the element now

$$P_D = \{\mathbf{j}\}^T [\mathbf{X}] \{\mathbf{j}\} \quad (3.42)$$

where $\{\mathbf{j}\}$ is the vector of nodal current density values and where

$$[\mathbf{X}] = \int_{\Psi} \boldsymbol{\rho}(x, y) \{\mathbf{N}(x, y)\}^T \{\mathbf{N}(x, y)\} d\Psi \quad (3.43)$$

Now, each element is characterised by an equation in the form

$$[\mathbf{X}] \{\mathbf{j}\} = \{\mathbf{e}\} \quad (3.44)$$

where $\{e\}$ is the vector of nodal electric field strength values. We assume that the original distribution of electric field strength $E(x, y)$ is equal to

$$E(x, y) = \sum_{k=1}^n N_k(x, y) e_k \quad (3.45)$$

and we obtain a definition for $\{e\}$ in this case from the assumption that

$$|\Psi| \{e\}^T \{j\} = \int_V E(x, y) J(x, y) dV = \text{Power being dissipated per unit length} \quad (3.46)$$

Note from this that the units of field strength $E(x, y)$ are (V/m) and that we obtain the vector $\{e\}$ from

$$\{e\} = \frac{\int_V E(x, y) \{N(x, y)\} dV}{|\Psi|} \quad (3.47)$$

It is clear, now, that we can assemble a model for the entire region from individual element models. Each element makes a contribution to both $[X]$ and $\{e\}$.

For the purpose of coupling electrical circuit models to the magnetic model, we will want nodal “currents” rather than “current densities”. We must prepare our basic electrical model using the “current density” as variables and then transfer it to “currents”. The transformation from current density to currents has to be done element by element. A given current density at one node will account for n contributions to current - one contributed from each of n elements. Each individual contribution to current is derived using the following argument:

The work done W_D by a current distribution $J(x, y)$ on a magnetic field described by the magnetic potential $A(x, y)$ is given by

$$W_D = \frac{1}{2} \int_{\Psi} \mathbf{J}(x, y) \mathbf{A}(x, y) d\Psi \quad (3.48)$$

If, here, Ψ represents only a single element then our magnetic potentials, $\mathbf{A}(x, y)$, will have been written as

$$\mathbf{A}(x, y) = \sum_{k=1}^n M_k(x, y) A_k \quad (3.49)$$

where A_k is the k -th nodal magnetic potential and $M_k(x, y)$ is the k -th shape function for magnetic potentials. For a purely “magnetic FEA” perspective, the element stiffness matrix is derived as

$$[\mathbf{K}][\mathbf{A}] = \{\mathbf{I}_z\} \quad (3.50)$$

The forcing vector $\{\mathbf{I}_z\}$ then corresponds to nodal currents and the work done on the magnetic field by the currents is given by

$$\frac{1}{2} \{\mathbf{I}_z\}^T \{\mathbf{A}\} \left(= \frac{1}{2} \{\mathbf{A}\}^T [\mathbf{K}][\mathbf{A}] \right) \quad (3.51)$$

From the above we obtain the definition

$$\{\mathbf{I}_z\} = [\mathbf{S}][\mathbf{j}] \quad (3.52)$$

where $S(i, j) = \int_{\Psi} M_i(x, y) N_j(x, y) d\Psi$ and often $M_i = N_i \forall i$. Now the resistance matrix $[\mathbf{R}]$ is calculated as

$$[\mathbf{R}] = [\mathbf{S}]^T [\mathbf{X}] [\mathbf{S}] \quad (3.53)$$

3.3.4 Calculation of the magnetomotive forces

In any electrical systems magnetomotive forces (MMFs) can be contributed by current carrying coils or permanent magnets or both. Calculations of equivalent nodal current excitations from the both sources are discussed separately.

3.3.4.1 MMF from current carrying coils

Equivalent nodal current excitation can be calculated when MMF source is current carrying coils. We define the term current density by dividing current by the cross-sectional area perpendicular to its direction. For a constant current density the excitation for j th element is calculated as

$$\{\mathbf{I}_j\} = \int_{\Psi} \mathbf{J}_0(x, y) \{\mathbf{N}_j\} d\Psi \quad (3.54)$$

where $\mathbf{J}_0(x, y)$ is the current density and $\{\mathbf{N}_j\}$ is the shape function of j th element. This provides a vector of nodal currents. It is assumed in this chapter that currents are known and they are calculated from the given current densities in the current-carrying regions. Electric machines are generally voltage fed and also it is quite common to find electrical machines fed by static converters and the field equations need to be written with the external electric/electronic circuits. This requires a special treatment to calculate the currents and will be discussed in the next chapter.

3.3.4.2 Magnetomotive force of permanent magnets

Equivalent nodal current excitations can be calculated for permanent magnet regions if the relative permeability, μ and remanent flux density vector, $\{\mathbf{B}_0\}$ are known. Relative permeability and remanent flux density can be calculated from the $B(H)$ curve of the permanent magnets. Figure (3.7) shows $B(H)$ curves of the four principal permanent magnet materials available. If the remanent flux densities with magnetisation directions and the respective relative permeabilities are known, the

coercive field intensities can be calculated. The remanent flux density vector, $\{\mathbf{B}_0\}$ is related to the coercive field intensity vector $\{\mathbf{H}_c\}$ by

$$\{\mathbf{B}_0\} = -\mu \{\mathbf{H}_c\} \quad (3.55)$$

Figure (3.8) shows magnetisation curve for a permanent magnet. Once the coercive field intensities are calculated, the equivalent nodal current excitations are calculated using Equation (3.56).

$$\{\mathbf{I}_m\} = \int_{\Psi} \left\{ \frac{\partial M_{cy}}{\partial x} - \frac{\partial M_{cx}}{\partial y} \right\} d\Psi \quad (3.56)$$

where M_{cx} and M_{cy} are the components of $\{\mathbf{H}_c\}$ along the two principal directions x and y respectively.

3.3.5 Calculation of magnetic flux density

Once the magnetic vector potential is calculated at each node the next step is to calculate the magnetic flux density and (if relevant) the resultant magnetic forces and moments. The magnetic potential for the j th element was stated in Equation (3.24),

$$\mathbf{A}(x, y) = \{\mathbf{N}\}^T \{\mathbf{A}_j\} = \sum_{i=1}^n N_i A_i \quad (3.57)$$

The magnetic flux density is the curl of magnetic vector potential, i.e. $\mathbf{B} = \nabla \times \mathbf{A}$. So the magnetic flux density along x-direction is $B_x = \frac{\partial A}{\partial y}$ and the magnetic flux density along y-direction is $B_y = -\frac{\partial A}{\partial x}$. Both B_x and B_y can be calculated from

$$\begin{Bmatrix} \frac{\partial \mathbf{A}}{\partial x} \\ \frac{\partial \mathbf{A}}{\partial y} \end{Bmatrix} = \begin{Bmatrix} \frac{\partial \{\mathbf{N}\}^T}{\partial x} \\ \frac{\partial \{\mathbf{N}\}^T}{\partial y} \end{Bmatrix} \{\mathbf{A}_J\} = [\mathbf{J}]^{-1} \begin{Bmatrix} \frac{\partial \{\mathbf{N}\}^T}{\partial \xi} \\ \frac{\partial \{\mathbf{N}\}^T}{\partial \eta} \end{Bmatrix} \{\mathbf{A}_J\} \quad (3.58)$$

3.4 Material properties

Generally permittivity and conductivity can be considered to be constant. However, permeability (or reluctivity) is dependent on the magnetic field intensity. Ferromagnetic materials are characterized by a $B(H)$ curve, with permeability varying depending on the location on the $B(H)$ curve. The $B(H)$ curve shown in Figure (3.9) has been considered for the ferromagnetic materials in this study. For effective use in the finite element this $B(H)$ curve is divided into four regions and each region is fitted with an equation maintaining C^1 continuity. These equations are given in Appendix A.

3.5 Non-linear finite element analysis

Section (3.2) describes the linear relationship between the nodal potentials and nodal currents in a domain. The permeability of ferromagnetic materials in any electromagnetic device is not constant and is dependent on the field intensity. Figure (3.9) shows the magnetization characteristics in $B(H)$ form of a typical electrical steel. The permeability changes hence the stiffness matrix changes with the field intensity. This implies that Equation (3.50) is non-linear since the stiffness matrix, $[\mathbf{K}]$ is a nonlinear function of the permeability of the materials. The permeability of the materials depends on the excitation and is calculated from its $B(H)$ curve. Equation (3.50) can be written in two different forms. The first one is the instantaneous relationship between the magnetic vector potentials and the currents and can be written as

$$[\mathbf{K}_{\text{mar}}] \{\Delta \mathbf{A}\} = \{\Delta \mathbf{I}\} \quad (3.59)$$

The second form is the linearised form and can be written as

$$[K_{\text{mar}}]\{A\} \approx \{I_z\} + \{b_z\} \quad (3.60)$$

where $[K_{\text{mar}}]$ is the *tangential* or *marginal* stiffness matrix. If we know the flux density everywhere, then we would be able to calculate the stiffness matrix $[K_{\text{mar}}]$ instantly and directly. The flux densities are calculated by an iterative procedure using a Newton-Raphson technique which is described in the next paragraph. $\{b_z\}$ is the free MMF vector. For a linear case the value of the vector $\{b_z\}$ will be zero and then Equation (3.60) will be similar to Equation (3.50). That is why linear problem is treated as a special case of non-linear problem throughout this thesis. To calculate the vector $\{b_z\}$, a point P_1 is considered in the non-linear region on the $B(H)$ as shown in Figure (3.10). If a tangent is drawn through P_1 as shown by a dotted line in Figure (3.10), then there will be a negative value for field intensity. This is shown as M in the figure. Based on the direction of the saturation there will be components of M . Once the components of M are obtained the free MMF vector can be calculated using the similar procedure explained in Section 3.3.4.2.

The Newton-Raphson procedure, an extension of the Newton method, is adopted because of its quadratic convergence to solve non-linear problem in this analysis. It works by guessing a trial solution, and then successively improving the “initial guess” by using the slope of the $B(H)$ curve. Figure (3.10) shows a schematic representation of the procedure adopted to solve the non-linear static electromagnetic problem using the Newton-Raphson method.

The procedure starts with an initial guess of the permeability and this is shown as μ_g in Figure (3.10). $\mathbf{B}_T(x, y)$ and $\mathbf{H}_T(x, y)$ are the flux density and field intensity respectively corresponding to μ_g . $\mathbf{M}(x, y)$ is referred here as the free MMF which is

$$\mathbf{M}(x, y) = \frac{\mathbf{B}_T(x, y)}{\mu_g} - \mathbf{H}_T(x, y) \quad (3.61)$$

At each point in the domain a linear approximation is made to the magnetic characteristics. The stiffness matrix and free MMF are calculated for this initial guess. Once the stiffness matrix and the free MMFs are calculated, the magnetic vector potentials are calculated using Equation (3.60). Now an excitation residue vector, $\{\mathfrak{R}\}$ is calculated using the equation

$$\{\mathfrak{R}\} = [\{I_z\} + \{b_z\}] - [K]\{A_{\text{current}}\} \quad (3.62)$$

The nominal correction proposed by the standard Newton-Raphson procedure for addition to the magnetic vector potential will be

$$\{\Delta A\} = [K]^{-1} \cdot \{\mathfrak{R}\} \quad (3.63)$$

The actual new magnetic vector potential is

$$\{A_{\text{new}}\} = \{A_{\text{current}}\} + \alpha \cdot \{\Delta A\} \quad (3.64)$$

Here α is a relaxation factor which helps to facilitate the convergence. Improvement of convergence characteristics of Newton-Raphson method for nonlinear magnetic field analysis by choosing the optimum relaxation factor is explained by Nakata (1992) and Oapos and Oapos (1995). The procedure for updating the estimated vector of potentials based on a known vector of excitation is continued until the norm of the residue satisfies the convergence criteria.

3.6 Computer code for finite element analysis of electromagnetic

The previous sections mainly focus on the general procedure of finite element modelling in electromagnetic field problems. A particular interest is devoted to the modelling of magnetic material behaviour and to the coupling with the electromagnetic field computation. The procedures described above are general in nature and can be applied to the analysis of any electromagnetic systems.

Computational codes called **MagFEA** (*Magnetic Finite Element Analysis*) for two-dimensional electromagnetic field problems have been developed in the MATLAB™ environment based on these procedures. The results are verified by a commercial software called ‘MEGA™’ developed by the University of Bath, UK. The results obtained from the MagFEA and MEGA for a simple electromagnetic device have been presented in Appendix. Most of the numerical routines that have been used are standard routines within MATLAB. This is the main reason for choosing MATLAB for this study. **MagFEA** comprises a pre-processor where the model is built, a solver where excitations are applied and responses are computed and a postprocessor, for producing graphical output. The solver has the capability to solve linear as well as nonlinear transient problem.

3.6.1 Pre-processor

In the pre-processor facilities are provided which assist the user in creating a description of his model. The design of the pre-processor of MagFEA is generic and can model any 2D geometry. Mesh generation is semi-automatic. At the first stage the user has to identify the key regions of the model and then specify the discretisation level. An isoparametric element is used to map the local element to the global element. The procedure of mesh generation can be summarised as follows:

- User divides the meshable region into key regions (or elements).
- Generate information about the nodal coordinate of the key nodes and connectivity of the nodes of the key region.
- Generate information about the material properties and excitation of individual key elements.
- User decides the discretisation level depending on the requirement.
- Discretise individual key elements as per the discretisation level using isoparametric elements.

The model comprises of seven arrays and these are KEYNODES, KEYELEMS, KDIV, NODES, ELEMS, PERM, EXCT.

- KEYNODES comprises of three columns and stores the information about the nodal coordinates of the key nodes of the domain to be discretised. The first

column stores the keynode labels, and the other two columns stores the x- and y-coordinates respectively.

- KEYELEMS comprises of eleven columns. It stores the information about the connectivity of the keynodes, indices for the material properties, excitation and element types. The first eight column stores the connectivity of the keynodes. Some of the entries of these eight columns will be zero if we use 4-noded quadrilateral, 3-noded triangular and 6-nodes triangular elements.
- KDIV stores the information about the discretisation level and comprises two columns. The number of rows of KDIV is equal to the number of key elements. The first column stores the number of divisions along the local x-axis and the second column stores the number of divisions along the local y-axis of a particular key element.
- Similar to the KEYNODES, NODES comprises of three columns and stores the information about the nodal coordinates of all nodes of the whole domain once it is discretised. These columns store exactly the same information as the columns of KEYNODES.
- Similar to the KEYELEMS, ELEMS comprises of eleven columns and stores the information about the connectivity of all nodes for the whole domain once it is discretised. These columns store exactly the same information as the columns of KEYELEMS.
- PERM comprises of two columns and stores the information about the material properties specified by the ninth column of ELEMS. The two columns of a particular row represent the permeabilities along the two orthogonal directions and they are μ_{xx} and μ_{yy} . In case of isotropic materials $\mu_{xx} = \mu_{yy}$ but in case of orthotropic materials $\mu_{xx} \neq \mu_{yy}$.
- EXCT stores the information about the excitation applied to the elements. The excitations are mainly constant current density. This array is optional because in most of the application of this study we do not have prior information about the excitations in terms of current density.

3.6.2 Solver

The solver is capable of solving 2D magneto-static electromagnetic problems. An excitation is applied as a current density. The solver is also capable of modelling permanent magnets. To solve for the permanent magnet remanent flux, the relative permeability and magnetization direction are provided as an input to the solver. Any permanent magnet portions of the model are modelled using current distributions. The solver has the following capabilities

- Linear and non-linear 2D magneto-static analysis of electromagnetic system, electromechanical actuators, electrical machines.
- Steady state characteristics of electrical machines in general and induction machine in particular.
- Transient solver including motion-induced eddy currents.

This solver also includes the coupling of electromagnetic equation to the mechanical equations of motion, so that the movement of an electrical machine is accurately simulated. The rotor and stator of an electrical machine are modelled completely independently and combined at the middle of the airgap to take care of the rotor movement. The solver re-meshes only the airgap regions to take care of the rotor movement. A method where the solver does not have to be re-meshed to take care of the movement is explained later Chapter 7.

3.6.3 Post-processor

In the post-processor the computed results from the analysis are displayed. The post-processor has the following features

- Plot contours of the magnetic flux at any location in the finite element domain.
- Calculate and plot the flux densities along the two orthogonal directions at any location in the finite element domain.
- Calculate and plot the magnetic stresses along the two orthogonal directions at any location in the finite element domain.
- Calculate the forces along the two orthogonal directions.

3.7 Case studies for Static Unbalance Magnetic Pull (UMP)

This section presents three case studies to validate the non-linear finite element code developed which is explained in the previous section and also to calculate static UMP. In the following section the results from the finite-element code (MagFEA) are presented. Static UMP is calculated for two different electrical machines. The first one is a 2 kW, 3-phase induction motor. The configuration of the stator and electromagnetic parameters of this motor are similar to the experimental rig discussed in later chapters. The only difference between the two is the configuration of rotor. Unlike the rotor in the experimental rig, the rotor in the machine studied here has non-magnetic slot wedges. The numerical modelling code has the provision to study machines with either magnetic or non-magnetic slot wedges.

3.7.1 Case study I: Unbalanced magnetic pull of an induction machine

The first case study aims to calculate the static UMP of a 2 kW induction motor. The main electromagnetic parameters of the motor are presented in Table (3.1). The stator and rotor are modelled separately and discretised with eight noded quadrilateral elements. These two meshes are connected at the middle of the airgap with six noded triangular elements. Figure (3.11) shows the finite element mesh considered for this study. Currents are applied at the stator windings which vary sinusoidally about the machine periphery producing a four pole field in the motor. Forces are calculated using the non-linear solver of **MagFEA** when 3-phase sinusoidal currents with peak currents of 100A, 200A and 300A per slot respectively in the stator for different eccentricities of the rotor. Induced currents in the rotor are not considered as the radial force is calculated for the worst case of the motor. A contour plot of magnetic vector potentials is shown in Figure (3.12) when a 3-phase current with a peak of 200A is applied in the stator for a concentric rotor. Figures (3.13) and (3.14) show the normal and tangential components of flux density in the middle of the airgap respectively for the same operating current but with an eccentricity of 10% of the airgap. The magnetic normal and shear stresses are calculated using Equations (2.23) and (2.24) of Chapter 2 once the components of flux densities are known at the airgap. Normal

and shear stresses in the airgap are shown in Figures (3.15) and (3.16) as a function of the angular position.

The mean airgap for the above study is kept constant at 0.4 mm. Forces are calculated by shifting the rotor from its central position along the positive x -direction as well as along the negative x -direction. Because of the discretization there will be some vertical force associated with this horizontal movement. Figure (3.17) shows the horizontal and vertical forces per meter of axial length for different eccentricities when 3-phase current with a peak of 200 A (per slot) is applied. For a 30% rotor eccentricity a force of 1800 N per meter of axial length is generated. From Figure (3.17) negative stiffness is calculated as 1.883×10^6 (N/m) per meter of axial length. From Figure (3.17), it is clear that force is varying quite linearly with eccentricities of up to 30% of the airgap. Figure (3.18) shows the horizontal and vertical forces per meter of axial length for 3-phase currents with different peaks per slot. The effect of magnetic non-linearity in the iron is distinct from Figure (3.18). For a peak current of 300 A per slot, the force no longer varies linearly with the current. As the machine is saturated the magnetic fluxes are distributed uniformly reducing the amount of unbalance flux in the airgap and in turn reduces the unbalance force in the airgap.

3.7.2 Case study II: Unbalanced magnetic pull of a small high speed permanent magnet alternator (PMA)

The second case study investigates UMP for a small high speed 14-pole permanent magnet alternator with an overhung rotor. This case study serves as an excellent example to demonstrate how severe the effects of UMP can be. It is found from this small study that a significant reduction of critical speed is possible due to UMP. This reduction was not appreciated fully by the system designers during the mechanical modelling of the alternator. The main parameters of the alternator are given in Table (3.2).

The stator and rotor of the permanent magnet alternator are modelled separately using eight-noded quadrilateral element and the two are combined by stitching the airgap using six-noded triangular elements. Horizontal and vertical forces are calculated for

different eccentric position of the rotor in the same way as they were calculated for case study I. In this case the excitation is considered from the permanent magnets on the rotor. Stator currents are constrained to remain zero in this analysis. Figure (3.19) shows the FE mesh considered for the analysis. The remanent flux density of the permanent magnet material is 1.2 Tesla with and its relative permeability is taken to be 1. Figure (3.20) shows the contour plot of the magnetic vector potential. Once the model is solved using the non-linear solver of **MagFEA** the normal and tangential components of flux density are calculated at the middle of the airgap. The airgap radial thickness of the PMA is 0.635 mm. Figures (3.21) and (3.22) show the normal and tangential components of flux density in the middle of the airgap of the PMA. A normal component 0.65 Tesla can be achieved in the middle of the airgap for remanent flux density of 1.2 Tesla of the permanent magnets. The normal and tangential stresses at the middle of the airgap are shown in Figures (3.23) and (3.24) respectively. Figure (3.25) shows the forces per meter of axial length along x-direction for different eccentric positions of the rotor. The negative stiffness calculated for the PMA is 7.276×10^5 (N/m) per meter of axial length.

3.7.2.1 Reduction of critical speed due to negative stiffness

As stated in Equation (2.11) of Chapter 2, the natural frequency of a coupled electro-mechanical model can be calculated as

$$\omega_c = \sqrt{\left(\frac{K_{mech} - K_{mag}}{m} \right)} \quad (3.65)$$

where K_{mech} is the mechanical stiffness and K_{mag} is negative stiffness due to UMP. Equation (3.65) shows that due to negative stiffness the natural frequency is reduced. True critical speed of the PMA is calculated for a wide range of mechanical stiffness which is taken as multiples of the negative stiffness. Figure (3.26) shows the variation of true critical speed of the PMA against the predicted critical speed only from mechanical stiffness. Each predicted critical speed is associated with a particular bearing deflection. Critical speed is 'zero' until the bearing stiffness is equal to the negative stiffness. If the operating critical speed without negative stiffness is 25000

rpm, the reduction of critical speed is 6% if negative stiffness is considered. The reduction of the critical speed is 20% if the operating critical speed is 15000 rpm.

3.7.3 Case study III: Investigation of tooth passing spatial harmonics (TPSH) excitation with non-magnetic and magnetic slot wedges

The third Case is an investigation carried out for a company considering the design of a 2-pole generator for a defence application. The aim of this investigation is to study the magnitude of the tooth passing spatial harmonics (TPSH) of the normal stress in the airgap of a 2-pole generator with non-magnetic and magnetic slot wedges. The dimensions of the slot are shown in Figure (3.27). The main parameters of the generator are given in Table (3.3). Figure (3.28) and (3.29) show the finite element mesh of one half of the machine. In these two figures 'cyan' colored regions represent the slot wedge. Taking advantage of the symmetry only one half of the machine is analyzed. The machine is solved for three levels of current density i.e. 5A/mm^2 , 10A/mm^2 and 15A/mm^2 in the rotor slots for cases with non-magnetic and magnetic slot wedge respectively. Figures (3.30) and (3.31) show the contour plots for a machine with non-magnetic and magnetic slot wedge for a current density of 15 A/mm^2 . Once the nodal magnetic vector potentials are known for the model, the magnetic normal stress and shear stress are calculated from the normal and tangential component of magnetic flux density. Figures (3.32) and (3.33) show the normal and tangential components of magnetic flux density in the airgap with non-magnetic slot wedge for a current density of 15 A/mm^2 . Similarly, Figures (3.35) and (3.36) show the normal and tangential components of magnetic flux density in the airgap with magnetic slot wedge for a current density of 15 A/mm^2 . Figures (3.34) and (3.37) show the normal components of magnetic normal stress in the airgap with non-magnetic and magnetic slot wedge respectively for a current density of 15 A/mm^2 . The magnetic normal stress is reduced because of the use of magnetic slot wedge and this is clearly seen from Figure (3.37). Taking the advantage of symmetry, the magnetic normal stress is calculated for angle 0 to 2π . The TPSH component of magnetic normal stress is calculated by taking an FFT of the normal stress. It is found that incorporating magnetic slot wedges in place of non-magnetic slot wedges reduces

the magnitude of the tooth passing spatial harmonics of the normal stress by 60%. There is a slight loss of performance associated with the inclusion of magnetic slot wedges since they provide a magnetic “short-circuit” around the rotor conductors.

3.8 Magnetic Pull (UMP) for overhung machine

Figure (3.38) shows a schematic view of an electrical machine with an overhung rotor and Figure (3.39) shows the corresponding equivalent system. The extended length and the weight of the overhung rotor cause a considerable amount of unbalanced magnetic pull. From the Figure (3.39) the equivalent stiffness of the system is

$$K_{EQUIV} = \frac{K_{MECH_STATOR} \times K_{UMP}}{(K_{MECH_STATOR} + K_{UMP})} \quad (3.66)$$

where K_{MECH_STATOR} is the mechanical stiffness of the stator and K_{UMP} is the negative stiffness because of UMP. If the mechanical stiffness of the stator, K_{MECH_STATOR} is large compared to the negative stiffness of the rotor, K_{UMP} then K_{UMP} is the equivalent stiffness. However, if $K_{MECH_STATOR} \approx K_{UMP}$ then the stiffness of the rotor reduced significantly and there is a tendency to pull the stator towards the rotor.

3.9 Summary of the chapter

The basic procedures of finite element analysis of electromagnetic devices are discussed. The relationship between the nodal currents and the magnetic potentials has been established. For a given current density we can calculate the magnetic potentials. The procedure for calculating resistance matrix of an electromagnetic device using the finite element method is also discussed. Using these procedures a non-linear finite element code, called MagFEA, is developed. Three case studies have been performed using this FE code. The first two case studies investigate the static UMP and the third case study investigates the effect of the tooth passing spatial harmonics in case of the magnetic and the non-magnetic slot wedge.

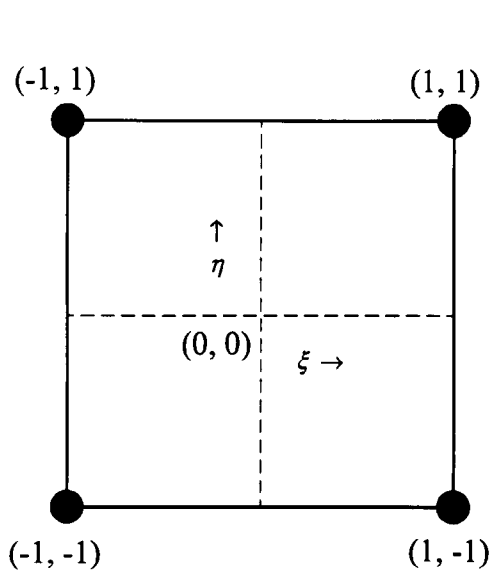


Figure (3.1): Master element

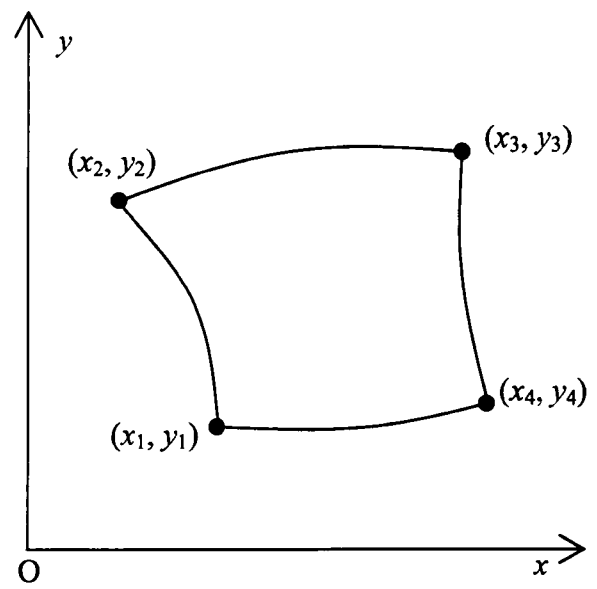


Figure (3.2): Isoparametric element

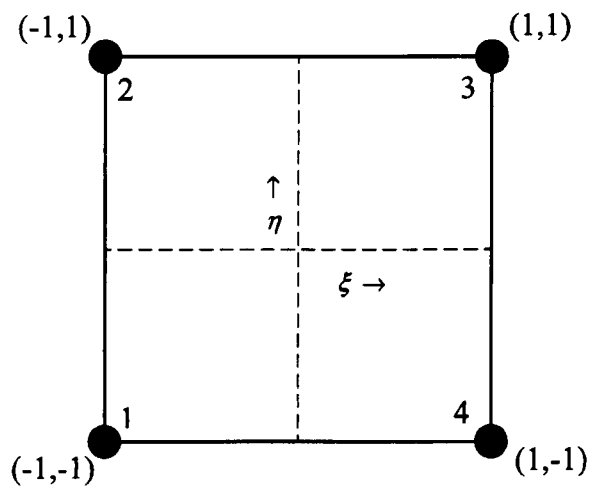


Figure (3.3): Node point ordering of a 4-noded quadrilateral element

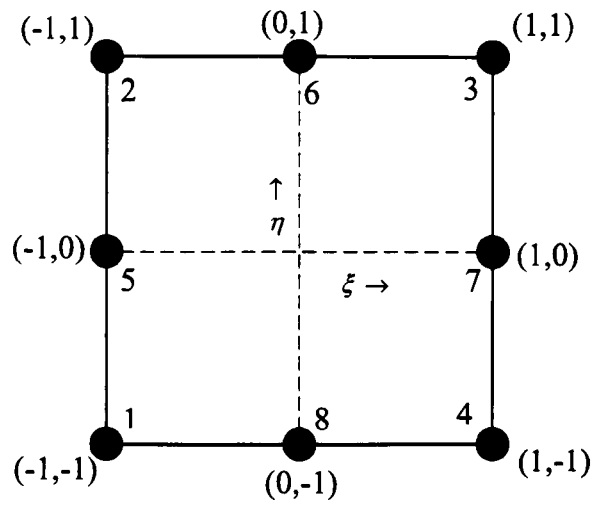


Figure (3.4): Node point ordering of a 8-noded quadrilateral element

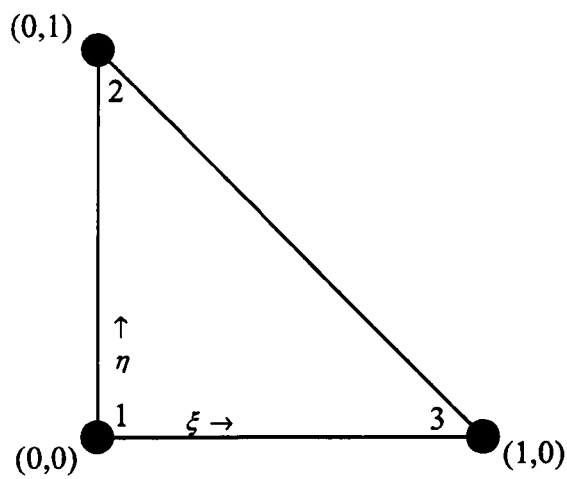


Figure (3.5): Node point ordering of a 3-noded triangular element

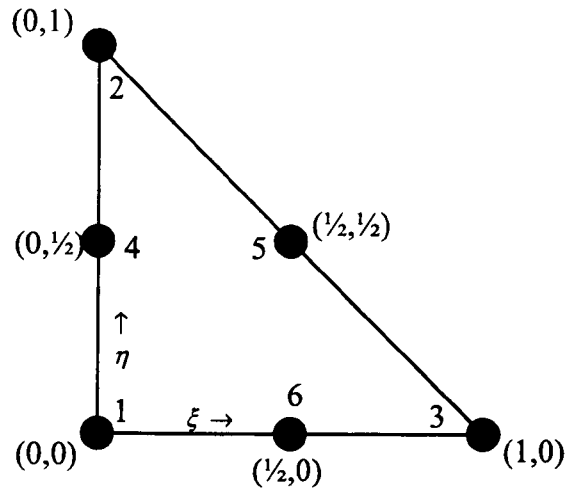


Figure (3.6): Node point ordering of a 6-noded triangular element

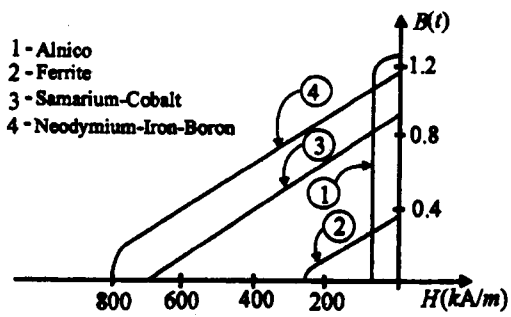


Figure (3.7): $B(H)$ curves for some permanent magnet (Bastos and Sadowski, 2003)

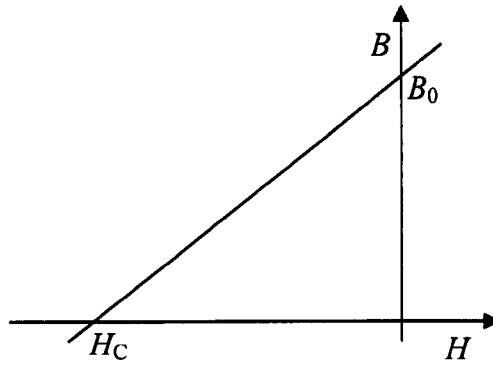


Figure (3.8): Magnetisation curve for a permanent magnet

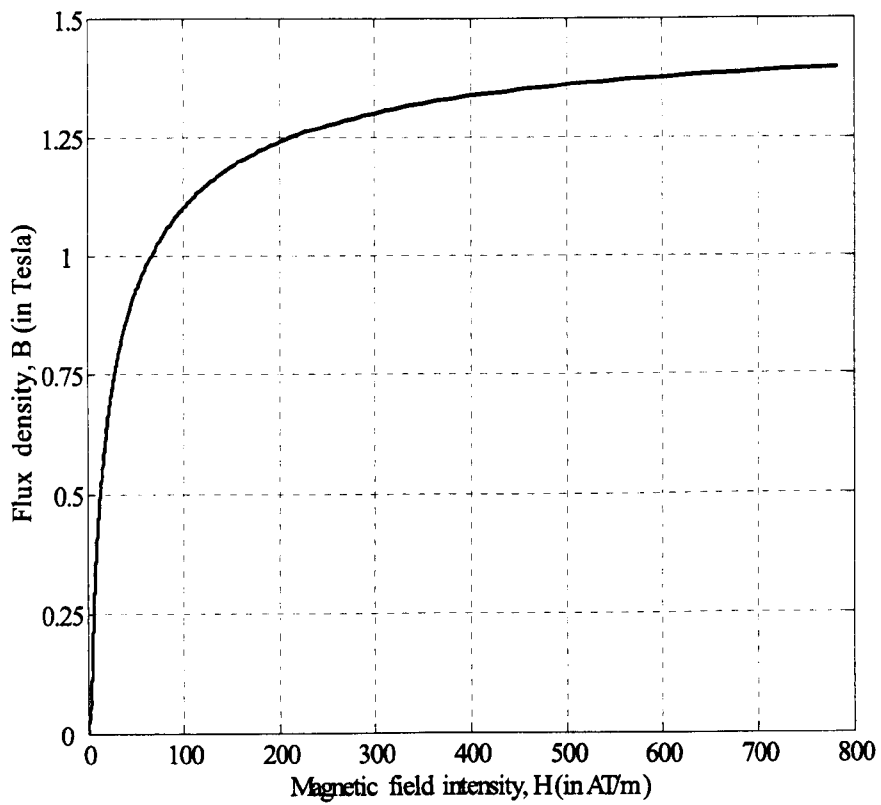


Figure (3.9): Magnetization characteristics in $B(H)$ -form of a typical electrical steel

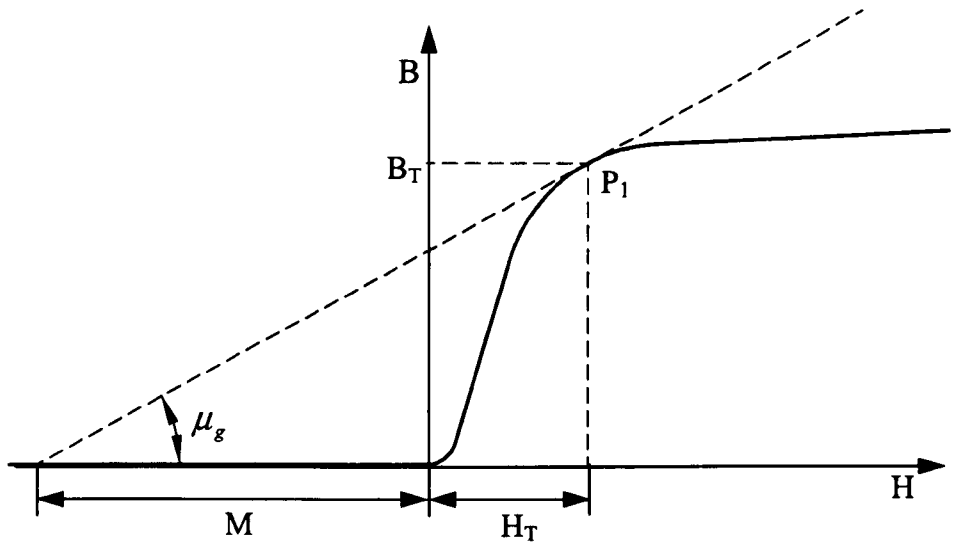


Figure (3.10): Schematic representation of solution procedure of non-linear static electromagnetic problem

Table (3.1): Parameters of the 2 kW induction motor

Parameters	Value
Number of poles	4
Number of phase	3
Number of stator slots	36
Outer diameter of the stator [mm]	153
Inner diameter of the stator [mm]	93
Number of rotor slots	32
Outer diameter of the rotor [mm]	92.2
Airgap [mm]	0.4
Rated voltage [V]	415
Rated frequency [Hz]	50
Rated power [kW]	2

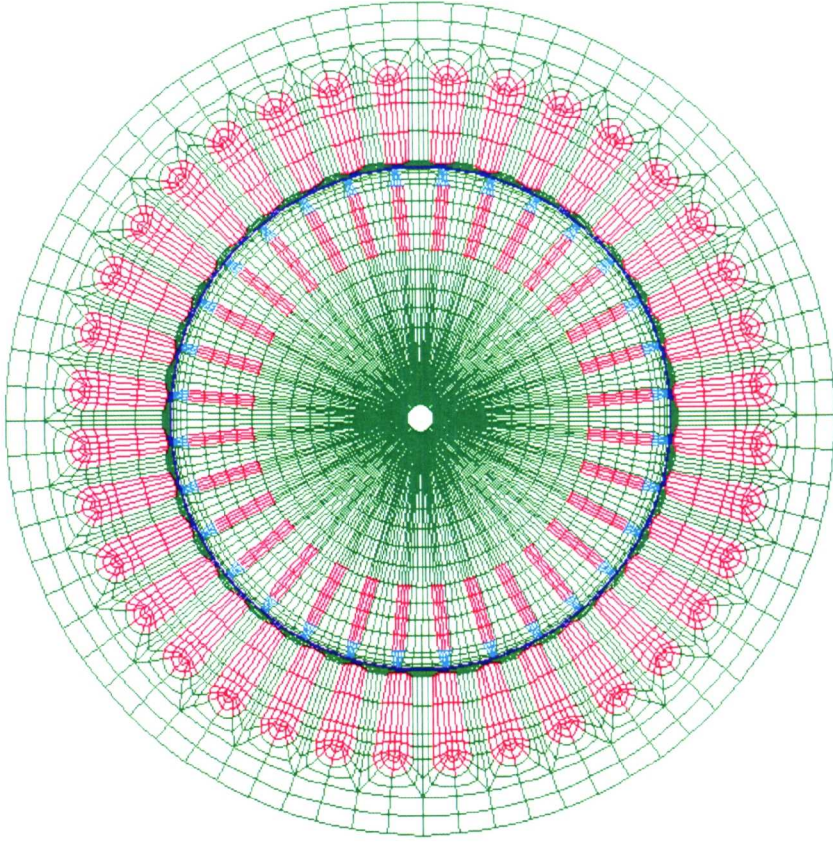


Figure (3.11): FE mesh of the induction motor considered for case study I

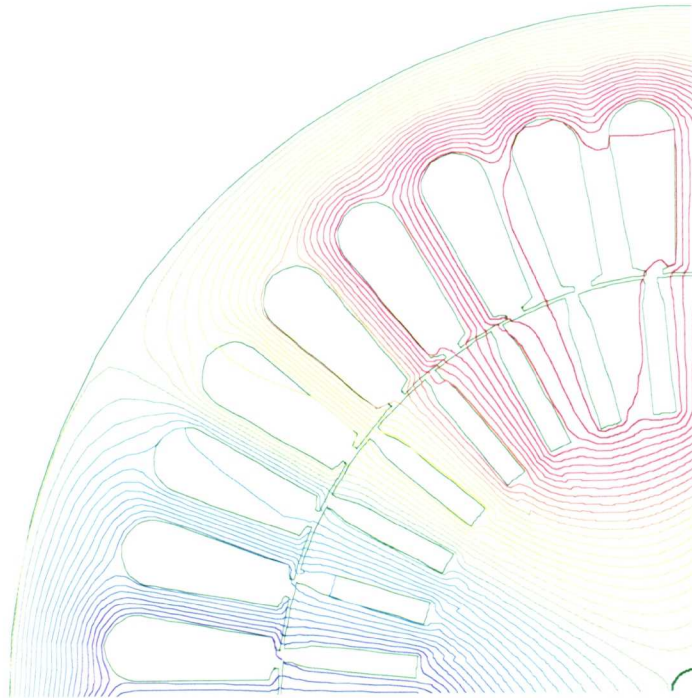


Figure (3.12): Contour of magnetic vector potential when a sinusoidal current when 3-phase current with a peak of 200 Amps (per slot) is applied.

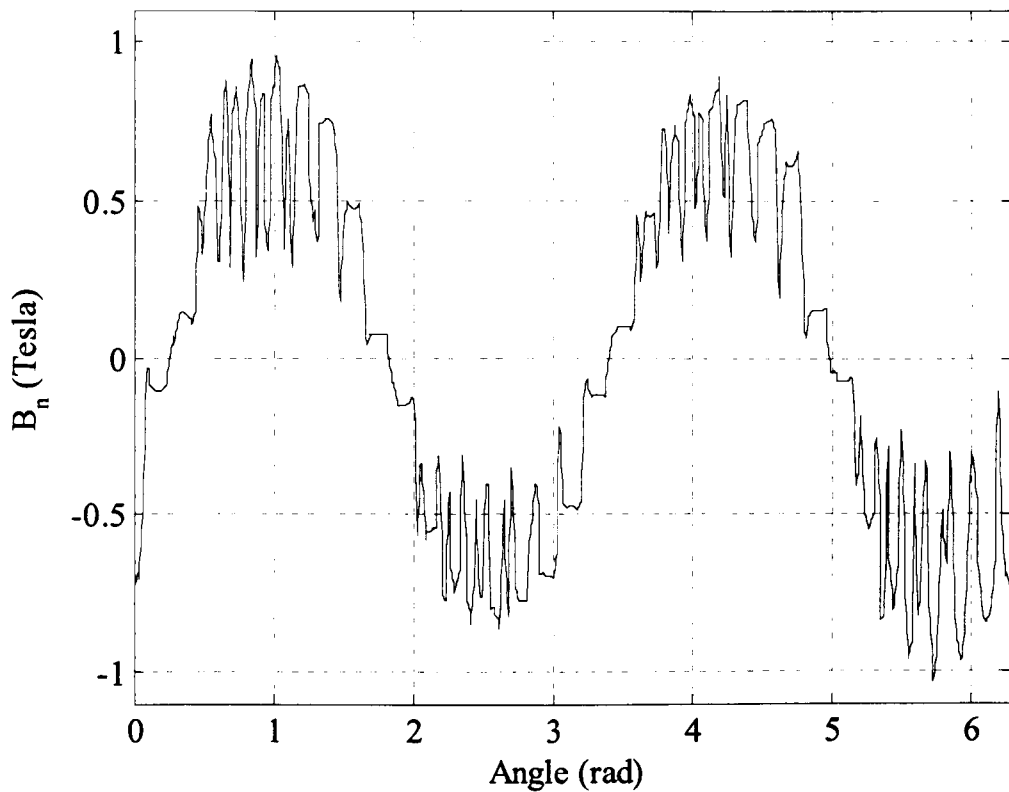


Figure (3.13): Normal component of flux density in the middle of the airgap when 3-phase current with a peak of 200 Amps (per slot) is applied.

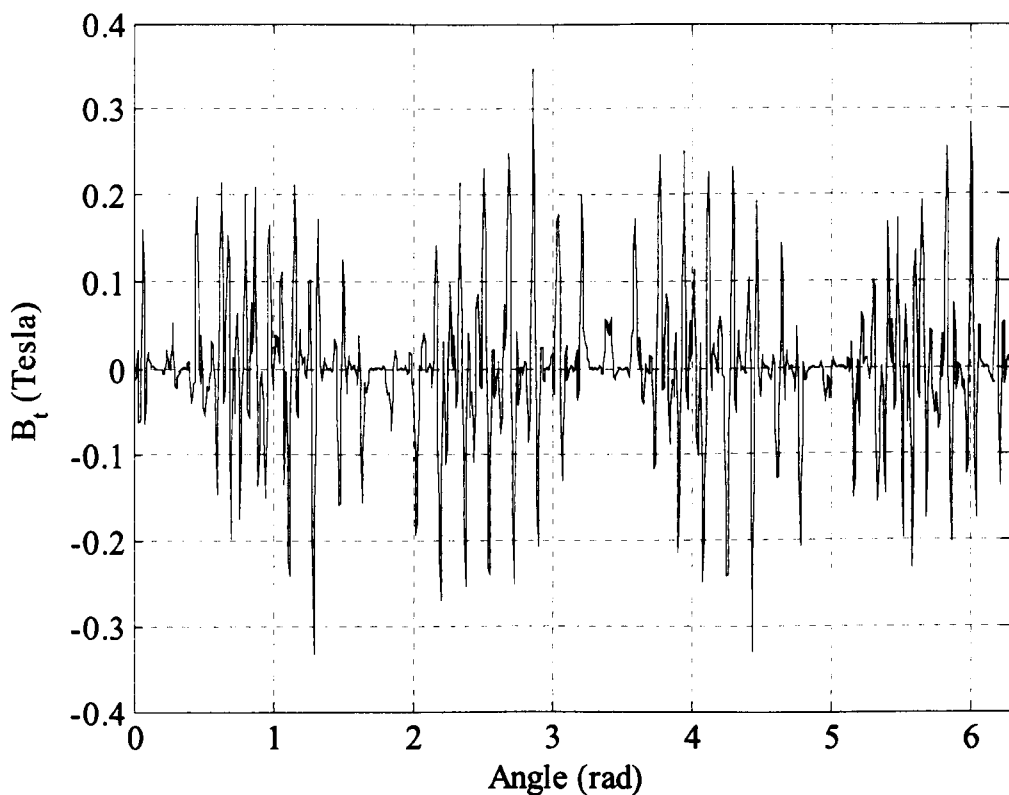


Figure (3.14): Tangential component of flux density in the middle of the airgap when 3-phase currents with a peak of 200 (per slot) Amps is applied

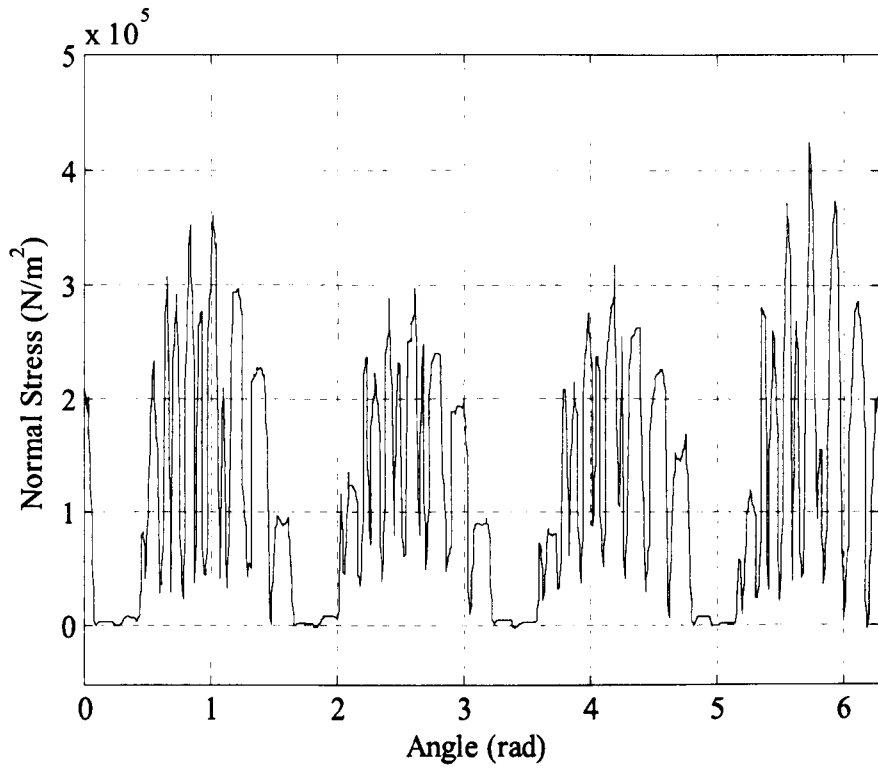


Figure (3.15): Normal stress at the middle of the airgap when a sinusoidal current when 3-phase current with a peak of 200 Amps (per slot) is applied

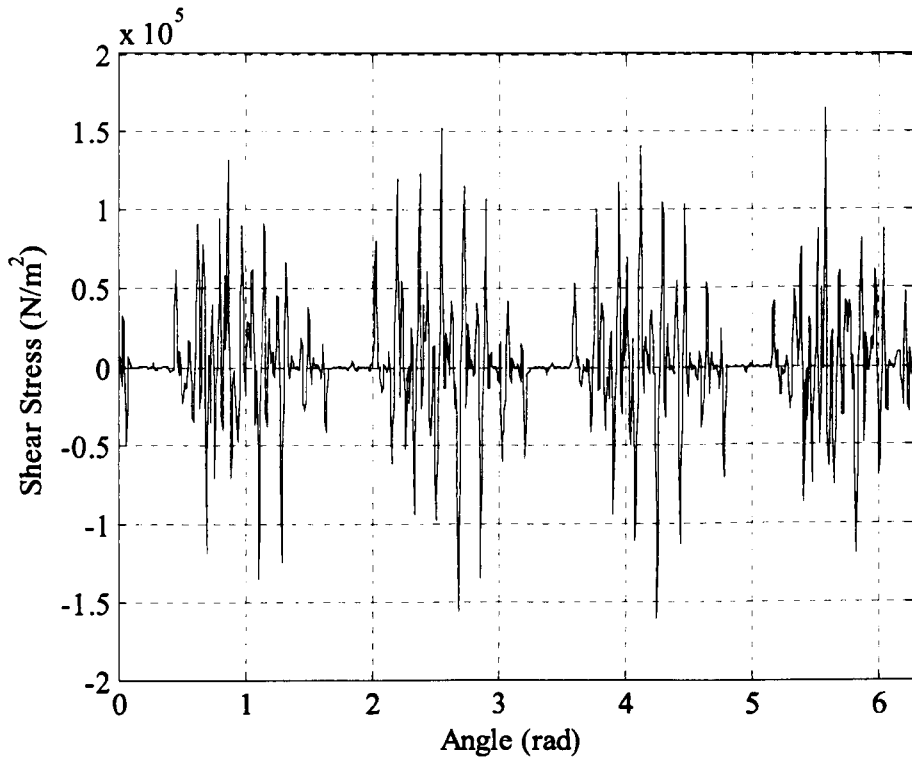


Figure (3.16): Shear stress at the middle of the airgap when a sinusoidal current when 3-phase current with a peak of 200 Amps (per slot) is applied

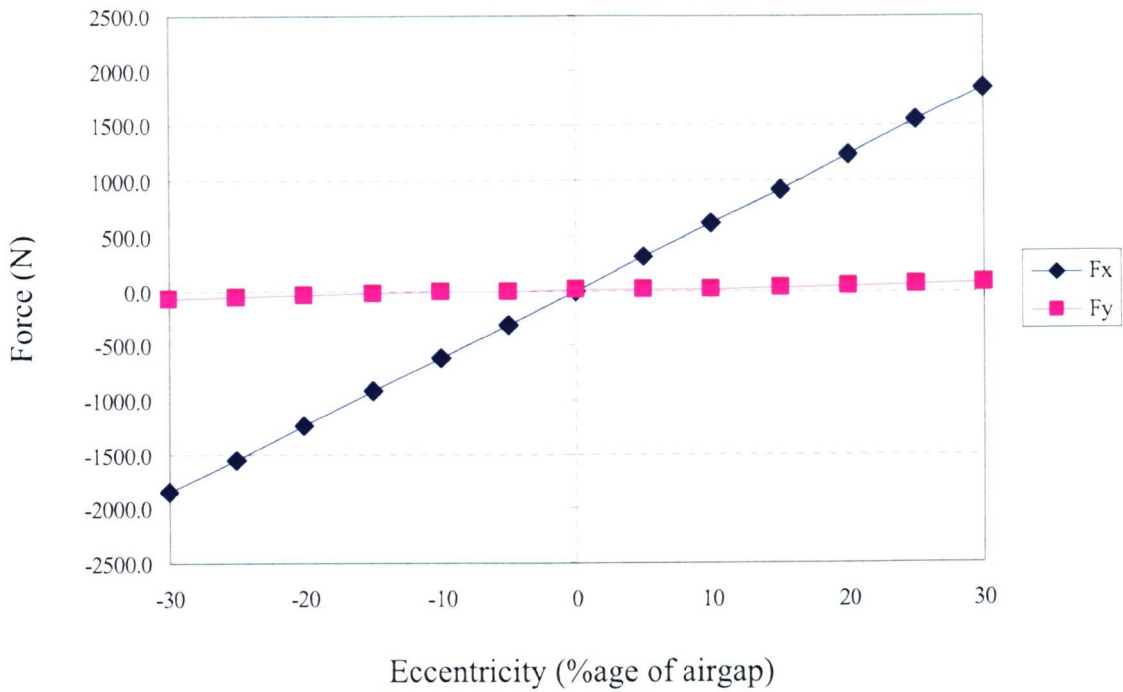


Figure (3.17): Horizontal and vertical force versus eccentricity for the induction machine considered for Case Study I when 3-phase currents with a peak of 200 Amps (per slot) is applied

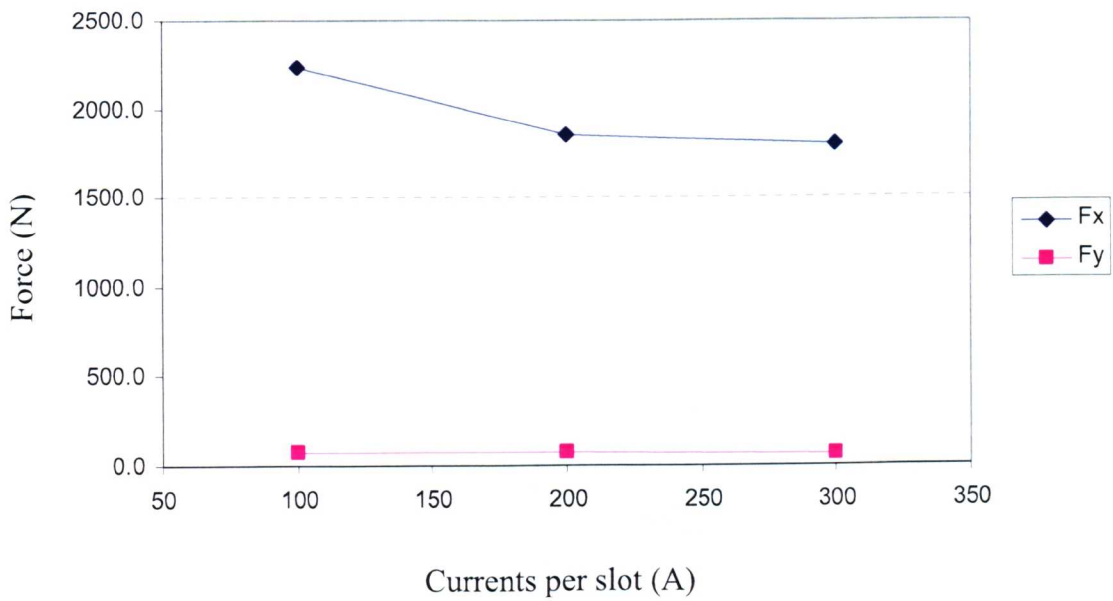


Figure (3.18): Horizontal and vertical forces for 3-phase currents with different peaks (per slot) in the stator for the induction motor considered for case study I

Table (3.2): Parameters of the permanent magnet alternator

Parameters	Value
Number of poles	14
Number of phase	3
Number of stator slots	21
Thickness of the permanent magnet [mm]	3.2
Outer diameter of the rotor [mm]	36.5
Outer diameter of the stator [mm]	50.0
Remanent flux density of permanent magnet [Tesla]	1.2
Relative permeability of the permanent magnet	1.0
Airgap [mm]	0.635
Mass of the rotor which includes magnet, sleeve, carrier, nut, and oil flinger [kg]	0.836
Length of the rotor [mm]	67
Rated frequency [Hz]	50

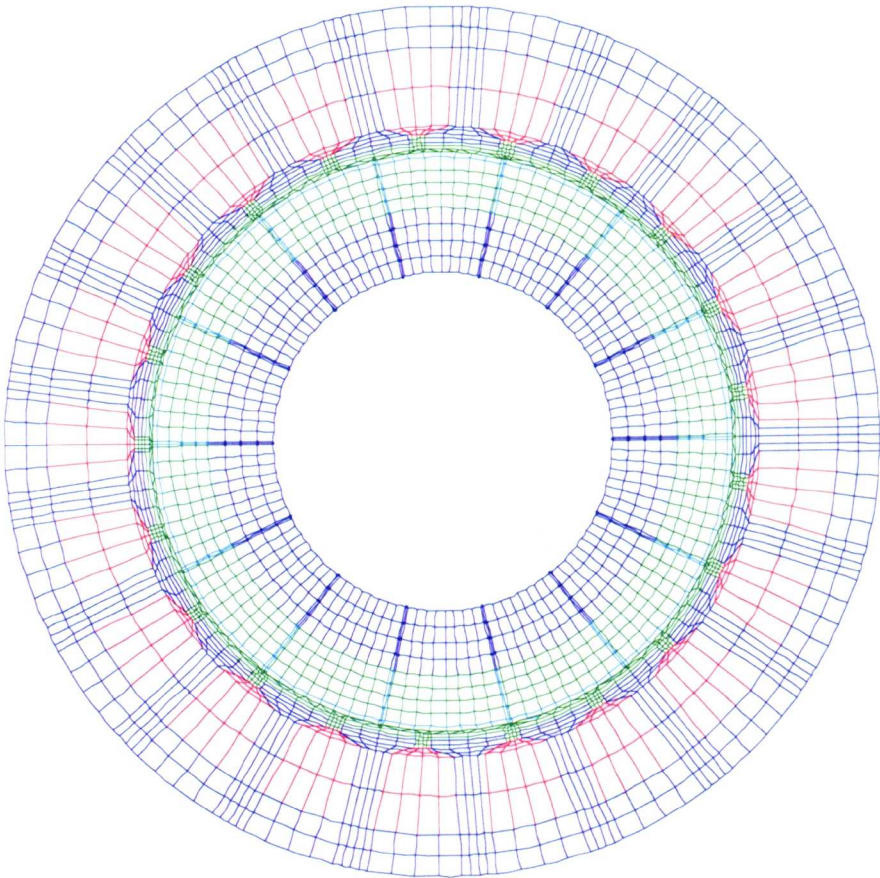


Figure (3.19): FE mesh of permanent magnet alternator (PMA)

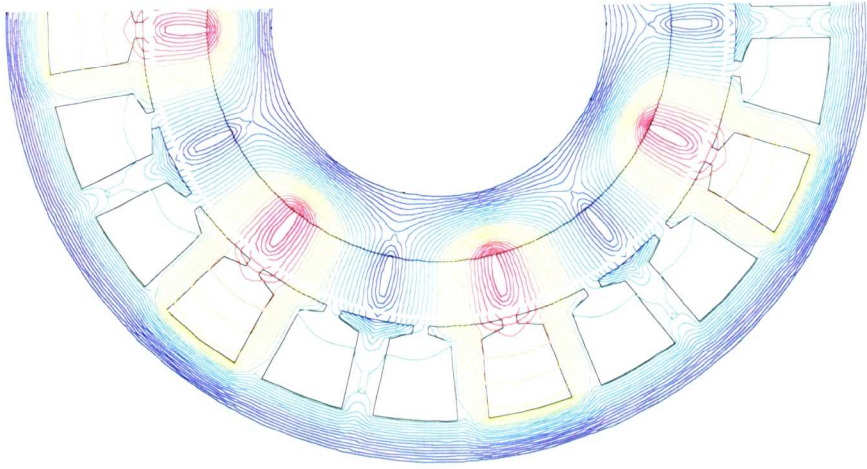


Figure (3.20): Contour plot of magnetic vector potentials of the PMA considering permanent magnet excitation only

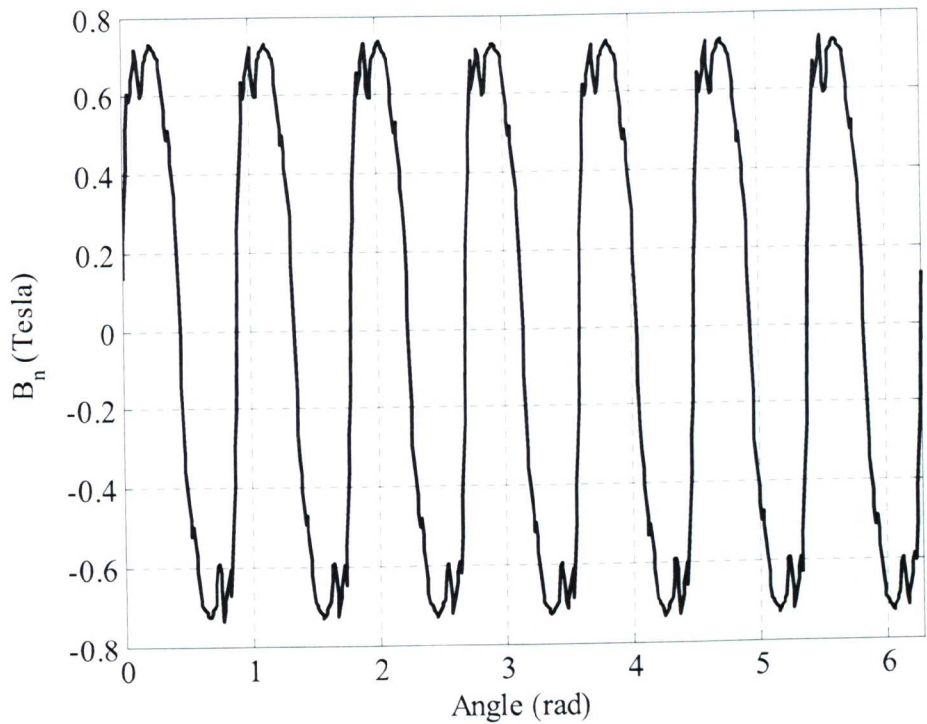


Figure (3.21): Normal component of flux density in the middle of the airgap of the PMA

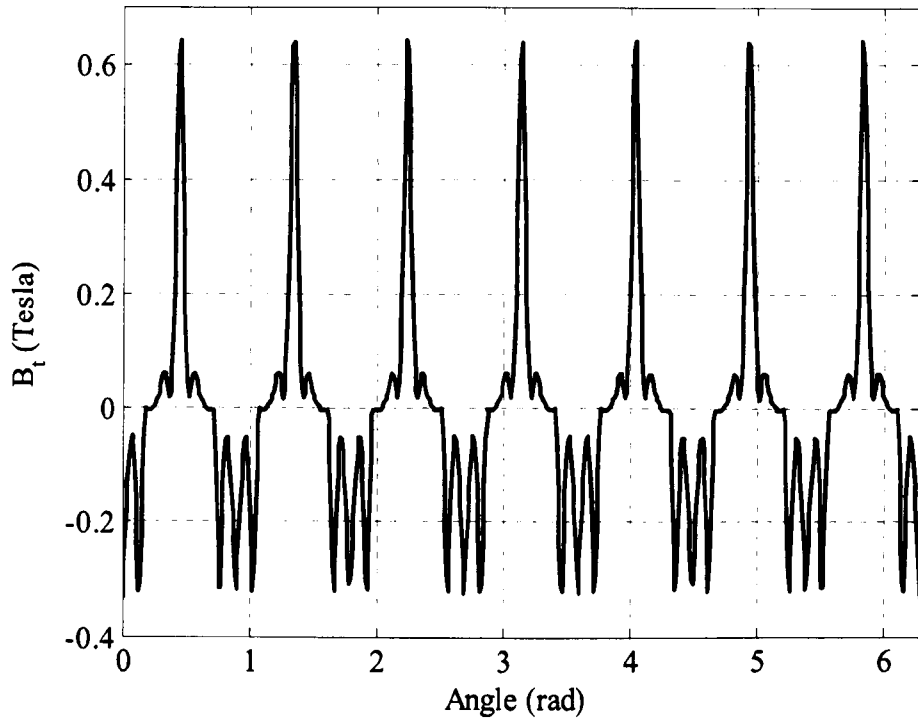


Figure (3.22): Tangential component of flux density in the middle of the airgap of the PMA (when the rotor is concentric with the stator).

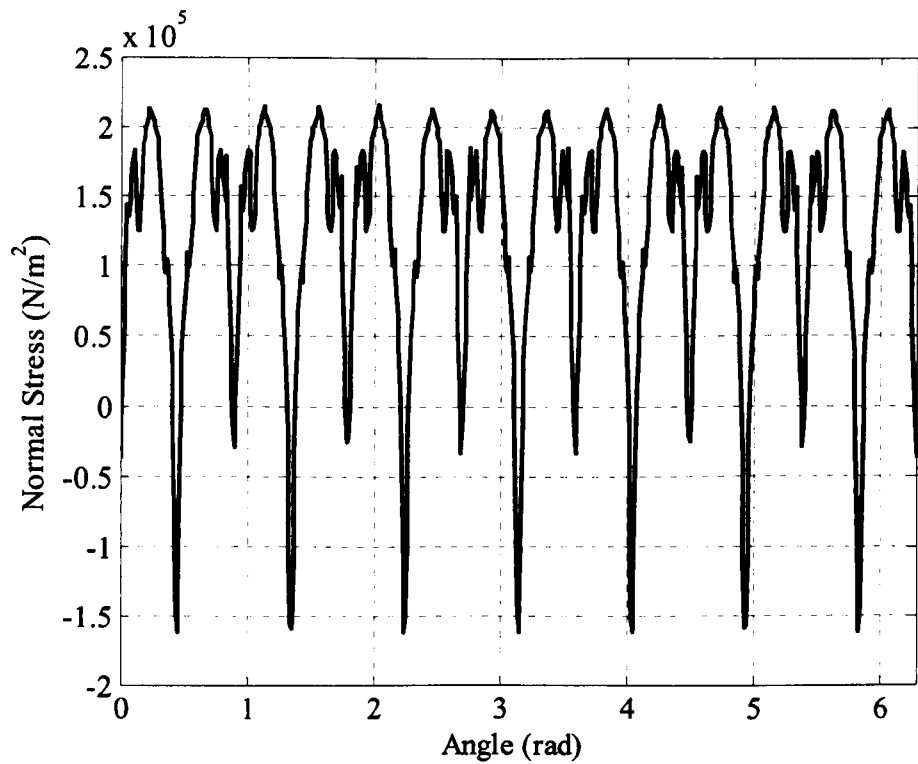


Figure (3.23): Normal stress in the middle of the airgap of the PMA (when the rotor is concentric with the stator)

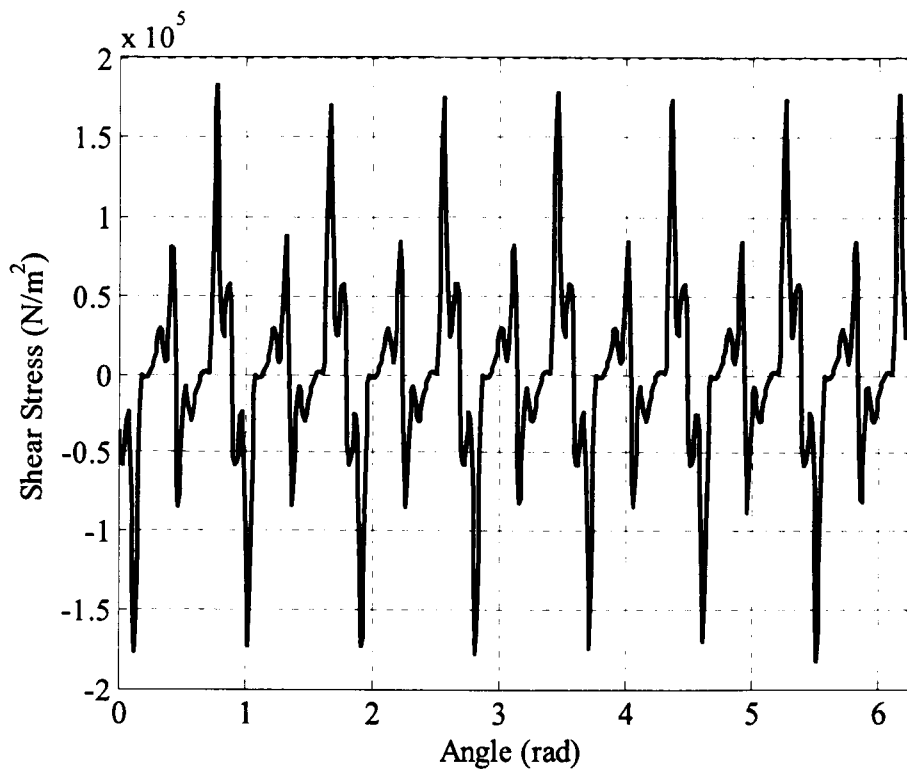


Figure (3.24): Shear stress in the middle of the airgap of the PMA
(when the rotor is concentric with the stator)

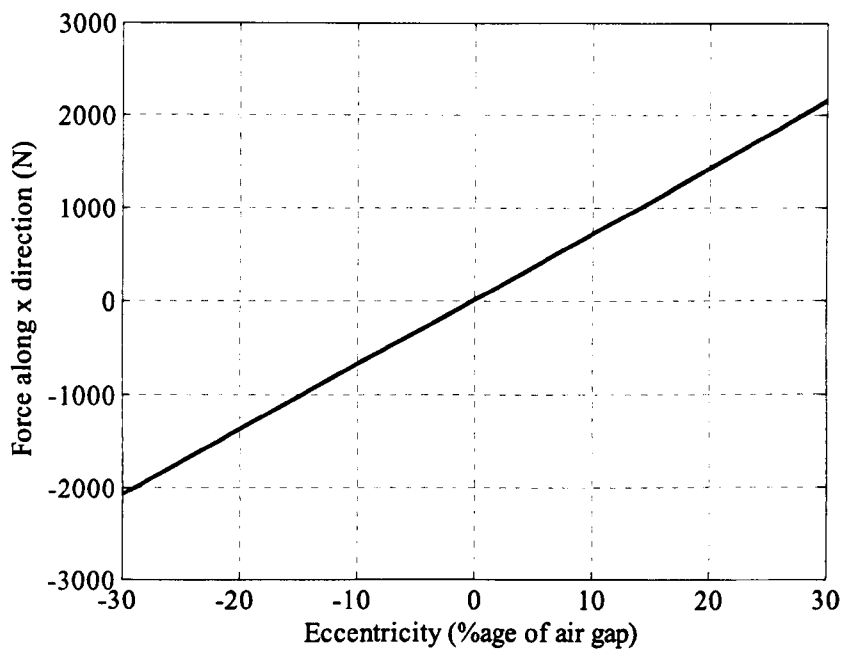


Figure (3.25): Forces on the rotor along x-direction for different eccentricities in case
of PMA

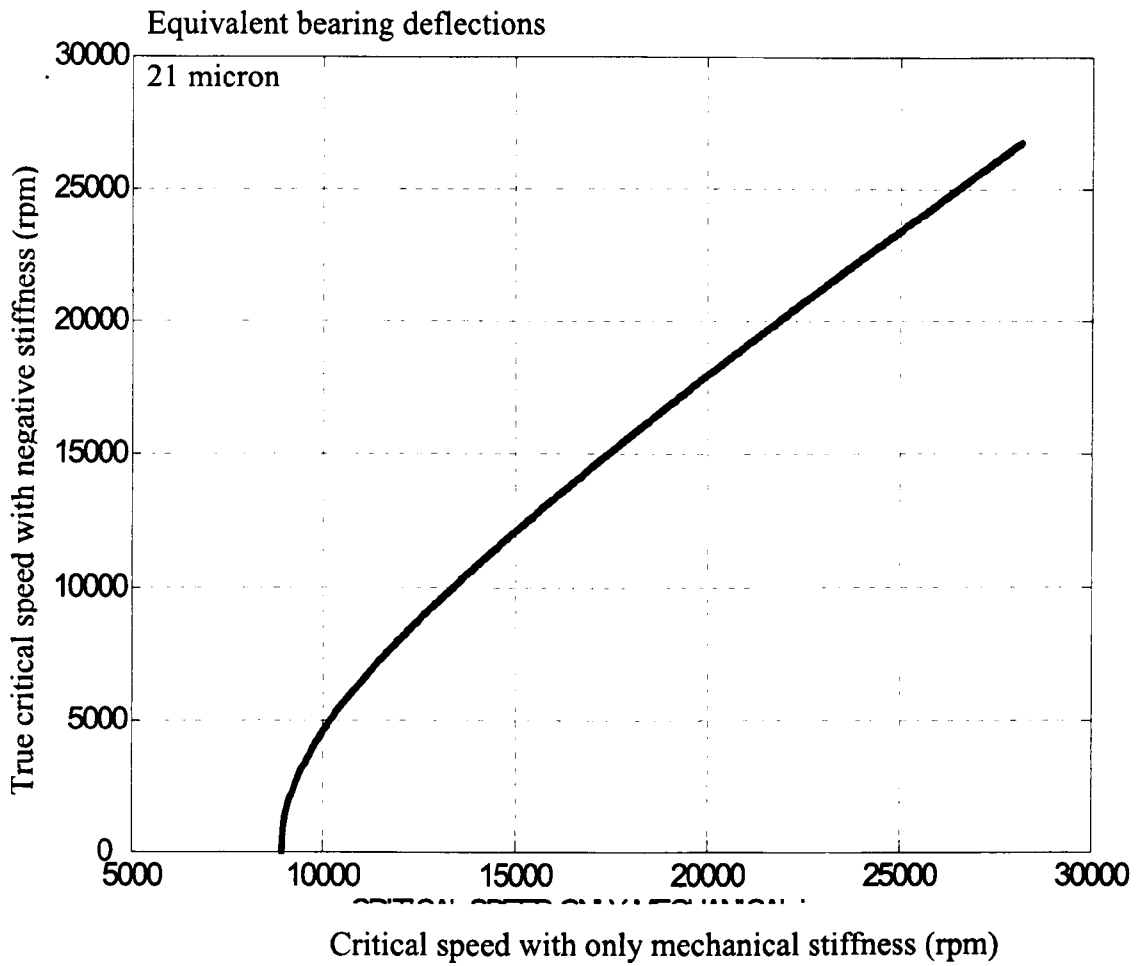


Figure (3.26): True critical speed when negative stiffness due to UMP is also considered along with mechanical stiffness versus predicted critical speed of the PMA.

Table (3.3): Parameters of the 2-pole generator

Parameters	Value
Number of poles	2
Number of phase	3
Number of rotor slots	14
Outer diameter of the rotor [mm]	200
Inner diameter of the stator [mm]	220
Outer diameter of the stator [mm]	380
Airgap [mm]	10

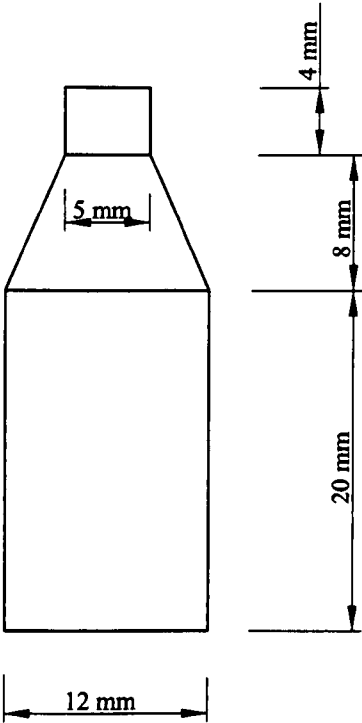


Figure (3.27): Dimension of the slot

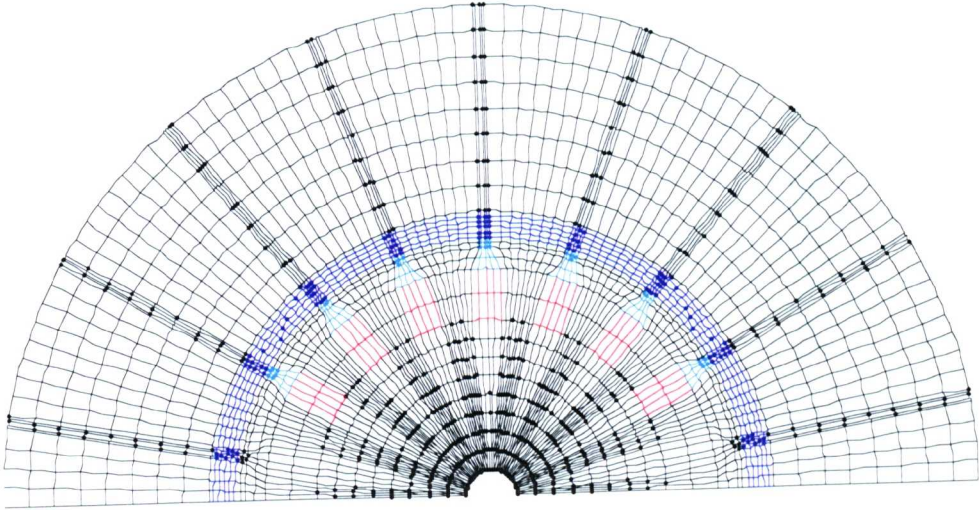


Figure (3.28): A FE mesh

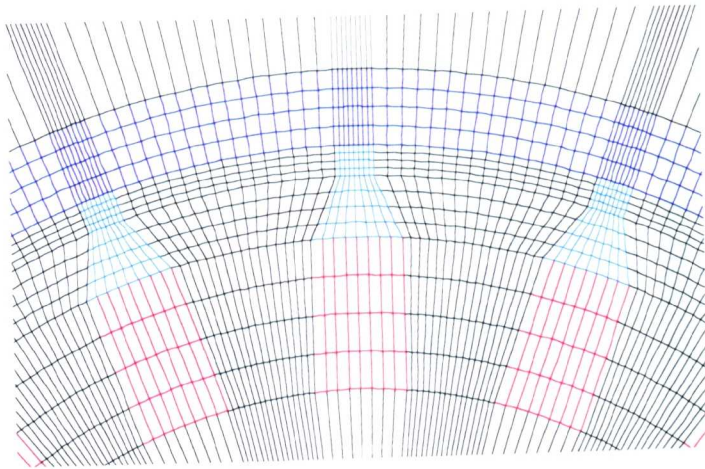


Figure (3.29): A FE mesh

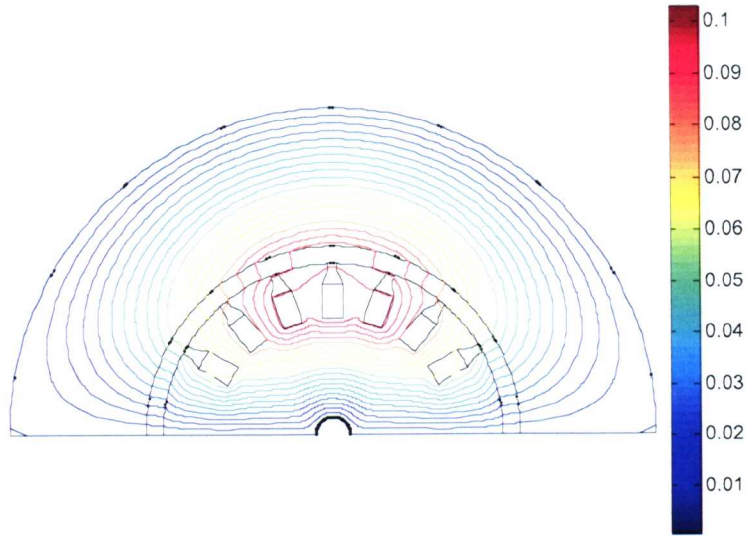


Figure (3.30): Flux contour with non-magnetic slot wedge with current density of 15 A/mm^2

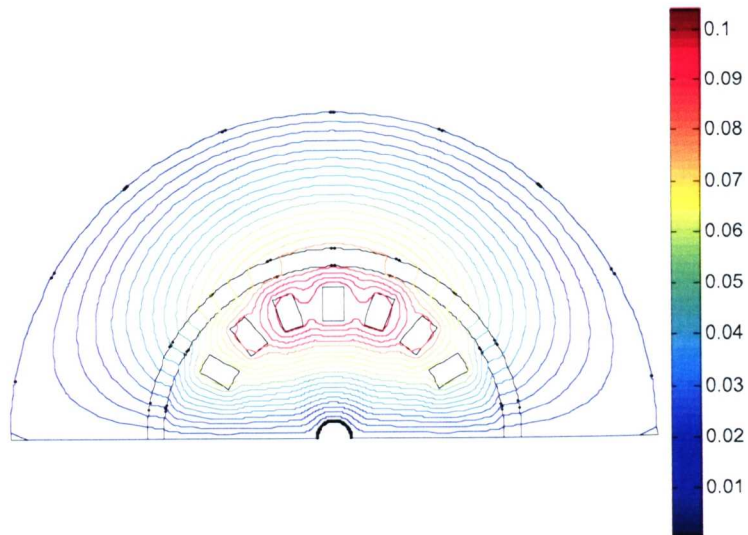


Figure (3.31): Flux contour with magnetic slot wedge with current density of 15 A/mm^2

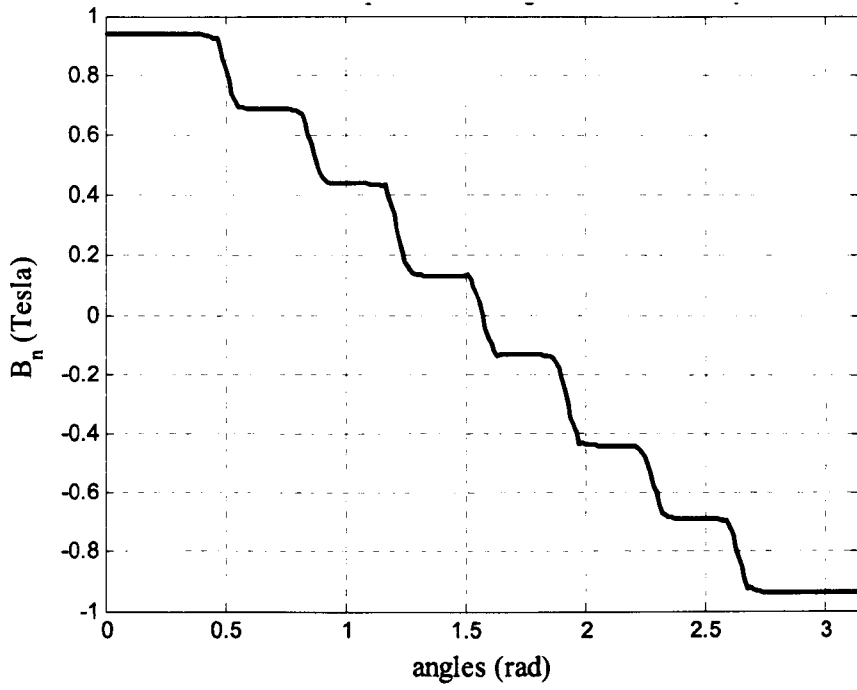


Figure (3.32): Normal component of flux density in the airgap with current density of 15 A/mm^2 for non-magnetic slot wedge

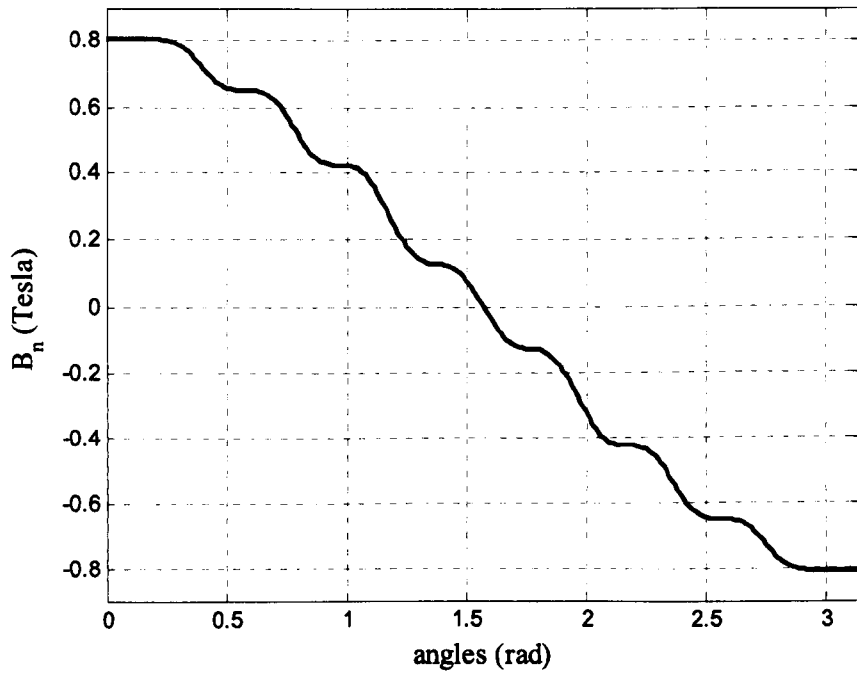


Figure (3.33): Normal component of flux density in the airgap with current density of 15 A/mm^2 for magnetic slot wedge

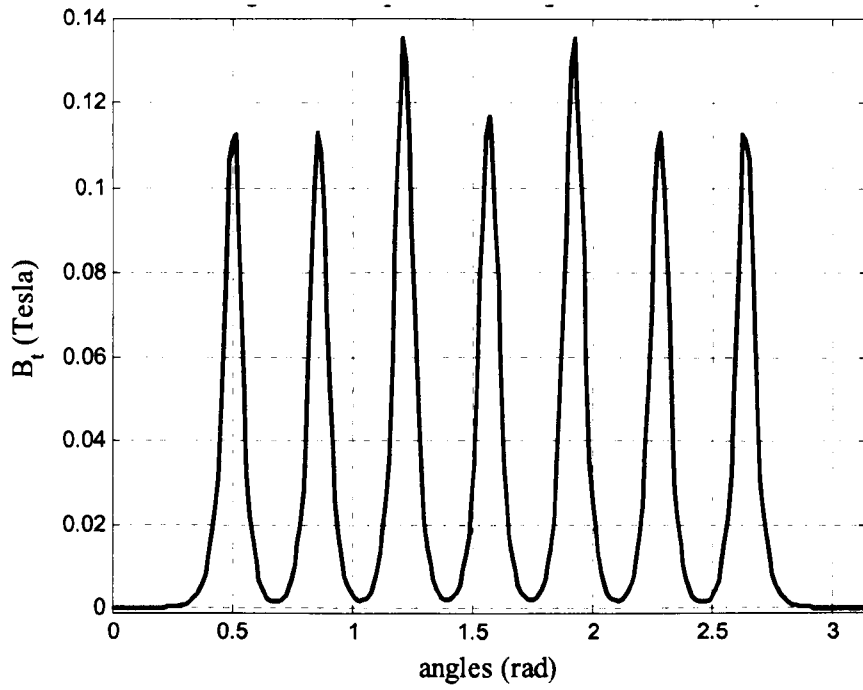


Figure (3.34): Tangential component of flux density in the airgap with current density of 15 A/mm^2 for non-magnetic slot wedge

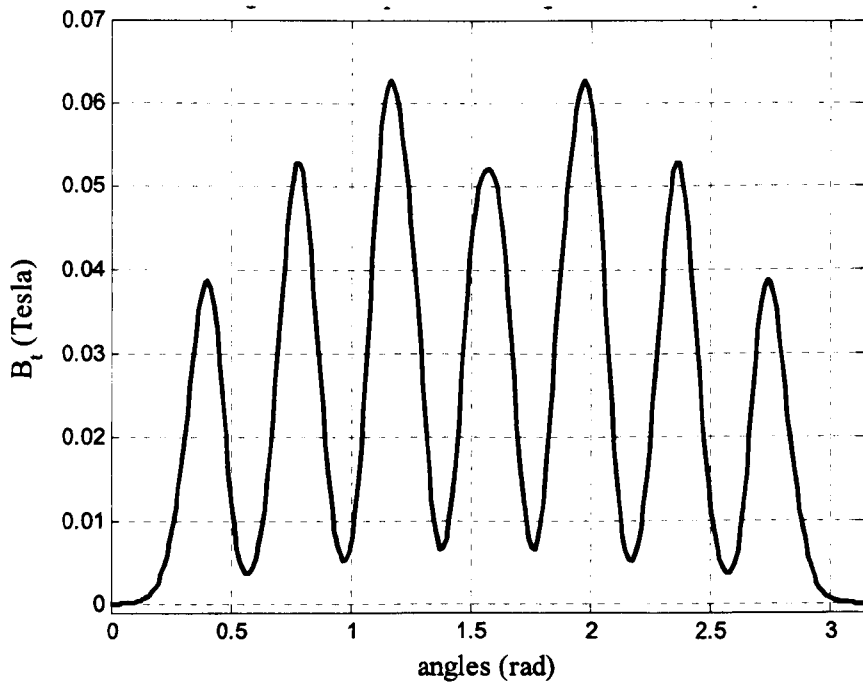


Figure (3.35): Tangential component of flux density in the airgap with current density of 15 A/mm^2 for non-magnetic slot wedge

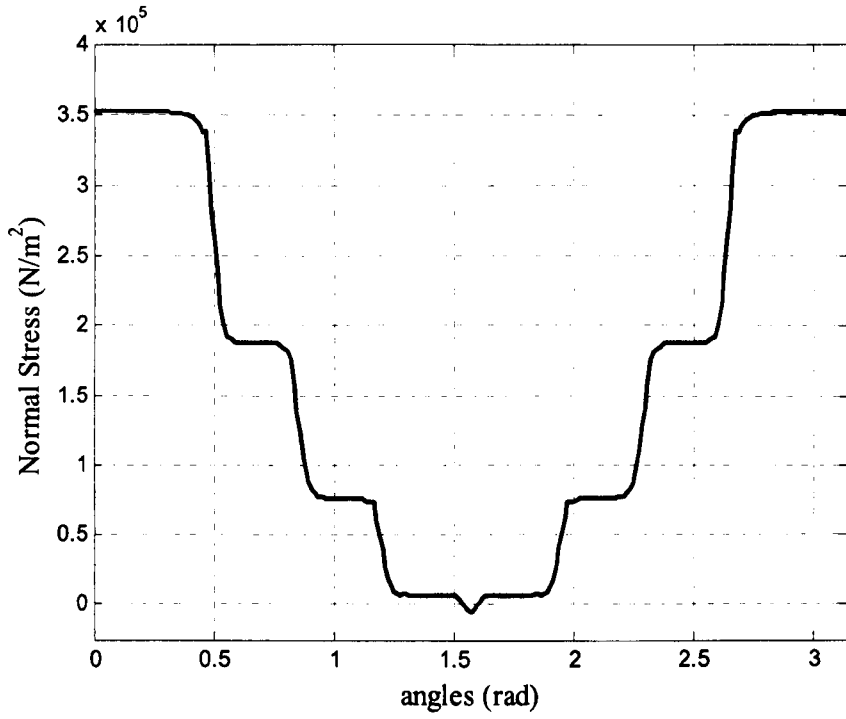


Figure (3.36): Normal stress in the airgap with current density of 15 A/mm^2 for non-magnetic slot wedge

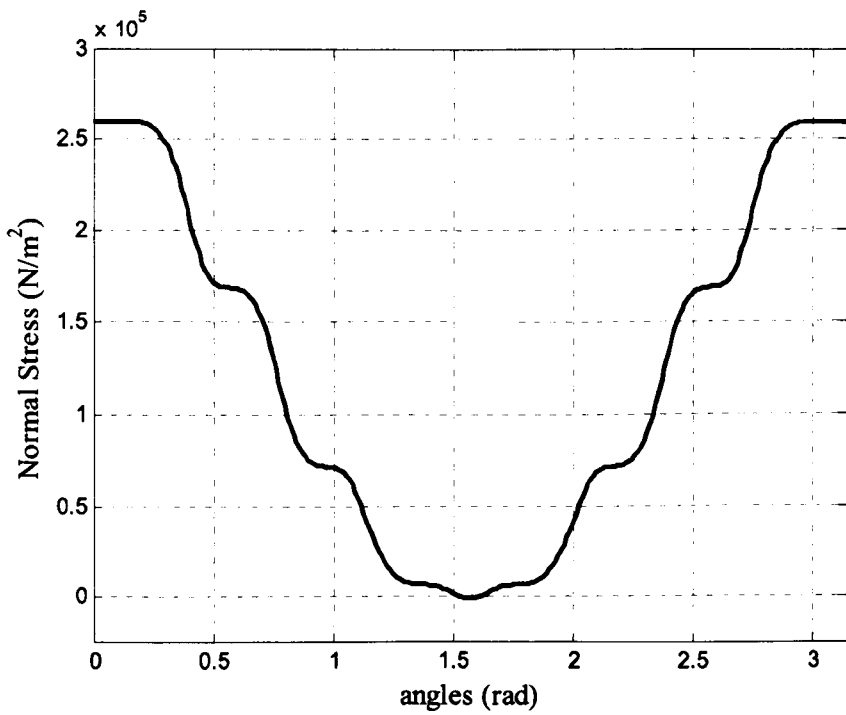


Figure (3.37): Normal stress in the airgap with current density of 15 A/mm^2 for magnetic slot wedge

Table (3.4): Fourier coefficients of the normal stress in the airgap for different levels of currents in the rotor slot

	Normal stress in case of nonmagnetic slot wedges at the tooth tip			Normal stress in case of magnetic slot wedges at the tooth tip		
Spatial Harmonics	Current density in the rotor slots			Current density in the rotor slots		
	5 (A/mm ²)	10 (A/mm ²)	15 (A/mm ²)	5 (A/mm ²)	10 (A/mm ²)	15 (A/mm ²)
TPSH-6	7.3515E2	2.4344E3	3.8671E3	2.0870E3	3.3518E3	4.9412E3
TPSH-4	1.9142E3	4.9760E3	5.6994E3	1.2201E3	2.5845E3	3.4724E3
TPSH-2	3.6368E3	7.7403E3	9.4927E3	1.8937E2	3.7520E3	5.8764E3
TPSH	4.5649E3	1.2169E4	1.5723E4	3.9895E3	5.5286E3	5.6631E3
TPSH +2	3.1310E3	7.1593E3	8.2507E3	2.32166E 3	6.5880E3	8.6818E3
TPSH +4	5.6454E3	1.4287E4	1.7651E4	2.1202E3	2.4431E3	2.0911E3
TPSH +6	1.1245E3	3.0872E3	3.5190E3	1.0838E3	1.5152E3	1.5505E3

TPSH – Tooth Passing Spatial Harmonics

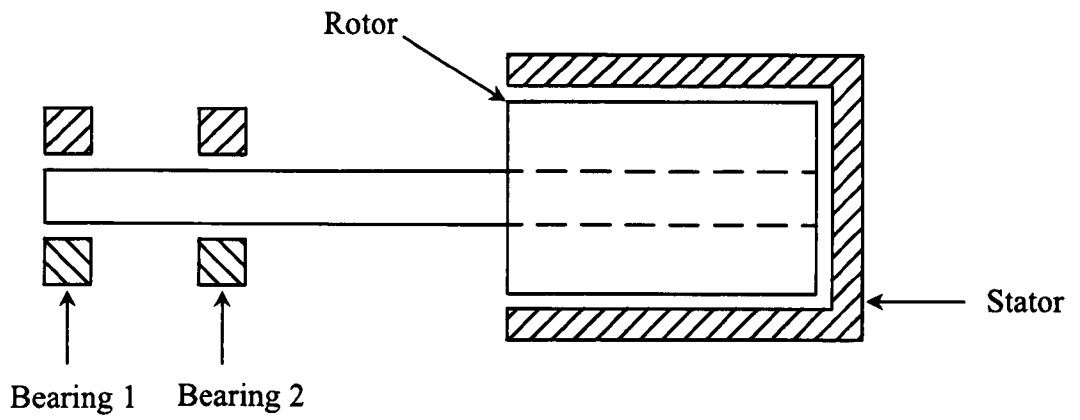


Figure (3.38): Schematic view of an electrical machine with an overhung rotor

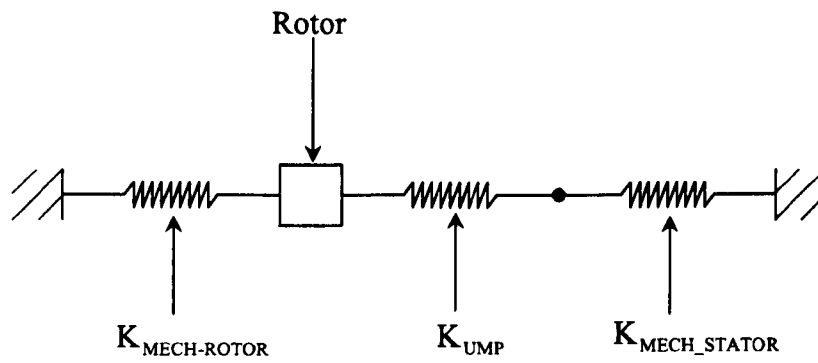


Figure (3.39): Equivalent system

Chapter Four

Co-ordinate Transformations Used in the Magnetic FEA

4.1 Introduction

The 2D finite element analysis of electromagnetics explained in the previous chapter is very general in nature. There, the view was taken that FEA would be used to create an instantaneous relationship between nodal currents and nodal potentials. This relationship takes the general form

$$\{A\} = f(\{I\}) \quad (4.1)$$

where $\{A\}$ = vector of magnetic potentials at nodes

$\{I\}$ = vector of nodal currents

In other words the magnetic FEA that is used here is magneto-static. In the case of a linear magnetic system

$$[K]\{A\} = \{I\} \quad (4.2)$$

where $[K]$ is the stiffness matrix

Electrical machines are electromagnetic devices with very complex geometries and phenomena, having moving parts, magnetic saturation and induced currents. Their simulations by finite element methods require special consideration. In the previous chapter it was assumed that the currents were known and these were specified by setting current densities in the domain of the analysis.

The FE models used throughout this work have been 2D. Each model comprises a large number of nodes (typically 10,000) and these nodes are connected by finite elements (often numbering around 3,000). In a fully general view of 2D magnetic FEA, a single nodal current can be associated with every single node and also a single magnetic potential can be associated with each. If the FEA formulation was intended to capture eddy-currents intrinsically, each node would have had to be allowed three components of the magnetic vector potential. Chapter 3 explained why all induced currents were going to be modelled explicitly and why this (eddy currents) formulation was not chosen.

This chapter addresses coordinate transformations of two basic types.

- Transformations that express the full length vector of nodal currents in terms of a reduced length vector.
- Transformations that express the full length vector of nodal potentials in terms of a reduced length vector.

It will be seen that the transformations are applied in stages with each stage reducing the number independent variables (entries) in the vector of currents (potentials). Each time that there is a reduction in the number of currents (potentials) a constraint of some description is, in effect, applied. In some cases the constraint is known first and the stage of the transformation is designed so as to satisfy that constraint. In other cases, the main purpose of the stage of transformation is to reduce the computational burden of working with the model. Then the transformation stage is designed such that the constraints which are applied have the least impact on the fidelity of the model.

In this chapter different transformations are used which transform the independent terminal currents of the stator to nodal currents in the stator and also transform the very large number of rotor nodal currents to the rotor bar currents. These transformations are used in the subsequent chapters to calculate the steady state currents from the electrical dynamics and also during the coupling of the electromagnetic dynamics with the mechanical dynamics.

4.2 General principles of the coordinate transformations

Sometimes we use a formal method to obtain the transformation matrix and sometimes by inspection. For both nodal currents and nodal magnetic potentials, we will come across sets of constraints which must be applied. These are discussed specifically in later sections but a single treatment can be outlined here. Because we encounter the situation most commonly in connection with currents, we use that situation here.

Let $\{I_0\}$ represent a “full length” vector of currents. If there are nodal currents, then there is a corresponding vector $\{A_0\}$ of magnetic potentials having the same length. In a fully nonlinear model we have (at any instant)

$$\{A_0\} = f(\{I_0\}) \quad (4.3)$$

But it is always possible to find a linearised form to this as

$$[K]\{A_0\} = \{I_0\} + \{b_0\} \quad (4.4)$$

where $[K]$ is the “tangential” or “marginal” stiffness and $\{b_0\}$ is the vector of free MMF. Some constraints are known to apply to $\{I_0\}$ in the form

$$[E]^T \{I_0\} = 0 \quad (4.5)$$

It is always possible to enforce these constraints by introducing the coordinate transformation

$$\{I_0\} = [T]\{I_1\} \quad (4.6)$$

where the matrix $[T]$ must satisfy two requirements. where $[T]$ is any matrix selected in order that

- $[E]^T [T] = 0$
- $[Y][Y]^T$ non-singular where $[Y] := [E \ T]$

There are several methods by which such transformation matrices may be found and each of these will result in a different matrix, $[T]$. If any matrix $[T]$ has been found satisfying the above criteria, a number of alternatives $[T']$ may be found through $[T'] = [T][X]$ where $[X]$ is any square invertible matrix of the appropriate dimension. We now describe one method commonly used in Finite Element analysis for developing the transformation. This method is highly efficient and it has good properties of numerical stability. It deals with one constraint at a time and the final transformation, $[T]$, is developed as the product of p intermediate transformations, $[T_p]$ where p is less than or equal to the number of constraints (columns in $[E]$). Each $[T_i]$ is effectively an identity matrix with an additional row inserted.

$$[T] = [T_1] \times [T_2] \times \dots [T_p] \quad (4.7)$$

For reasons which become clear shortly, we employ a duplicate notation for $[E]$ here and we refer to that also as $[E_0]$. The number of rows in $[E_0]$ equals the number of degrees of freedom in the original system and is denoted n_0 . Matrix $[T_1]$ has dimensions $(n_0 \times (n_0 - 1))$ and it is found by considering only the first column of $[E_0]$. Let k be the position of the entry having the largest absolute value in this column. $[T_1]$ can then be described entry-by entry as follows:

- $[T_1](i, i) = 1 \quad \forall \quad 0 < i < k$
- $[T_1](i, i) = 1 \quad \forall \quad 0 < i < k, i \neq j < n_0$
- $[T_1](k, j) = \left(-\frac{[E_0](j, 1)}{[E_0](k, 1)} \right) \quad \text{if } 0 < j < k$
- $[T_1](k, j) = \left(-\frac{[E_0](j+1, 1)}{[E_0](k, 1)} \right) \quad \text{if } k \leq j < n_0$
- $[T_1](i, i-1) = 1 \quad \forall \quad i > k$
- $[T_1](i, j) = 0 \quad \forall \quad i > k, (i-1) \neq j < n_0$

Example (4.1): A simple example illustrates this nicely. Consider the case of a 6 degree of freedom system to which a single constraint is applied with $[E_0]$ given by

$$[E_0]^T = [2 \quad -10 \quad 6 \quad -4 \quad 5 \quad 20]$$

The sixth entry here has the largest absolute value and hence $k = 6$. Then

$$[T_1] = \begin{bmatrix} 1 & 0 & 0 & 0 & 0 \\ 0 & 1 & 0 & 0 & 0 \\ 0 & 0 & 1 & 0 & 0 \\ 0 & 0 & 0 & 1 & 0 \\ 0 & 0 & 0 & 0 & 1 \\ -0.1 & 0.5 & -0.3 & 0.2 & -0.25 \end{bmatrix}$$

The procedure for multiple constraints is a very small extension. Having found $[T_1]$, calculate $[E_1]^T = [E_0]^T [T_1]$. The first column of $[E_1]$ contains only zeros and requires no further work. The next step, finding $[T_2]$, proceeds precisely as the first step except that $[E_1]$ is used in place of $[E_0]$ and its second column is considered.

Example (4.2): Consider the case of a 6 degree of freedom system to which two constraints are applied with $[E_0]$ given by

$$[E_0]^T = \begin{bmatrix} 2 & -10 & 6 & -4 & 5 & 20 \\ 4 & 5 & -2 & 8 & 1 & 0 \end{bmatrix}$$

Proceed as in the previous example to find $[T_1]$. Then evaluating $[E_1]^T = [E_0]^T [T_1]$ yields

$$[E_1]^T = \begin{bmatrix} 0 & 0 & 0 & 0 & 0 \\ 4 & 5 & -2 & 8 & 1 \end{bmatrix}$$

Evidently, the first constraint requires no further attention. The second column of $[E_1]$ informs the determination of $[T_2]$ which emerges as

$$[T_2]^T = \begin{bmatrix} 1 & 0 & 0 & 0 \\ 0 & 1 & 0 & 0 \\ 0 & 0 & 1 & 0 \\ -0.5 & -0.625 & 0.25 & -0.125 \\ 0 & 0 & 0 & 1 \end{bmatrix}$$

The product $[T] = [T_1][T_2]$ is then determined easily. The procedure here can be applied for any number of constraints. In some cases, the constraints are not all independent. A particular case of this may be encountered in an electric circuit shown in Figure (4.1) where each one of 5 different nodes produced a different constraint but there are only 4 degrees of freedom in the original system and it transpires that only 4 of the constraint equations are independent. When the procedure described here is applied to such cases, after $[T_4]$ and $[E_4]$ have been obtained, it is found that all columns of $[E_4]$ are zero. The fact that its first four columns comprise zeros is not surprising. The fact that all other columns comprise zeros points to the lack of independence in the original constraints. In order to prevent round-off errors from introducing spurious constraints, an account should be kept of the original magnitudes of the columns of $[E_0]$ and compared against the magnitudes of $[E_i]$ after the general step i . The process is complete when all of these magnitudes are very low compared with their original values.

4.3 Transformations of the stator currents

Most of the stators in electrical machines are powered by a three phase supply and it is usual that only three independent currents are required to describe fully the currents flowing in the stator. In Δ -connected machines or Y-connected machines with a floating star point only two currents are needed. Similar constraints also exist in the case of wound rotors. Arrangements must be put in place in our stator model to accommodate a transformation of three phase currents to the nodal currents.

Also, in the later part of this thesis while validating out numerical model we have used a special kind of winding scheme, which can be used as a passive reduction of unbalanced magnetic pull along with its torque producing capability. Unlike the usual winding scheme this particular winding scheme has six stator currents. Amongst these three are the phase currents and other three are so-called *levitation* currents. For a concentric rotor where magnetic fields are symmetric the levitation currents are zero. This is explained in detail in later chapters.

The full set of nodal currents in the stator is transformed to the terminal currents in five different stages. Figure (4.2) shows a schematic of the different transformations. The following subsections discuss each transformation separately. To illustrate the transformations of the stator currents a 4-pole induction machine is considered. The stator of the machine and its winding connections are shown in Figures (4.3) and (4.4). The machine has 36 stator slots. The winding is a dual layer distributed winding with fractional pitch coils. The pitch of each coil is (6/9) or 120 electrical degrees.

4.3.1 Transformation of the full set of nodal currents in the stator to the nodal currents correspond to the conducting regions in the stator (Stage I)

In the FE models every single node has an associated nodal current but many of these are always zero. Non-zero currents are associated only with those nodes which are either boundary or within the conducting regions of the FE model. The full set of nodal currents in the stator is transformed to a smaller set of nodal currents corresponding to the nodes of the conducting regions. This is accomplished by the following transformation:

$$\{I_{Snc}\} = [T_{S1}] \{I_{Scnc}\} \quad (4.8)$$

where $\{I_{Snc}\}$ is the full set of nodal currents and $\{I_{Scnc}\}$ is the smaller set of nodal currents corresponding to the nodes of the conducting regions. The number of columns of the transformation matrix, $[T_{S1}]$ will be the same as the number of entries

of $\{I_{\text{Senc}}\}$. Most of the entries of $[T_{\text{Sl}}]$ will be zeros as majority of the nodes will not carry currents.

Consider any part of the domain of a stator as shown in Figure (4.5), which has conducting as well as non-conducting regions. This part is discretised with three 4-noded finite elements and element 2 is the only conducting region. Suppose $i_1, i_2, i_3 \dots i_8$ are the nodal currents corresponding to nodes 1, 2, 3,... 8 respectively, the transformation in this case will be

$$\begin{Bmatrix} i_1 \\ i_2 \\ i_3 \\ i_4 \\ i_5 \\ i_6 \\ i_7 \\ i_8 \end{Bmatrix} = \begin{bmatrix} 0 & 0 & 0 & 0 \\ 0 & 0 & 0 & 0 \\ 1 & 0 & 0 & 0 \\ 0 & 1 & 0 & 0 \\ 0 & 0 & 1 & 0 \\ 0 & 0 & 0 & 1 \\ 0 & 0 & 0 & 0 \\ 0 & 0 & 0 & 0 \end{bmatrix} \begin{Bmatrix} i_3 \\ i_4 \\ i_5 \\ i_6 \end{Bmatrix} \quad (4.9)$$

4.3.2 Transformation of the nodal currents corresponds to the conducting regions to the coil side currents in the stator (Stage II)

In this transformation the nodal currents corresponding to the nodes of the conducting regions, $\{I_{\text{Senc}}\}$ are transformed to “coil-side” currents. A coil-side represents a conducting region in a particular stator slot having, in effect, a constant current density. In Figures (4.3) and (4.4), $+a_1$ represents one coil side. Since the example machine has 36 slots with dual layered windings, it will have 72 entries in the coil side current vector. This transformation is explained with the following illustration.

Consider a stator slot with double layer windings as shown in Figure (4.6). Here the two layers are distinguished by two different colours. Each layer is discretised with finite elements. Figure (4.7) shows layer 1 having been discretised with two 8-noded finite elements. Currents corresponding to layer 1 have one entry in the “coil side”

current vector. Suppose $i_1, i_2, i_3 \dots i_{13}$ are the nodal currents corresponding to nodes 1, 2, 3,... 13 respectively as shown in Figure (4.7). $\{I'\}$ and $\{I''\}$ are the currents for elements 1' and 1'' respectively. Assuming constant current density in the region of one set of coil

$$\begin{Bmatrix} i_1 \\ i_2 \\ i_3 \\ i_4 \\ i_5 \\ i'_6 \\ i'_7 \\ i'_8 \end{Bmatrix} = \begin{Bmatrix} \frac{a'_1}{A'_1} \\ \frac{a'_2}{A'_1} \\ \frac{a'_3}{A'_1} \\ \frac{a'_4}{A'_1} \\ \frac{a'_5}{A'_1} \\ \frac{a'_6}{A'_1} \\ \frac{a'_7}{A'_1} \\ \frac{a'_8}{A'_1} \end{Bmatrix} \{I'\} \quad (4.10)$$

and similarly

$$\begin{Bmatrix} i''_6 \\ i''_7 \\ i''_8 \\ i_9 \\ i_{10} \\ i_{11} \\ i_{12} \\ i_{13} \end{Bmatrix} = \begin{Bmatrix} \frac{a''_6}{A''_1} \\ \frac{a''_7}{A''_1} \\ \frac{a''_8}{A''_1} \\ \frac{a''_9}{A''_1} \\ \frac{a''_{10}}{A''_1} \\ \frac{a''_{11}}{A''_1} \\ \frac{a''_{12}}{A''_1} \\ \frac{a''_{13}}{A''_1} \end{Bmatrix} \{I''\} \quad (4.11)$$

where $a'_1, a'_2, \dots a'_8$ are the areas associated with the nodes correspond to element 1' and $a''_6, a''_7, \dots a''_{13}$ are the areas shared by nodes correspond to element 1'' and also note that $a'_1 + a'_2 + \dots + a'_8 = A'_1$, $a''_6 + a''_7 + \dots + a''_{13} = A''_1$. Here A'_1 and A''_1 are the areas for elements 1' and 1'' respectively. These areas are determined by the corresponding shape functions. i'_6, i'_7 and i'_8 are the nodal currents of nodes 6, 7, and 8 respectively contributed by element 1' only. i''_6, i''_7 , and i''_8 are the nodal currents of nodes 6, 7, and 8 respectively contributed by element 1' only. Nodes sharing more than one element

such as nodes 6, 7, and 8 will have contributions from the two elements. Finally these thirteen nodal currents can be written in terms of only one slot current as

$$\begin{Bmatrix} i_1 \\ i_2 \\ \vdots \\ i_7 \\ \vdots \\ i_{13} \end{Bmatrix} = \begin{Bmatrix} a'_1/A \\ a'_2/A \\ \vdots \\ (a'_7 + a''_7)/A \\ \vdots \\ a''_{13}/A \end{Bmatrix} \{I'\} \quad (4.12)$$

Following this, the nodal current in a particular stator slot can be written in terms of its corresponding “coil side” currents by transformation matrix, $[T_{S2}]$.

$$\{I_{Scnc}\} = [T_{S2}] \{I_{Scsc}\} \quad (4.13)$$

Here $\{I_{Scsc}\}$ is the “coil-side” current vector. Since the stator has 36 slots with dual layer of winding, it has 72 coil sides and 72 current variables entries. The number of columns of $[T_{S2}]$ is the same as the number of coil side current variables.

4.3.3 Transformation of the coil side currents to the full coil currents in the stator (Stage III)

Every full coil current corresponds to two half-coil currents. In Figure (4.4) a_1 represents one full coil. This transformation imposes a constraint that current going down in slot $-a_1$ is equal in magnitude to the current coming up in slot $+a_1$ ($+a_1$ is not shown in the figure) but opposite in sign. This transformation can be written by inspection. The transformation can be written as:

$$\{I_{Scsc}\} = [T_{S3}] \{I_{Sfcc}\} \quad (4.14)$$

where $\{I_{Sfcc}\}$ is the vector of full coil currents. For the machine considered $\{I_{Sfcc}\}$ will have 36 entries. The size of the transformation matrix $[T_{S3}]$ is (72×36). We can write the transformation for this as

$$\begin{Bmatrix} i_{+a_1} \\ i_{-a_1} \\ i_{+a_2} \\ i_{-a_2} \\ \vdots \end{Bmatrix} = \begin{bmatrix} 1 & 0 & \dots \\ -1 & 0 & \dots \\ 0 & 1 & \dots \\ 0 & -1 & \dots \\ \vdots & \vdots & \dots \end{bmatrix} \begin{Bmatrix} i_{a_1} \\ i_{a_2} \\ \vdots \end{Bmatrix} \quad (4.15)$$

where i_{+a_1} , i_{-a_1} , i_{+a_2} , i_{-a_2} are the coils side currents of coil sides $+a_1$, $-a_1$, $+a_2$, and $-a_2$ respectively and i_{a_1} , i_{a_2} are the full coil currents of full coils a_1 , and a_2 respectively [refer Figures (4.3) and (4.4)].

4.3.4 Transformation of the full coil currents to the coil group currents in the stator (Stage IV)

The six full coils a_1 , a_2 , a_3 , a_4 , a_5 , and a_6 together form one “coil group” and since they are connected in series as per the winding scheme shown in Figure (4.4), they have the same currents. This transformation transforms the coil currents within $\{I_{Sfcc}\}$ to the coil group currents. The transformation is:

$$\{I_{Sfcc}\} = [T_{S4}] \{I_{Scgc}\} \quad (4.16)$$

where $\{I_{Scgc}\}$ is the vector of coil group currents. The vector $\{I_{Sfcc}\}$ has 6 entries. The size of the transformation matrix $[T_{S4}]$ is (36×6).

$$\left\{ \begin{matrix} i_{a_1} \\ \vdots \\ i_{a_6} \\ i_{aa_1} \\ \vdots \\ i_{aa_6} \\ i_{b_1} \\ \vdots \\ i_{b_6} \\ i_{bb_1} \\ \vdots \\ i_{bb_6} \\ i_{c_1} \\ \vdots \\ i_{c_6} \\ i_{cc_1} \\ \vdots \\ i_{cc_6} \end{matrix} \right\} = \begin{bmatrix} 1 & 0 & 0 & 0 & 0 & 0 \\ \vdots & 0 & 0 & 0 & 0 & 0 \\ 1 & 0 & 0 & 0 & 0 & 0 \\ 0 & 1 & 0 & 0 & 0 & 0 \\ \vdots & 0 & \vdots & 0 & 0 & 0 \\ 0 & 1 & 0 & 0 & 0 & 0 \\ 0 & 0 & 1 & 0 & 0 & 0 \\ 0 & 0 & \vdots & 0 & 0 & 0 \\ 0 & 0 & 1 & 0 & 0 & 0 \\ 0 & 0 & 0 & 1 & 0 & 0 \\ 0 & 0 & 0 & \vdots & 0 & 0 \\ 0 & 0 & 0 & 1 & 0 & 0 \\ 0 & 0 & 0 & 0 & 1 & 0 \\ 0 & 0 & 0 & 0 & 0 & 1 \\ 0 & 0 & 0 & 0 & 0 & \vdots \\ 0 & 0 & 0 & 0 & 0 & 1 \end{bmatrix} \left\{ \begin{matrix} i_a \\ i_{aa} \\ i_b \\ i_{bb} \\ i_c \\ i_{cc} \end{matrix} \right\} =: [T_{S4}] \{I_{Scgc}\} \quad (4.17)$$

In Equation (4.17) $i_{a_1}, \dots, i_{a_6}, i_{aa_1}, \dots, i_{aa_6}$ are the full coil currents of full coils $a_1, \dots, a_6, aa_1, \dots, aa_6$ respectively corresponding to phase A. Currents with subscripts b and c correspond to phases B and C respectively.

4.3.5 Transformation of the coil group currents to the terminal currents (Stage V)

This transformation converts the 6 coil group currents to 3 terminal currents. The transformation is

$$\{I_{Scgc}\} = [T_{S5}] \{I_S\} \quad (4.18)$$

where $\{I_S\}$ is the vector of terminal or phase currents. The vector $\{I_S\}$ has 3 entries of the three phase currents as:

$$\{I_s\} = \begin{Bmatrix} i_{Aph} \\ i_{Bph} \\ i_{Cph} \end{Bmatrix} \quad (4.19)$$

The size of the transformation matrix $[T_{ss}]$ is (6×3) . If the resistance of the six coil groups are same and also the EMFs due to changing magnetic field in the two coil group in a particular phase are same then we can write

$$\begin{Bmatrix} i_a \\ i_{aa} \\ i_b \\ i_{bb} \\ i_c \\ i_{cc} \end{Bmatrix} = \begin{bmatrix} \frac{1}{2} & 0 & 0 \\ \frac{1}{2} & 0 & 0 \\ 0 & \frac{1}{2} & 0 \\ 0 & \frac{1}{2} & 0 \\ 0 & 0 & \frac{1}{2} \\ 0 & 0 & \frac{1}{2} \end{bmatrix} \begin{Bmatrix} i_{Aph} \\ i_{Bph} \\ i_{Cph} \end{Bmatrix} =: [T_{ss}]\{I_s\} \quad (4.20)$$

where $i_a, i_{aa}, i_b, i_{bb}, i_c, i_{cc}$ are the coil group currents and $i_{Aph}, i_{Bph}, i_{Cph}$ are the three terminal currents. Finally the overall transformation can be written as

$$\{I_{Snc}\} = [T_s]\{I_s\} \quad (4.21)$$

The final transformation matrix can be written as

$$[T_s] = [T_{s1}] \times [T_{s2}] \times [T_{s3}] \times [T_{s4}] \times [T_{s5}] \quad (4.22)$$

where $[T_s]$ is the transformation matrix which determines the transformation of nodal currents to the terminal currents.

4.3.6 Transformation of the coil group currents according to the bridge windings

In a usual winding scheme (similar to Figure (4.4)) there will be three independent stator phase currents but in some special windings scheme such as (Khoo, 2005) there

can be more than three currents. Here without going about the detail of the bridge configured winding scheme introduced by Khoo (2005), an explanation is given for the transformation of stator slot currents to the independent stator phase currents. One reason for choosing this winding scheme for explanation is that it is used in the experimental rig developed to study electromechanical interaction of an induction machine. Another reason is that it contains more than three currents. Some features of this winding scheme are explained in Chapters 7 and 8. Figure (4.8) shows the equivalent bridge connection for the winding connection shown in Figure (4.3). The branch currents, phase currents and the levitation currents are shown for phase A in the figure. Unlike the conventional winding scheme, this particular winding scheme has one “levitation current” per phase. The usage of this levitation current will be explained in detail in Chapter 5. A transformation matrix which transforms all the slot currents (or branch currents as shown in Figure (4.8)) to the phase currents and levitation currents is required. Assuming the same resistance in each branch of the bridge the transformation matrix for the phase A is calculated as follows,

$$\begin{Bmatrix} i_A \\ i_B \\ i_C \\ i_D \end{Bmatrix} = \begin{bmatrix} \frac{1}{2} & \frac{1}{2} \\ \frac{1}{2} & -\frac{1}{2} \\ \frac{1}{2} & -\frac{1}{2} \\ \frac{1}{2} & \frac{1}{2} \end{bmatrix} \begin{Bmatrix} i_{Aph} \\ i_{Alev} \end{Bmatrix} \quad (4.23)$$

i_A , i_B , i_C , and i_D are the currents in four branches of the bridge for phase A. It is also assumed here that EMFs due to changing magnetic fields are identical for each branch of the bridge. Similar transformations shown in Equation (4.23) are also obtained for phases B and C. These comprise a different transformation matrix $[T_{ssn}]$, similar to $[T_{ss}]$ explained in Section (4.4.5), which transforms the stator coil group currents to the phase currents. i_A , i_B , i_C , and i_D are the four entries of the current vector $\{I_{scgc}\}$. Similar currents variables are obtained for phases B and C. Unlike the current vector, $\{I_s\}$ shown in Equation (4.21), the vector $\{I_s\}$ there will have six entries when we use the bridge configured windings, i.e.

$$\{I_s\} = \begin{Bmatrix} i_{Aph} \\ i_{Alev} \\ i_{Bph} \\ i_{Blev} \\ i_{Cph} \\ i_{Clev} \end{Bmatrix} \quad (4.24)$$

where i_{Alev} , i_{Blev} and i_{Clev} are the three levitation currents in the bridge.

4.4 Transformations of the rotor bar currents

In case of a rotor of squirrel cage induction machine currents flows axially along the cage. Similarly, current flows axially along one set of damper-bars in a synchronous machine. The transformation enforces the constraint zero total currents must flow axially along the cage or along one set of damper-bars. It is well known that the density of current in rotor bars of a cage induction machine varies with radial position of the rotor bar due to skin effects.

Figure (4.9) show a cross-section of a rotor of an induction machine with 32 rotor bars. At low slip, the rotor's frequency is very small and the reactances of all the parallel paths through the bar are small compared to their resistances (Chapman, 1998). The impedances of all parts of the bar are then approximately equal, so current flows through all parts of the bar equally. The resulting large cross-sectional area makes the rotor resistance quite small, resulting in good efficiency at low slips. At high slip (starting conditions), the reactances are large compared to the resistances in the rotor bars, so all the current is inclined to flow in the lower-reactance path of the bar near the stator. With a high rotor resistance at starting conditions, the starting torque is usually higher. There is a limit reached but this has no practical significance.

Another reason of transforming rotor bar currents is that there are very many different currents in the model. To solve the FE model with these currents as nodal currents may not be practical for more number of bars and also for more number of nodes in the rotor bar region. Like the transformation of stator currents, transformations are

needed for the rotor bar currents so that we can represent the full set of nodal currents of the rotor with fewer current variables. If current densities were constant, we would use only one current variable per bar. As mentioned above current density in a rotor bar is a function of radius and radial depth of the rotor. To take care of these effects provisions have to be made in the numerical model. The transformations from the full set of nodal currents in the rotor to the smaller number of current variables are achieved in four different stages. These stages are shown in Figure (4.10).

4.4.1 Transformation of the full set of nodal currents in the rotor to the nodal currents corresponding to the conducting regions (Stage I)

Similar to the stator (Section 4.3.1), in the FE models of rotor every single node has an associated nodal current but many of these are always zero. Non-zero currents are associated only with these nodes which are either boundary or within the conducting regions of the FE model. The full set of nodal currents in the rotor is transformed to a smaller set of nodal currents corresponding to the nodes of the conducting regions. This is accomplished by the following transformation:

$$\{I_{Rnc}\} = [T_{R1}]\{I_{Renc}\} \quad (4.25)$$

where $\{I_{Rnc}\}$ is the full set of nodal currents of the rotor and $\{I_{Renc}\}$ is the smaller set of nodal currents corresponding to the nodes of the conducting region in rotor bars. The number of columns of the transformation matrix, $[T_{R1}]$ is the same as the number of entries of $\{I_{Renc}\}$. Most of the entries of $[T_{R1}]$ are zeros since the majority of the nodes in the rotor do not carry currents. The structure of the transformation matrix $[T_{R1}]$ is similar to the transformation matrix $[T_{S1}]$ (refer Section 4.3.1).

4.4.2 Transformation of the nodal currents corresponding to the conducting regions in the rotor to the set of currents based on the “modes” of conduction (Stage II)

After applying the transformation described in Section (4.4.1) the set of nodal currents corresponding to the conducting regions still contains very many nodal currents and it is still not possible to keep them as independent current variables. Since the current density in a bar is not constant as explained, the nodal currents in a bar cannot be transformed into one current variable. This is performed by considering a few eigen modes of the conductance. The modes of conduction and hence the transformation matrix for this stage is evaluated as follows.

Firstly note that the modelling we are using is 2D and “prismatic” in the sense that we expect that the same 2D analysis applies at any cross section over the entire length of the 3D object which we are trying to model (electrical machine in the present case).

In general, we will not have uniform continuous electrical field strength $\mathbf{E}(x, y)$ and we will not have continuous uniform current density $\mathbf{J}(x, y)$ either. We often have uniform continuous resistivity $\rho(x, y)$ but we do not need to assume this. In-plane currents will occur.

Define $q(x, y, z)$ as electrical potential. In plane current densities J_x and J_y occur where

$$J_x = -\left(\frac{\partial q}{\partial x} / \rho\right) \quad (4.26)$$

$$J_y = -\left(\frac{\partial q}{\partial y} / \rho\right) \quad (4.27)$$

We define $z = 0$ to be the axial centre of a machine. In-plane currents are zero here (by symmetry). It is convenient to define as $q(x, y, z) = 0$. Away from $z = 0$

$$\frac{\partial \mathbf{q}}{\partial z} = \mathbf{E}(x, y) - \mathbf{J}_z(x, y) \mathbf{p}(x, y) \quad (4.28)$$

From Kirchoff (in effect)

$$\text{div}(\mathbf{J}) = 0 \quad (4.29)$$

In our analysis, we intend to use 2D and hence the effects of in-plane currents are ignored. We can write mean square current density and mean square current gradient as follows

$$\text{Mean square current density} := \frac{\int_{\Psi} \mathbf{J}^2 d\Psi}{\int_{\Psi} d\Psi} = \frac{\{\mathbf{j}\}^T [\mathbf{Z}] \{\mathbf{j}\}}{|\Psi|} \quad (4.30)$$

$$\text{Mean square current gradient} := \frac{\int_{\Psi} \left(\left(\frac{\partial \mathbf{J}}{\partial x} \right)^2 + \left(\frac{\partial \mathbf{J}}{\partial y} \right)^2 \right) d\Psi}{\int_{\Psi} d\Psi} = \frac{\{\mathbf{j}'\}^T [\mathbf{Y}] \{\mathbf{j}'\}}{|\Psi|} \quad (4.31)$$

We carry out model reduction using the logic that $\mathbf{J}_z(x, y)$ will have relatively low mean square current gradients compared with the mean square current values. Hence the conduction modes we will derive from the lowest modes of $\text{eig}([\mathbf{Y}], [\mathbf{Z}])$, where $[\mathbf{Z}]$ is built up from element matrices as

$$z(i, j) = \int_{\Psi} (\mathbf{N}(x, y))^T \mathbf{N}(x, y) d\Psi \quad (4.32)$$

And $[\mathbf{Y}]$ is built up from element matrices as

$$y(i, j) = \int_{\Psi} \left(\frac{\partial N_i}{\partial x} \cdot \frac{\partial N_j}{\partial x} + \frac{\partial N_i}{\partial y} \cdot \frac{\partial N_j}{\partial y} \right) d\Psi \quad (4.33)$$

where $N(x, y)$ are the shape functions. The eigenvectors corresponding to the respective conduction modes of $\text{eig}([Y], [Z])$ constitutes the column of the transformation matrix. The transformation can be written as

$$\{I_{Renc}\} = [T_{R2}]\{I_{Rmcc}\} \quad (4.34)$$

where $\{I_{Rmcc}\}$ is the set of nodal currents based on the “modes” of conduction of the rotor bars. The transformation of the rotor bars having the same physical dimension (as shown in Figure (4.9)) will have the same structure. In this case the transformation matrix has blocks equal to the number of rotor bars.

Suppose b is the number of nodes in each bar and three eigenmodes are considered for a rotor bar, then the nodal currents for a particular bar, $\{I_{Rmcc1}\}$ can be written as

$$\{I_{RBAR1}\} = [T_{R21}]\{I_{Rmcc1}\} \quad (4.35)$$

where $[T_{R21}]$ is the transformation matrix which transforms the nodal currents to a smaller number of currents and $\{I_{RBAR1}\}$ is the nodal currents for a particular bar and this is a subset of nodal currents corresponds to the conducting regions of the rotor, $\{I_{Renc}\}$. If the numbers of nodes in each bar is b then the $\{I_{RBAR1}\}$ is

$$\{I_{RBAR1}\} = \begin{Bmatrix} i_{r11} \\ i_{r12} \\ \vdots \\ i_{r1b} \end{Bmatrix} \quad (4.36)$$

and

$$[T_{R21}] = \begin{bmatrix} v_{11} & v_{21} & v_{31} \\ v_{12} & v_{22} & v_{32} \\ \vdots & \vdots & \vdots \\ v_{1b} & v_{2b} & v_{3b} \end{bmatrix} \quad (4.37)$$

Here $[v_{11} \ v_{12} \ \dots \ v_{1b}]^T$ is the eigenvectors correspond to the three eigenmodes considered. Figures (4.11a), (4.11b) and (4.11c) show three modes of conduction of a typical rotor bar. Appendix A shows the effect of different number of modes in a typical electrical machine.

$$\{I_{Rmcc1}\} = \begin{Bmatrix} i_{r11} \\ i_{r21} \\ i_{r31} \end{Bmatrix} \quad (4.38)$$

If the numbers of bars in the rotor is k , then the transformation matrix for the whole rotor can be written as Equation (4.39).

$$\begin{Bmatrix} I_{RBAR1} \\ I_{RBAR2} \\ \vdots \\ I_{RBARk} \end{Bmatrix} = \begin{bmatrix} T_{R21} & & & \\ & T_{R21} & & \\ & & \ddots & \\ & & & T_{R21} \end{bmatrix} \begin{Bmatrix} I_{Rmcc1} \\ I_{Rmcc2} \\ \vdots \\ I_{Rmcck} \end{Bmatrix} =: [T_{R2}] \{I_{Rmcc}\} \quad (4.39)$$

4.4.3 Transformation of the set of currents based on the “modes” of conduction to the set of nodal currents from the Fourier transform (stage III)

In this stage the reduced vector of currents calculated based on “modes of conduction” is further reduced by considering the Fourier coefficients. The transformation can be written as

$$\{I_{Rmcc}\} = [T_{R3}] \{I_{Rfcc}\} \quad (4.40)$$

where $\{I_{Rfcc}\}$ is the set of currents based on the Fourier coefficients. The number of rotor bars is k . We will typically use fewer harmonics than $\frac{k}{2}$ (which is the maximum). If the number of harmonics considered is q , then the transformation matrix, $[T_{R3}]$ for a 4-pole induction machine will be

$$[T_{R3}] = \begin{bmatrix} 1 & I \cos\left(\frac{2\pi \cdot 0}{k}\right) & I \sin\left(\frac{2\pi \cdot 0}{k}\right) & \dots & I \cos q\left(\frac{2\pi \cdot 0}{k}\right) & I \sin q\left(\frac{2\pi \cdot 0}{k}\right) \\ 1 & I \cos\left(\frac{2\pi(i-1)}{k}\right) & I \sin\left(\frac{2\pi(i-1)}{k}\right) & \dots & I \cos q\left(\frac{2\pi(i-1)}{k}\right) & I \sin q\left(\frac{2\pi(i-1)}{k}\right) \\ \vdots & \vdots & \vdots & \ddots & \vdots & \vdots \\ 1 & I \cos\left(\frac{2\pi(k-1)}{k}\right) & I \sin\left(\frac{2\pi(k-1)}{k}\right) & \dots & I \cos q\left(\frac{2\pi(k-1)}{k}\right) & I \sin q\left(\frac{2\pi(k-1)}{k}\right) \end{bmatrix} \quad (4.41)$$

4.4.4 Transformation of the set of nodal currents from the Fourier transform (stage IV)

This transformation relates to the “0” harmonics of the transformation matrix $[T_{R3}]$. The sum of total currents coming out of the rotor bars should be zero. A constraint must be applied to make sure that this condition is satisfied and this reduces the number of current variable by one. This is the fourth transformation matrix, $[T_{R4}]$. Finally the overall transformation can be written as

$$\{I_{Rnc}\} = [T_R] \{I_R\} \quad (4.42)$$

where $[T_R]$ is the transformation matrix which determines the transformation of nodal currents in the rotor to a reduced number of current variables and

$$[T_R] = [T_{R1}] \times [T_{R2}] \times [T_{R3}] \times [T_{R4}] \quad (4.43)$$

$\{I_R\}$ is the reduced current vector of the rotor only.

4.5 Transformations of the magnetic potentials

In this chapter most of the magnetic potentials in the 2D model are considered to be independent. In a later chapter on model reduction for magnetic FEA of machines, this situation will be changed. To enforce a *tangential-flux* condition at the outside border of a magnetic analysis, it is common to impose constraints forcing all of the nodal potentials at this outside border to be zero. Sometimes in the case of hollow-

rotor machines, it is appropriate also to restrict the modelled domain using an internal border also and in these cases, further constraints are used to ensure that all nodal potentials at the inner border are equal. The imposition of constraints is one reason for employing coordinate transformations and this is discussed later. In this section some transformations applied to the magnetic potentials are discussed. These two transformations are discussed in the following sub-sections. Further transformations on magnetic potentials are considered in later chapters.

4.5.1 Transformation on the set of nodal potentials in the stator to apply the tangential-flux conditions

Consider a simple cylinder shown in Figure (4.12), which represents a notional stator of electrical machines. The stator is discretised with eight 4-noded elements. Tangential-flux condition is applied at the outer diameter of the stator by imposing the constraint and forcing the nodal potentials of nodes 1, 2, 3, 4 to be zero. Suppose p_1, p_2, \dots, p_{12} are the nodal potentials corresponding to the nodes 1, 2, 3, ..., 12 respectively. After applying the constraint we can write

$$\begin{Bmatrix} p_1 \\ p_2 \\ p_3 \\ p_4 \\ p_5 \\ p_6 \\ p_7 \\ p_8 \\ p_9 \\ p_{10} \\ p_{11} \\ p_{12} \end{Bmatrix} = \begin{bmatrix} 0 & 0 & 0 & 0 & 0 & 0 & 0 & 0 \\ 0 & 0 & 0 & 0 & 0 & 0 & 0 & 0 \\ 0 & 0 & 0 & 0 & 0 & 0 & 0 & 0 \\ 0 & 0 & 0 & 0 & 0 & 0 & 0 & 0 \\ 1 & 0 & 0 & 0 & 0 & 0 & 0 & 0 \\ 0 & 1 & 0 & 0 & 0 & 0 & 0 & 0 \\ 0 & 0 & 1 & 0 & 0 & 0 & 0 & 0 \\ 0 & 0 & 0 & 1 & 0 & 0 & 0 & 0 \\ 0 & 0 & 0 & 0 & 1 & 0 & 0 & 0 \\ 0 & 0 & 0 & 0 & 0 & 1 & 0 & 0 \\ 0 & 0 & 0 & 0 & 0 & 0 & 1 & 0 \\ 0 & 0 & 0 & 0 & 0 & 0 & 0 & 1 \end{bmatrix} \begin{Bmatrix} p_5 \\ p_6 \\ p_7 \\ p_8 \\ p_9 \\ p_{10} \\ p_{11} \\ p_{12} \end{Bmatrix} \quad (4.44)$$

This transformation is analogous to state I transformation of stator and rotor currents.

4.5.2 Transformation on the set of nodal potentials of a hollow rotor to apply the equal-flux conditions

Consider a simple cylinder shown in Figure (4.13), which represents a notional rotor of an electrical machine. The rotor is discretised with four 4-noded elements. A tangential flux condition is applied at the inner diameter of the cylinder by imposing constraints that force the nodal potentials of nodes 5, 6, 7, 8 to be equal. Suppose p_1, p_2, \dots, p_8 are the nodal potentials corresponding to the nodes 1, 2, 3, ..., 8 respectively. After applying the constraint we can write

$$\begin{Bmatrix} p_1 \\ p_2 \\ p_3 \\ p_4 \\ p_5 \\ p_6 \\ p_7 \\ p_8 \end{Bmatrix} = \begin{bmatrix} 1 & 0 & 0 & 0 & 0 \\ 0 & 1 & 0 & 0 & 0 \\ 0 & 0 & 1 & 0 & 0 \\ 0 & 0 & 0 & 1 & 0 \\ 0 & 0 & 0 & 0 & 1 \\ 0 & 0 & 0 & 0 & 1 \\ 0 & 0 & 0 & 0 & 1 \\ 0 & 0 & 0 & 0 & 1 \end{bmatrix} \begin{Bmatrix} p_1 \\ p_2 \\ p_3 \\ p_4 \\ p_5 \end{Bmatrix} \quad (4.45)$$

We can write the nodal potentials corresponding to the nodes 5, 6, 7, 8 in terms of one nodal potential variable only. It is often but not always acceptable to constrain these potentials to zero. A zero constraint here would mean that there could be zero net circulation of flux about the machine axis.

4.6 Conclusions

Separate coordinate transformations for stator and rotor are explained for analysing the coupled electro-mechanical model of an induction machine without compromising the accuracy. Recall Equation (3.50),

$$[K]\{A_z\} = \{I_z\} \quad (4.46)$$

where $[K]$, $\{A_z\}$ and $\{I_z\}$ represent the magnetic stiffness matrix, magnetic vector potentials and nodal currents for stator as well rotor respectively. Most of the entries in $\{I_z\}$ are 'zero' because not all the nodes carry currents. We can write nodal current vector as

$$\begin{aligned} \begin{Bmatrix} I_{Snc} \\ I_{Rnc} \end{Bmatrix} &= \begin{bmatrix} T_S & - \\ - & T_R \end{bmatrix} \begin{Bmatrix} I_S \\ I_R \end{Bmatrix} \\ \Rightarrow \{I_z\} &= [U]\{I_{RS}\} \end{aligned} \quad (4.47)$$

where $[U]$ is a transformation matrix which transforms the rotor and stator terminal currents to the nodal currents. Combining $[T_R]$ and $[T_S]$, the transformation matrix for stator and rotor, $[U]$ is created and $\{I_{RS}\} = \begin{Bmatrix} I_S \\ I_R \end{Bmatrix}$. The main coordinate transformations are explained in this chapter. Some further transformations on magnetic potentials are explained in later chapters.

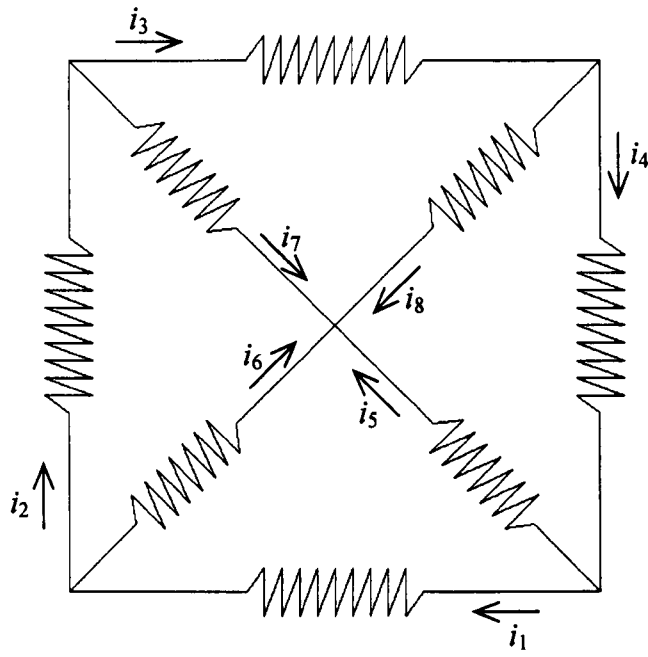


Figure (4.1): An electric circuit (For illustration purpose only)

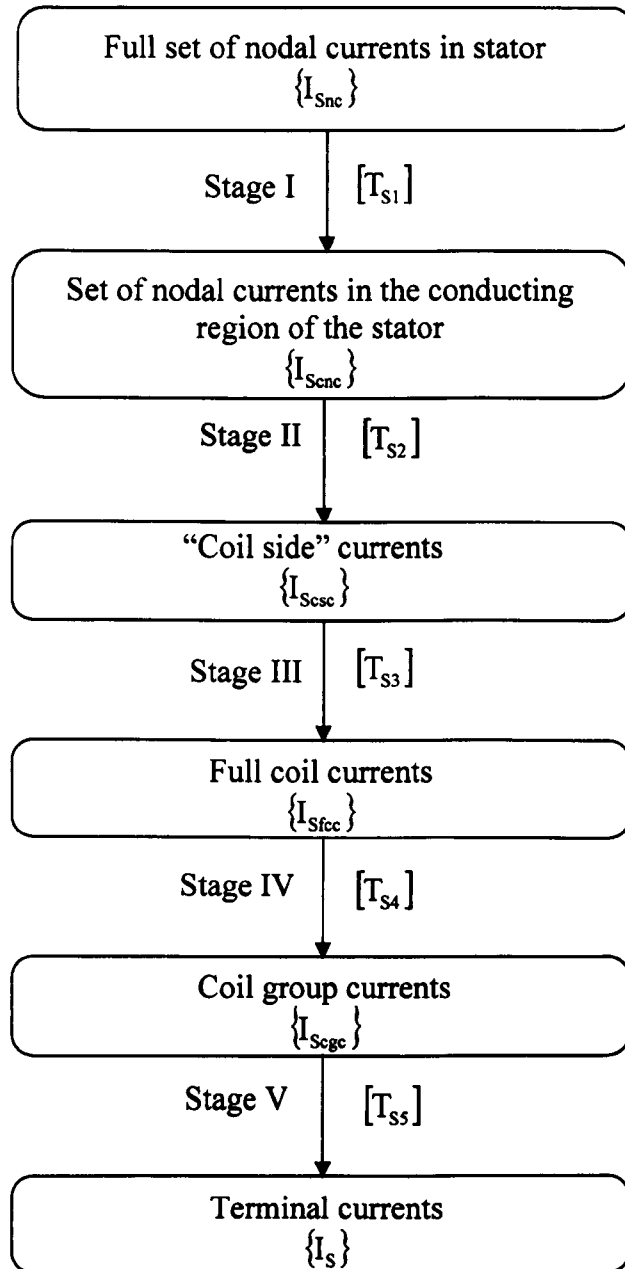


Figure (4.2): Flow diagram showing the different transformations of stator currents

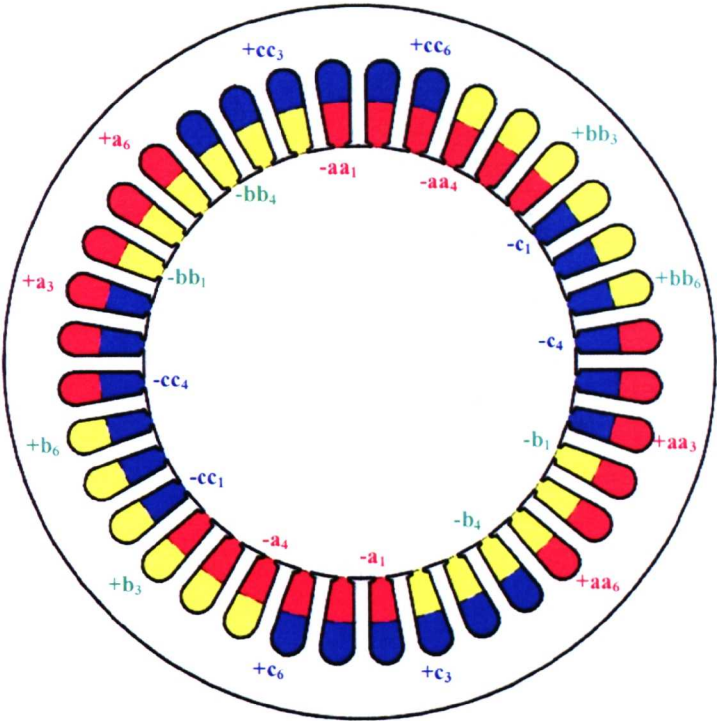


Figure (4.3): Stator of an induction machine showing the winding connection. Red, blue and yellow colours show the three different phases.

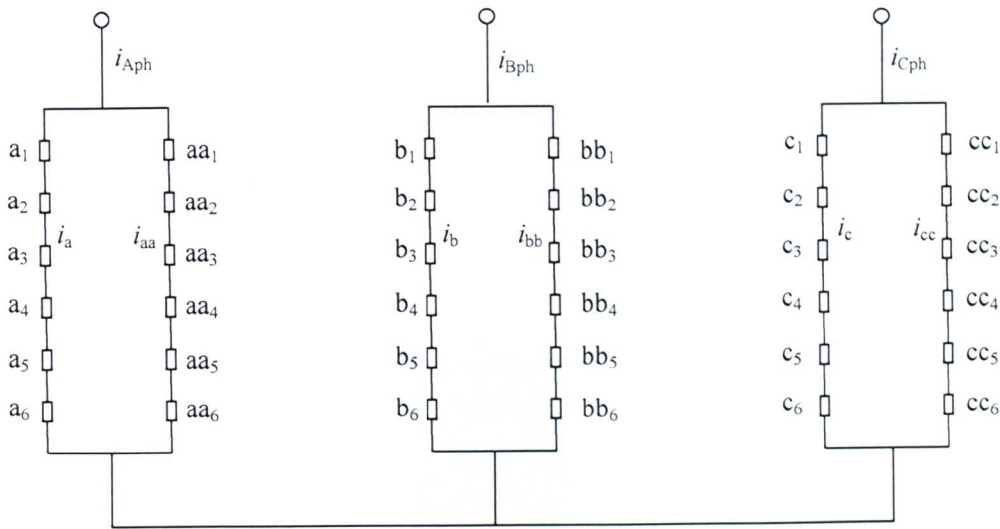


Figure (4.4): Winding connection of a 4-pole, 3-phase Induction Motor

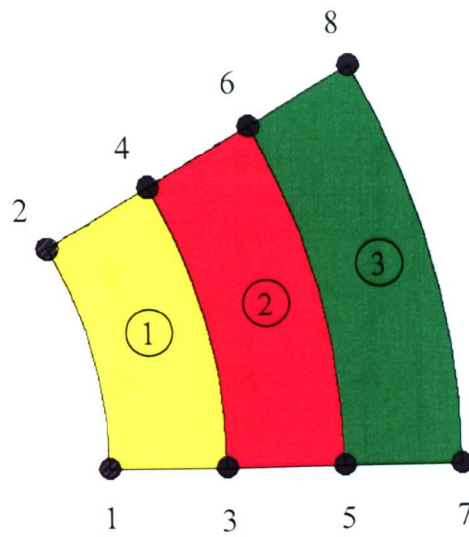


Figure (4.5): Part of the stator core discretised with three 4-noded elements
(For illustration purpose only)

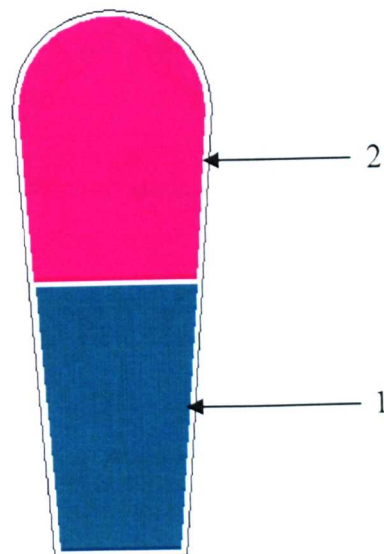


Figure 4.6: Stator slot with two sets of coil 1 and 2

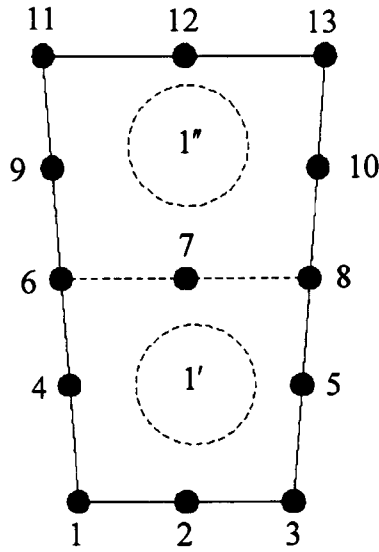


Figure 4.7: One stator slot shown in Figure (4.6) showing the finite element nodes when discretized with two elements

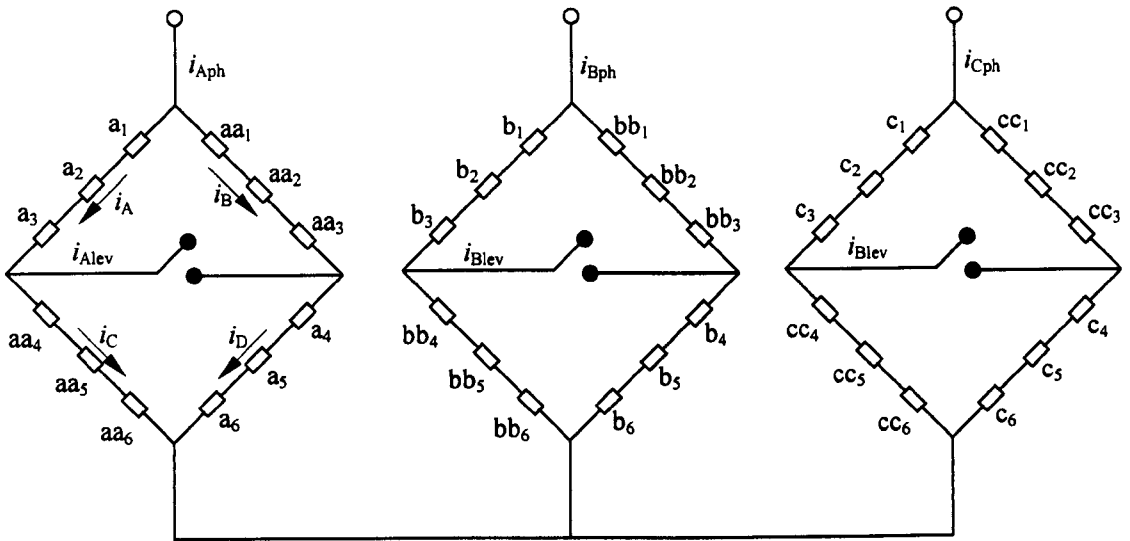


Figure (4.8): 4-pole, 3-phase Induction Motor with a Bridge Configured Windings

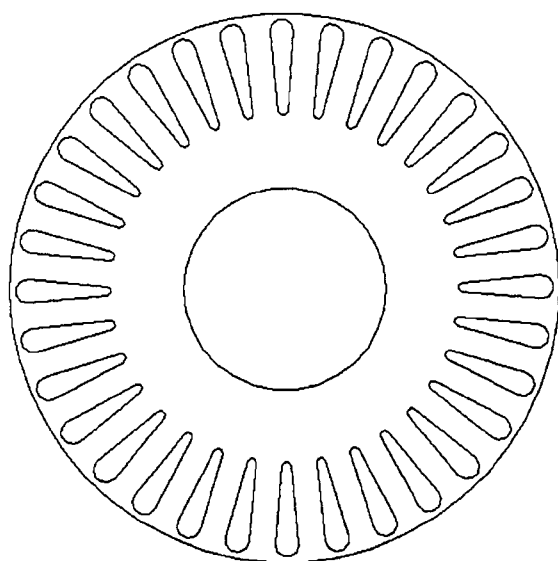


Figure (4.9): Rotor of an induction machine with 32 bars

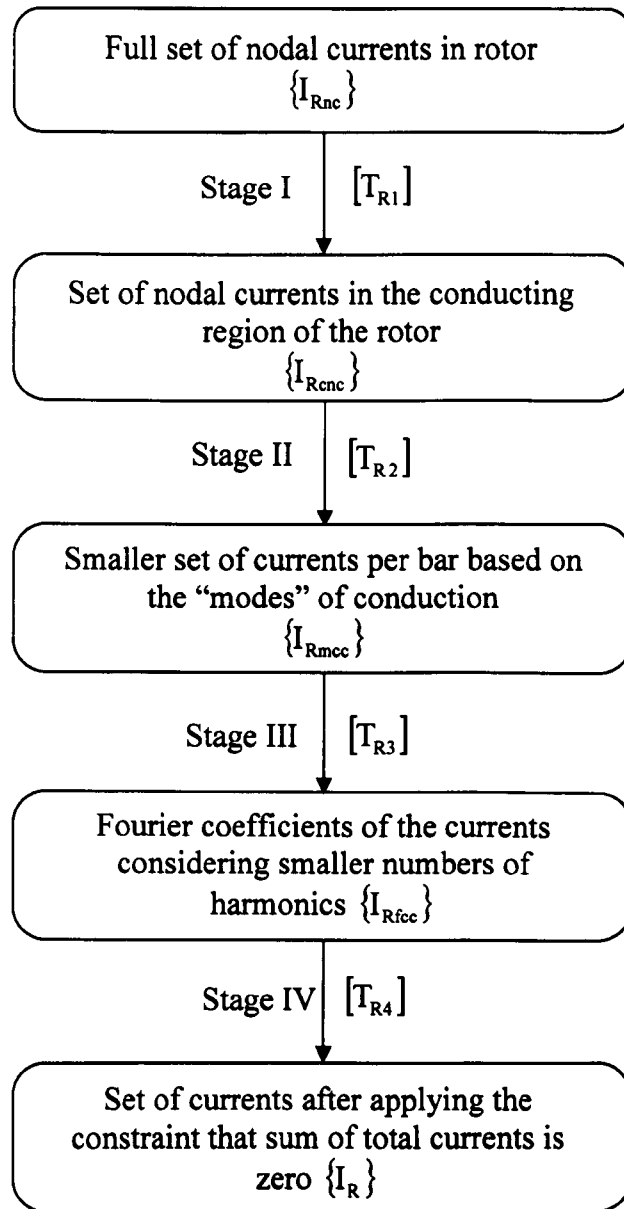
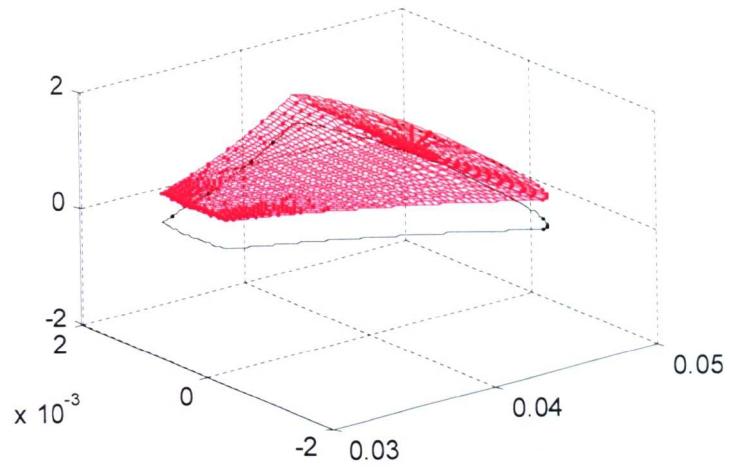
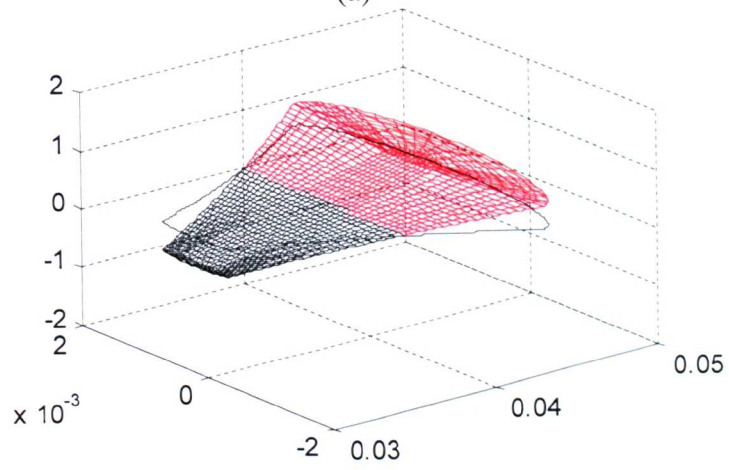


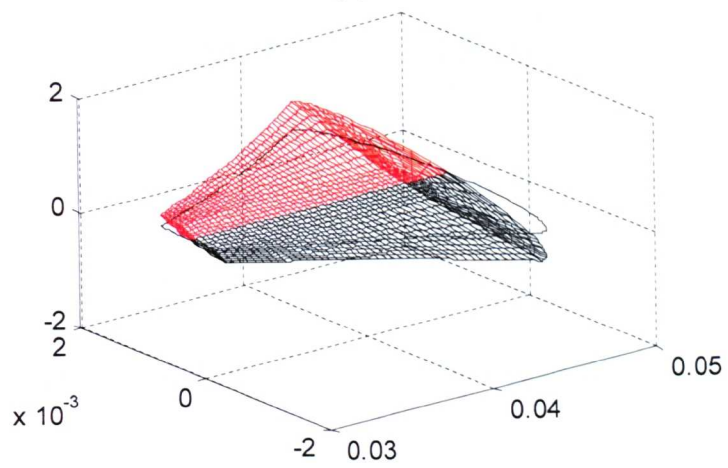
Figure (4.10): Flow diagram showing the different transformation of rotor currents



Mode I
(a)



Mode II
(b)



Mode III
(c)

Figure (4.11): First three modes of conduction of a typical rotor bar

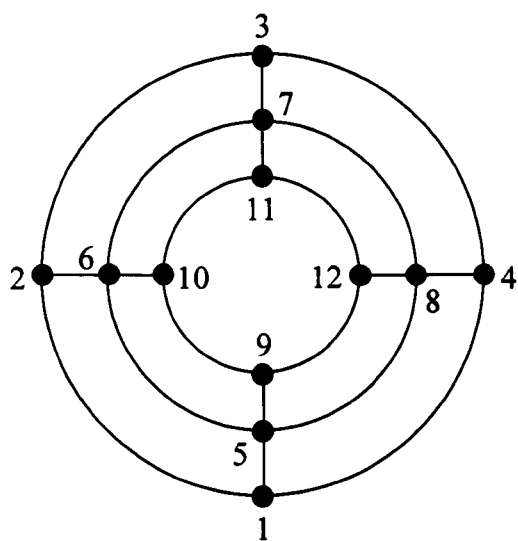


Figure (4.12): A notional stator of an electrical machine

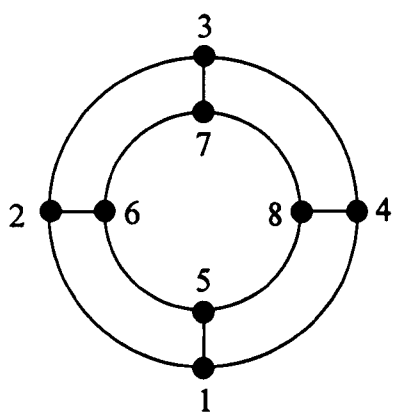


Figure (4.13): A notional rotor of an electrical machine

Chapter Five

Modelling of Electro-Magneto-Mechanical (EMM) Devices

When solving the magneto-static field equation, the excitation takes the form of electrical currents. This has been discussed in Chapter 3. The circuit equation provides the linkage between these currents and voltages applied to the machine. Methods for coupling field and circuit equations are well known. Numerous procedures for combining transient field and circuit equations are already published in the literature such as [Williamson and Smith, (1980), Strangas, (1985), Salon *et al.*, (1990), Ho *et al.*, (2000)].

One parameter in the circuit equation yet to be discussed is the resistance matrix of an electro-magneto-mechanical (EMM) device. In Chapter 3 an explanation is given for how the nodal resistance matrix is calculated from 2D FEA of an EMM device. Most 2D FE models comprise a large number of nodes and one nodal current can be associated with every single node. The model has few independent currents. As explained in Chapter 4 the higher dimensional vector of nodal currents can be reduced to a vector of independent currents with smaller dimensions with proper transformations. The resistance matrix associated with these independent currents can be calculated by post- and pre-multiplying the full-dimensional resistance matrix by a transformation matrix and its transpose respectively. The resistance matrix associated with the independent currents is diagonal and positive-definite.

5.1 Introduction

In the finite element modeling of EMM prismatic devices, the most profound approximation is that the device can be modelled using a two-dimensional section

orthogonal to the axis of the device. We expect that the same 2D analysis applies at any cross section over the entire length of the 3D object which we are trying to model. The model should be capable of incorporating additional terms due to three-dimensional effect such as stator end-winding, and rotor end-rings.

From 2D FEA we get an instantaneous relationship between nodal currents and nodal magnetic potentials and this is already stated in the previous chapter. For a linear system

$$[K]\{A\} = \{I_z\} \quad (5.1)$$

where $[K]$ is the stiffness matrix

$\{A\}$ is the vector of magnetic potentials at nodes

$\{I_z\}$ is the vector of nodal currents (out of plane)

If we incorporate nonlinearity in Equation (5.1) can be written as

$$[K_{\text{mar}}]\{\Delta A\} = \{\Delta I\} \quad (5.2)$$

where $[K_{\text{mar}}]$ is the *tangential* or *marginal* stiffness matrix which is determined by the $B(H)$ curves of the magnetic materials. $[K_{\text{mar}}]$ is a nonlinear function of current and geometry. With constant geometry, $[K_{\text{mar}}]$ depends on current only.

This chapter describes the general procedures for modeling an EMM device and how they can be extended to model an induction machine.

5.2 Calculation of the resistance matrix from finite element method

This section explains how the resistance matrices for the stator and rotor are obtained. Chapter 3 outlines how the resistance matrices can be obtained for the current-

carrying regions from 2D FEA. Nodes which lie on the elements corresponding to conductors are current-carrying nodes. Nodes at the boundaries of a region of permanent magnet material are also current-carrying nodes and the sum of these nodal currents must be zero. Chapter 4 outlines how coordinate transformations are used for both stator and rotor of an induction machine such that the number of independent current degrees of freedom is much reduced. As explained in Chapter 3, using proper transformations, the full vector of nodal currents can be transformed into a vector of independent currents with smaller number of current variables and we can write this transformation as

$$\{I_{nc}\} = [T]\{I\} \quad (5.3)$$

where $\{I_{nc}\}$ is the full set of nodal currents, $\{I\}$ is the set of independent currents and $[T]$ is the corresponding transformation matrix. If $[R_{nc}]$ is the resistance matrix associated with the nodal currents, then the resistance matrix $[R_1]$ associated with the set of independent currents is calculated as

$$[R_1] = [T]^T [R_{nc}] [T] \quad (5.4)$$

5.3 Resistance of the end windings

The resistance matrix, $[R_1]$ discussed in the previous section does not represent completely the resistance of the whole device because electric current (like magnetic flux) must flow in loops, 2D magneto-static analysis is necessarily incomplete in terms of the corresponding estimation of conductor resistance properties. The electrical circuits must be completed by end-windings of some description outside the plane of the analysis. The term “end-windings” is used in the generic sense as a connection between the conductors in the prismatic section of an EMM device. The resistance for the end-windings is explained in this section. Figure (5.1) shows a section of an end-ring. The nodes of the end-ring can be divided into two categories. Category A represents the nodes having zero into-plane currents and nodes 1, 2, ..., 6, 16, ..., 21 fall in this category and is distinguished by green colour. Category B

represents the nodes having non-zero into-plane currents and nodes 7, 8, ..., 15 fall in this category and is distinguished by red colour. In some EMM devices such as the stator in an electrical machine, knowing the into-plane currents instantly determines the above-plane currents. In other words, there is a unique set of above-plane currents for a set of into-plane currents. This is not true for all EMM devices. In some EMM devices, there is no unique set of above-plane currents for a set of into-plane currents. In these devices the resistance of the end-windings is calculated by determining the combination of end-winding currents which minimises the total resistive losses.

Let $\{I_{B0}\}$ represent the full vector of nodal currents of category B nodes, let $\{I_{ER}\}$ represent the full vector of currents in the end-ring links, and let $[R_E]$ be the diagonal matrix of link resistances for the end-ring. Figure (5.2) shows part of the rotor end-ring with seven links. Links 1-2, 3-4 and 5-6 are the links in the circumferential direction and links 1-3, 2-4, 3-5 and 4-6 are the links in the radial direction. The three different areas associated with three circumferential links are shown by three different dashed regions in the figure. Links 1-2 and 5-6 are associated with only one finite element and link 3-4 is associated with two finite elements. Therefore, the area associated with link 3-4 is more than the areas associated with the other two links in the circumferential direction. Similarly we can calculate the area associated with a particular link in the radial direction. If the width of the area associated with a particular link is w_1 , the length of the link is l_1 and the thickness of the end-ring is t_1 , then the resistance of that link can be calculated as

$$R_{EI} = \frac{\rho l_1}{t_1 w_1} \quad (5.5)$$

where ρ is the resistivity of the end-ring materials. Matrix $[R_B]$ represents the nodal resistance matrix of category B nodes. The number of end-ring links connected to category B nodes is smaller than the total number of end-ring links and naturally, the number of variables of $\{I_{ER}\}$ is much more than the number of variables of $\{I_{B0}\}$. The sum of end-ring (above-plane) currents flowing into a category B node is equal to the

into-plane currents associated with that node and the sum of end-ring (above-plane) currents in a category A node is 'zero'.

We can write Kirchoff's current law in the form

$$\{I_{B0}\} = [H_0]^T \{I_{ER}\} \quad (5.6)$$

where $[H_0]^T$ is some transformation matrix which relates end-ring currents to the rotor bar currents.

The objective is to find the matrix G_0 such that we can write

$$\{I_{ER}\} = [G_0] \{I_{B0}\} \quad (5.7)$$

If we know all of the currents in the rotor bars, there is a unique pattern of end-ring currents.

Combining Equations (5.6) and (5.7) gives us

$$[H_0]^T [G_0] = [I] \quad (5.8)$$

and

$$[G_0][H_0]^T \neq [I] \quad (5.9)$$

Now there are many choices of $[G_0]$ which satisfy Equation (5.8). The general case is this

$$[G_0] = [H_0^+]^T + [H_0^\perp][F_0] \quad (5.10)$$

Note that

$$[H_0]^T \left([H_0^+]^T + [H_0^\perp] [F_0] \right) = [I] \quad (5.11)$$

Here $[H_0^+]$ is the left pseudo-inverse of $[H_0]$ and $[H_0^\perp]$ is a matrix of spanning the space of all columns normal to $[H_0]$. $[F_0]$ is arbitrary in the sense that Equation (5.8) will be always true for all $[F_0]$. We apply additional reasoning to determine a unique $[F_0]$. This is based on the minimization of total resistive losses. We choose $[F_0]$ such that \forall vectors $\{I_{B0}\}$ the term $\{I_{B0}\}^T ([G_0]^T [R_E] [G_0]) \{I_{B0}\}$ will be minimum. Omitting certain tedious details, we find that

$$[F_0] = - \left([H_0^\perp]^T [R_E] [H_0^\perp] \right)^{-1} \left([H_0^\perp]^T [R_E] [H_0^+] \right) \quad (5.12)$$

The detail derivation of Equation (5.12) is given in Appendix A. Then the matrix $[G_0]$ is found from Equation (5.10) and the total resistance matrix is the combination of the resistance matrix associated with the nodal currents and the resistance matrix of the end-rings.

5.4 Coupled electromagnetic model for an EMM device with changeable geometry

This section describes the coupled electromagnetic model for an EMM device with changeable geometry. Here by changeable geometry we mean rigid body changes as well as deformations. The magnetic field equation of the machine is solved using a finite element procedure. A magnetic potential solution provides an instantaneous relationship between the magnetic flux and the vector of currents, $\{I_z\}$, present in the model. A fully-general version of the circuit equation is

$$\{V(t)\} = [R] \{I_{RS}(t)\} + [P] \frac{d\{\Phi(t)\}}{dt} \quad (5.13)$$

where $\{V(t)\}$ is the vector of externally-applied voltages (EMFs), $\{\Phi(t)\}$ is a vector representing magnetic flux and $[P]$ is a matrix dictating how the individual flux quantities in $\{\Phi(t)\}$ are coupled to the current variables. Flux vector, $\{\Phi(t)\}$ is calculated from solving magneto-static field equation using FE method and the instantaneous relationship between nodal currents and nodal potentials is shown in Equations (5.1) and (5.2). $[R]$ is the resistance matrix of the machine including the effect of the end-windings. The resistance matrix is symmetric and positive-definite. With an appropriate definition for the vectors $\{V\}$ and $\{I_{RS}\}$, the instantaneous electrical power P_I being fed into the machine is.

$$P_I = (\{I_{RS}\}^T \{V\}) \quad (5.14)$$

The instantaneous geometry of an EMM device can be expressed using a small number of variables which we arrange in the vector, $\{x\}$. If vector, $\{I_z\}$ contains one entry for every node in the two-dimensional finite-element model and the vector $\{V_z\}$ contains a corresponding entry for the net (externally applied) voltage tending to drive that current, then it is usual to construct a single transformation

$$\{V\} = [U]^T \{V_z\} \quad (5.15)$$

$$\{I_z\} = [U] \{I_{RS}\} \quad (5.16)$$

which allows the complete current state of the machine to be expressed concisely with a relatively small number of independent quantities within $\{I_{RS}\}$.

At any instant, if $\{I_{RS}\}$ and $\{x\}$ are known, the state of flux of the machine can be determined through a static relationship and Equation (5.2) can be represented in a different form as

$$\{\Phi\} = [\Theta(\{I_{RS}\}, \{x\})][P]^T \{I_{RS}\} \quad (5.17)$$

where $\{\Phi\}$ is a vector representing magnetic flux. Here, the matrix function $[\Theta(.,.)]$, essentially embodies a finite-element solution for magnetic potentials given the corresponding vector of nodal currents $([P]^T \{I_{RS}\})$. It is clear why $[\Theta(.,.)]$ is dependent on geometry. Its dependence on $\{I_{RS}\}$ arises because of the nonlinear magnetic characteristics of the iron in most machines. At low levels of flux, $[\Theta(.,.)]$ is independent of $\{I_{RS}\}$.

At any given instant, $t = t_0$, if the machine currents and geometry are known as $\{I_{RS}\} = \{I_0\}$ and $\{x\} = \{x_0\}$ respectively, Equation (5.17) can be applied to determine $\{\Phi_0\}$. Then this equation can be approximated by this following linear form for sufficiently small perturbations

$$(\{\Phi\} - \{\Phi_0\}) = [A][P]^T (\{I_{RS}\} - \{I_0\}) + [B](\{x\} - \{x_0\}) \quad (5.18)$$

If the flux in the machine is low enough everywhere that there is no magnetic saturation, then $([P][A][P]^T)$ is precisely the inductance matrix associated with the current vector, $\{I_{RS}\}$. Also in this case, the matrix $[B]$ is proportional to $\{I_{RS}\}$ so that if the currents are doubled, then $[B]$ is also doubled. Matrices, $[A]$ and $[B]$ should not be confused with $\{A\}$ and $\{B\}$ which are used to represent magnetic potential and magnetic flux density respectively.

We can write Equation (5.18) in differential form as

$$d\{\Phi\} = [A][P]^T d\{I_{RS}\} + [B]d\{x\} \quad (5.19)$$

Now pre-multiplying Equation (5.19) by half of the nodal currents $\frac{1}{2}([P]^T d\{I_{RS}\})^T$ and also assuming that there is no geometry change, we will get

$$\frac{1}{2} \{I_{RS}\}^T [P]^T d\{\Phi\} = \frac{1}{2} \{I_{RS}\}^T [P][A][P]^T d\{I_{RS}\} \quad (5.20)$$

The right hand side of Equation (5.20) is the increment of energy invested in the magnetic field. Comparing the left hand side with the increment in stored energy in an inductor it can be recognised that $([P]^T[A][P])$ is the “tangent inductance” or “marginal inductance” matrix. This matrix is always symmetric and positive definite. In general, matrices $[A]$ and $[B]$ of Equation (5.19) can be obtained by differentiation from Equation (5.17). This differentiation can be done analytically but a numerical approach is much more straightforward. Differentiating Equation (5.17)

$$d\{\Phi\} = d[\Theta(\{I_{RS}\}, \{x\})][P]^T \{I_{RS}\} + \Theta(I_{RS}, x)[P]^T d\{I_{RS}\} \quad (5.21)$$

$$d\{\Phi\} = \left[[\Theta(\{I_{RS}\}, \{x\})][P]^T + \frac{\partial[\Theta(\{I_{RS}\}, \{x\})]}{\partial\{I_{RS}\}} [P]^T \{I_{RS}\} \right] d\{I_{RS}\} + \frac{\partial[\Theta(\{I_{RS}\}, \{x\})]}{\partial\{x\}} [P]^T \{I_{RS}\} d\{x\} \quad (5.22)$$

Here $\frac{\partial[\Theta(\{I_{RS}\}, \{x\})]}{\partial\{I_{RS}\}}$ is a 3D tensor. Plane k of this is a matrix representing the sensitivity of $[\Theta(\{I_{RS}\}, \{x\})]$ to small changes in the k -th entry of $d\{I_{RS}\}$. Similarly $\frac{\partial[\Theta(\{I_{RS}\}, \{x\})]}{\partial\{x\}}$ is also a 3D tensor and plane k of this is a matrix representing the sensitivity of $[\Theta(\{I_{RS}\}, \{x\})]$ to small changes in the k -th entry of $d\{x\}$. Comparing Equations (5.19) and (5.22)

$$[A] = \left[[\Theta(\{I_{RS}\}, \{x\})] + \frac{\partial[\Theta(\{I_{RS}\}, \{x\})][P]^T \{I_{RS}\}}{\partial\{I_{RS}\}} \right] \quad (5.23)$$

$$[B] = \frac{\partial[\Theta(\{I_{RS}\}, \{x\})]}{\partial\{x\}} [P]^T \{I_{RS}\} \quad (5.24)$$

If the linearization described in Equation (5.18) has been applied at the instant $t = t_0$, then at that instant Equation (5.13) applies with this effect

$$\{V\} = [R]\{I_{RS}\} + ([P][A][P]^T) \frac{d\{I_{RS}\}}{dt} + ([P][B]) \frac{d\{x\}}{dt} \quad (5.25)$$

From this, the rate of change of the current vector can be determined. Through this, it is clear that a time-stepping integration can be carried out to determine currents provided that $\{V\}$ and $\{x\}$ (and its rate of change) are known at every instant.

We make one final remark in this section. Equation (5.17) implies that no flux is present if there is no current and hence appears to exclude the analysis of machines having permanent magnets. In fact, it is not difficult to model permanent magnet portions arbitrarily accurately using current distributions. All that is necessary here is the inclusion of more entries in $\{I_{RS}\}$ than there are “physical” independent currents. We choose zero voltage, zero resistance and large inductance associated with these currents. With proper initialisation of these currents can be kept constant during the time stepping integration process.

5.5 Modelling of an induction machine

An induction machine is a complex EMM device and consists of mainly two parts. One is stationary part called stator and another is rotating part called rotor. In general (for a 3-phase machine having no parallel paths) the stator currents are represented by three independent currents. The resistance matrix associated with the three terminal currents is a 3×3 diagonal and positive-definite matrix. Each diagonal entry represents the resistance associated with one terminal current. As explained in Section (4.3) of Chapter 4, the nodal currents of a stator can be transformed into terminal currents by the following transformation

$$\{I_{Snc}\} = [T_s]\{I_s\} \quad (5.26)$$

where $\{I_{Snc}\}$ is the full set of nodal currents of the stator, $\{I_s\}$ is the vector of terminal currents of the stator and $[T_s]$ is the corresponding transformation matrix. If $[R_{Snc}]$ is

the resistance matrix associated with the stator nodal currents, then the resistance matrix, $[R_s]$ associated with the terminal currents is calculated as

$$[R_s] = [T_s]^T [R_{snc}] [T_s] \quad (5.27)$$

The resistance matrix associated with the reduced vector of rotor bar currents is also a diagonal and positive-definite matrix. The size of this matrix is determined by the number of reduced rotor bar currents. Each diagonal entry represents the resistance associated with one of the reduced rotor bar currents. As explained in Section (4.4) of Chapter 4, the nodal currents of a rotor can be transformed into a reduced number of rotor bar currents by the following transformation

$$\{I_{Rnc}\} = [T_R] \{I_R\} \quad (5.28)$$

where $\{I_{Rnc}\}$ is the full set of nodal currents of the rotor, $\{I_R\}$ is the reduced vector number of rotor bar currents and $[T_R]$ is the corresponding transformation matrix. If $[R_{Rnc}]$ is the resistance matrix associated with the rotor nodal currents, then the resistance matrix associated with the reduced number of rotor bar currents, $[R_R]$ is calculated as

$$[R_R] = [T_R]^T [R_{Rnc}] [T_R] \quad (5.29)$$

The resistance matrices for the rotor and stator are calculated separately and finally each of these becomes a diagonal block partition in the resistance matrix for stator windings and rotor bar. The resistance matrix for the stator windings and rotor bar of an induction machine can be written as

$$[R_i] = \begin{bmatrix} R_s & \text{---} \\ \text{---} & R_R \end{bmatrix} \quad (5.30)$$

here $[R_1]$ is the resistance matrix for the stator windings and rotor bars.

The resistance for the end-windings of the stator can be calculated easily (see Section 5.3) and the end-winding currents can be written in terms of stator terminal currents. This transformation can be written by inspection. The resistance matrix, $[R]$ consists of the resistance of the stator and rotor and also the effects of end-windings of the stator and rotor.

For a two-dimensional analysis of an induction machine, the vector $\{x\}$ describing the instantaneous geometry usually comprise only three entries provided that neither the rotor nor the stator can deform significantly in the plane and provided that the stator is fixed in space. As shown in Figure (5.3) these three entries can be written as

$$\{x\} := \begin{Bmatrix} u \\ v \\ \theta \end{Bmatrix} \quad (5.31)$$

where u and v are the horizontal and vertical positions of the rotor centre respectively and θ is the angle of turn of the rotor.

The electro-magneto-mechanical equation for an induction machine is the same as Equation (5.25)

$$\{V\} = [R]\{I_{RS}\} + ([P][A][P]^T) \frac{d\{I_{RS}\}}{dt} + ([P][B]) \frac{d\{x\}}{dt} \quad (5.32)$$

where $\{V\}$ is the vector of externally-applied voltages, $[R]$ is the resistance matrix of the machine including the effect of the end-windings, $\{I_{RS}\}$ is the vector of independent currents of the machine and this includes the stator and rotor independent currents. Matrix $([P][A][P]^T)$ is the tangential inductance and is a function of currents and geometry. If there is no translation of the rotor and only rotation is considered,

then the geometry vector, $\{x\}$ is a scalar and $\{x\} = \theta$. So, when we consider only rotation Equation (5.22) can be written as

$$d\{\Phi\} = \left[[\Theta(I_{RS}, \theta)] [P]^T + \frac{\partial [\Theta(I_{RS}, \theta)]}{\partial \{I_{RS}\}} [P]^T \{I_{RS}\} \right] d\{I_{RS}\} + \frac{\partial [\Theta(I_{RS}, \theta)]}{\partial \theta} [P]^T \{I_{RS}\} d\theta \quad (5.33)$$

For a constant mechanical speed of the rotor, Ω_{mech} , $d\theta = \Omega_{mech} dt$ and Equation (5.13) can be written as

$$\begin{aligned} \{V\} = [R]\{I_{RS}\} + [P] \left[[\Theta(I_{RS}, \theta)] [P]^T + \frac{\partial [\Theta(I_{RS}, \theta)]}{\partial \{I_{RS}\}} [P]^T \{I_{RS}\} \right] \frac{d\{I_{RS}\}}{dt} + \\ [P] \frac{\partial [\Theta(I_{RS}, \theta)]}{\partial \theta} [P]^T \Omega_{mech} \{I_{RS}\} \end{aligned} \quad (5.34)$$

Equation (5.34) can also be written as

$$\{V\} = \left([R] + \Omega_{mech} \frac{d[L_{mar}(I_{RS}, \theta)]}{d\theta} \right) \{I_{RS}\} + [L_{mar}(I_{RS}, \theta)] \frac{d\{I_{RS}\}}{dt} \quad (5.35)$$

where $[L_{mar}]$ is the marginal inductance.

5.6 Conclusions

This chapter focuses on the modelling of electro-magneto-mechanical devices using 2D FE model. The presented model can be applied to any EMM devices including induction machines. The effects of end-windings are incorporated in the 2D model by writing the end-winding currents (above-currents) in terms of rotor bar currents (into-currents). If the current density is uniform this transformation is obvious. For variable current densities this transformation is obtained from the minimisation of resistive losses. An example of how the procedures can be extended to model an induction machine has also been discussed.

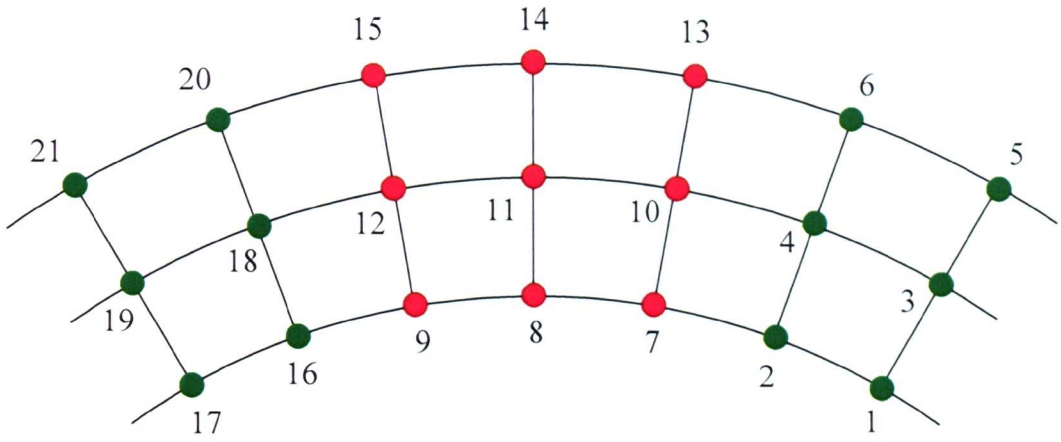


Figure (5.1): Cross section of rotor end-rings

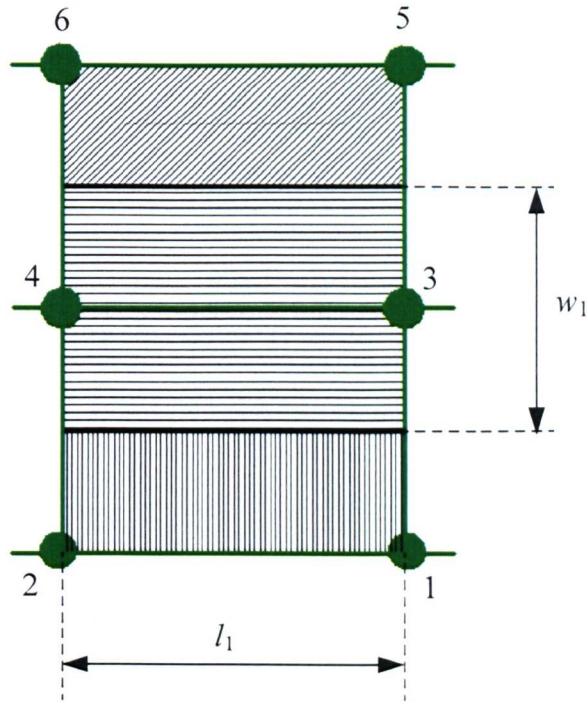


Figure (5.2): Cross section of rotor end-rings with seven links (three along the circumferential and four along the radial direction)

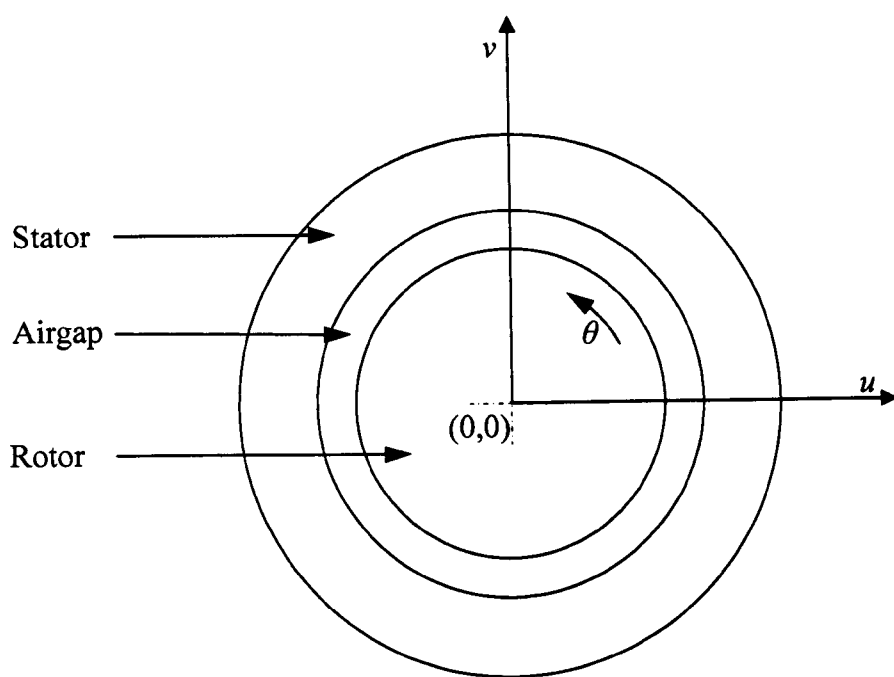


Figure (5.3): Stator, rotor and airgap of an electric machine

Chapter Six

Time-marching Simulations of Rotating Electric Machinery

6.1 Introduction

Chapters 3 to 5 of this thesis have addressed the rudiments of modelling coupled electro-magneto-mechanical systems. Chapter 3 outlined the basics of magneto-static FEA such as is used throughout this work. Chapter 4 explained a number of essential transformations which are made (some relating only to the vector of currents and others to the vector of magnetic potentials as well as to the vector of currents). In Chapter 5, the principles of how to deal with changing geometry in an electro-magneto-mechanical system were outlined but their implementation within an FEA context was not explored. This chapter concentrates on precisely that implementation. In particular, it addresses the time-domain simulation of electrical machines which are obviously particular cases of electro-magneto-mechanical systems. In some cases, the changes in geometry are restricted only to the rotation of the rotor relative to the stator. In the most general case, however, the rotor is also allowed to translate relative to the stator. Time-domain simulation is really the workhorse tool for modern machine designers. Approximate design calculations can bring the machine designer to the point where his design is close to optimal. It is now commonplace for machine designers to check their final design by simulating its behaviour numerically so as to ascertain whether the many assumptions which are common in basic machine design programs are valid in his particular case.

The remainder of this chapter comprises four main sections. In section 6.2, we examine the set of ways by which it is possible to accommodate the movement of the rotor relative to the stator.

In section 6.3, we firstly recall the structure of the FEA model formulation. It is obvious from this revision that certain matrix quantities will be needed at every instant in the simulation. The remainder of section 6.3 addresses some general principles by which these quantities can be acquired. Finally two distinct methods which are used within this thesis for accommodating relative motion of rotor and stator are discussed. These are: (a) the "airgap stitching" method and (b) the "central circle" method. It will be seen that the latter has many advantages and attractions over the former but that it suffers from the drawback that it cannot easily be used to simulate machines where the rotor is not concentric with the stator.

At several points in this chapter, the reader will encounter some sections that look similar because (1) arguments applied to the rotor are also applied to the stator, (2) similarities between the two main methods explained here and (3) explanations given for linear are extended to non-linear.

6.2 Accommodating movement in rotating electric machine modelling

6.2.1 Established approaches for accommodating movement in FE models

In rotating electrical machines, electromagnetic finite element modelling must be able to account for mechanical displacements caused by the relative movement between the stator and rotor. One simple approach is to separate the solution domain into a stationary and a rotating part, discretise them separately so that there is a space between them and then stitch the two parts with (largely triangular) elements in that space. The magnetic field formulations of the stationary and the rotating parts are each then derived in their own respective coordinate systems and constraints are applied in the airgap to take care of the relative movement. Different methods for modelling movement of rotors have been described by Bastos and Sadowski, (2003) and Rodger *et al.* (1990). A number of different methods exist to cater for the relative movement of two parts linked by a magnetic field. The available methods can be broadly categorized as

- 1 Boundary element modelling is used for the airgap and integrated with the FE models for the rotor and stator. This is a hybrid method combining both BE and FE methods. Klimke (2004) in his article described a hybrid magnetic field solver based on this concept. The disadvantage with this method is that the magnetic stiffness matrix is no longer sparse and can increase the computational time. A positive attribute is that this method can be used to take care of the movement of an eccentric rotor.
- 2 In an alternative set of methods the rotating and stationary parts are modelled separately and then connected at the airgap. Re-meshing is required to take care of the relative movement between the stator and rotor. Arkkio (1987) gave a detailed review of this method.
- 3 In a third class of methods rotor movement is accommodated by airgap element. The airgap element is an *macroelement* originally proposed by Abdel-Razek *et al.* (1982) for modelling annular airgap in electrical machine. The finite elements in the airgap are replaced by a single element macroelement. This macroelement is based on the analytical solution of the magnetic field of the airgap. The advantages of using an airgap element are that it avoids the re-meshing the airgap and since an analytical solution is used the results are more accurate. Later Wang *et al.* (2002) developed airgap element method to use in some special machines such as the linear machine or the disc-type rotating machine. The disadvantage of this method is the substantial increase of the computational time caused by the insertion of dense matrix blocks into the sparse FE matrices [Gersem and Weiland, 2005].
- 4 Another method exists for a class of problem where rotating and stationary parts are modelled separately with non-coinciding nodes from both the stator and rotor sides being present at the same sliding interface. This subdivides further into (4a) constraints being applied to reduce the number of independent potentials again and (4b) introduction of Lagrangian multipliers. In the Lagrange multiplier method the rotating and stationary parts are modelled completely independently and Lagrange multipliers are used to couple these independent meshes at a suitable interface. Rodger *et al.* (1990) used the Lagrange multiplier method to account for the relative movement between a stationary part and a rotating part in 2D. Later Lai *et al.* (1992) extended this method for 3D problems. Moving surface technique is implemented in a

commercial package called Maxwell 2DTM to handle the rotational movement. Both the stationary and moving parts are meshed separately. Finite element shape functions are then used to couple these two independent meshes at the moving surface. Fu *et al.* (2005) used a similar method using sliding surface.

6.2.2 Approaches used in this thesis for accommodating movement

In the analyses reported in this thesis, the rotor movement is modelled in two different ways. One of them is called the airgap stitching method and another is called the central circle method. In the first method the rotor and stator are modelled using completely separate FEA models – each including some fraction of the airgap. The two subsystem models are combined by stitching the outer diameter of the rotor and the inner diameter of the stator in the airgap. During the simulation, at least some of the airgap has to be re-meshed to account for the rotor movement. This means that the element matrices for (some of) the airgap must be derived at every time step during the simulation even if the magnetic saturation is not considered. At the very least, one whole radial layer of airgap elements will have to be derived afresh. This method falls on the second category described above where the rotor and stator are modelled separately connected at the airgap using finite elements. Figure (6.1) shows where the relative movement of the stationary and the rotating part of a typical rotating electrical machine is taken care by airgap stitching method. The airgap stitching method has two main disadvantages:

- (a) In reality, it is obvious that the machine inductance matrix should be a continuous function of rotor angle. With the stitching method, at instants where the connectivity of rotor and stator nodes has to be changed, discontinuities will appear in the inductance.
- (b) Even for analyses which are magnetically linear, the element matrices must be derived afresh for the stitching elements at each instant in time.

A strong advantage of this method is that it can cope with the case of eccentric rotor and stator provided that the eccentricity is smaller than the thickness of the stitched band.

In the second method employed in this work, the FE models for the rotor and stator have coincident circular boundaries (usually in mid-airgap). Initially, the magnetic potentials at these two boundaries are completely independent but constraint equations are applied to ensure that flux traversing the common boundary is conserved. This method falls on the category where non-coincident rotor nodes and stator nodes are both present at the same sliding interface and constraints are applied to reduce the number of independent potentials. Figure (6.2) shows a stator, a rotor and the central circle in the middle of the airgap of a typical rotating electrical machine. This method has two disadvantages:

- (a) When constraints are applied the sparsity of the stiffness matrix is reduced.
- (b) It can not cope with the case of eccentric rotor and stator.

6.3 Some general features of machine modelling

In this section the first of the two subsections describe the model that is solved in this chapter. The second section describes some general notes on inductance matrix and its derivatives.

6.3.1 Revisit of the electro-magneto-mechanical model

From the 2D FEA proposed and used in this work, we get an instantaneous relationship between nodal currents and nodal potentials and this is already stated in the Chapter 3. The full nodal vector of currents can be reduced to a smaller number of independent currents variables by imposing constraints. Recalling the transformations discussed in Chapter 4, for a magnetically linear rotating electromagnetic machine we can write

$$[K]\{A\} = [U]\{I_{RS}\} \quad (6.1)$$

where $[K]$ is the stiffness matrix, $\{A\}$ is the vector of magnetic potentials at nodes, $[U]$ is the transformation matrix and $\{I_{RS}\}$ is the reduced vector of independent currents of the machine. The current vector $\{I_{RS}\}$ comprises two partitions. The first

partition is the terminal or phase currents of the stator and the second partition is the reduced number of rotor bar currents. If we incorporate nonlinearity in Equation (6.1) we can write

$$[K_{\text{mar}}]\{\Delta A\} = \{\Delta I\} \quad (6.2)$$

where $[K_{\text{mar}}]$ is the *tangential* or *marginal* stiffness matrix and $[K_{\text{mar}}]$ is a nonlinear function of current and instantaneous geometry. It is already discussed how $[K_{\text{mar}}]$ can be found out from $B(H)$ curve. Equation (6.2) can also be written in the form

$$[K_{\text{mar}}]\{A_z\} \approx [U]\{I_{\text{RS}}\} + \{b_z\} \quad (6.3)$$

where $\{b_z\}$ can be described as a vector of free MMF. The coupled electro-magneto-mechanical model has already been described in Chapter 5. The linearised coupled equation of this electro-magneto-mechanical model of an electrical machine with constant mechanical speed, Ω_{mech} is

$$\{V\} = \left([R] + \Omega_{\text{mech}} \frac{d[L]}{d\theta} \right) \{I_{\text{RS}}\} + [L_{\text{mar}}] \frac{d\{I_{\text{RS}}\}}{dt} \quad (6.4)$$

where $\{V\}$ is the vector of externally-applied voltages, $[R]$ is the resistance matrix of the machine including the effect of the end-windings, $\{I_{\text{RS}}\}$ is the vector of independent currents and $[L_{\text{mar}}]$ is the marginal inductance matrix and is a function of the independent current vector, $\{I_{\text{RS}}\}$ and the rotor position θ . To calculate the current vector $\{I_{\text{RS}}\}$, Equation (6.4) is integrated in time domain. Two methods are employed to calculate the marginal inductance and its rate of change. These two methods are airgap stitching method and central circle method and these two methods are discussed in the subsequent sections.

6.3.2 Definition and calculation of marginal inductance and its derivative

The marginal inductance $[L_{\text{mar}}]$ mentioned in Equation (6.4) is calculated from the instantaneous relationship between the magnetic nodal potentials and nodal currents. The increment in stored energy in a magnetically coupled circuit can be written as

$$E = \frac{1}{2} \{A_z\}^T [K_{\text{mar}}] \{\Delta A_z\} \quad (6.5)$$

Using Equation (6.2) we can write the increment of stored energy of this as

$$E = \frac{1}{2} \{I_{\text{RS}}\}^T [U]^T [K_{\text{mar}}]^{-1} [U] \{\Delta I_{\text{RS}}\} \quad (6.6)$$

The stored energy of an inductor, E_s is

$$E_s = \frac{1}{2} \{I\}^T [L] \{I\} \quad (6.7)$$

Comparing Equation (6.6) and (6.7) the marginal inductance $[L]$ of the machine can be written as

$$[L] = [U]^T [K_{\text{mar}}]^{-1} [U] \quad (6.8)$$

For a magnetically linear system $\{\Delta A_z\} = \{A_z\}$ and $[K_{\text{mar}}] = [K]$. It is noted that $[U]$ has fewer columns than rows and also most of the entries of $[U]$ are zeros. The non-zero entries correspond to the current carrying nodes. From Equation (6.8) it is seen that only the components corresponding to the current carrying nodes are used to calculate the inductance matrix. Therefore, we can reduce the stiffness matrix further and in turn reduce the computational time. This feature is used in the calculation of steady state currents and is discussed in the next Chapter. A detailed explanation is given in Appendix A.

The rate of change of inductance i.e. $\frac{d[L]}{dt}$ can be calculated either by a direct analytical differentiation (which would involve determining the sensitivity of each element stiffness matrix to the position of its nodes) or by a numerical differentiation. The latter is preferred here and a central difference method is employed whereby perturbing the model by a small angle. For a particular mechanical speed the rate of change of inductance is $\frac{d[L]}{dt} = \Omega_{\text{mech}} \frac{d[L]}{d\theta}$. From Equation (6.8)

$$\frac{d[L]}{d\theta} = [U]^T \frac{d[K]^{-1}}{d\theta} [U] \quad (6.9)$$

But we know that

$$\frac{d[K]^{-1}}{d\theta} = -[K]^{-T} \frac{d[K]}{d\theta} [K]^{-1} \quad (6.10)$$

So,

$$\frac{d[L]}{d\theta} = -([K]^{-1} [U])^T \frac{d[K]}{d\theta} ([K]^{-1} [U]) \quad (6.11)$$

Therefore, to calculate $\frac{d[L]}{d\theta}$ we need to calculate $\frac{d[K]}{d\theta}$ and $\frac{d[K]}{d\theta}$ is calculated using the central difference as

$$\frac{d[K]}{d\theta} \approx \frac{[K](\theta + \Delta\theta) - [K](\theta - \Delta\theta)}{2\Delta\theta} \quad (6.12)$$

For linear case, since we have already calculated the term $([K]^{-1} [U])$ while calculating the inductance [Equation (6.8)], we can save a substantial amount of time by using Equation (6.12). In this work the value of $\Delta\theta$ used for numerical differentiation was 1% of 1°.

If no geometry change occurs in the machine, the above prescribed method can be used directly to calculate inductance and its rate of change. If there is geometry change some additional modifications can be incorporated to speed up the calculation of inductance and its derivative. The following sections discuss how the inductance and its derivative are calculated using airgap stitching method and central circle method.

6.4 Airgap stitching method

Figure (6.1) shows a simple machine whose airgap is divided into three bands. The inner most band which is nearest to the outer diameter of the rotor is stitched with triangular elements. In terms of computational effort linear and non-linear FEA can be very different and so they have to be handled separately. Therefore, this section is divided into two main sub-sections

- Calculation of marginal inductance and its rate of change using airgap stitching method from non-linear FEA
- Calculation of marginal inductance and its rate of change using airgap stitching method from linear FEA

6.4.1 Marginal inductance and its rate of change using airgap stitching method from non-linear FEA

As stated in Chapter 3 for higher currents the relationship between nodal currents and nodal potentials is no longer linear. If nonlinearity is incorporated in the instantaneous relationship between nodal currents and nodal potentials, Equation (6.1) can be written as

$$[K_{\text{mar}}]\{\Delta A\} = [U]\{\Delta I_{\text{RS}}\} \quad (6.13)$$

Since there is geometry change here, $[K_{\text{mar}}]$ will be functions of current and geometry change. The stiffness matrix, $[K_{\text{mar}}]$, has to be derived at every time step. The element matrices for non-ferromagnetic materials need be derived only once - except for those

air gap elements which change with the motion of the rotor. Similar to Section (6.3) we can write the inductance as

$$[L] = [U]^T [K_{\text{mar}}]^{-1} [U] \quad (6.14)$$

The inductance matrix computation in Equation (6.14) is performed after convergence of the nonlinear magnetic field problem has been achieved for the machine currents i.e. stator phase currents and the rotor bar currents. Rate of change of inductance is calculated using the procedure described in Equation (6.11).

6.4.2 Marginal inductance and its rate of change using airgap stitching method from linear FEA

If the geometry change is not considered the calculation of the marginal inductance from linear FEA is quite simple because it has to be calculated only once. If the geometry change is considered in the calculation of marginal inductance from linear FEA the element matrices also need to be derived only once except for those airgap elements which change with the motion of the rotor. In an electric machine, geometry changes occur mainly due to the rotor movement. While modelling the movement of the rotor in the time domain simulation, the stiffness matrix $[K]$ has to be derived at every time step. This process can be computationally very expensive. To avoid that the full magnetic vector potential vector $\{A_z\}$ is written in terms of airgap potentials when modelling the rotor movement since the changes occur only in the airgap if the magnetic saturation is neglected. Thus, only the element stiffness matrices of the airgap elements need to be derived at every time step to take care of the rotor movement. The vector of nodal currents $\{I_z\}$ is divided into five different partitions as

$$\{I_z\} = \begin{Bmatrix} I_1 \\ I_2 \\ I_3 \\ I_4 \\ I_5 \end{Bmatrix} = \begin{Bmatrix} U_1 \\ U_2 \\ U_3 \\ U_4 \\ U_5 \end{Bmatrix} \{I_{RS}\} \quad (6.15)$$

Correspondingly, magnetic potentials are also divided into five regions as

$$\{A_z\} = \begin{Bmatrix} A_1 \\ A_2 \\ A_3 \\ A_4 \\ A_5 \end{Bmatrix} \quad (6.16)$$

Here, $\{A_1\}$ contains magnetic vector potentials at stator nodes excluding those stator nodes bordering the airgap, $\{A_2\}$ contains magnetic vector potentials at nodes on the stator-airgap boundary, $\{A_3\}$ contains magnetic vector potentials at air gap nodes not common to either stator or rotor, $\{A_4\}$ contains magnetic vector potentials at nodes on the rotor-airgap boundary, $\{A_5\}$ contains magnetic vector potentials at nodes excluding those rotor nodes bordering the airgap. Figure (6.3) shows a quarter of an electrical machine model discretized with 8-noded quadrilateral and 6-noded triangular finite elements. For this example we can write $\{A_1\}$, $\{A_2\}$, $\{A_3\}$, $\{A_4\}$, and $\{A_5\}$ as

$$\{A_1\} = \begin{Bmatrix} a_6 \\ a_7 \\ a_{13} \\ a_{14} \\ a_{20} \\ a_{21} \\ a_{27} \\ a_{28} \end{Bmatrix}, \{A_2\} = \begin{Bmatrix} a_5 \\ a_{12} \\ a_{19} \\ a_{26} \end{Bmatrix}, \{A_3\} = \begin{Bmatrix} a_4 \\ a_{11} \\ a_{18} \\ a_{25} \end{Bmatrix}, \{A_4\} = \begin{Bmatrix} a_3 \\ a_{10} \\ a_{17} \\ a_{24} \end{Bmatrix}, \{A_5\} = \begin{Bmatrix} a_1 \\ a_2 \\ a_8 \\ a_9 \\ a_{15} \\ a_{16} \\ a_{22} \\ a_{23} \end{Bmatrix} \quad (6.17)$$

where $a_1, a_2, a_3, \dots, a_{28}$ are the nodal magnetic vector potentials of nodes 1, 2, 3, ..., 28 respectively. Arranging $[K]$ matrix according to the order mentioned in Equation (6.15) we can write Equation (6.1) as

$$\begin{bmatrix} K_{11} & K_{12} & O & O & O \\ K_{21} & K_{22} & K_{23} & O & O \\ O & K_{32} & K_{33} & K_{34} & O \\ O & O & K_{43} & K_{44} & K_{45} \\ O & O & O & K_{54} & K_{55} \end{bmatrix} \begin{Bmatrix} A_1 \\ A_2 \\ A_3 \\ A_4 \\ A_5 \end{Bmatrix} = \begin{Bmatrix} U_1 \\ U_2 \\ U_3 \\ U_4 \\ U_5 \end{Bmatrix} \{I_{RS}\} \quad (6.18)$$

From Equation (6.18) we can write the following Equations from (6.19) to (6.22)

$$[K_{11}]\{A_1\} + [K_{12}]\{A_2\} = [U_1]\{I_{RS}\} \quad (6.19)$$

$$\{A_1\} = [K_{11}]^{-1}([U_1]\{I_{RS}\} - [K_{12}]\{A_2\}) \quad (6.20)$$

$$[K_{54}]\{A_4\} + [K_{55}]\{A_5\} = [U_5]\{I_{RS}\} \quad (6.21)$$

$$\{A_5\} = [K_{54}]^{-1}([U_5]\{I_{RS}\} - [K_{54}]\{A_4\}) \quad (6.22)$$

For the linear case we can write the full vector of magnetic potential in terms of the airgap potentials as

$$\begin{Bmatrix} A_1 \\ A_2 \\ A_3 \\ A_4 \\ A_5 \end{Bmatrix} = \begin{bmatrix} -K_{11}^{-1}K_{12} & O & O \\ I & O & O \\ O & I & O \\ O & O & I \\ O & O & -K_{55}^{-1}K_{54} \end{bmatrix} \begin{Bmatrix} A_2 \\ A_3 \\ A_4 \end{Bmatrix} + \begin{Bmatrix} K_{11}^{-1}U_1 \\ O \\ O \\ O \\ K_{55}^{-1}U_5 \end{Bmatrix} \{I_{RS}\} \quad (6.23)$$

or
$$\{A_z\} = [T_1]\{A_{red}\} + [T_2]\{I_{RS}\} \quad (6.24)$$

where the definitions of the quantities in Equation (6.24) are obvious from Equation (6.23). Substituting $\{A_z\}$ of Equation (6.24) to Equation (6.18) and pre-multiplying by $[T_1]^T$, we obtain

$$\begin{bmatrix} (K_{22} - K_{21}K_{11}^{-1}K_{12}) & K_{23} & 0 \\ K_{32} & K_{33} & K_{34} \\ 0 & K_{43} & (K_{44} - K_{45}K_{55}^{-1}K_{54}) \end{bmatrix} \begin{Bmatrix} A_2 \\ A_3 \\ A_4 \end{Bmatrix} = \begin{bmatrix} U_2 - K_{21}K_{11}^{-1}U_1 \\ U_3 \\ U_4 - K_{45}K_{55}^{-1}U_5 \end{bmatrix} \{I_{RS}\} \quad (6.25)$$

$$[K_{D1}]\{A_{red}\} = [U_{D1}]\{I_{RS}\} \quad (6.26)$$

$\{A_{red}\}$ is the reduced vector of magnetic potentials consisting only the nodes corresponding to the outer diameter of the rotor, inner diameter of the stator and the air gap nodes. The energy stored in a magnetically coupled circuit is given by

$$E = \frac{1}{2} \{A_z\}^T [K] \{A_z\} = \frac{1}{2} \left[([T_1]\{A_{red}\} + [T_2]\{I_{RS}\})^T [K] ([T_1]\{A_{red}\} + [T_2]\{I_{RS}\}) \right] \quad (6.27)$$

Inserting the expressions of $\{A_{red}\}$ from Equation (6.26) in Equation (6.27) and simplification leads to

$$E = \frac{1}{2} \{I_{RS}\}^T \left([U_1]^T [K_{11}]^{-1} [U_1] + [U_{D1}]^T [K_{D1}]^{-1} [U_{D1}] + [U_5]^T [K_{55}]^{-1} [U_5] \right) \{I_{RS}\} \quad (6.28)$$

where E is the total energy stored in the machine. Comparing Equation (6.28) to the stored energy of an inductor, as Equation (6.11) we obtain the inductance of the machine as

$$[L] = \overbrace{[U_1]^T [K_{11}]^{-1} [U_1]}^{T1} + \overbrace{[U_{D1}]^T [K_{D1}]^{-1} [U_{D1}]}^{T2} + \overbrace{[U_5]^T [K_{55}]^{-1} [U_5]}^{T3} \quad (6.29)$$

As shown in the above equation the inductance matrix consists of three terms. The first term, $T1$, corresponds to the stator nodes excluding those stator nodes bordering the airgap. The element matrix for this region does not depend on the movement of the rotor so for a linear case it is calculated only once. The second part, $T2$, corresponds to the nodes on the stator-airgap boundary where the air gap nodes are not common to either the stator or rotor and nodes on the rotor-airgap boundary. The element matrix for this region depends on the movement of the rotor and has to be calculated at every time step. The third part, $T3$, corresponds to the rotor nodes

excluding those rotor nodes bordering the airgap. The element matrix for this region does not depend on the movement of the rotor so for a linear case it is calculated only once.

The rate of change of inductance i.e. $\frac{d[L]}{dt}$ can be calculated using the similar procedure prescribed in Equation (6.11).

6.5 The central circle (CC) method

In this section we present a method for calculating steady state solution of an induction machine and we call this method the ‘central circle method’. This method has significant advantages over the airgap stitching method described above. In this method the rotor and stator are modelled separately which share a common circle named as ‘central circle’ at the middle of the airgap. Figure (6.4) shows the rotor and stator along with the common central circle. Nodes corresponding to one half of the airgap form an integral part of the rotor model and nodes corresponding to another half form an integral part of the stator model. Nodes of the stator model at the central circle are not required to coincide with nodes of the rotor side. This particular characteristic makes this method different from the other method. Another feature of this method is that the rotor and stator are analysed completely independently. The effects of the stator on the rotor flux are represented to the rotor by a set of fictitious currents acting at the “central circle”. This set of currents is denoted by $\{I_{RC}\}$. Similarly the effects of the rotor on the stator flux are represented to the stator by a set of fictitious currents acting at the “central circle”. This set of currents is denoted by $\{I_{SC}\}$.

The nodal potentials of rotor at the central circle are approximated by a Fourier series. Similarly the nodal potentials of stator at the central circle are also approximated by a Fourier series. A constraint is imposed on these two sets of potentials to take care of the relative movement between the rotor and the stator. As the rotor and stator nodes are concerned; both side see same pattern of potentials but shifted. These steps are explained in the following subsections.

6.5.1 Formulation for the rotor

Figure (6.4) shows a notional electric machine separated into halves, i.e. stator and rotor, by the central circle at the middle of the airgap. The instantaneous relationship between the nodal potentials and the nodal currents for the rotor can be written as

$$[K_R]\{A_R\} \approx \{I_{RN}\} + \{b_R\} \quad (6.30)$$

where $[K_R]$ is the stiffness matrix of the rotor, $\{A_R\}$ is the nodal potential vector of the rotor, $\{I_{RN}\}$ is the nodal current vector of the rotor and $\{b_R\}$ is the nodal free MMF vector in the rotor. $\{A_R\}$ is divided into two parts as

$$\{A_R\} = \begin{Bmatrix} A_{RM} \\ A_{RCN} \end{Bmatrix} \quad (6.31)$$

Here $\{A_{RM}\}$ contains potentials at rotor nodes excluding those rotor nodes on the central circle and $\{A_{RCN}\}$ contains potentials at nodes on the central circle in the rotor. The nodal magnetic vector potentials at the central circle in the rotor are approximated using a Fourier series. We can write this transformation as

$$\{A_{RCN}\} = [T_{RCN}]\{A_{RC}\} \quad (6.32)$$

where $\{A_{RC}\}$ is the Fourier components of the potential on the central circle in the rotor and $[T_{RCN}]$ is the transformation matrix. If the number of nodes on the central circle in the rotor is n and if the number of harmonics considered is p , Equation (6.32) can be written as

$$\{A_{RCN}\} = \begin{Bmatrix} a_{ro1} \\ a_{ro2} \\ \vdots \\ a_{ron} \end{Bmatrix} = \begin{bmatrix} \cos \theta_{ro1} & \sin \theta_{ro1} & \cdots & \cos p\theta_{ro1} & \sin p\theta_{ro1} \\ \cos \theta_{ro2} & \sin \theta_{ro2} & \cdots & \cos p\theta_{ro2} & \sin p\theta_{ro2} \\ \vdots & \vdots & \ddots & \vdots & \vdots \\ \cos \theta_{ron} & \sin \theta_{ron} & \cdots & \cos p\theta_{ron} & \sin p\theta_{ron} \end{bmatrix} \begin{Bmatrix} a_{rc1} \\ a_{rc1} \\ \vdots \\ a_{rcp} \\ a_{rcp} \end{Bmatrix} =: [T_{RCN}]\{A_{RC}\} \quad (6.33)$$

where $a_{r01}, a_{r02}, \dots, a_{r0n}$ are the nodal potentials on the central circle in the rotor, $\theta_{r01}, \theta_{r02}, \dots, \theta_{r0n}$ are the angular positions of the nodes 1, 2, \dots , n respectively with respect to the rotor reference frame and $a_{rc1}, a_{rs2}, \dots, a_{rcp}, a_{rsp}$ are the Fourier components of the potential on the central circle in the rotor. So Equation (6.30) can be written as

$$\begin{bmatrix} K_{RMM} & K_{RMC} \\ K_{RCM} & K_{RCC} \end{bmatrix} \begin{Bmatrix} A_{RM} \\ A_{RCN} \end{Bmatrix} = \begin{Bmatrix} I_{RM} \\ I_{RCN} \end{Bmatrix} + \begin{Bmatrix} b_{RM} \\ b_{RCN} \end{Bmatrix} \quad (6.34)$$

Now, not every node in the rotor can carry current. In fact, the space of possible vectors, $\{I_{RM}\}$, is substantially smaller than the dimension of this vector. There is some transformation, $[T_R]$, such that

$$\{I_{RM}\} = [T_R] \{I_R\} \quad (6.35)$$

The method to form $[T_R]$ has already been explained in Chapter 4. Thus, Equation (6.34) can be written as

$$\begin{bmatrix} K_{RMM} & K_{RMC} \\ K_{RCM} & K_{RCC} \end{bmatrix} \begin{Bmatrix} A_{RM} \\ A_{RCN} \end{Bmatrix} = \begin{Bmatrix} T_R I_R \\ I_{RCN} \end{Bmatrix} + \begin{Bmatrix} b_{RM} \\ b_{RCN} \end{Bmatrix} \quad (6.36)$$

Writing $\{A_{RCN}\}$ in terms of $\{A_{RC}\}$ and from Equations (6.33) and (6.36) we obtain

$$\begin{bmatrix} K_{RMM} & K_{RMC} T_{RCN} \\ T_{RCN}^T K_{RCM} & T_{RCN}^T K_{RCC} T_{RCN} \end{bmatrix} \begin{Bmatrix} A_{RM} \\ A_{RC} \end{Bmatrix} = \begin{Bmatrix} T_R I_R \\ T_{RCN}^T I_{RCN} \end{Bmatrix} + \begin{Bmatrix} b_{RM} \\ T_{RCN}^T b_{RCN} \end{Bmatrix} \quad (6.37)$$

$\{T_{RCN}^T I_{RCN}\}$ is the vector of Fourier components of the fictitious currents at nodes on the central circle in the rotor. Replacing $\{T_{RCN}^T I_{RCN}\}$ with $\{I_{RC}\}$ we can write Equation (6.37) as

$$\begin{bmatrix} K_{RMM} & K_{RMC} T_{RCN} \\ T_{RCN}^T K_{RCM} & T_{RCN}^T K_{RCC} T_{RCN} \end{bmatrix} \begin{Bmatrix} A_{RM} \\ A_{RC} \end{Bmatrix} = \begin{Bmatrix} T_R I_R \\ I_{RC} \end{Bmatrix} + \begin{Bmatrix} b_{RM} \\ T_{RCN}^T b_{RCN} \end{Bmatrix} \quad (6.38)$$

6.5.2 Formulation for the stator

We can write the formulation for the stator similarly to that of the rotor. The instantaneous relationship between nodal potentials and nodal currents for the stator can be written as

$$[K_s]\{A_s\} \approx \{I_{SN}\} + \{b_s\} \quad (6.39)$$

where $[K_s]$ is the stiffness matrix of the stator, $\{A_s\}$ is the nodal potential vector of the stator, $\{I_{SN}\}$ is the nodal current vector of the stator and $\{b_s\}$ is the free MMF vector. $\{A_s\}$ is divided into two parts as

$$\{A_s\} = \begin{Bmatrix} A_{SM} \\ A_{SCN} \end{Bmatrix} \quad (6.40)$$

Here $\{A_{SM}\}$ contains potentials at stator nodes excluding those stator nodes on the central circle in the stator and $\{A_{SCN}\}$ contains potentials at nodes on the central circle in the stator. The nodal magnetic vector potentials on the central circle in the stator are approximated using a Fourier series. We can write this transformation as

$$\{A_{SCN}\} = [T_{SCN}]\{A_{SC}\} \quad (6.41)$$

where $\{A_{SC}\}$ is the Fourier components of the potentials on the central circle in the stator and $[T_{SCN}]$ is the transformation matrix. If the number of nodes on the central circle in the stator is q and if the number of harmonics considered is p , Equation (6.41) can be written as

$$\{A_{SCN}\} = \begin{Bmatrix} a_{si1} \\ a_{si2} \\ \vdots \\ a_{siq} \end{Bmatrix} = \begin{bmatrix} \cos \theta_{si1} & \sin \theta_{si1} & \cdots & \cos p\theta_{si1} & \sin p\theta_{si1} \\ \cos \theta_{si2} & \sin \theta_{si2} & \cdots & \cos p\theta_{si2} & \sin p\theta_{si2} \\ \vdots & \vdots & \ddots & \vdots & \vdots \\ \cos \theta_{siq} & \sin \theta_{siq} & \cdots & \cos p\theta_{siq} & \sin p\theta_{siq} \end{bmatrix} \begin{Bmatrix} a_{sc1} \\ a_{sc2} \\ \vdots \\ a_{scp} \end{Bmatrix} = [T_{SCN}]\{A_{SC}\} \quad (6.42)$$

where $a_{si1}, a_{si2}, \dots, a_{sin}$ are the nodal potentials on the central circle in the stator, $\theta_{si1}, \theta_{si2}, \dots, \theta_{sin}$, are the angular positions of the nodes 1, 2, ..., n respectively with respect to the stator reference frame and $a_{sc1}, a_{ss2}, \dots, a_{scp}, a_{ssp}$ are the Fourier components of the potentials on the central circle in the stator. Therefore, Equation (6.39) can be written as

$$\begin{bmatrix} K_{SMM} & K_{SMC} \\ K_{SCM} & K_{SCC} \end{bmatrix} \begin{Bmatrix} A_{SM} \\ A_{SCN} \end{Bmatrix} = \begin{Bmatrix} I_{SM} \\ I_{SCN} \end{Bmatrix} + \begin{Bmatrix} b_{SM} \\ b_{SCN} \end{Bmatrix} \quad (6.43)$$

Now, not every point in the stator can carry current. In fact, the space of possible vectors, $\{I_{SM}\}$, is substantially smaller than the dimension of this vector. There is some transformation, $[T_s]$, such that

$$\{I_{SM}\} = [T_s] \{I_s\} \quad (6.44)$$

The method to form $[T_s]$ has already been explained in Chapter 4. Thus, Equation (6.43) can be written as

$$\begin{bmatrix} K_{SMM} & K_{SMC} T_{SCN} \\ T_{SCN}^T K_{SCM} & T_{SCN}^T K_{SCC} T_{SCN} \end{bmatrix} \begin{Bmatrix} A_{SM} \\ A_{SCN} \end{Bmatrix} = \begin{Bmatrix} T_s I_s \\ I_{SCN} \end{Bmatrix} + \begin{Bmatrix} b_{SM} \\ b_{SCN} \end{Bmatrix} \quad (6.45)$$

Writing $\{A_{SCN}\}$ in terms of $\{A_{SC}\}$ and from Equations (6.43) and (6.45) we get

$$\begin{bmatrix} K_{SMM} & K_{SMC} T_{SCN} \\ T_{SCN}^T K_{SCM} & T_{SCN}^T K_{SCC} T_{SCN} \end{bmatrix} \begin{Bmatrix} A_{SM} \\ A_{SC} \end{Bmatrix} = \begin{Bmatrix} T_s I_s \\ T_{SCN}^T I_{SCN} \end{Bmatrix} + \begin{Bmatrix} b_{SM} \\ T_{SCN}^T b_{SCN} \end{Bmatrix} \quad (6.46)$$

$\{T_{SCN}^T I_{SCN}\}$ is the vector Fourier components of the nodal fictitious currents on the central circle in the stator. Replacing $\{T_{SCN}^T I_{SCN}\}$ with $\{I_{SC}\}$, we can write Equation (6.46) as

$$\begin{bmatrix} K_{SMM} & K_{SMC} T_{SCN} \\ T_{SCN}^T K_{SCM} & T_{SCN}^T K_{SCC} T_{SCN} \end{bmatrix} \begin{Bmatrix} A_{SM} \\ A_{SC} \end{Bmatrix} = \begin{Bmatrix} T_S I_S \\ I_{SC} \end{Bmatrix} + \begin{Bmatrix} b_{SM} \\ T_{SCN}^T b_{SCN} \end{Bmatrix} \quad (6.47)$$

6.5.3 Coupling the rotor and stator models

The stator and rotor reference frames are shown in Figure (6.4). If the angular position of the rotor is ϕ with respect to the stator reference frame, then with the appropriate transformations applied to take account of the effect of the rotation of the rotor relative to the stator,

$$\{I_{SC}\} = -[T(\phi)]\{I_{RC}\} \quad (6.48)$$

And the compatibility of the magnetic potential dictates that

$$\{A_{SC}\} = [T(\phi)]\{A_{RC}\} \quad (6.49)$$

where $[T(\phi)]$ is a simple rotation matrix comprising block 2×2 rotation matrices on its diagonal. We can write

$$\begin{Bmatrix} a_{scl} \\ a_{ssl} \\ \vdots \\ a_{scp} \\ a_{ssp} \end{Bmatrix} = \begin{bmatrix} \cos(\phi) & -\sin(\phi) & \cdots & 0 & 0 \\ \sin(\phi) & \cos(\phi) & \cdots & 0 & 0 \\ \vdots & \vdots & \ddots & \vdots & \vdots \\ 0 & 0 & \cdots & \cos(p\phi) & -\sin(p\phi) \\ 0 & 0 & \cdots & \sin(p\phi) & \cos(p\phi) \end{bmatrix} \begin{Bmatrix} a_{rc1} \\ a_{rs1} \\ \vdots \\ a_{r\phi p} \\ a_{r\psi p} \end{Bmatrix} =: [T(\phi)]\{A_{RC}\} \quad (6.50)$$

Combining Equations (6.38) and (6.47)

$$\begin{bmatrix} K_{RMM} & K_{RMC} T_{RCN} & O & O \\ T_{RCN}^T K_{RCM} & T_{RCN}^T K_{RCC} T_{RCN} & O & O \\ O & O & K_{SMM} & K_{SMC} T_{SCN} \\ O & O & T_{SCN}^T K_{SCM} & T_{SCN}^T K_{SCC} T_{SCN} \end{bmatrix} \begin{Bmatrix} A_{RM} \\ A_{RC} \\ A_{SM} \\ A_{SC} \end{Bmatrix} = \begin{Bmatrix} T_R I_R \\ I_{RC} \\ T_S I_S \\ I_{SC} \end{Bmatrix} + \begin{Bmatrix} b_{RM} \\ T_{RCN}^T b_{RC} \\ b_{SM} \\ T_{SCN}^T b_{SC} \end{Bmatrix} \quad (6.51)$$

Now

$$\begin{Bmatrix} A_{RM} \\ A_{RC} \\ A_{SM} \\ A_{SC} \end{Bmatrix} = \begin{bmatrix} I & O & O \\ O & O & I \\ O & I & O \\ O & O & T(\phi) \end{bmatrix} \begin{Bmatrix} A_{RM} \\ A_{SM} \\ A_{RC} \end{Bmatrix} =: [P(\phi)] \begin{Bmatrix} A_{RM} \\ A_{SM} \\ A_{RC} \end{Bmatrix} \quad (6.52)$$

$\{A_{RC}\}$ is the distribution of magnetic potential on the central circle in the rotor and is considered at the rotor fixed frame of reference and $[P(\phi)]$ takes care of the rotation. Applying Equations (6.51) and (6.52) and pre-multiplying by $[P(\phi)]^T$, we obtain

$$\begin{bmatrix} K_{RMM} & O & K_{RMC}T_{RCN} \\ O & K_{SMM} & K_{SMC}T_{SCN}T(\phi) \\ T_{RCN}^T K_{RCM} & T(\phi)^T T_{SCN}^T K_{SCM} & T_{RCN}^T K_{RCC}T_{RCN} + T(\phi)^T (T_{SCN}^T K_{SCC}T_{SCN})T(\phi) \end{bmatrix} \begin{Bmatrix} A_{RM} \\ A_{SM} \\ A_{RC} \end{Bmatrix} = \begin{bmatrix} T_R I_R \\ T_S I_S \\ O \end{bmatrix} + \begin{Bmatrix} b_{RM} \\ b_{SM} \\ b_{CC} \end{Bmatrix} \quad (6.53)$$

Simplifying Equation (6.53)

$$\begin{bmatrix} K_{RMM} & O & K_{RMC1} \\ O & K_{SMM} & K_{SMC1}(\phi) \\ K_{RCM1} & K_{SCM1}(\phi) & K_{CC}(\phi) \end{bmatrix} \begin{Bmatrix} A_{RM} \\ A_{SM} \\ A_{RC} \end{Bmatrix} = \begin{bmatrix} O & T_R \\ T_S & O \\ O & O \end{bmatrix} \{I_{RS}\} + \begin{Bmatrix} b_{RM} \\ b_{SM} \\ b_{CC} \end{Bmatrix} \quad (6.54)$$

$$[K_M]\{A_{z1}\} = [U_M]\{I_{RS}\} + \{b_M\} \quad (6.55)$$

where the definitions of the partitions in Equation (6.54) are evident from Equation (6.53). We now proceed to show how this formulation of the machine can be used in simulation.

6.5.4 Marginal inductance and its rate of change from non-linear finite element analysis with geometry change

Since there is geometry change here, $[K_M]$ will be a function of current and geometry change. The stiffness matrix, $[K_M]$, has to be derived at every time step. The element matrices for non-ferromagnetic materials need be derived only once except for those airgap elements which change with the motion of the rotor. Similar to Section (6.3) we can write the inductance as

$$[L_{\text{mar}}] = [U_M]^T [K_M]^{-1} [U_M] \quad (6.56)$$

The inductance matrix computation in Equation (6.56) is performed after convergence of the nonlinear magnetic field problem has been achieved, for the machine currents i.e. stator phase currents and the rotor bar currents.

Rate of change of inductance is calculated using the procedure described in Equation (6.11).

6.5.5 Marginal inductance and its rate of change from linear finite element analysis with changeable geometry

When material non-linearity is not considered, Equation (6.54) can be written as

$$\begin{bmatrix} K_{\text{RMM}} & O & K_{\text{RMC1}} \\ O & K_{\text{SMM}} & K_{\text{SMC1}}(\phi) \\ K_{\text{RCM1}} & K_{\text{SCM1}}(\phi) & K_{\text{CC}}(\phi) \end{bmatrix} \begin{Bmatrix} A_{\text{RM}} \\ A_{\text{SM}} \\ A_{\text{RC}} \end{Bmatrix} = \begin{bmatrix} T_{\text{R}} & O \\ O & T_{\text{S}} \\ O & O \end{bmatrix} \{I_{\text{RS}}\} \quad (6.57)$$

From Equation (6.57) we can write the rotor and stator magnetic potentials in terms central circle magnetic potentials as

$$\{A_{\text{RM}}\} = -[K_{\text{RMM}}]^{-1} [K_{\text{RMC}}] \{A_{\text{RC}}\} + [K_{\text{RMM}}]^{-1} [T_{\text{R}}] \{I_{\text{RS}}\} \quad (6.58)$$

$$\{A_{\text{SM}}\} = -[K_{\text{SMM}}]^{-1} [K_{\text{SMC1}}] \{A_{\text{RC}}\} + [K_{\text{SMM}}]^{-1} [T_{\text{S}}] \{I_{\text{RS}}\} \quad (6.59)$$

Finally,

$$\begin{Bmatrix} A_{\text{RM}} \\ A_{\text{SM}} \\ A_{\text{RC}} \end{Bmatrix} = \begin{bmatrix} -K_{\text{RMM}}^{-1} K_{\text{RMC}} \\ -K_{\text{SMM}}^{-1} K_{\text{SMC1}} \\ I \end{bmatrix} \{A_{\text{RC}}\} + \begin{bmatrix} K_{\text{RMM}}^{-1} T_{\text{R}} \\ K_{\text{SMM}}^{-1} T_{\text{S}} \\ O \end{bmatrix} \{I_{\text{RS}}\} \quad (6.60)$$

$$\{A_{\text{z1}}\} = [T_3] \{A_{\text{RC}}\} + [T_4] \{I_{\text{RS}}\} \quad (6.61)$$

From Equations (6.57) and (6.61) we can write

$$[K_{D2}]\{A_{RC}\} = [U_{D2}]\{I_{RS}\} \quad (6.62)$$

where

$$[K_{D2}] = ([K_{CC}] - [K_{RCM1}][K_{RMM}]^{-1}[K_{RCM1}] - [K_{SCM1}][K_{SMM}]^{-1}[K_{SMC1}]) \quad (6.63)$$

$$[U_{D2}] = -[K_{RCM1}][K_{RMM}]^{-1}[T_R] + [K_{SCM1}][K_{SMM}]^{-1}[T_S] \quad (6.64)$$

The energy stored in a magnetically coupled circuit is given by

$$E = \frac{1}{2} \{A_{z1}\}^T [K_M] \{A_{z1}\} \quad (6.65)$$

$$= \frac{1}{2} [(T_3)\{A_{RC}\} + (T_4)\{I_{RS}\}]^T [K_M] [(T_3)\{A_{RC}\} + (T_4)\{I_{RS}\}] \quad (6.66)$$

After simplification we can write Equation (6.66) as

$$E = \frac{1}{2} \{I_{RS}\}^T \left([T_R]^T [K_{RMM}]^{-1} [T_R] + [U_{D2}]^T [K_{D2}]^{-1} [U_{D2}] + [T_S]^T [K_{SMM}]^{-1} [T_S] \right) \{I_{RS}\} \quad (6.67)$$

Equation (6.67) can be compared to the stored energy of an inductor as shown in Equation (6.7). Thus, the inductance is

$$[L] = \overbrace{[T_R]^T [K_{RMM}]^{-1} [T_R]}^{T1} + \overbrace{[U_{D2}]^T [K_{D2}]^{-1} [U_{D2}]}^{T2} + \overbrace{[T_S]^T [K_{SMM}]^{-1} [T_S]}^{T3} \quad (6.68)$$

$[K_{D2}]$ and $[U_{D2}]$ in Equations (6.63) and (6.64) respectively can be expanded as

$$[K_{D2}] = \begin{bmatrix} [T_{RCN}]^T [K_{RCC}] [T_{RCN}] \\ + [T(\phi)]^T ([T_{SCN}]^T [K_{SCC}] [T_{SCN}]) T(\phi) \\ - [T_{RCN}]^T [K_{RCM}] [K_{RMM}]^{-1} [K_{RMC}] [T_{RCN}] \\ - T(\phi)^T [T_{SCN}]^T [K_{SCM}] [K_{SMM}]^{-1} [K_{SMC}] [T_{SCN}] T(\phi) \end{bmatrix} \quad (6.69)$$

$$[U_{D2}] = -([T_{RCN}]^T [K_{RCM}] [K_{RMM}]^{-1} [T_R] + T(\phi)^T [T_{SCN}]^T [K_{SCM}] [K_{SMM}]^{-1} [T_s]) \quad (6.70)$$

The first, $T1$ and third, $T3$, terms of Equation (6.68) are independent of rotor position, so they are calculated only once. The second term, $T2$ depends on the rotor position. Therefore, only the rotation matrix, $[T(\phi)]$ is derived at every time step of the simulation. Unlike the airgap stitching method the element matrices do not need to be derived at every time step. For the linear analysis the rate of change of inductance i.e. $\frac{d[L]}{dt}$ is calculated simply by differentiating Equation (6.68). From Equation (6.68)

$$\frac{d[L]}{dt} = [U_{D2}]^T \frac{d[K_{D2}]}{dt} [U_{D2}] \quad (6.71)$$

But

$$\frac{d[K_{D2}]}{dt} = -[K_{D2}]^{-1} \frac{d[K_{D2}]}{dt} [K_{D2}]^{-1} \quad (6.72)$$

So,

$$\frac{d[L]}{dt} = -([K_{D2}]^{-1} [U_{D2}])^T \frac{d[K_{D2}]}{dt} ([K_{D2}]^{-1} [U_{D2}]) \quad (6.73)$$

From Equation (6.69) $\frac{d[K_{D2}]}{dt}$ can be easily calculated. As already we have calculated the term $([K_{D2}]^{-1} [U_{D2}])$ while calculating the inductance, using Equation (6.72) we can save substantial amount of time.

6.6 Case studies

The case study described here presents the steady state currents for a typical electrical machine from the methods discussed in Sections (6.4) and (6.5). The case study is to compare the steady state currents of a typical electrical machine from the airgap

stitching and the central circle method. The main parameters of the induction machine are given in Table 6.1.

The machine considered is a 4-pole, 3-phase induction motor wound with double layered windings. The stator of this machine has three independent currents. The number of rotor bars is 32. If five modes of conductance are considered for the rotor bar and the number of harmonics for the Fourier approximation of the rotor bar is also five, the transformations in Chapter 4 leads to a total of 44 independent rotor currents. The stator and rotor currents can be written as

$$\{I_{RS}\} = \left\{ \begin{array}{cccccc} \text{Stator currents} & \text{Rotor currents (DC components)} & \text{Rotor currents (1st harmonics, cos)} & \text{Rotor currents (1st harmonics, sin)} & \text{Rotor currents (2nd harmonics, cos)} & \text{Rotor currents (2nd harmonics, sin)} \\ i_1 & \dots & i_3 & i_4 & \dots & i_7 & i_8 & \dots & i_{12} & i_{13} & \dots & i_{17} & i_{18} & \dots & i_{23} & i_{23} & \dots & i_{27} & \dots & i_{47} \end{array} \right\} \quad (6.74)$$

here i_1, \dots, i_3 are the three stator currents, i_4, \dots, i_7 are the DC components of the rotor currents, i_8, \dots, i_{12} are the cosine components of the first harmonics of the rotor currents and so on. For the airgap stitching method the airgap is divided into three bands and two bands are attached to the stator. The stator and rotor of the machine are modelled separately with 8-noded quadrilateral finite elements. Outer band of the rotor is combined with the inner band of the stator by stitching using triangular element airgap elements to take care of the relative movement between the stator and rotor. Figure (6.3) shows one quarter of a machine cross-section where the stator and rotor are discretized with 4-noded quadrilateral finite elements and airgap is stitched with triangular elements. For the central circle method the airgap is divided into two parts by a central circle passing through the middle of the airgap. One half of the airgap is attached to the rotor and the other half of the airgap is attached to the stator. The stator and rotor of the machine are modelled separately with 8-noded quadrilateral finite elements. The stator and rotor are combined at the central circle to take care of the relative movement between these two by applying constraints.

Figure (6.5) shows the three stator currents from the linear and non-linear FEA by airgap stitching method for the case where the slip is 10% and supply voltage is 20 V. Figure (6.6) shows the two rotor currents (shown as i_{18} and i_{23} in Equation (6.74)) from the linear and non-linear FEA by airgap stitching method. The steady state currents are calculated using the linear FEA from time 0 to 0.2 sec. Considering these currents as initial guess the steady state currents are calculated from the non-linear FEA from time 0.2 to 0.3 sec.

Figure (6.7) shows the three stator currents computed from the linear and non-linear FEA by central circle method for the same slip (10%) and same supply voltage (20 V). Figure (6.8) shows the two rotor currents (shown as i_{18} and i_{23} in Equation (6.74)) from the linear and non-linear FEA by central circle method. From time 0 to 0.2 sec the currents calculated from linear FEA. Similar to the airgap stitching method, the steady state currents are calculated using the linear FEA from time 0 to 0.2 sec. Considering these currents as initial guess the steady state currents are calculated from the non-linear FEA from time 0.2 to 0.3 sec. For the results presented in Figures from (6.5) to (6.8), it is seen that the results of airgap stitching method and central circle method match very well with each other.

For the linear FEA case the central circle method is computationally more efficient than airgap stitching method because in case of central circle method no element derivation is required during the simulation.

For the non-linear FEA element matrices are required to be derived at every time step of the simulation. The airgap stitching method is computationally more effective than central circle method because sparsity is reduced in case if central circle method.

6.7 Conclusions

Two general methods for calculating steady state currents of an induction motor are discussed in this chapter. One case study is presented where the steady state currents are calculated using these two methods. It makes a huge difference in terms of

computational time if non-linearity due to magnetic saturation of the iron cores is considered in the calculations.

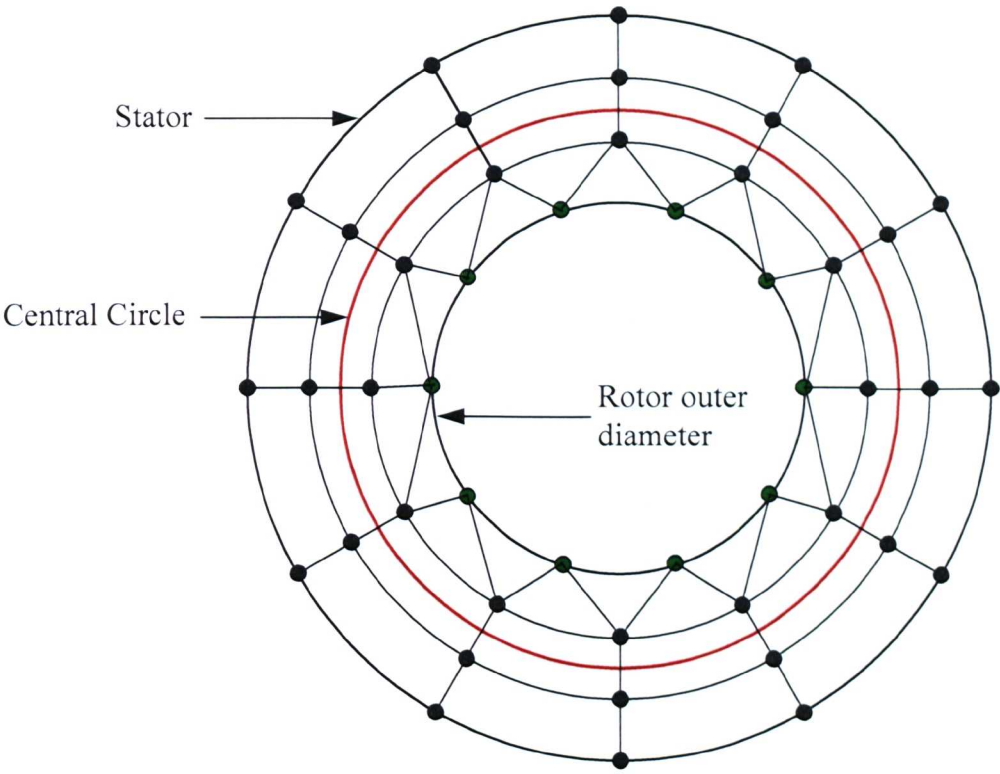


Figure (6.1): Rotor movement modeling by the airgap stitching method

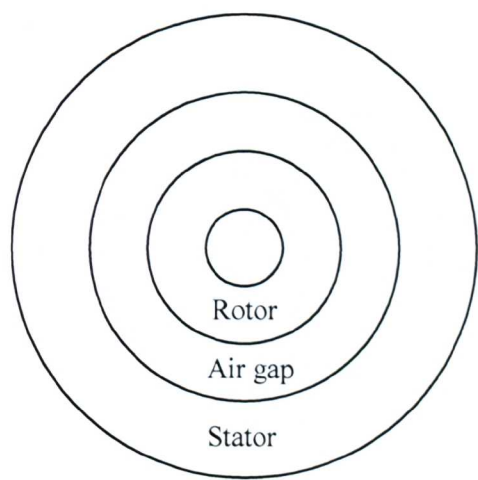


Figure (6.2): Rotor movement modeling by the central circle method

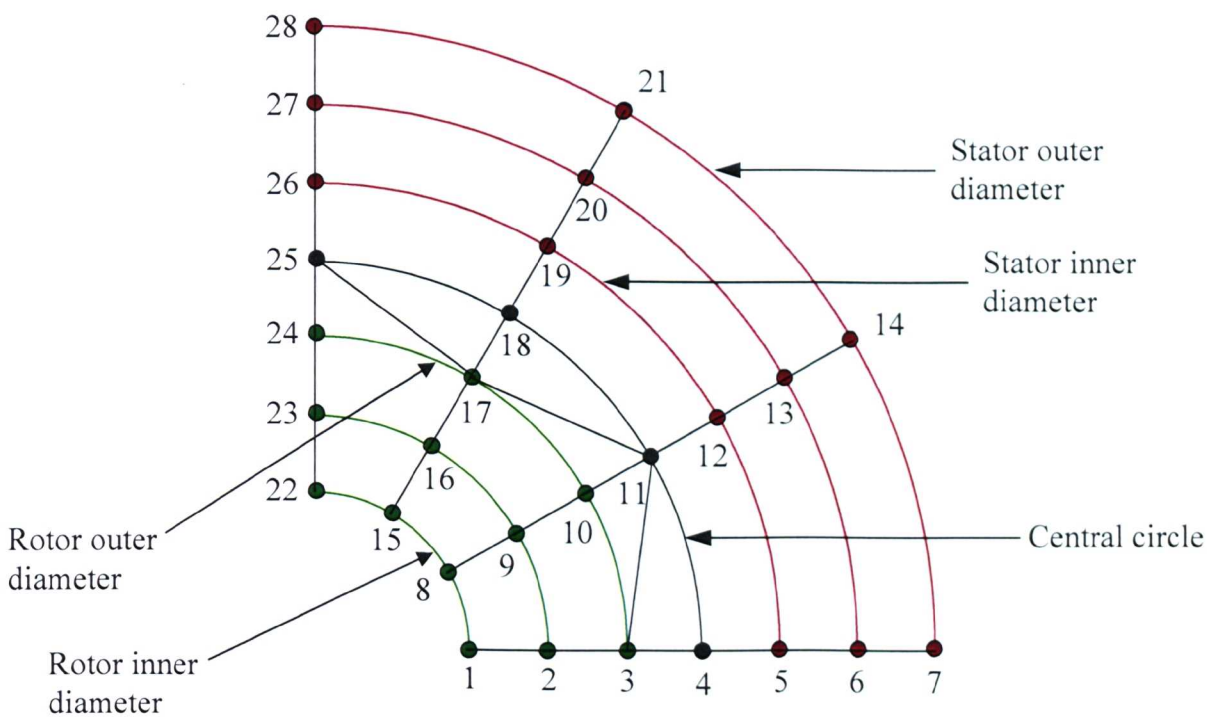


Figure (6.3): One quarter of an electric machine discretized with 4-noded quadrilateral and 3-noded triangular finite elements

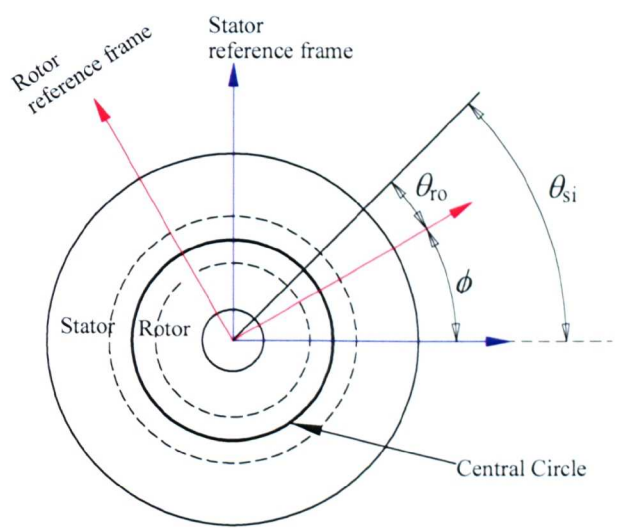


Figure (6.4): Rotor and stator with common central circle

Table (6.1): Main electromagnetic parameters of the machine

Parameters	Value
Number of poles	4
Number of phase	3
Number of stator slots	36
Outer diameter of the stator [mm]	152
Inner diameter of the stator [mm]	90
Number of rotor slots	32
Outer diameter of the rotor [mm]	89.2
Air gap radial thickness [mm]	0.4
Length of the rotor [mm]	123
Rated voltage [V]	415
Rated frequency [Hz]	50
Rated power [kW]	2

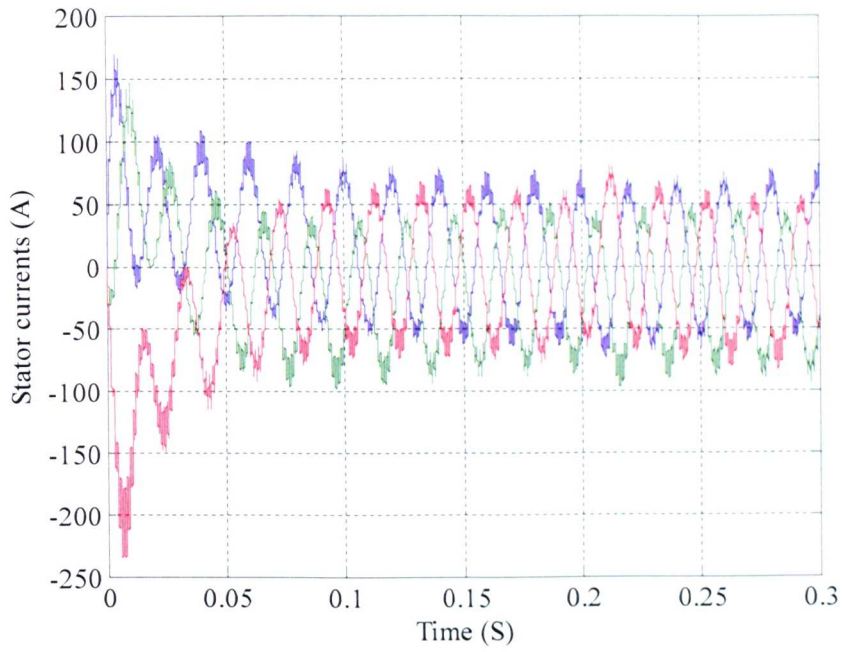


Figure (6.5): Stator currents of an induction machine by the airgap stitching method when slip = 10% and supply voltage = 20V

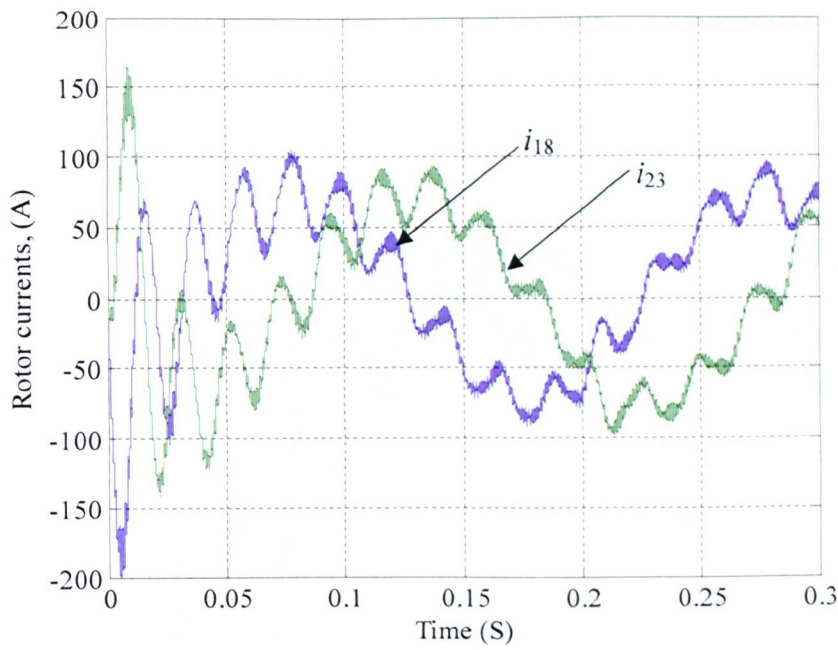


Figure (6.6): Rotor currents of an induction machine by the airgap stitching method when slip = 10% and supply voltage = 20V

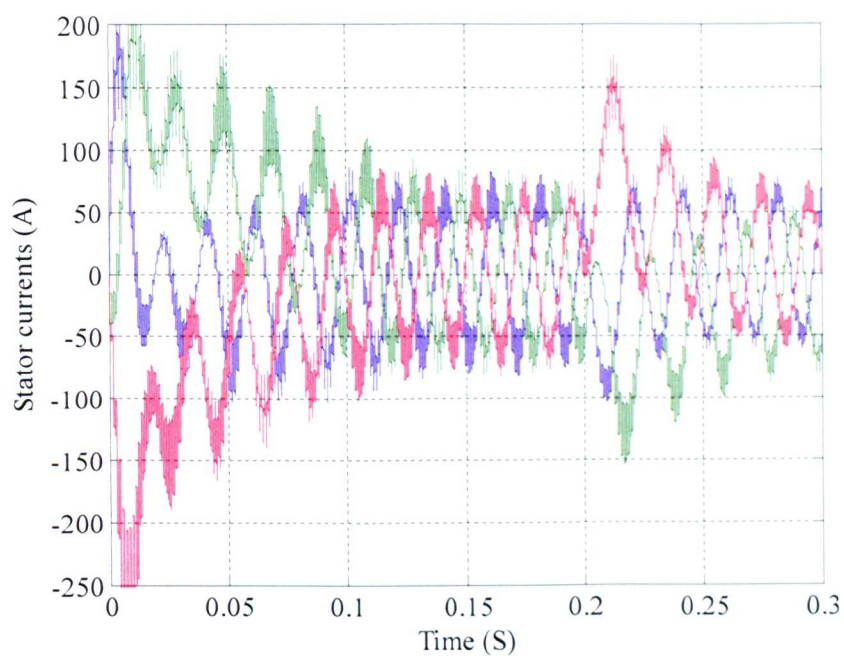


Figure (6.7): Stator currents of an induction machine by the central circle method when slip = 10% and supply voltage = 20V

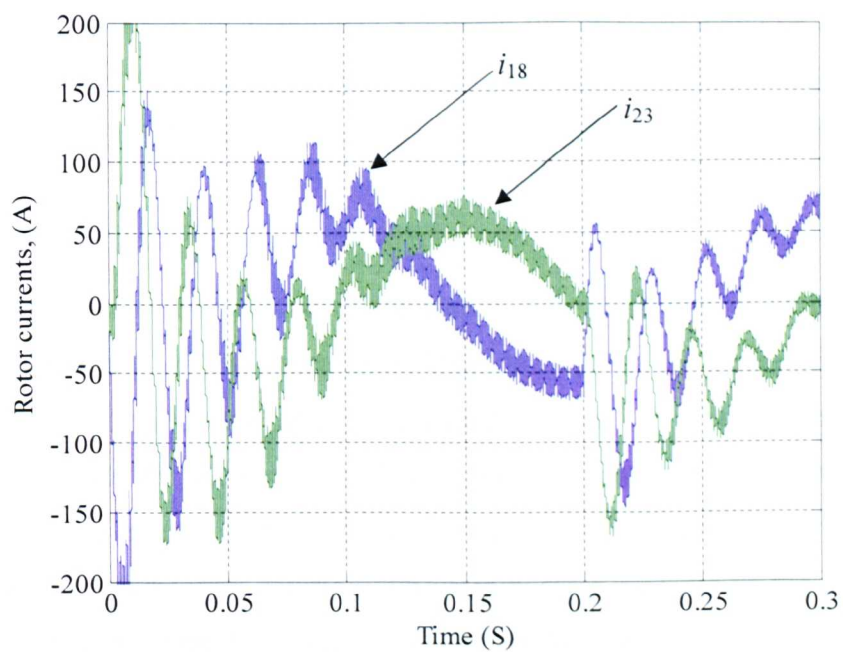


Figure (6.8): Rotor currents of an induction machine by the central circle method when slip = 10% and supply voltage = 20V

Chapter Seven

Method of Calculating Steady State Solutions for Induction Machines

7.1 Introduction

Any induction machine fed from a balanced sinusoidal supply with known voltage and frequency and constrained such that the rotor rotates at a constant speed about the geometric centre will develop periodic machine currents in both the rotor and stator and a fairly steady airgap torque. The machine will also attain an equilibrium thermal state and equilibrium torque losses from friction and windage. The determination of these machine states (currents, torques and temperature-rises above ambient) is an important capability in the design of the machine. Knowing the rotational speed and the net torque (airgap torque less the sum of friction and windage loss torques), the output mechanical power can be calculated. Knowing the periodic machine currents, the machine designer can also calculate the net real input power, the harmonic distortion fed into the supply and the reactive power. The net machine efficiency follows.

This chapter addresses the computation of the steady-state behaviour of an induction machine. The importance of this calculation extends beyond the determination of machine efficiency, power-factor and temperature-rise etc. The entire approach advocated in this thesis for the rotordynamic analysis of induction machines (and indeed for any rotating electrical machine) is based on linearisation of the machine dynamics around the steady-state solution. The steady-state currents of the machine are the quantities of interest for this purpose. If we have knowledge of these for every instant, then we can perform a magneto-static 2D FE computation to determine the complete state of flux within the machine.

At first sight, it appears (at least conceptually) straightforward to determine the steady-state of a machine by doing a time-marching simulation and simply continuing this until all transient effects have died down. Three distinct difficulties arise in this. The first difficulty is that the motion of the rotor relative to the stator must be captured. The second difficulty is that all practical (iron-bearing) machine designs operate with at least some of the iron being partially saturated magnetically. The third difficulty is that the equations may be mathematically stiff with the result that the computational time taken to carry out the simulation can be very long.

In this chapter one very novel method of calculating steady state solution of an induction machine is explained. The newly proposed method calculates the stator and rotor currents of an induction machine taking the material nonlinearity into account but without requiring that the complete set of element matrices be calculated each time step. In other methods the element matrices for all saturable elements in the in the model are calculated.

7.2 Available approaches to calculate steady state solution

There are many ways to calculate the steady state currents of an induction machine. One option is to perform the full non-linear time domain simulation using the methods prescribed in Chapter 6. These methods are computationally very expensive. Another option is to solve the linear problem in time domain to steady state. Examine one period of the steady state. Modify the permeability at every Gauss point in the element based on the rms flux density at that point. Then solve linear problem again. This process can be solved iteratively until a converged result is reached. One main disadvantage of this method is that the final solution has constant permeability. Despite many recent advances, electrical machine modelling using finite element can be computationally very expensive (Rodger *et. al.*, 2004). Several techniques are put forwarded by Rodger *et. al* (2004). One of their techniques is to use the previous answer as starting points. A torque speed curve is generated for the higher speeds first and used the results as the initial guess for the lower speeds. They have observed that this method is four times faster than a conventional method. Another method for

speeding up the calculation of torque speed curve by shaping the applied voltage waveform in order to reduce the initial transient effects of switching the excitation on.

7.3 Central circle method with non-linear model reduction

Section (6.5) of Chapter 6 discusses the general features of central circle method and outlined its advantages over the airgap stitching method. One of the main features of the central circle method is that while analyzing electric machines the relative movement between the rotor and stator can be modelled very efficiently using the central circle method. Other features includes the calculation of inductance matrix considering no geometry change as well as geometry change from linear FEA and the calculation of inductance matrix considering no geometry change as well as geometry change from non-linear FEA. These features are similar to the airgap stitching method and discussed in detail in Section (6.4). One disadvantage of central circle, which might occur in calculation of inductance matrix from non-linear FEA, is that it may reduce the sparsity of the stiffness matrix if the number of harmonics is large.

This section discusses another feature of central circle method. Section (6.5) discusses the calculation of inductance matrix from nonlinear FEA using airgap stitching method and central circle method. During the process of simulation to calculate the steady state currents of an induction machine this inductance matrix and its rate of change also, if there is geometry change, have to be calculated several times at every time step. To solve the differential equation [Equation (6.4)] an ode45 routine of MATLABTM is used. The ode45 routine integrates a system of ordinary differential equations using the 4th and 5th order embedded formulas from Dormand and Prince or Fehlberg. This requires 6 function evaluations per integration step. The element matrices for the ferromagnetic materials need to be derived afresh few times at each of this function evaluation to calculate the conversed values of permeabilities from the $B(H)$ curve. This process is very time consuming as permeability of each node depends on its nodal excitation. The method presented here overcomes this by reducing the dependency for non-linearity. The stiffness matrices for the stator and rotor are derived separately and the stiffness for the stator and rotor is derived as a nonlinear function of the magnetic potentials at the central circle.

7.3.1 Formulation of the rotor

Applying Equation (3.59) to the specific case of the rotor we can write

$$[K_R]\{A_R\} \approx \{I_{RN}\} + \{b_R\} \quad (7.1)$$

where $[K_R]$ is the stiffness matrix in the rotor, $\{A_R\}$ is the nodal potential vector in the rotor, $\{I_{RN}\}$ is the nodal current vector in the rotor and $\{b_R\}$ is the nodal free MMF vector in the rotor. Vectors $\{A_R\}$ and $\{I_{RN}\}$ are divided into two parts as

$$\{A_R\} = \begin{Bmatrix} A_{RM} \\ A_{RCN} \end{Bmatrix} \text{ and } \{I_R\} = \begin{Bmatrix} I_{RM} \\ I_{RCN} \end{Bmatrix} \quad (7.2)$$

Here $\{A_{RM}\}$ contains potentials at rotor nodes excluding those rotor nodes at the central circle, $\{A_{RCN}\}$ contains potentials at nodes on the central circle in the rotor, $\{I_{RM}\}$ contains currents at rotor nodes excluding those rotor nodes on the central circle in the rotor, $\{I_{RCN}\}$ contains currents at nodes on the central circle in the rotor Using Equation (7.2) we can write Equation (7.1) as

$$\begin{bmatrix} K_{RMM} & K_{RMC} \\ K_{RCM} & K_{RCN} \end{bmatrix} \begin{Bmatrix} A_{RM} \\ A_{RCN} \end{Bmatrix} = \begin{Bmatrix} I_{RM} \\ I_{RCN} \end{Bmatrix} + \begin{Bmatrix} b_{RM} \\ b_{RC} \end{Bmatrix} \quad (7.3)$$

Here $\{b_{RM}\}$ contains free MMF at rotor nodes excluding those rotor nodes on the central circle in the rotor and $\{b_{RC}\}$ contains free MMF at nodes on the central circle in the rotor.

The nodal magnetic vector potentials at the central circle in the rotor are approximated using a Fourier series. We can write this transformation as

$$\{A_{RCN}\} = [T_{RCN}]\{A_{RC}\} \quad (7.4)$$

where $\{A_{RC}\}$ is the Fourier components of the potential on the central circle in the rotor and $[T_{RCN}]$ is the transformation matrix. Section (6.5.1) explains how $[T_{RCN}]$ is constructed.

Not every point in the rotor can carry current. In fact, the space of possible current vectors, $\{I_{RM}\}$, is substantially smaller than the dimension of this vector. There is some transformation matrix, $[T_R]$, such that

$$\{I_{RM}\} = [T_R] \{I_R\} \quad (7.5)$$

where $\{I_R\}$ is the reduced vector of rotor bar currents [refer Section 4.4]. We are interested in the calculation of the marginal inductance from the solution of the magnetic field. Now the combinations of nodal potentials in the rotor which are orthogonal to $[T_R]$ are of no direct significance to us. It will be convenient to write

$$\begin{Bmatrix} A_{RM} \\ A_{RCN} \end{Bmatrix} = \begin{bmatrix} T_R & V_R & O \\ O & O & T_{RCN} \end{bmatrix} \begin{Bmatrix} A_{RB} \\ A_{RO} \\ A_{RC} \end{Bmatrix} =: [X_R] \begin{Bmatrix} A_{RB} \\ A_{RO} \\ A_{RC} \end{Bmatrix} \quad (7.6)$$

where $[V_R]$ is a matrix spanning the space orthogonal to $[T_R]$. $\{A_{RB}\}$ contains magnetic potentials at current carrying nodes excluding nodes on the central circle, $\{A_{RO}\}$ contains potentials at rotor nodes, which do not carry currents, excluding nodes on the central circle. Using Equations (7.3) and (7.6) and pre-multiplying by $[X_R]^T$ we obtain

$$\begin{bmatrix} T_R^T K_{RMM} T_R & T_R^T K_{RMM} V_R & T_R^T K_{RMC} T_{RCN} \\ V_R^T K_{RMM} T_R & V_R^T K_{RMM} V_R & V_R^T K_{RMC} T_{RCN} \\ T_{RCN}^T K_{RCM} T_R & T_{RCN}^T K_{RCM} V_R & T_{RCN}^T K_{RCC} T_{RCN} \end{bmatrix} \begin{Bmatrix} A_{RB} \\ A_{RO} \\ A_{RC} \end{Bmatrix} = \begin{bmatrix} T_R^T T_R I_R \\ O \\ T_{RCN}^T I_{RCN} \end{bmatrix} + \begin{bmatrix} T_R^T b_{RM} \\ V_R^T b_{RM} \\ T_{RCN}^T b_{RC} \end{bmatrix} \quad (7.7)$$

Writing Equation (7.7) in simple form and replacing $[T_{RCN}] \{I_{RCN}\}$ with $\{I_{RC}\}$

$$\begin{bmatrix} K_{RBB} & K_{RBO} & K_{RBC} \\ K_{ROB} & K_{ROO} & K_{ROC} \\ K_{RCB} & K_{RCO} & K_{RCC2} \end{bmatrix} \begin{Bmatrix} A_{RB} \\ A_{RO} \\ A_{RC} \end{Bmatrix} = \begin{bmatrix} T_R^T T_R I_R \\ O \\ I_{RC} \end{bmatrix} + \begin{bmatrix} T_R^T b_{RM} \\ V_R^T b_{RM} \\ T_{RCN}^T b_{RC} \end{bmatrix} \quad (7.8)$$

where the definitions of the partitions are obvious from comparing Equations (7.7) and (7.8). From Equation (7.8) the potentials at rotor nodes can be written in terms of the potentials at current carrying rotor nodes as

$$\begin{bmatrix} (K_{RBB} - K_{RBO} K_{ROO}^{-1} K_{ROB}) & (K_{RBC} - K_{RBO} K_{ROO}^{-1} K_{ROC}) \\ (K_{RCB} - K_{RCO} K_{ROO}^{-1} K_{ROB}) & (K_{RCC2} - K_{RCO} K_{ROO}^{-1} K_{ROC}) \end{bmatrix} \begin{Bmatrix} A_{RB} \\ A_{RC} \end{Bmatrix} = \begin{bmatrix} T_R^T T_R & O \\ O & I \end{bmatrix} \begin{Bmatrix} I_R \\ I_{RC} \end{Bmatrix} + \begin{bmatrix} T_R^T b_{RM} - K_{RBO} K_{ROO}^{-1} V_R^T b_{RM} \\ T_{RCN}^T b_{RC} - K_{RCO} K_{ROO}^{-1} V_R^T b_{RM} \end{bmatrix} \quad (7.9)$$

Equation (7.9) can be simplified to

$$\begin{bmatrix} K_{RUU} & K_{RUC} \\ K_{RCU} & K_{RCC} \end{bmatrix} \begin{Bmatrix} A_{RB} \\ A_{RC} \end{Bmatrix} = \begin{bmatrix} T_R^T T_R & O \\ O & I \end{bmatrix} \begin{Bmatrix} I_R \\ I_{RC} \end{Bmatrix} + \begin{Bmatrix} b_{RB} \\ b_{RC} \end{Bmatrix} \quad (7.10)$$

where the definitions of partitions in Equation (7.10) are clear from Equations (7.9) and (7.10).

7.3.2 Formulation of the stator

Similar to the rotor Equation (3.59) can be written for the stator as

$$[K_S] \{A_S\} \approx \{I_{SN}\} + \{b_S\} \quad (7.11)$$

where $[K_S]$ is the stiffness matrix in the stator, $\{A_S\}$ is the nodal potential vector in the stator, $\{I_{SN}\}$ is the nodal current vector in the stator and $\{b_S\}$ is the nodal free MMF vector in the stator. Vectors $\{A_S\}$ and $\{I_{SN}\}$ is divided into two parts as

$$\{A_s\} = \begin{Bmatrix} A_{SM} \\ A_{SCN} \end{Bmatrix} \text{ and } \{I_{SN}\} = \begin{Bmatrix} I_{SM} \\ I_{SCN} \end{Bmatrix} \quad (7.12)$$

Here $\{A_{SM}\}$ contains potentials at stator nodes excluding those stator nodes at the central circle, $\{A_{SCN}\}$ contains potentials at nodes on the central circle in the stator, $\{I_{SM}\}$ contains currents at stator nodes excluding those stator nodes on the central circle in the stator and $\{I_{SCN}\}$ contains currents at nodes on the central circle in the stator. Using Equation (7.12) we can write Equation (7.11) as

$$\begin{bmatrix} K_{SMM} & K_{SMC} \\ K_{SCM} & K_{SCC1} \end{bmatrix} \begin{Bmatrix} A_{SM} \\ A_{SCN} \end{Bmatrix} = \begin{Bmatrix} I_{SM} \\ I_{SCN} \end{Bmatrix} + \begin{Bmatrix} b_{SM} \\ b_{SC} \end{Bmatrix} \quad (7.13)$$

Here $\{b_{SM}\}$ contains free MMF at stator nodes excluding those stator nodes on the central circle in the stator and $\{b_{SC}\}$ contains free MMF at nodes on the central circle in the stator. The nodal magnetic vector potentials at the central circle in the stator are approximated using a Fourier series. We can write this transformation as

$$\{A_{SCN}\} = [T_{SCN}] \{A_{SC}\} \quad (7.14)$$

where $\{A_{SC}\}$ is the vector of Fourier components of the potential on the central circle in the stator and $[T_{SCN}]$ is the transformation matrix. Section (6.5.2) explains how $[T_{SCN}]$ is constructed.

Similar to the rotor, not every point in the stator can carry current. In fact, the space of possible current vectors, $\{I_{SM}\}$, is substantially smaller than the dimension of this vector. There is some transformation matrix, $[T_s]$, such that

$$\{I_{SM}\} = [T_s] \{I_s\} \quad (7.15)$$

where $\{I_s\}$ is the reduced vector of stator phase currents [refer Section (4.3)]. We are interested in the calculation of marginal inductance from the solution of magnetic field. Now the combinations of nodal potentials in the stator which are orthogonal to $[T_s]$ are of no direct significance to us. It will be convenient to write

$$\begin{Bmatrix} A_{SM} \\ A_{SCN} \end{Bmatrix} = \begin{bmatrix} T_s & V_s & O \\ O & O & T_{SCN} \end{bmatrix} \begin{Bmatrix} A_{SB} \\ A_{SO} \\ A_{SC} \end{Bmatrix} \quad (7.16)$$

where $[V_s]$ is a matrix spanning the space orthogonal to $[T_s]$. $\{A_{SB}\}$ contains magnetic potentials at current carrying nodes excluding nodes on the central circle, $\{A_{SO}\}$ contains potentials at stator nodes, which do not carry currents, excluding nodes on the central circle. Using Equations (7.13) and (7.16) and pre-multiplying by $[X_s]^T$ we obtain

$$\begin{bmatrix} T_s^T K_{SMM} T_s & T_s^T K_{SMM} V_s & T_s^T K_{SMC} T_{SCN} \\ V_s^T K_{SMM} T_s & V_s^T K_{SMM} V_s & V_s^T K_{SMC} T_{SCN} \\ T_{SCN}^T K_{SCM} T_s & T_{SCN}^T K_{SCM} V_s & T_{SCN}^T K_{SCC1} T_{SCN} \end{bmatrix} \begin{Bmatrix} A_{SB} \\ A_{SO} \\ A_{SC} \end{Bmatrix} = \begin{bmatrix} T_s^T T_s I_s \\ O \\ T_{SCN}^T I_{SCN} \end{bmatrix} + \begin{bmatrix} T_s^T b_{SM} \\ V_s^T b_{SM} \\ T_{SCN}^T b_{SC} \end{bmatrix} \quad (7.17)$$

Writing Equation (7.17) in simple form and replacing $[T_{SCN}]^T \{I_{SCN}\}$ with $\{I_{SC}\}$

$$\begin{bmatrix} K_{SBB} & K_{SBO} & K_{SBC} \\ K_{SOB} & K_{SOO} & K_{SOC} \\ K_{SCB} & K_{SCO} & K_{SCC2} \end{bmatrix} \begin{Bmatrix} A_{SB} \\ A_{SO} \\ A_{SC} \end{Bmatrix} = \begin{bmatrix} T_s^T T_s I_s \\ O \\ I_{SC} \end{bmatrix} + \begin{bmatrix} T_s^T b_{SM} \\ V_s^T b_{SM} \\ T_{SCN}^T b_{SC} \end{bmatrix} \quad (7.18)$$

where the definitions of the partitions are obvious from comparing Equations (7.17) and (7.18).

From Equation (7.18) the potentials at stator nodes can be written in terms of the potentials at current carrying stator nodes as

$$\begin{bmatrix} (K_{SBB} - K_{SBO}K_{SOO}^{-1}K_{SOB}) & (K_{SBC} - K_{SBO}K_{SOO}^{-1}K_{SOC}) \\ (K_{SCB} - K_{SCO}K_{SOO}^{-1}K_{SOB}) & (K_{SCC} - K_{SCO}K_{SOO}^{-1}K_{SOC}) \end{bmatrix} \begin{bmatrix} A_{SB} \\ A_{SC} \end{bmatrix} = \begin{bmatrix} T_s^T T_s & O \\ O & I \end{bmatrix} \begin{bmatrix} I_s \\ I_{sc} \end{bmatrix} + \begin{bmatrix} T_s^T b_{SM} - K_{SBO}K_{SOO}^{-1}V_s^T b_{SM} \\ T_{scN}^T b_{SC} - K_{SCO}K_{SOO}^{-1}V_s^T b_{SM} \end{bmatrix} \quad (7.19)$$

Equation (7.19) can be simplified to

$$\begin{bmatrix} K_{SUU} & K_{SUC} \\ K_{SCU} & K_{SCC} \end{bmatrix} \begin{bmatrix} A_{SB} \\ A_{SC} \end{bmatrix} = \begin{bmatrix} T_s^T T_s & O \\ O & I \end{bmatrix} \begin{bmatrix} I_s \\ I_{sc} \end{bmatrix} + \begin{bmatrix} b_{SB} \\ b_{SC} \end{bmatrix} \quad (7.20)$$

where the definitions of partitions in Equation (7.20) are clear from comparing Equations (7.19) and (7.20).

7.3.3 Coupling the rotor and stator models and accounting for the non-linearity

Combining Equations (7.10) and (7.20) we can write

$$\begin{bmatrix} K_{RUU} & K_{RUC} & O & O \\ K_{RCU} & K_{RCC} & O & O \\ O & O & K_{SUU} & K_{SUC} \\ O & O & K_{SCU} & K_{SCC} \end{bmatrix} \begin{bmatrix} A_{RB} \\ A_{RC} \\ A_{SB} \\ A_{SC} \end{bmatrix} = \begin{bmatrix} T_r^T T_r & O & O & O \\ O & I & O & O \\ O & O & T_s^T T_s & O \\ O & O & O & I \end{bmatrix} \begin{bmatrix} I_r \\ I_{rc} \\ I_s \\ I_{sc} \end{bmatrix} + \begin{bmatrix} b_{RB} \\ b_{RC} \\ b_{SB} \\ b_{SC} \end{bmatrix} \quad (7.21)$$

Now

$$\begin{bmatrix} A_{RB} \\ A_{RC} \\ A_{SB} \\ A_{SC} \end{bmatrix} = \begin{bmatrix} I & O & O \\ O & O & I \\ O & I & O \\ O & O & T(\phi) \end{bmatrix} \begin{bmatrix} A_{RB} \\ A_{RC} \\ A_{SB} \\ A_{SC} \end{bmatrix} =: [P(\phi)] \begin{bmatrix} A_{RB} \\ A_{RC} \\ A_{SB} \\ A_{SC} \end{bmatrix} \quad (7.22)$$

where $[A_{RC}]$ is the distribution of magnetic potential on the central circle in the rotor and considered at the rotor fixed frame of reference and $[P(\phi)]$ takes care of the rotation. Applying Equations (7.21) and (7.22) and pre-multiplying by $[P(\phi)]^T$, we obtain

$$\begin{bmatrix} K_{RUU} & O & K_{RUC} \\ O & K_{SUU} & K_{SUC}T(\phi) \\ K_{RCU} & T(\phi)^TK_{SCU} & K_{RCC} + T(\phi)^T(K_{SCC})T(\phi) \end{bmatrix} \begin{Bmatrix} A_{RB} \\ A_{SB} \\ A_{RC} \end{Bmatrix} = \begin{bmatrix} O & T_R^T T_R \\ T_S^T T_S & O \\ O & O \end{bmatrix} \begin{bmatrix} I_S \\ I_R \\ O \end{bmatrix} + \begin{Bmatrix} b_{RB} \\ b_{SB} \\ b_{RC} + T(\phi)^T b_{RC} \end{Bmatrix} \quad (7.23)$$

$$\text{or} \quad [K_x]\{A_x\} = [U_x]\{I_{RS}\} + \{b_x\} \quad (7.24)$$

where $[K_x]$ is the reduced stiffness matrix of the rotor and stator and is a function of the nodal potentials, $\{A_x\}$ is the vector of potentials at current carrying nodes in the rotor and stator and Fourier components of potentials on the central circle in the rotor, $\{I_{RS}\}$ is the reduced stator and rotor bar currents and Fourier components of currents on the central circle in the rotor and $\{b_x\}$ is the vector of reduced free MMFs at the rotor and stator nodes and Fourier components of free MMFs on the central circle in the rotor. Differentiating the above

$$[K_x]\{\Delta A_x\} + [\Delta K_x]\{A_x\} = \{\Delta I_{RS}\} + \{\Delta b_x\} \quad (7.25)$$

The term, $[\Delta K_x]$ consists of two parts i.e. one from the change of the machine geometry and the other from the change of material permeability because of magnetic saturation. We can write $[\Delta K_x]$ as

$$[\Delta K_x] = [\Delta K_{xrp}] + [\Delta K_{xnl}] \quad (7.26)$$

where $[\Delta K_{xrp}]$ and $[\Delta K_{xnl}]$ correspond to the changes of $[K_x]$ from the machine geometry and from the non-linearity respectively. From Equations (7.25) and (7.26) we can write as

$$[K_x]\{\Delta A_x\} + [\Delta K_{xrp}]\{A_x\} + [\Delta K_{xnl}]\{A_x\} = \{\Delta I_{RS}\} + \{\Delta b_x\} \quad (7.27)$$

The terms $[\Delta K_{xnl}]\{A_x\}$ and $\{\Delta b_x\}$ are equivalent by definition. The above equation simplifies to

$$[K_x]\{\Delta A_x\} + [\Delta K_{xrp}]\{A_x\} = \{\Delta I_{RS}\} \quad (7.28)$$

There are two discrete regions in the model namely the rotor and the stator. The finite element representations of these two regions are derived separately. These representations of the rotor and stator are combined to take care of the rotation by applying the transformation matrix $[T(\phi)]$, which depends on the rotor and stator relative positions. In the time domain Equation (7.28) becomes

$$[K_x] \frac{d\{A_x\}}{dt} + \frac{d[K_{xrp}]}{dt} \{A_x\} = \frac{d\{I_{RS}\}}{dt} \quad (7.29)$$

Along with Equation (6.4), Equation (7.29) is also integrated at every time step to calculate $\{A_x\}$. The next subsection shows how we can find the nonlinear stiffness matrix if the Fourier coefficients of the potentials on the central circle are known.

The full nonlinear stiffness matrix, $[K_x]$ in Equation (7.29), is function of the nodal magnetic vector potentials and the nodal vector potentials varies with the slip frequency in the rotor and with the supply frequency in the stator. The saturation modulates the rotor stiffness matrix at twice the slip frequency and modulates the stator stiffness matrix at twice the supply frequency. This is because the modulation is dependent on the absolute value of the flux density.

The reduced stiffness matrices for the rotor and the stator [refer to Equations (7.10) and (7.20) respectively] are approximated as functions of magnetic vector potentials in the central circle. Once the nonlinear stiffness matrices are approximated the inductance matrix can be calculated as explained in the previous sections. More details about this are explained with examples in the next sections.

7.3.3.1 Method I of accounting for non-linearity

In method I it is assumed that the reduced stiffness matrices for the rotor and the stator are functions of the radial component of magnetic vector potentials in the

central circle only. The Fourier coefficients of the radial component of magnetic flux density in the central circle from the rotor side, $\{B_{RC}\}$ can be calculated from

$$\{B_{RC}\} = \frac{1}{r} \frac{\partial \{A_{RC}\}}{\partial \theta} \quad (7.30)$$

Here 'r' is the radius of the central circle. Similarly the Fourier coefficients of the radial component of magnetic flux density in the central circle from the stator side, which is denoted by $\{B_{SC}\}$ can also be calculated.

The reduced nonlinear stiffness matrix for the rotor in Equation (7.13) can be approximated as the power series

$$[K_R]\{B_{RC}\} = [K_R](0) + \sum_{i=1}^{2h} [M_{R_i}] \left(\frac{\{B_{RC}\}(i)}{A_{ref}} \right)^2 \quad (7.31)$$

$[M_{R_i}]$ are the nonlinear coefficients of the power series for calculating the non-linear approximate $[K_R]$ matrix and $\{B_{RC}\}$ is the radial component of the magnetic flux density vector in the central circle. $[K_R](0)$ is the stiffness matrix for the linear case.

Similarly, the reduced stiffness matrix for the stator in Equation (7.20) can be approximated as the power series

$$[K_S]\{B_{SC}\} = [K_S](0) + \sum_{i=1}^{2h} [M_{S_i}] \left(\frac{\{B_{SC}\}(i)}{B_{ref}} \right)^2 \quad (7.32)$$

$[M_{S_i}]$ are the nonlinear coefficients of the power series for calculating the non-linear approximate $[K_S]$ matrix and $\{B_{SC}\}$ is the radial component of the magnetic flux density vector in the central circle. $[K_S](0)$ is the stiffness matrix in the linear

case. The reference magnetic flux density, $\{B_{ref}\}$ is the key parameter, which will determine the accuracy of the approximation of the power series.

7.3.3.2 Method II of accounting for non-linearity

A series of numerical study show that the dependency of stiffness matrix of the rotor with the radial component of the magnetic flux density in the central circle is not enough to represent fully the nonlinear characteristics of the stiffness matrix. In method II it is overcome by extending the dependency to radial as well as tangential magnetic flux at the central circle by incorporating rotor bar currents in addition with the magnetic flux density vector in the power series. It is observed that value of the stiffness matrix increases with the increase of the rotor bar currents to produce the same reference flux density in the corresponding position in the Fourier coefficients of the central circle magnetic vector potentials. A series of numerical study by the author revealed that the cosine and sine terms of a particular rotor bar current harmonics have effect on the cosine and sine terms of the magnetic vector potentials of the same harmonics i.e. two pole cosine rotor bar currents have effect on the two pole cosine terms of the magnetic vector potentials, similarly two pole sine bar currents have effect on the two pole sine terms of the magnetic vector potentials.

The reduced nonlinear stiffness matrix for the rotor in Equation (7.10) can be approximated as the power series

$$[K_R]\{B_{RC}\} = [K_R](0) + \sum_{i=1}^{2h} [M_{A_i}] \left(\frac{\{B_{RC}\}(i) - \alpha \{I_R\}(i)}{B_{ref}} \right)^2 + \sum_{i=1}^{2h} [M_{B_i}] \left(\frac{\{B_{RC}\}(i) + \alpha \{I_R\}(i)}{B_{ref}} \right)^2 \quad (7.33)$$

where α is reference parameter and $\alpha = \frac{B_{ref}}{I_{Rref}}$, I_{Rref} is the reference value of the rotor bar currents. The reduced stiffness matrix for the stator in Equation (7.20) is approximated as Equation (7.32). In method II the two main key parameters are $\{B_{ref}\}$ and α .

7.3.2.3 The method of calculation of the nonlinear coefficients of the power series

To calculate the nonlinear coefficients of the power series in Equations (7.31) and (7.32), we solve inverse nonlinear problems equal to the number of harmonics considered in the central circle. For an example to calculate the term $[M_{R_3}]$, we solve an inverse problem to calculate the pattern of currents in the central circle, which will produce an flux density equal to the reference flux density in the cosine term of second harmonics in the central circle.

7.4 Case studies

This section presents two case studies to validate the non-linear model reduction proposed in Section (7.3) using a simple electromagnetic device in static condition. The situation is chosen here is similar to that of the locked-rotor condition of an induction machine. This electromagnetic device with the dimensions is shown in Figure (7.1). To represent the central circle a line is drawn in the middle of the airgap as shown in the figure and this line is referred here as central circle. The model is divided into two halves, region A and region B, in the central. The region below the central circle is referred as region A and represents the rotor of an induction machine. As shown in the figure region A contains a thin layer of current conducting sheet. In these case studies voltages are applied to generate current. The region above the central circle is referred as region B and represents the stator of an induction machine. Region B has two current carrying slots and a single turn conductor is used. Voltage is supplied to the coil in region B. The two currents in region B are constrained and represented by only one current, i_b as follows

$$i_b = \begin{bmatrix} 1 & 0 \\ 0 & -1 \end{bmatrix} \begin{Bmatrix} i_{b+} \\ i_{b-} \end{Bmatrix} \quad (7.34)$$

where i_{b+} and i_{b-} are the two slot currents for the slots b+ and b- respectively. The airgap is shown exaggerated in Figure (7.1).

The magnetisation characterisation of the iron is assumed as the $B(H)$ curve shown in Figure (3.9). Two regions are discretised completely independently by 8-noded quadrilateral element. Both regions are coupled at the central circle by imposing the constraint that the magnetic potentials at the central circle from region A must be equal to the magnetic potential at the central circle from region B. Tangential boundary conditions are applied on the sides AB, BC, CD and DA. Figure (7.2) and (7.3) show the FE mesh of the model and a snapshot of the magnetic potentials contour when two arbitrary currents are applied to region A and region B respectively.

Approximate functions are derived separately for the rotor and the stator as a function of the sine component of the first harmonics of the magnetic potentials in the central circle. The reference value of the magnetic potential is chosen the threshold value of the sine component of the first harmonics of the magnetic potentials in the central circle above which value the machine will saturate. To calculate the coefficients of the approximate functions we solve a series of full non-linear FE problems with different level of current density in region A and region B allowing the machine to be saturated. We store the marginal inductances for region A and region B separately for each case. We also store the sine component of the magnetic potentials in the central circle. Then, the following inverse problem is solved to calculate the coefficients of the region A.

$$\begin{bmatrix} 1 & a_{A1} \\ 1 & a_{A2} \\ \vdots & \vdots \\ 1 & a_{An} \end{bmatrix} \begin{bmatrix} K_{A1} \\ K_{A2} \end{bmatrix} = \begin{bmatrix} K_1 \\ K_2 \\ \vdots \\ K_n \end{bmatrix} \quad (7.35)$$

where n is the number of full nonlinear FE problem solved, $a_{A1}, a_{A2}, \dots, a_{An}$ are the sine components of the magnetic potentials in the central circle for cases 1, 2, ..., n respectively, $[K_1], [K_2], \dots, [K_n]$ are the marginal stiffness matrices for cases 1, 2, ..., n respectively and $[K_{A1}]$ and $[K_{A2}]$ are the two coefficients for the approximate function. Similarly, we can find the coefficients for the region B.

The two currents are calculated by integrating Equation (6.4) in time domain until they reach the steady state. The first of the two case studies solves the two currents with a low level of saturation when the voltages are applied at both region A and region B. The supply voltage is chosen such that the machine is saturated. The second case study solves the currents with a high level of saturation when the voltages are applied at both region A and region B.

7.4.1 Case study I: Sinusoidal voltage with a low level of saturation

The first case study presents the results for a low level of saturation of the device. The following sinusoidal voltages are applied in the two regions.

$$\begin{aligned}v_A &= 1 \sin(\omega t) \\v_B &= 5 \sin(\omega t)\end{aligned}$$

where v_A and v_B are the voltages applied to the region A and region B respectively. While applying these voltages it is ensured that the machine will have a low level of saturation.

Figure (7.4) shows currents i_a from linear, approximate method I and complete non-linear methods. Figure (7.5) shows the currents i_b from linear, approximate method I and complete non-linear. It has been observed that the results from the approximate method agree very well the results from the full non-linear FE solution.

7.4.2 Case study II: Sinusoidal voltage with a high level of saturation

The second case study presents the results for a high level of saturation. The following sinusoidal voltages are applied in the two regions.

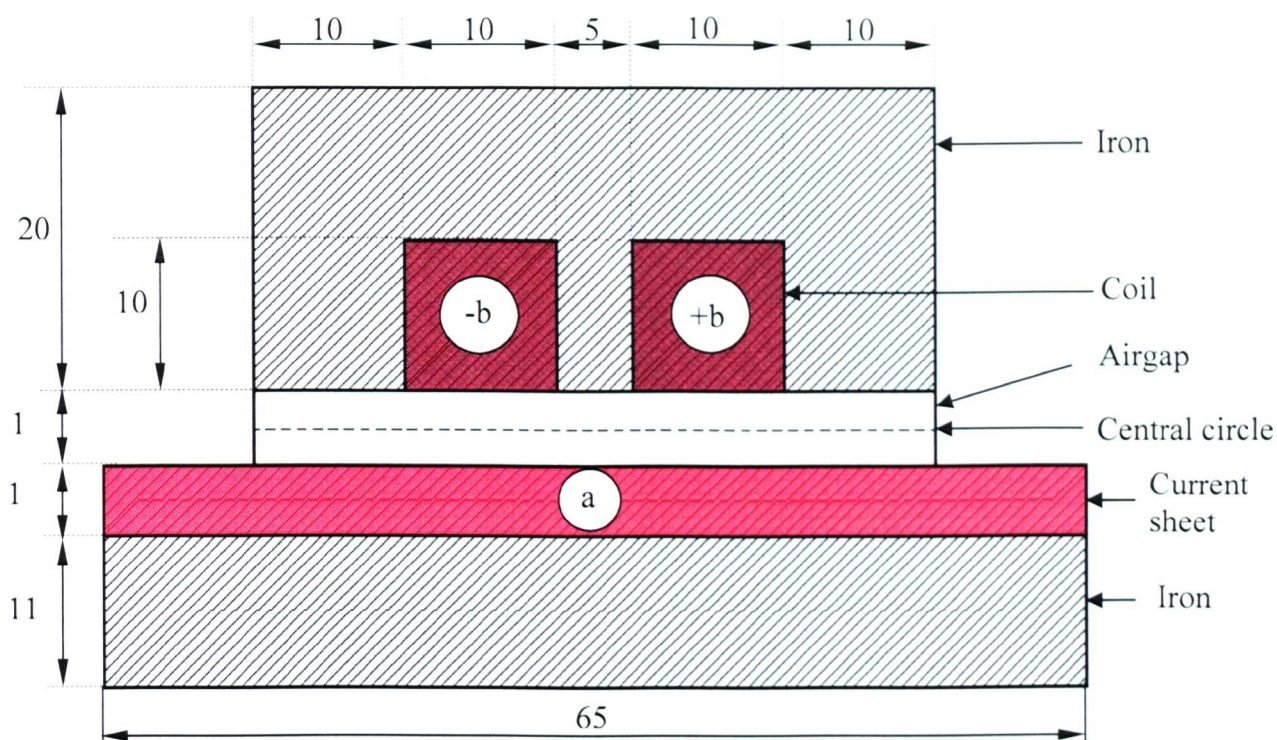
$$\begin{aligned}v_A &= 1.5 \sin(\omega t) \\v_B &= 7.5 \sin(\omega t)\end{aligned}$$

where v_A and v_B are the voltages applied to the region A and region B respectively. The device is highly saturated when the above voltages are applied in the two regions.

Figure (7.6) shows currents i_a from linear, approximate method I and complete non-linear. Figure (7.7) shows the currents i_b from linear, approximate method I and complete non-linear method. It has been observed that when the level of saturation is high the results from the approximate method do not agree very well the results from the full non-linear FE solution. Approximation of the stiffness matrix can be improved by using method II. Figures (7.8) and (7.9) show the improved results using the approximate method II.

7.5 Conclusions

Efficient ways for calculating steady state currents of a rotating electric machine are presented here. If the magnetic saturation is not considered a substantial amount of computation time can be saved using these methods. These methods are used to calculate the steady state currents in an induction machine and some of the results are presented in Chapter 8. Next chapter presents a coupled model combining the electrical and mechanical dynamics. In the next chapter it will be clear about the need of an efficient method to calculate steady state currents. Two approximate methods for non-linear model reduction are also presented and verified using a simple electromagnetic problem. For low level of saturation the results from the first approximate method agree very well with the results of complete non-linear FE solution. For higher level of saturation the results from the first approximate method do not agree very well with the results of complete non-linear FE solution. There is a limit of the level of saturation beyond which the results will be less accurate. Accuracy can be improved by performing more number of numerical experiments while calculating the coefficients of the approximate function. This method can be used in rotating electric machines when the machine is not highly saturated.



All dimensions are in mm

Figure (7.1): A simple electromagnetic device

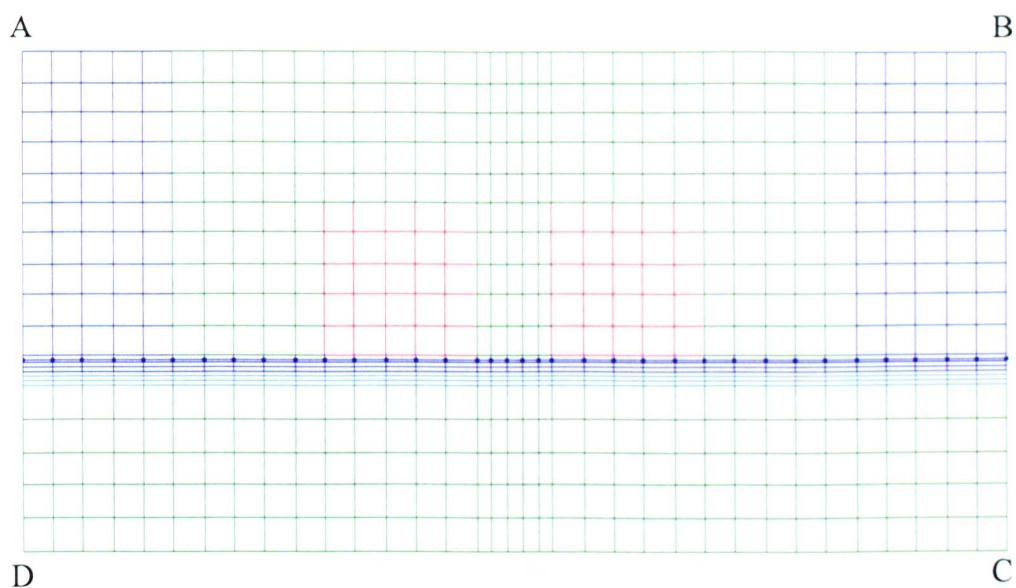


Figure (7.2): FE Mesh of the model (region A and region B)

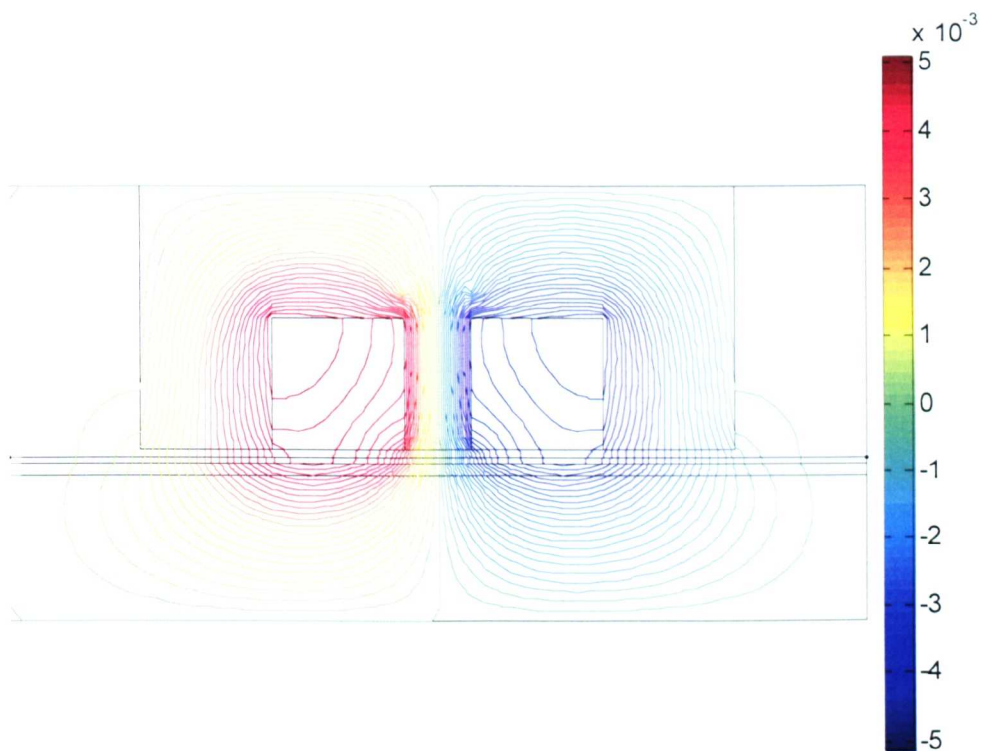


Figure (7.3): Contour plot of magnetic potentials

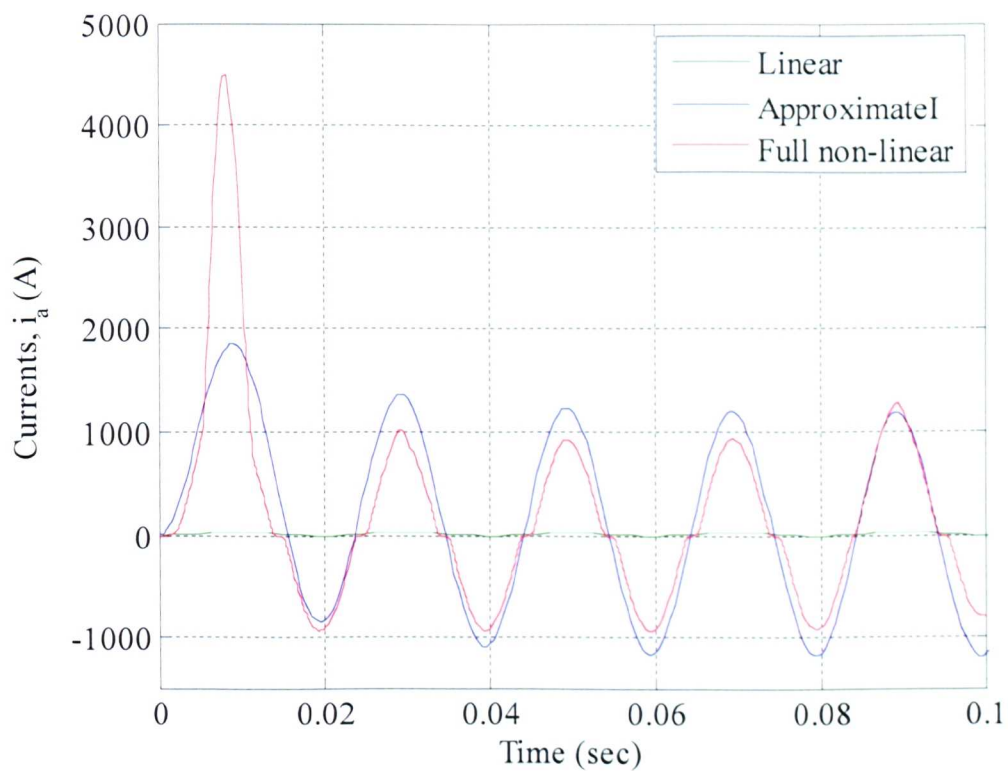


Figure (7.4) Currents in the region A, i_a from linear, approximateI and full non-linear methods for case study I

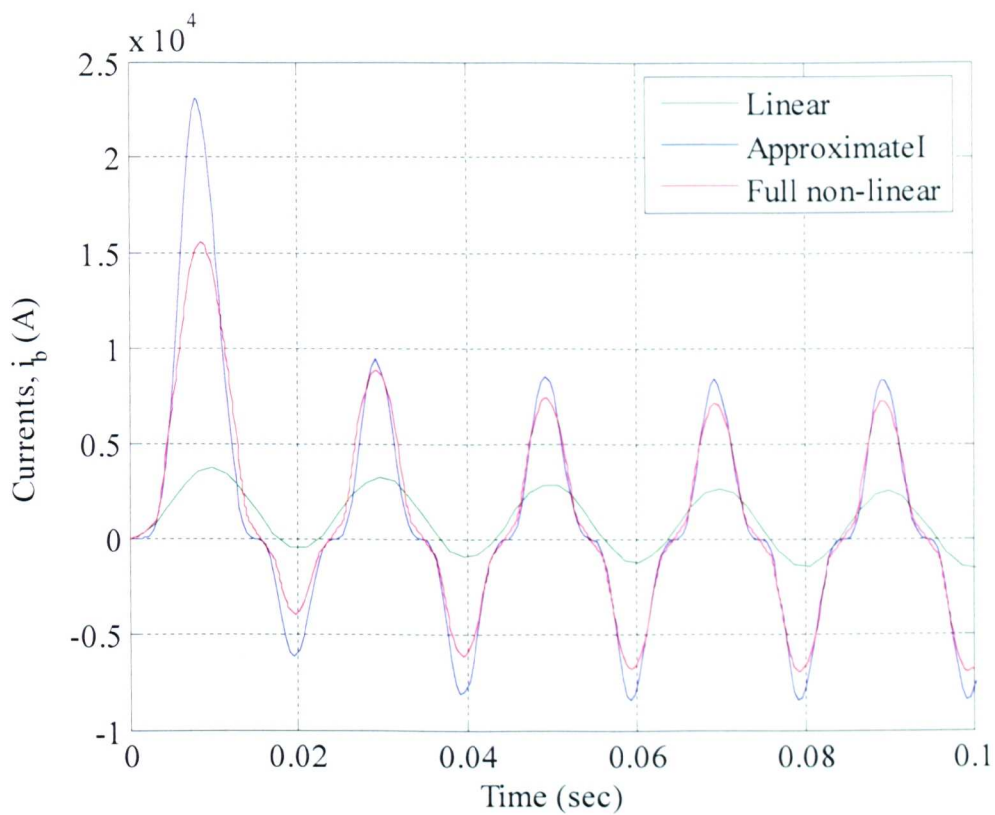


Figure (7.5) Currents in the region B, i_b from linear, approximateI and full non-linear methods for case study I

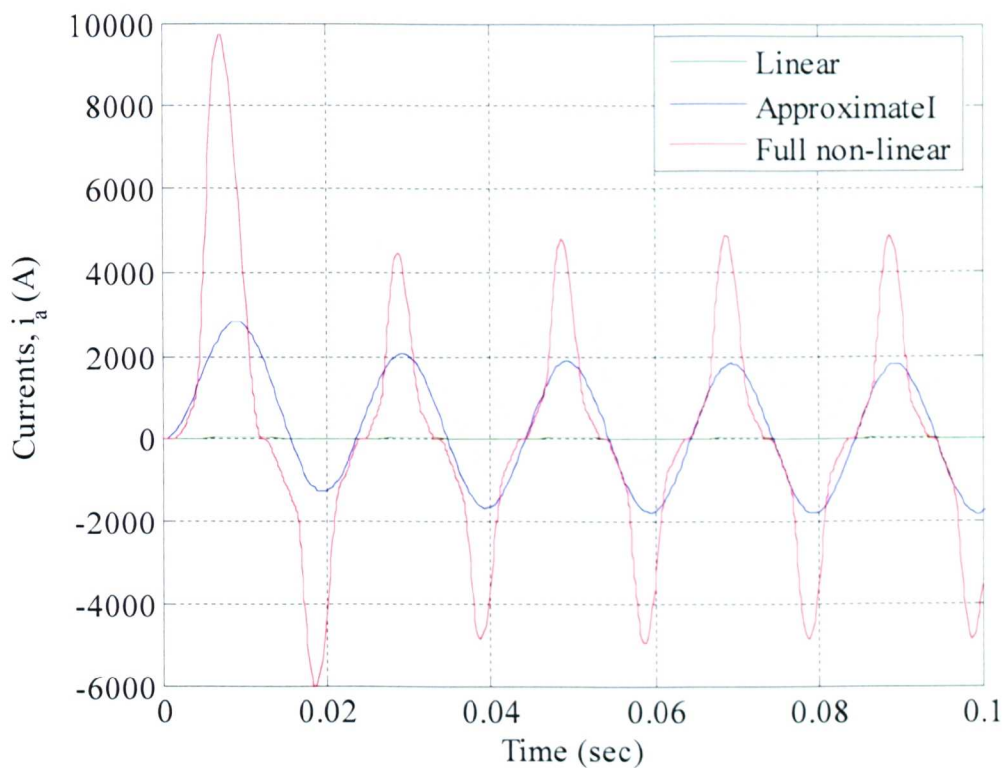


Figure (7.6) Currents in the region A, i_a from linear, approximateI and full non-linear methods for case study II

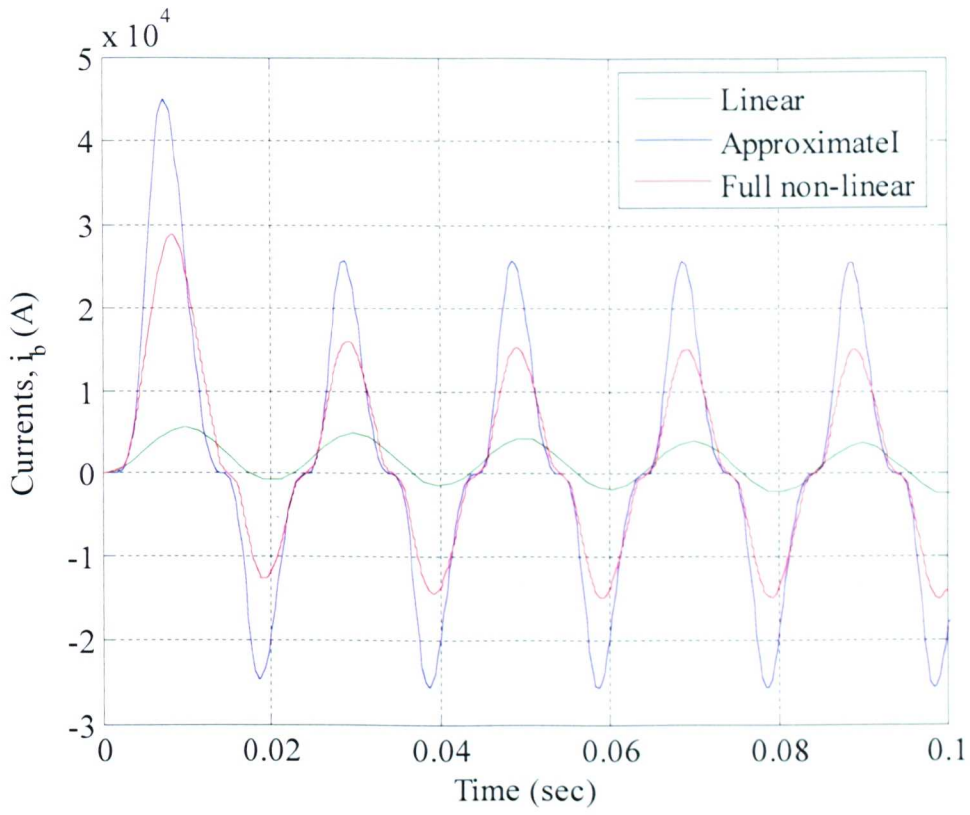


Figure (7.7) Currents in the region B, i_b from linear, approximateI and full non-linear methods for case study II

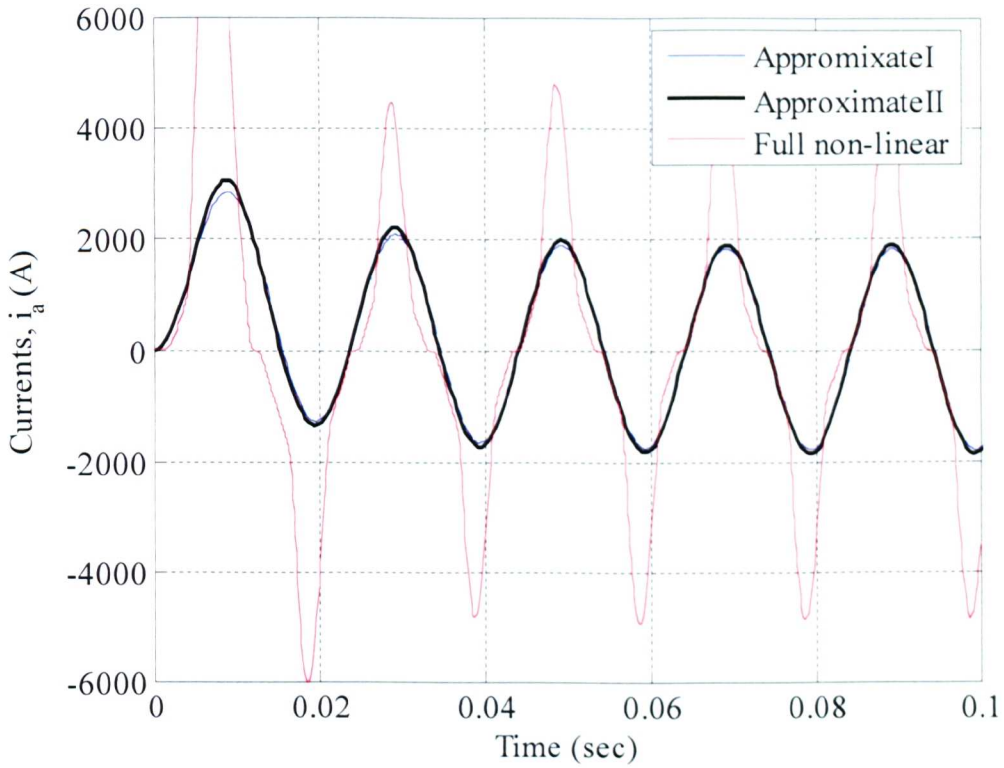


Figure (7.8) Currents in the region A, i_a from approximateI, approximateII and full non-linear methods for case study II

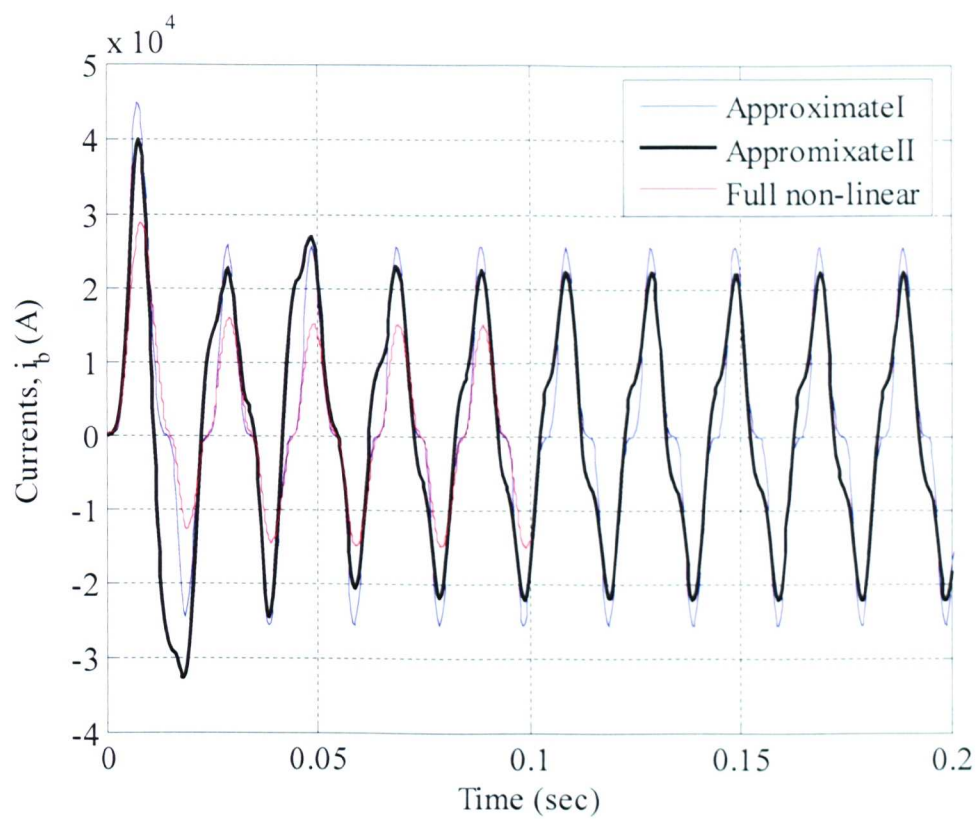


Figure (7.9) Currents in the region B, i_b from approximateI, approximateII and full non-linear methods for case study II

Chapter Eight

Unified Electromagnetic Dynamic and Rotordynamics Model

8.1 Introduction

Procedures for using finite element analysis to approximate magnetic field quantities in an electrical device are well known ([Arkkio, (1987), Hameyer and Belmans, (1999), Bastos and Sadowski, (2003)]. To study the mechanical dynamic behaviour of an electrical machine there is a need for an accurate UMP model (incorporating a number of current degrees of freedom) and for a high-dimensional rotor dynamics model. Previous work on the study of coupled (mechanical and electromagnetic) behaviour of electrical machines have either reduced the electrical behaviour to static (or very low-dimensional dynamic behaviour) and then focused on the mechanics or else they have taken very simplistic models of the mechanical behaviour and viewed the system from the standpoint of the electrical system.

Previous chapters describe how the electromagnetic field equation of an electrical machine is solved at every time step of the simulation in order to calculate the inductance matrix of an electrical machine incorporating the material non-linearity. It also describes how the electromagnetic field equation can be coupled to the circuit equation to form the electro-magneto-mechanical model. In this chapter a detailed mechanical model is presented and this detailed model is coupled with a high dimensional electromagnetic model to study the behaviour of the coupled system.

The combined model coupling electrical and mechanical dynamics facilitates the following

- Voltage is applied to the terminals of the machine and mechanical speed is taken to be a known input quantity to specify the electrical problem, and the internal currents are calculated as unknowns. Parameters of the coupled dynamics are calculated for this set of internal currents.
- Equations for mechanical motion are coupled to the electrical dynamics.

The numerical model developed here to study the coupled dynamics of electrical and mechanical dynamics is generic. In the first application of the model, only cage induction motors without parallel paths in the stator windings are studied, in the second application of the model, the effect of parallel winding paths in the system is incorporated. These parallel paths tend to reduce the net unbalanced magnetic pull by allowing different amplitude of current to flow in the parallel branches similar to the effect of rotor cage currents. This model is also used to calculate the equalising currents in parallel paths.

The chapter is divided mainly into two sections. The first section describes the proposed combined model coupling electrical and mechanical dynamics. The electrical dynamics is described by an electro-magneto-mechanical model and this has already been explained in Chapter 4. A mechanical model of an electric machine is developed to describe the mechanical dynamics. A coupled model is developed to describe the combined electrical and mechanical dynamics of an electrical machine. The second section describes a case study which solves this coupled problem. A 4-pole three phase induction machine is considered for this study. The machine is wound in a special way known as the bridge configured windings as described in Section (4.36) of Chapter 4. Chapter 10 describes the fundamental properties of this machine presenting the no-load and locked-rotor conditions. The machine has parallel paths in its stator windings which facilitate to study the effect of the parallel paths in the machine dynamics. To the knowledge of the author there is as yet no literature available to include the parallel paths into a rotor dynamic model. One of the additional features of this coupled model is that it can be easily extended to include

the effects of parallel paths. In this section the additional damping offered by the parallel windings is calculated in terms of energy dissipated in the windings.

8.2 Electro-magneto-mechanical model

The coupled electro-magneto-mechanical model has already been described in Chapter 5. The linearised coupled equation of this electro-magneto-mechanical model of an electrical machine is

$$\{V\} = [R]\{I_{RS}\} + ([P][A][P]^T) \frac{d\{I_{RS}\}}{dt} + ([P][B]) \frac{d\{x\}}{dt} \quad (8.1)$$

where $\{V\}$ is the vector of externally-applied voltages, $[R]$ is the resistance matrix of the machine including the effect of the end-windings, $\{I_{RS}\}$ is the vector of independent currents and $\{x\}$ is the vector which describe the instantaneous geometry of the machine. For a two-dimensional analysis $\{x\}$ comprises only three entries assuming that neither the rotor nor the stator can deform significantly in the plane and provided that the stator is fixed in space. The vector, $\{x\}$ can be written as

$$\{x\} := \begin{Bmatrix} u \\ v \\ \theta \end{Bmatrix} \quad (8.2)$$

where u and v are the horizontal and vertical positions of the rotor centre respectively and θ is the angle of turn of the rotor. Matrices $[A]$ and $[B]$ are calculated by differentiating Equation (5.17) and is already explained in Section (5.4) of Chapter 5 how these two matrices can be obtained. For relatively smaller currents, the machine is not saturated and the matrix $[B]$ is proportional to $\{I_{RS}\}$ and $([P][A][P]^T)$ is the “tangent inductance” or “marginal inductance” matrix. Matrices $[B]$ and $([P][A][P]^T)$ are calculated from the magneto-static field equation using 2D FE method.

8.3 Mechanical model

The development of mechanical models for rotor-stator-bearing systems is well-established (Lalanne and Ferraris, 1990) and these models commonly emerge in the natural second-order form

$$[M]\{\ddot{q}\} + ([D] + \Omega[G])\{\dot{q}\} + ([K_{\text{mech}}] + \Omega[F])\{q\} = \{f\} \quad (8.3)$$

where $\{[M], [D], [K_{\text{mech}}]\}$ denote mass, damping and stiffness matrices of the mechanical system. Very often, these are all symmetric and positive (semi-)definite. Matrices $[F]$ and $[G]$ are both skew-symmetric and they represent force contributions from gyroscopic effects and from internal rotor damping respectively. Vectors $\{q\}$ and $\{f\}$ represent the displacements and (externally-applied) forces respectively. With appropriate definitions for these vectors, $\{\dot{q}\}^T \{f\}$ represents the instantaneous power flowing into the mechanical system from the externally applied forces. In fact, the observations about the symmetry in the matrices above depend fundamentally on this convention. The mean rotational speed of the rotor is denoted by Ω in Equation (8.3).

In order to couple the mechanical model to the electromagnetic one, it is necessary to express the relevant geometry variables of $\{x\}$ from the previous section in terms of the displacements in $\{q\}$.

$$\{x\} = [S]^T \{q\} + \begin{bmatrix} 0 \\ 0 \\ \Omega t \end{bmatrix} =: \{x_{\Delta}\} + \begin{bmatrix} 0 \\ 0 \\ \Omega t \end{bmatrix} \quad (8.4)$$

$$\{\dot{x}\} = [S]^T \{\dot{q}\} + \begin{bmatrix} 0 \\ 0 \\ \Omega \end{bmatrix} =: \{\dot{x}_{\Delta}\} + \begin{bmatrix} 0 \\ 0 \\ \Omega \end{bmatrix} \quad (8.5)$$

where $[S]$ is a *selection* matrix having three columns. The first two columns of $[S]$ pick out which (linear combinations) of the displacements within $\{q\}$ constitute the horizontal and vertical motions of the rotor centre (u and v) respectively. If the

mechanical model includes entries in $\{q\}$ representing rotor twist relative to a frame of reference rotating at constant speed Ω , then the third column of $[S]$ contains some non-zero coefficients. Otherwise, this column contains only zeros. The total force acting, $\{f\}$ in Equation (8.3) on the mechanical system is the sum of those components due to mechanical causes and those due to the electro-magnetic effects

$$\{f\} = \{f_M\} + \{f_E\} \quad (8.6)$$

The mechanical force vector, $\{f_M\}$, is presumed to be known at any instant in time and it arises from unbalance and other known sources. In the simulations of interest here, this vector is zero. In most other cases, it would be a sinusoidal forcing associated with imbalance and/or bend on the rotor. In the 2D electromagnetic modelling case where $\{x\}$ is defined according to Equation (8.2), the electromagnetic force vector $\{f_E\}$ can have only three independent components – net horizontal force, U, net vertical force, V, and net (oscillatory component of) torque, T_m and $\{f_E\}$ may always be written as

$$\{f_E\} = [S] \begin{bmatrix} U \\ V \\ T - T_m \end{bmatrix} =: [S] \left(\{X\} - \begin{bmatrix} 0 \\ 0 \\ T_m \end{bmatrix} \right) \quad (8.7)$$

involving the same matrix $[S]$ that appeared in Equation (8.4) and using T_m to represent the mean torque exerted by some mechanical load. The product (ΩT_m) is the useful mechanical power being delivered to that load. The vector $\{X\}$ is part of the electromagnetic force vector and contains U and V. This can be obtained in several different ways. The method favoured here is to draw a closed curve around the rotor (usually a circle dividing the air gap into a rotor side and a stator side of similar radial depths) and to integrate force and torque contributions due to Maxwell stresses (magnetic stresses) around that circle. The method of calculating the force and torque using Maxwell stresses is explained in Chapter 3. Given the ability to compute $\{f_E\}$

and $\{f_M\}$ at every instant, it is clear that we do have the wherewithal to perform time-domain simulation of the mechanical system also.

If the magnetic field has been computed at a given instant, $t = t_0$, then it is straightforward to do the integration of Maxwell stresses numerically to obtain $\{X\} = \{X_0\}$. For small excursions, $\{x_\Delta\}$ from the reference-geometry at this instant, the time-dependent forcing vector $\{X\}$ can be approximated well by the linear expression:

$$(\{X\} - \{X_0\}) \approx [K_{UMP}]\{x_\Delta\} + [C](\{I\} - \{I_0\}) \quad (8.8)$$

where $[K_{UMP}]$ is usually positive-definite and (because of our definition for $\{X\}$ as a force exerted by the system rather than on the system) this matrix has a de-stabilising effect. $[K_{UMP}]$ may be determined by straightforward numerical differentiation in the magnetic finite-element model at any instant. The matrix $[C]$ represents the influence of small changes in machine currents on the mechanical system. The quantity $(\{\dot{x}_\Delta\}^T [C](\{I\} - \{I_0\}))$ represents the instantaneous marginal power being drawn from the electrical circuits into the oscillatory mechanical motions. By conservation of energy, this must be identical to $((\{I\} - \{I_0\})^T ([P][B])\{\dot{x}_\Delta\})$. It can be concluded that

$$[C] = ([P][B])^T \quad (8.9)$$

8.4 Coupled linearised model

In Chapter 5, we outlined the development and format of the electromagnetic model. This model included the effects of geometry changes and the linearised version of this model was presented as Equation (8.1) for any instant $t = t_0$. Accepting that we have a reference solution for the machine, it is clear that this linearization of the electromagnetics is applicable at all times. The linearization includes the effects of small geometry changes from the expected machine geometry (i.e. the reference solution does recognise the fact that the rotor is rotating).

In Section (8.3), the development and format of the mechanical model is outlined. The purely mechanical aspects of this model were assumed to be linear. The model included the effects of magnetic forces and the linearization of these forces around the reference solution was presented as Equation (8.3) for any instant $t = t_0$. Note that $\{q\}=0$ for all times in the reference solution. However since $\{I\}$ is certainly not zero in the reference solution, it is convenient for us to define

$$\{I_{\Delta}\} \equiv (\{I\} - \{I_{\text{ref}}\}) \quad (8.10)$$

We deliberately use a vector of charge displacements in place of currents as the basic time-dependent electrical quantity because of the pleasing structure that it creates in the time-dependent matrices later. Thus we define

$$\{Q_{\Delta}\}(t) = \int_0^t \{I_{\Delta}\}(\tau) d\tau, \quad \{Q_{\text{ref}}\}(t) = \int_0^t \{I_{\text{ref}}\}(\tau) d\tau, \quad \{Q\}(t) = \int_0^t \{I\}(\tau) d\tau \quad (8.11)$$

Now, this time-dependent linearization of the coupled machine model can be put together as

$$\begin{bmatrix} (PAP^T) & 0 \\ 0 & M \end{bmatrix} \begin{Bmatrix} \ddot{Q}_{\Delta} \\ \ddot{q} \end{Bmatrix} + \begin{bmatrix} (R + \Omega H) & (PBS^T) \\ -(PBS^T)^T & (D + \Omega G) \end{bmatrix} \begin{Bmatrix} \dot{Q}_{\Delta} \\ \dot{q} \end{Bmatrix} + \begin{bmatrix} 0 & 0 \\ 0 & (K_{\text{mech}} + \Omega F - SK_{\text{UMP}}S^T) \end{bmatrix} \begin{Bmatrix} Q_{\Delta} \\ q \end{Bmatrix} = \begin{Bmatrix} (V - V_{\text{ref}}) \\ f_M \end{Bmatrix} \quad (8.12)$$

The forcing terms on the right hand side of the equation include the mechanical forces (usually originating from imbalance, rotor bend/misalignment) and slight differences from the reference voltage. All terms in Equation (8.12) have been defined before now with the exception of $[H]$. This matrix represents the sensitivity of the third column of $([P][B])$ to $\{I_{\Delta}\}$ and it arises because the vector $\{\dot{x}\}$ contains the non-infinitesimal entry, Ω (c.f. Equations (8.4) and (8.5)). In Equation (8.12), the matrices which depend on time are $[A]$, $[B]$, $[H]$ and $[K_{\text{UMP}}]$.

If the actual coupled response of the machine is of interest, then Equation (8.12) provides an extremely effective way to obtain that. We caution, however, that as this

is a linearised model, it is accurate only for small perturbations from the reference solution. Transverse deflections at the centre of the rotor should be substantially less than the radial thickness of the airgap for this analysis to be valid.

Our purposes for the linearised coupled model are two-fold. One interest is the time-domain response to (small) applied excitation. The other is to do with stability. If the forcing terms on the right hand side of Equation (8.12) are zero, then Equation (8.12) represents a homogeneous periodic time-varying linear system.

The period, T_p of any periodic system is defined as the time required repeating the state of the system. The method of calculating the period of an induction machine is given later in this chapter. For machines other than induction machines, the period is much more easily obtained. At any instant, this system has a state which is characterised by the state-vector

$$\{y\} := \begin{Bmatrix} \{Q_\Delta\} \\ \{q\} \\ \{\dot{Q}_\Delta\} \\ \{\dot{q}\} \end{Bmatrix} \quad (8.13)$$

If there are $2n$ entries in $\{y\}$, then we can discover a $(2n \times 2n)$ *State-Transition* matrix, $[Z]$ which relates the state at the end of a period, $\{y\}(T_p)$, to the state at the start of the period, $\{y\}(0)$, according to

$$\{y\}(T_p) := [Z] \{y\}(0) \quad (8.14)$$

Following the ideas developed by Floquet, the eigenvalues of $[Z]$ show whether the system is stable. If all eigenvalues are less than 1 in magnitude, the system is stable.

Recall that in the reference solution $([P][B])$ is proportional to the magnitude of the applied voltage – at least for low values of the magnitude of the applied voltage, $\{V_{ref}\}$. The negative magnetic stiffness, $[K_{UMP}]$ is proportional to the *square* of this applied voltage and the matrix $[H]$ is independent of this applied voltage. At very low

levels of applied voltage, the electrical and mechanical dynamics are completely independent and any instability which might occur will either be purely electrical in nature (which can occur since many eigenvalues of $[H]$ are negative) or purely mechanical in nature (which can also occur as a result of internal damping effects represented by $[F]$). Other sources of mechanical instability also exist but are not discussed here.

We study one particular 3-phase induction machine operating in 25 different conditions – 5 values of slip and 5 different voltage magnitudes.

8.5 The reference electromagnetic solution

Chapter 6 and 7 describe different methods for calculation of the steady state solution for induction machines. If the rotor is constrained to move concentrically within the stator and if it is required to rotate at constant mechanical speed Ω while a fixed-frequency balanced sinusoidal voltage is applied to the stator windings, then a time-stepping simulation can be carried out to establish the steady-state machine currents as a function of time. At this condition if the simulation is carried out by integrating Equation (8.1) without the final term on the right-hand side the steady state machine currents is called the reference currents.

For induction machines, this solution depends on both the magnitude of the applied voltage and its frequency. For reasons that will become clear later, we will invariably restrict our reference solutions to conditions where the machine rotor has rotated an integer number of slot-pitches after some periodic time T_p which is also an integer multiple of the periodic time for the applied voltage waveform. Obtaining this solution for any one machine condition can be relatively intensive in computation time – not least because transients must be allowed to die away before one period of reference solution is captured and Chapter 7 addresses means for finding this solution.

We have studied the coupled dynamics of the machine for different levels of applied voltage. A reference solution for a very low applied voltage (say 1V) can be obtained accurately and relatively quickly because the iron behaves linearly and so the element

matrices for each finite-element in the model need to be derived only once (in contrast to the nonlinear case where the matrices must be derived afresh for all ferromagnetic elements several times per time-step). With magnetic linearity assumed, the reference currents for an applied voltage of higher magnitude can be scaled – i.e. the reference solution for 2V is exactly twice the reference solution for 1V. Based on a single reference solution at low voltage, therefore, we can estimate with confidence at what voltage it will be necessary to allow for magnetic nonlinearity and moreover, we can start the simulation for this (slightly non-linear) reference solution with an initial estimate which will be close to the converged answer. We accept from this point forward that a reference solution can be obtained for any desired voltage level and any combination of supply frequency and shaft-speed, Ω .

8.6 The time period of an electrical machine

For an induction machine with p pole-pairs supplied by electrical frequency, ω_e (rad/s), the so-called “synchronous speed”, Ω_0 (rad/s), is given by

$$\Omega_0 = \frac{\omega_e}{p} \quad (8.15)$$

Synchronous speed is a speed at which the machine develops zero airgap torque. The time taken for the stator MMF to repeat itself is given by

$$T_m = \frac{2\pi}{\omega_e} \quad (8.16)$$

If the number of bars in the rotor is k and if the motor is running with a slip of s , then the time taken for the rotor to slip one rotor bar is

$$T_{bar} = \frac{2\pi}{k} \cdot \frac{1}{\Omega_0 s} = \frac{2\pi}{k} \cdot \frac{p}{\omega_e s} = \frac{p}{ks} T_m \quad (8.17)$$

The machine will have perfectly-periodic behaviour if the slip, s , is a rational number,

$s = \frac{a}{b}$, $\{a, b\} \in \mathbb{N}$. Then the period, T_p , is given by

$$cT_p = pbT_m \quad (8.18)$$

where c is the highest common factor of (pb) and (ka) . For machines other than induction machines, the period is much more easily obtained.

8.7 Case study of the coupled electrical and mechanics dynamics of an induction machine

This case study is about the electromechanical interactions of a 2kW induction motor having flexible rotor. The main electromagnetic parameters of the motor are presented in Table (8.1). This 4-pole, 3-phase induction motor is wound with a fractional pitch, double layered bridge configured windings. The stator of an induction machine with its windings connections and the bridge configured winding scheme are shown in Figures (4.3) and (4.8) of Section 4 respectively. As mentioned in Chapter 4, bridge configured windings have six independent currents. Three of them are phase or terminal currents, denoted by i_{Aph} , i_{Bph} and i_{Cph} , and the other currents are the bridge or equalising currents, denoted by i_{Alev} , i_{Blev} and i_{Clev} . There will be no current flowing across the bridge for a concentric rotor when the flux field is uniformly distributed. Any unbalance of field due to eccentricity will induce an EMF tending to drive currents in the closed circuit such that a MMF comes to exist opposing the rate of change of this field. Chapters 6 and 7 describe various methods for calculation of steady state currents of an induction machine for a concentric rotor. To calculate the equalising currents, which exist because of the rotor eccentricity, the electro-magneto-mechanical equation is solved by displacing the rotor by a known amount of eccentricity. The results are presented later in this chapter.

A schematic diagram of the motor is shown in Figure (8.1). The mechanical model of the motor is developed using mechanical FE software developed by Professor M I Friswell of the University of Bristol, UK. The rotor and the shaft are modelled using 1D beam elements. The laminations of the rotor are modelled using disc elements.

8.7.1 Finite element model of the flexible rotor

Typically the rotor is modelled using around 60 Timoshenko beam elements with four degrees of freedom per node to represent shaft stiffness and using rigid disc elements fixed at the appropriate shaft-stations to represent the additional mass of blade-stages (in the case of turbo-machines) or (in the case of electrical machines) the laminated core of the rotor. Each node of the model has two translational degrees of freedom and two rotational degrees of freedom. In some cases, (Garvey, *et al.*, 2004), it is critical to take account of the stiffening effects of the laminated rotor core on the shaft. Figure (8.2) shows a typical finite element model of an induction machine where the shaft is supported by two preloaded angular contact ball bearings at each end. The bearings are assumed to be isotropic and they are represented using equivalent stiffness and damping properties. The equivalent stiffness and damping properties of the bearings are shown in Table (8.2). Figures (8.3) and (8.4) show the system Campbell diagram and the mode-shapes associated with the first four (forward-whirling) critical speeds. These forward critical speeds occur at 3843, 8939, 15000 and 20040 rpm

8.7.2 Equalising currents for an eccentric rotor

An eccentric rotor creates an asymmetric flux distribution that causes the radial forces. The asymmetric field may induce circulating currents in the rotor cage and parallel paths of the stator winding. These currents tend to equalise the flux distribution and they may significantly reduce the amplitudes of these radial forces. Therefore, from the electrical dynamics alone we can measure the equalising currents for an eccentric rotor. In other words, these equalising currents are the measures of eccentricity of a particular machine at its operating conditions.

Numerical tests (linear) are carried out at 20V supply voltage with varying degree of static eccentricity. Figures (8.5), (8.6) and (8.7) show the levitation currents in the three bridges because of the static eccentricity of 2% of the air gap, which are otherwise 'zero' for a concentric rotor. Similarly, Figures (8.8), (8.9) and (8.10) show the levitation or equalising currents in the three bridges based on the 10% static

eccentricity in the airgap. The magnitudes of the equalising currents are 4% of the phase currents when the static eccentricity is 2% of the airgap. It can be seen from these figures that the equalising currents vary linearly with the eccentricity.

8.7.3 Minimum time period of the machine

The minimum time period of the induction machine is calculated using Equation (8.18) For example, if the supply frequency (f) is 25 Hz, the number of rotor bars (k) is 32 of a 4-pole induction machine, then the minimum time period is calculated as follows:

The time taken for the stator MMF to repeat itself, $T_m = \frac{1}{f} = 0.04$ sec

For a slip of 2.5% the time taken for the rotor to slip one rotor bar, $T_{bar} = \frac{p}{ks} T_m = 0.1$ sec. For slip 2.5%, $a = 25$ and $b = 1000$. The highest common factor, c of (pb) and (ka) in this case is 400 and the period of the machine is

$$T_p = \frac{pb}{c} T_m = 5 \times 0.04 = 0.2 \text{ sec}$$

8.7.4 Preparing the state transition matrix for the coupled model

To determine the system characteristics, we are interested in solutions for Equation (8.12) where forcing term, $\{f\}$, is zero for all time. We can write Equation (8.12) as

$$[M'(t)]\{\ddot{q}'(t)\} + [D'(t)]\{\dot{q}'(t)\} + [K'(t)]\{q'(t)\} = 0 \quad (8.19)$$

We can write Equation (8.19) in state-space form

$$\begin{aligned} \begin{bmatrix} K'(t) & 0 \\ 0 & -M'(t) \end{bmatrix} \begin{bmatrix} q'(t) \\ \dot{q}'(t) \end{bmatrix} + \begin{bmatrix} D'(t) & M'(t) \\ M'(t) & 0 \end{bmatrix} \begin{bmatrix} \dot{q}'(t) \\ \ddot{q}'(t) \end{bmatrix} &= \begin{bmatrix} 0 \\ 0 \end{bmatrix} \\ &= [A(t)]\{x(t)\} + [B(t)]\{\dot{x}(t)\} \end{aligned} \quad (8.20)$$

The time-varying coefficient matrices of the linearised coupled dynamic equation are periodic. The Floquet method is used to analyse the stability of this linear time varying periodic system. The state vector, $\{x(t)\}$, has $2n$ entries in it. Given any initial vector, $\{x(0)\}$, it is straightforward to integrate Equation (8.20) numerically through one time-period, T_{sys} , to develop $\{x(T_{sys})\}$. In fact, the fastest method for achieving this would take account of the second-order nature of the system. We apply Newmark-Beta (Newmark, 1959) algorithm for numerical integration. By generating $2n$ linearly-independent initial state vectors $\{x(0)\}$ and integrating each one through one complete period, we can develop a so-called *State Transition Matrix* (STM), $[Z]$, such that given any arbitrary initial state vector, $\{x(0)\}$, the state-vector at the end of the period is given by

$$\{x(T_{sys})\} = [Z]\{x(0)\} \quad (8.21)$$

8.7.5 Stability of the system

The stability of the linear system with time varying coefficients is analysed using the Floquet method. The eigenvalues of the STM are calculated for different slip conditions and different voltages at the end of one period and that determines the stability of the system. Table (8.4) shows the stability condition of the system for different slips and supply voltages. It is found that the system is stable for all slip conditions at 22.5 V and unstable for 51 V or above. At 25.5 V the system is stable at 2% of slip or less and unstable beyond 2%. At 34 V the system is stable at 0.5% of slip or less and unstable beyond 0.5%. It is also possible to draw a stability chart with slip versus the supplied voltage.

8.7.6 Energy transfer while closing the bridge

The one of the main points of interest of this study is the effective mechanical damping provided by the closure of the parallel-path circuits in the three different phases. The parallel paths do not stabilise any of the unstable conditions (which

appear to be dominated by negative magnetic stiffness) but they do reduce the real parts of eigenvalues in all cases. Effective electrical damping has been assessed by forcing the rotor centre to take a positive circular synchronous orbit of 1% of the air-gap and examining the energy transferred into the electrical circuits from the mechanical motion over the period of time, T_p . Tables (8.5) and (8.6) summarise the findings at 17V for each of the five conditions of slip with the parallel paths closed for forward whirling and backward whirling of the rotor respectively. These results are presented as time-constants (the mean total mechanical energy in the rotor divided by the mean power-loss into the electrical system).

Energy transferred to the electrical system from the mechanical system because of the displacement of the rotor from the central position as a function of time is shown in Figures (8.11) and (8.12) for forward and backward whirl respectively. As expected the energy transfer is greater when the rotor is in forward whirl than it is in backward whirl.

8.8 Conclusions

A coupled model combining the electrical and mechanical dynamics is proposed. The results of this coupled model are verified by experimental results and this is explained later in Chapter 10. The coupled system is a time varying linear system with periodic coefficients. A method for analysing stability of time varying periodic system is also described.

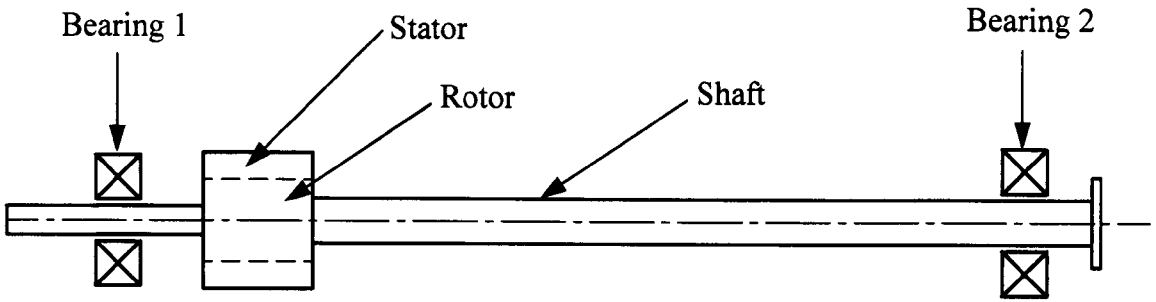


Figure (8.1): Schematic diagram of an induction machine

Table (8.1): Main electromagnetic parameters of the machine

Parameters	Value
Number of poles	4
Number of phase	3
Number of stator slots	36
Outer diameter of the stator [mm]	153
Inner diameter of the stator [mm]	93
Number of rotor slots	32
Outer diameter of the rotor [mm]	92.2
Air gap radial thickness [mm]	0.4
Length of the rotor [mm]	123
Rated voltage [V]	415
Rated frequency [Hz]	50
Rated power [kW]	2

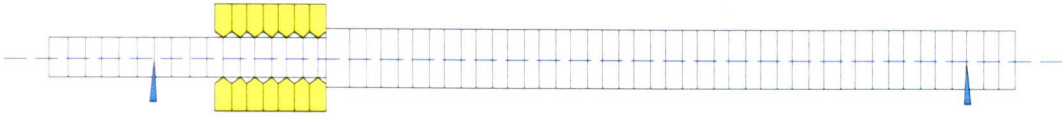


Figure (8.2): Finite element model of the induction machine

Table (8.2): Coefficients of the bearing

	Stiffness (in N/m ²)				Damping (in N/m ²)			
	k_{xx}	k_{xy}	k_{yy}	k_{yx}	c_{xx}	c_{xy}	c_{yy}	c_{yx}
Brg. #1	5.0 e7	0.0	5.0 e7	0.0	0.0	0.0	0.0	0.0
Brg. #2	5.0 e7	0.0	5.0 e7	0.0	0.0	0.0	0.0	0.0

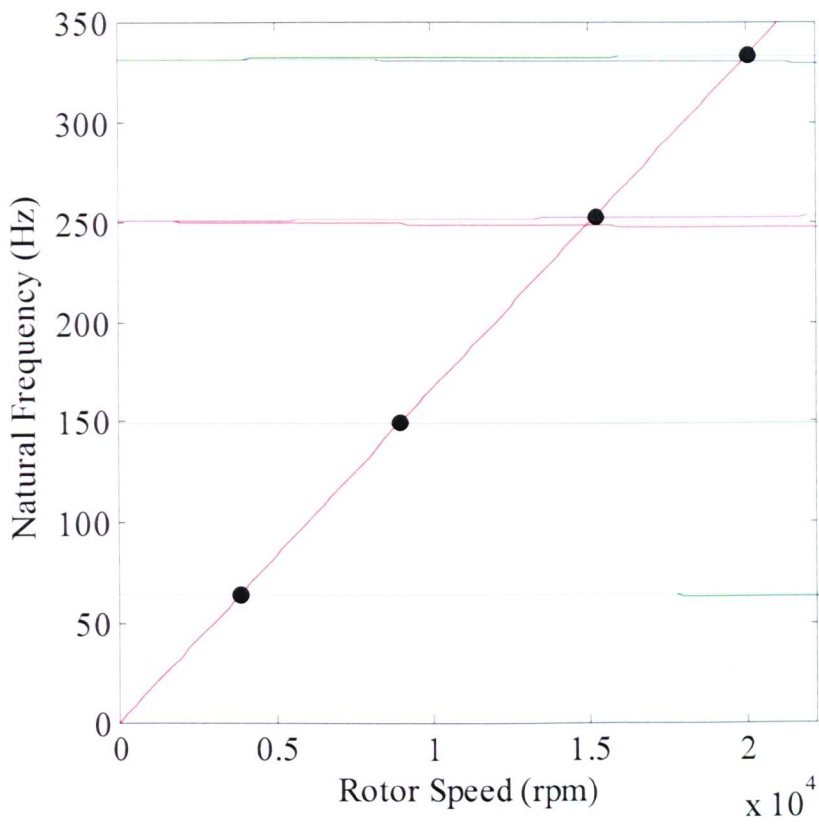


Figure (8.3): Natural speed versus rotor speed

First Critical

Second Critical



Third Critical

Fourth Critical



Figure (8.4): First four modes of the system

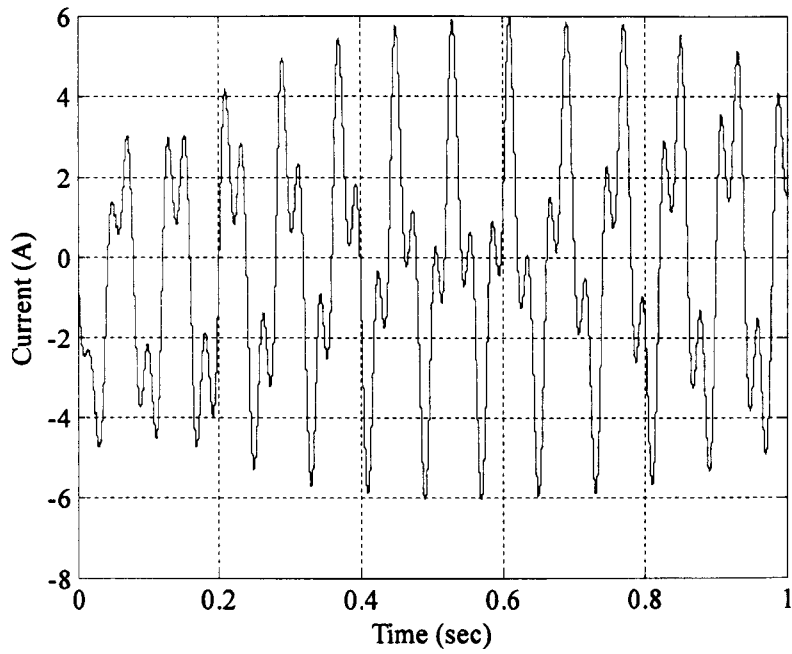


Figure (8.5): Equalising current per meter of axial length in phase A bridge for an eccentricity of 2% of the air gap and when supply frequency is 25 Hz and slip is 2%

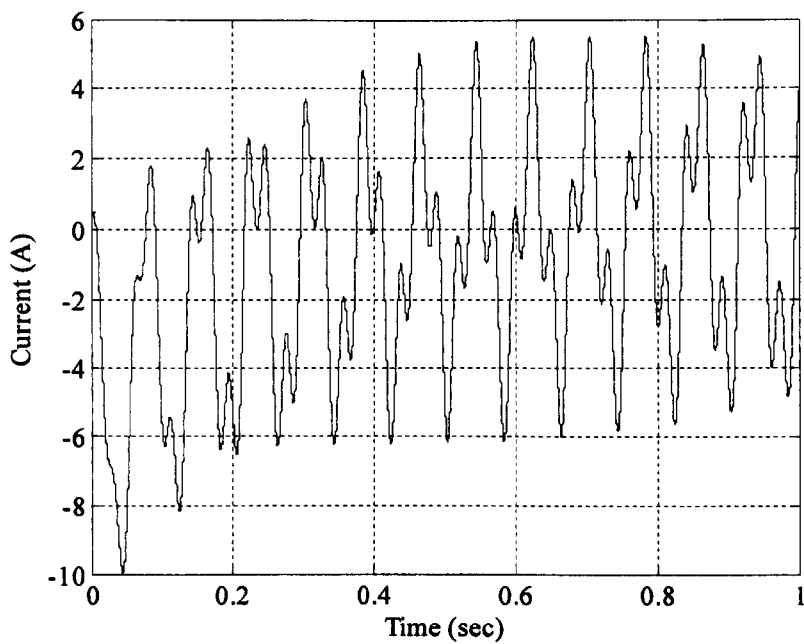


Figure (8.6): Equalising current per meter of axial length in phase B bridge for an eccentricity of 2% of the air gap and when supply frequency is 25 Hz and slip is 2%

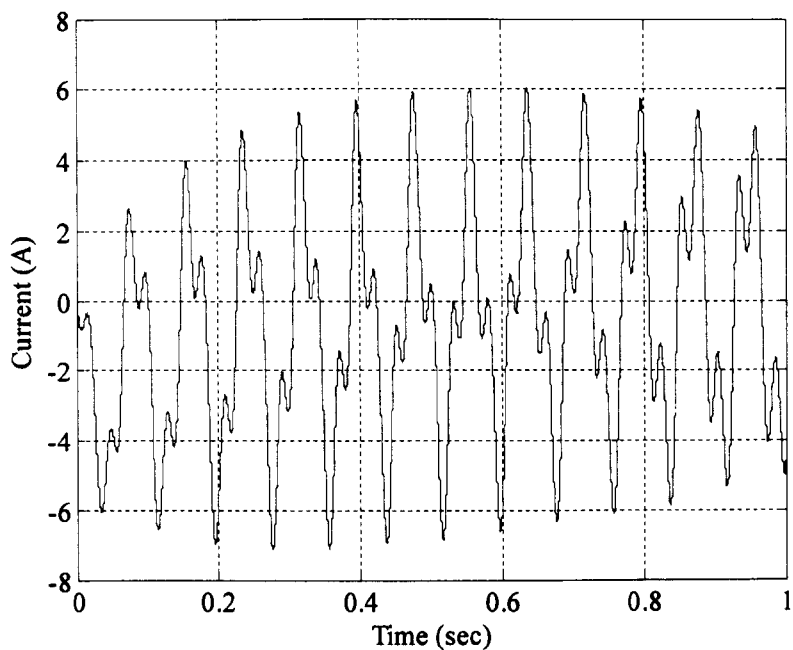


Figure (8.7): Equalising current per meter of axial length in phase C bridge for an eccentricity of 2% of the air gap and when supply frequency is 25 Hz and slip is 2%

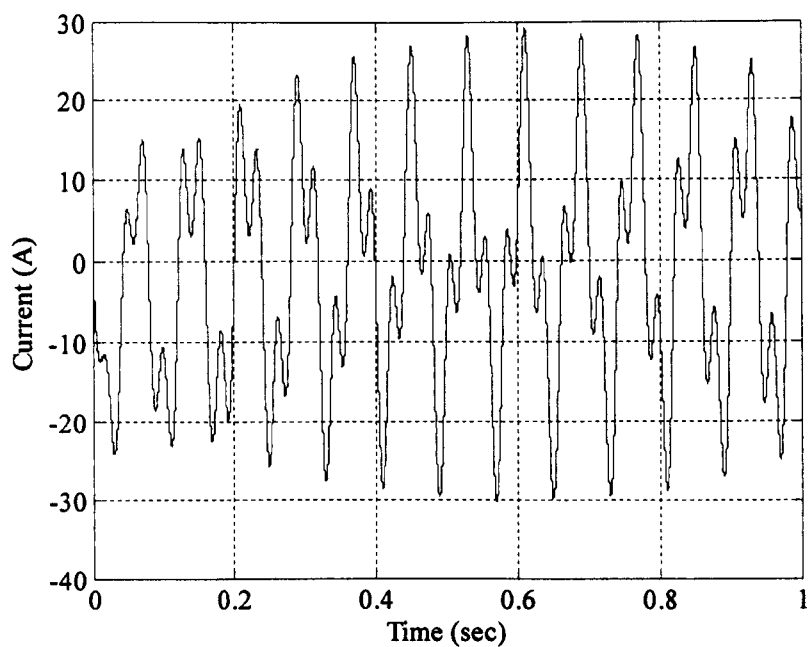


Figure (8.8): Equalising current per meter of axial length in phase A bridge for an eccentricity of 10% of the air gap and when supply frequency is 25 Hz and slip is 2%

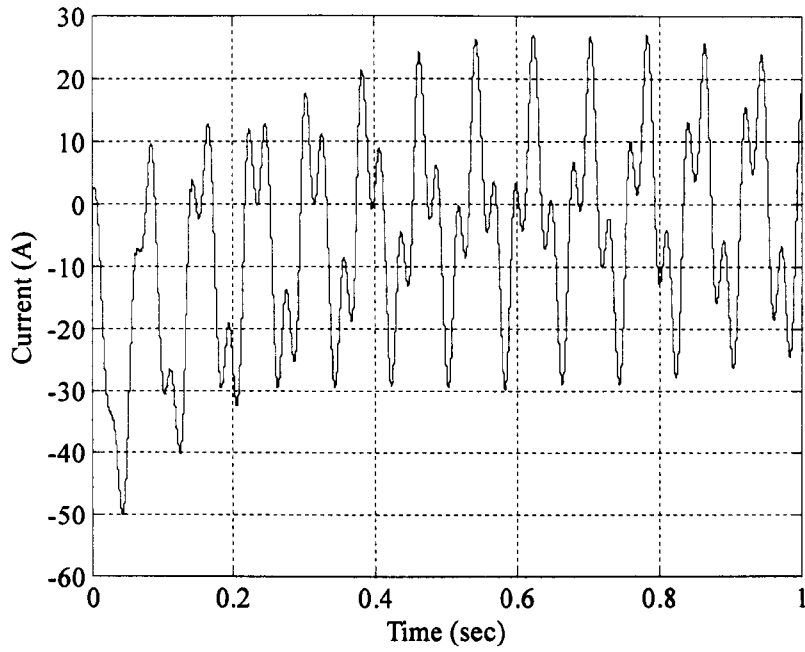


Figure (8.9): Equalising current per meter of axial length in phase B bridge for an eccentricity of 10% of the air gap and when supply frequency is 25 Hz and slip is 2%

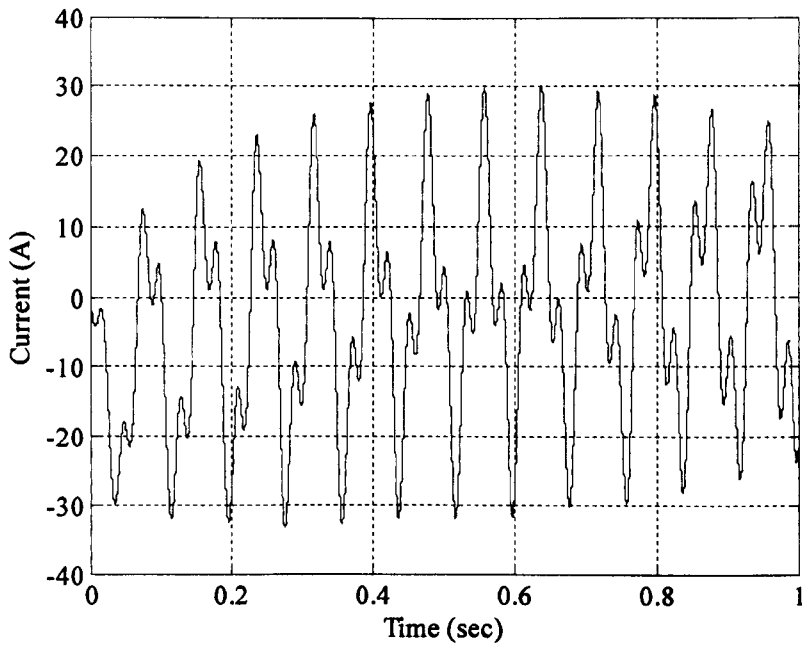


Figure (8.10): Equalising current per meter of axial length in phase C bridge for an eccentricity of 10% of the air gap and when supply frequency is 25 Hz and slip is 2%

Table (8.3): The minimum periods of a machine with parameters given in Table (8.1) for different slips

Slip (%)	Period of the system (s)
0.5	1.00
1.0	1.00
1.5	1.00
2.0	1.00
2.5	0.20
3.0	1.00
4.0	1.00
5.0	0.20

Table (8.4): Stability chart of the machine at different slips for different voltage levels

Supply Voltage (V)	Stability of the machine at different slips for different voltage levels					
	Slip = 0	Slip = 0.5% Period = 1s	Slip = 1% Period = 1s	Slip = 2 % Period = 1s	Slip = 2.5% Period = 0.2s	Slip = 5.0% Period = 0.2s
17.0	√	√	√	√	√	√
20.4	√	√	√	√	√	√
22.1	√	√	√	√	√	√
25.5	√	√	√	√	X	X
34.0	√	√	X	X	X	X
51.0	X	X	X	X	X	X

Table (8.5): Time constants with the parallel paths closed for five different slips in case of forward whirling

Supply Voltage	Time constants (s)				
	Slip = 0	Slip = 0.5% (Period= 1s)	Slip = 1% (Period= 1s)	Slip = 2 % (Period= 1s)	Slip = 5% (Period= 1s)
17V	0.00187160	0.00173507	0.00146956	0.00117471	0.00157921
34V	4.6790e-004	4.3377e-004	3.6739e-004	2.9368e-004	3.9480e-004

Table (8.6): Time constants with the parallel paths closed for five different slips in case of backward whirling

Supply Voltage	Time constants (s)				
	Slip = 0	Slip = 0.5% (Period= 1s)	Slip = 1% (Period= 1s)	Slip = 2 % (Period= 1s)	Slip = 5% (Period= 1s)
17V	0.39781394	0.37390752	0.29176840	0.20925626	0.15278131
34V	0.09945348	0.09347688	0.07294210	0.05231406	0.03819532

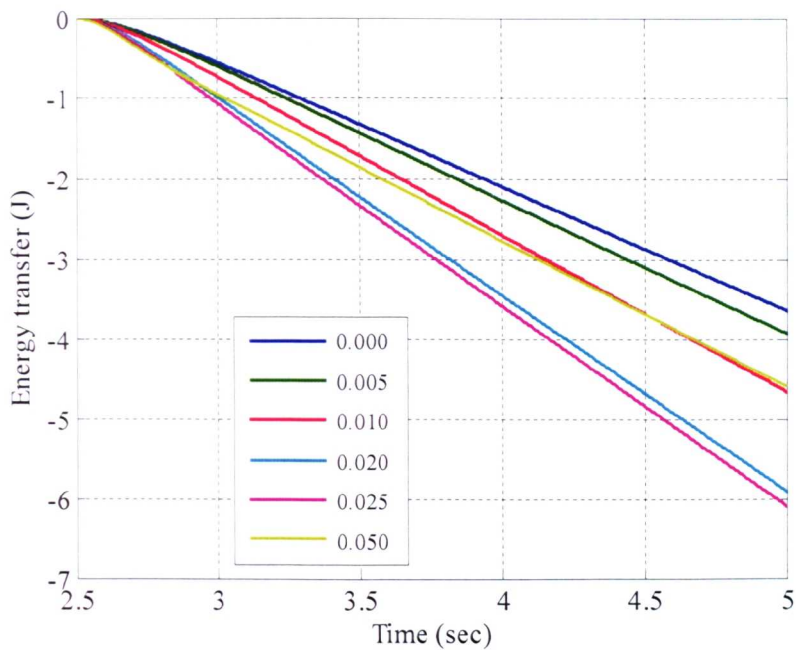


Figure (8.11): Energy transfer to the electrical system from the mechanical motion due to forward whirling for different slips

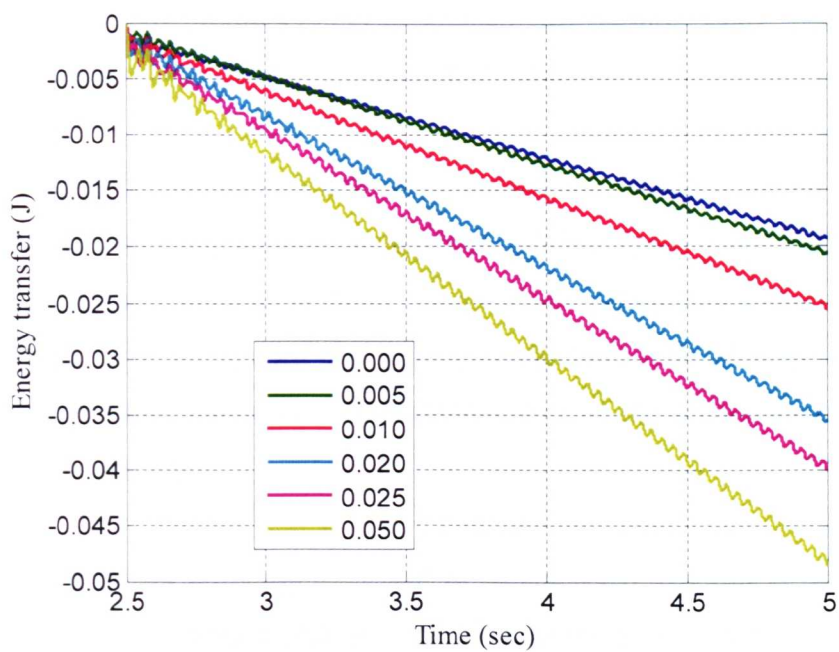


Figure (8.12): Energy transfer to the electrical system from the mechanical motion due to backward whirling for different slips

Chapter Nine

Methods for Reducing Unbalanced Magnetic Pull

9.1 Introduction

Several people have studied UMP due to eccentricity and most notably Belmans *et al.* (1984), Kovács (1977) and Frunchtenicht (1982) but very few people has recommended methods for reducing UMP. Among these are Bradford (1968), Krongl (1956) and Dorrell and Smith (1994). Bradford's (1968) experimental machine consists of a 6-pole series connected type which could be used in conjunction with a blank, wound and a cage rotor. He concluded that because of its parallel paths cage rotor damped the UMP much higher degree than blank and wound rotors. Krongl (1956) and Dorrell and Smith (1994) concluded that parallel stator windings damp UMP which in turn reduces the motor noise and vibrations.

A generic method for reducing UMP using secondary windings in the stator of an electrical machine was put forward by Kozisek (1935), Garvey and Watson (2004). One drawback of these methods is that it occupies some space in the stator slots which otherwise could have been used for torque production. The effectiveness can be increased by increasing the total cross sectional area of the secondary coils but at a sacrifice of main windings.

One passive method for reducing the UMP in an electrical machine is discussed here and its effectiveness is verified with an experimental setup in Chapter 10. The method uses the main torque producing winding to suppress the UMP due to eccentricity. In this chapter the working principles of this method is discussed.

9.2 Reduction of UMP in an induction machine using bridge windings

The bridge configured windings, first introduced by Khoo (2005), overcomes the drawback of secondary windings proposed by Garvey and Watson (2004). This unique scheme has three-phase terminals for torque production and additional terminals for active or passive magnetic bearing action control. Active control can be deployed by connecting the terminals devoted to lateral forces to closed-loop controllable current or voltage sources. Passive control of UMP can be accomplished by short circuiting the additional pairs of terminals or “closing the bridge”. In this work only the passive control of UMP feature of this bridge winding is introduced. Both torque-producing and induced currents flow in the same set of conductors in the bridge configured winding scheme. A detailed explanation about the bridge configured winding can be found in (Khoo, 2005).

Figure (9.1) depicts a three-phase induction motor having distributed coils wound on a 36-tooth stator. Coil groups “ a_1 - a_2 - a_3 ” and “ a_4 - a_5 - a_6 ” are wound and aligned at the same axis of symmetry. Likewise, coil group “ aa_1 - aa_2 - aa_3 ” and “ aa_4 - aa_5 - aa_6 ” are wound at the diametrically opposite tooth and their terminals are connected to coil group “ a_1 - a_2 - a_3 ” and “ a_4 - a_5 - a_6 ” to form a bridge. Coils in phases “B” and “C” are connected in a similar manner.

No current will flow across the bridge if the rotor is concentric and the stator MMF is symmetric (flux field is uniformly distributed) i.e. bridges i_{Alev} , i_{Blev} and i_{Clev} are zero. Any unbalance of field due to eccentricity will induce an EMF tending to drive currents in the closed circuit such that a MMF comes to exist opposing the rate of change of this field. The currents flowing across the bridge are known as equalising currents. The feature which makes the bridge winding different from the other passive methods for reducing UMP is its provision for active control. When the bridge is connected to a controllable power supply with feedback control, the rotordynamic behaviour of the machine can be controlled. Additional currents required to bring the rotor to the centre will be provided by the controllable power supply. With proper control strategy the response of a flexible system at critical speeds can be subdued

dramatically by using this controlled UMP within the electrical machine (Khoo, *et al.*, 2004).

9.3 Conclusions

One method of passive control of UMP of an electrical machine is discussed. Though only the passive feature of bridge configured winding is studied in this study, the machine with the bridge configured windings can be used for active control of UMP. The bridge configured winding possess many interesting features which are beyond the scope of this study. Some of them are explained in (Khoo, *et al.*, 2004) and (Khoo, *et al.*, 2005). For secondary windings to be effective in reducing the UMP one must increase the number of turns of the secondary windings and this call for extra space in the stator slot. For the same performance the machine with the bridge configured windings will be smaller in size and weight than those with secondary windings.

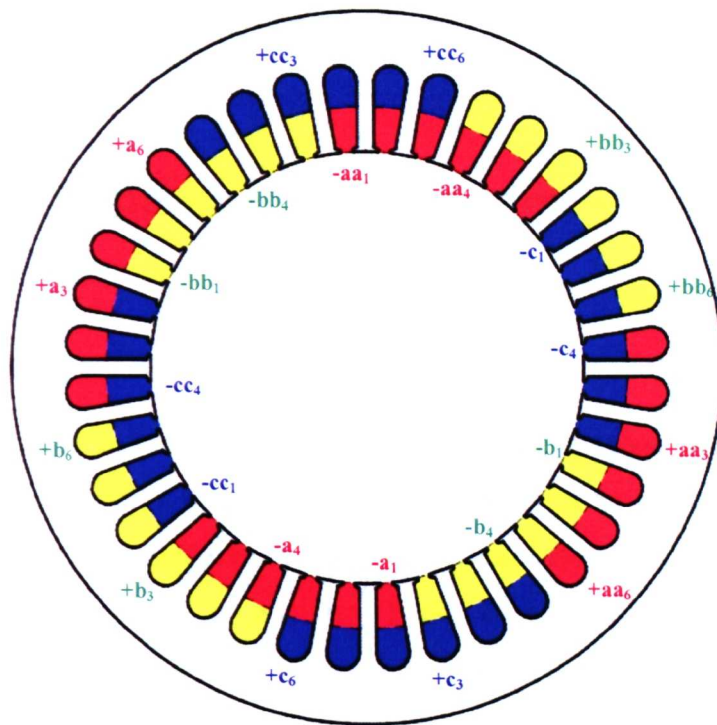


Figure (9.1): Stator of an electrical machine showing the winding connection. Red, blue and yellow colours show the three different phases.

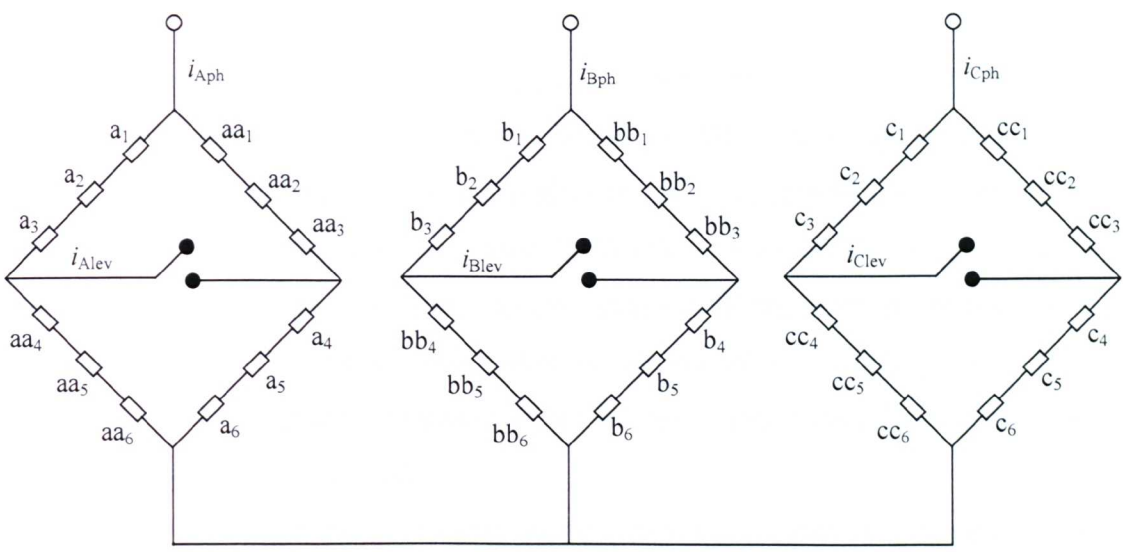


Figure (9.2): 4-pole, 3-phase induction motor with a bridge configured windings

Chapter Ten

Experimental Validation

Chapter 5 describes the modelling of an electro-magneto-mechanical device and describes the coupling of circuit equation and field equation of an electrical machine. Chapter 6 describes different methods of calculating steady state characteristics of an induction machine using linear as well non-linear FEA. Chapter 7 describes a numerical model which unifies electromagnetic and mechanical dynamics. Using this numerical model Chapter 8 also analyses the stability of a 4-pole, 3 phase 2 kW induction motor. Chapter 9 describes the method of reducing UMP using equalising connections.

10.1 Introduction

Often experiments are required for accurate determination of machine parameters. Some physical phenomena are difficult to model accurately and experiments are also required for clear understanding of these phenomena. An experimental setup has been commissioned to investigate the electromechanical interactions of an induction machine. The parameters of the machine are chosen to be the same as the machine for the case study in Chapter 8. The motor is wound as a 3 phase, 4-pole bridge configured windings, which as explained in Chapter 9. The aims of this experimental study can be summarised as follows:

- Verify the results of the coupled model (numerical) combining the electrical and mechanical dynamics proposed in Chapter 8.
- Investigate the effectiveness of the bridge configured windings as a passive method for reducing UMP.

In this chapter, the experimental procedures to investigate the electromechanical interaction of an induction machine are described. Experimental results are presented

and compared with the numerical results. The effects of equalising connections produced by bridge configured windings in reducing UMP are clearly demonstrated.

10.2 Design of the test rig

The design of the test rig is divided into two categories: electrical and mechanical design. They are discussed in the following sections.

10.2.1 Motor electrical design

The electrical motor is a 4-pole induction motor with 2 kW capacity. The main electromagnetic parameters of the machine are given in Table (8.1) of Chapter 8.

10.2.1.1 Winding scheme

The main torque-producing stator winding is connected according to the bridge configured winding scheme [Khoo, *et al.* (2002), Khoo, *et al.* (2005)], forming a four-pole motor configuration. The bridge configured winding is a unique scheme and it has three-phase terminals for torque production and additional terminals for active or passive bearing action control. The winding scheme of the machine in the experimental rig is a 4-pole, 3-phase double layered fractional pitch windings. Figure (8.1) depicts a three-phase induction motor having distributed coils wound on a 36-tooth stator. Coil group “ $a_1-a_2-a_3$ ” are connected in series with coil group “ $aa_4-aa_5-aa_6$ ” and this coil group in turn is connected in parallel with series group “ $aa_1-aa_2-aa_3$ ” and “ $a_4-a_5-a_6$ ”. Coils in phases “B” and “C” are connected in a similar manner. Details about the passive control of UMP using this winding scheme can be found in Chapter 9.

10.2.1.2 Full pitch and fractional pitch

The pole pitch is the angular distance between two adjacent poles on a machine. The pole pitch of a machine in mechanical degrees is

$$\rho_p = \frac{360^\circ}{2p} \quad (10.1)$$

where ρ_p is the pole pitch in mechanical degrees and p is the number of pole pairs of the machine. Regardless of the number of poles on the machine, one pole pitch is always 180 electrical degrees. If the stator coil stretches across the same angle as the pole pitch, it is called a full-pitch coil. If the stator coil stretches across an angle smaller than a pole pitch, it is called a fractional-pitch coil. The pitch of a fractional-pitch coil is expressed as a fraction indicating the portion of the pole pitch it spans. There are good reasons for using fractional-pitch windings (Chapman, 1998). These concern the effect of the non-sinusoidal flux density distribution in real machines. The MMF produced by the coils is not sinusoidal and it contains many harmonics. When the voltage waveform is symmetric about the centre, no even harmonics are present in the phase voltage. However, all the odd harmonics (third, fifth, seventh, ninth, etc) are present in the phase voltage to some extent and need to be dealt with the machines. Table (10.1) shows the harmonics for full pitch and fractional pitch of the voltage waveform. In the test rig we have chosen the fractional- $\frac{6}{9}$ because amongst the cases shown in the table it has the lowest proportion of the third harmonic. The fractional-pitch reduces the magnitude of the output voltage slightly, but at the same time attenuates the harmonics components. Figure (10.2) shows the MMF harmonics with fractional pitch - $\frac{6}{9}$ of the stator windings.

10.2.1.3 Number of turns in each coil

In this subsection the calculation used in designing the machine winding is described. The number of turns per coil is calculated for the winding scheme proposed in the experimental rig based on the total flux density of 1 Tesla in the airgap. We assume that the MMF distribution is sinusoidal. First the individual fluxes for the three coils a_1 , a_2 and a_3 are calculated.

$$\text{Coil } a_1 \text{ has flux, } \Phi_1 = r l B_{\max} \int_{-(11\pi/36)}^{+(7\pi/36)} \cos(2\theta) d\theta = r l B_{\max} \text{ Wb}$$

where l is the axial length of the machine, r is radius of the rotor and B_{\max} is the maximum flux density.

$$\text{Coil } a_2 \text{ has flux, } \Phi_2 = r l B_{\max} \int_{-(\pi/4)}^{+(\pi/4)} \cos(2\theta) d\theta = 0.939 r l B_{\max} \text{ Wb}$$

$$\text{Coil } a_3 \text{ has flux, } \Phi_3 = r l B_{\max} \int_{-(7\pi/36)}^{+(11\pi/36)} \cos(2\theta) d\theta = 0.939 r l B_{\max} \text{ Wb}$$

Total flux, $\Phi = 2.878 r l B_{\max}$ Wb. For a rotor of length, $l = 123$ mm and radius, $r = 46$ mm and $B_{\max} \approx 1.0$ Tesla, the total flux, Φ is 16×10^{-3} Wb.

In the case of bridge configured windings three full coils, a_1 , a_2 , and a_3 together forms a coil group as shown in Figure (8.2) of Chapter 8. There are four coil groups per phase. Since there are four coil groups per phase and the total voltage, E_{\max} in one phase in which the coils each carry N turns is

$$E_{\max} = 4\Phi(2\pi f)N \quad (10.2)$$

where f is the supply frequency. From Equation (10.2) we get

$$N = \frac{E_{\max}}{4\Phi(2\pi f)} \quad (10.3)$$

Using the above calculated values for Φ and considering the values for E_{\max} and supply frequency is 415 V and 50 Hz respectively, the value of N is found to be 17.

10.2.2 Drive system for the motor and electrical sensors

10.2.2.1 Drive system for the motor

A frequency converter is the best way to control the speed of an induction machine. The most common frequency converter type is the voltage-source converter with pulse width modulation (PWM). The frequency converter used to control the

induction used is manufactured by ABB (ACS140) and has a power ratings of up to 2.2 kW. The motor voltage consists of rectangular pulses with a switching frequency as high as (3-20 kHz). The currents are nearly sinusoidal since the motor is inductive and the very high frequency components associated with carrier frequency and multiples of that are fairly effectively filtered out.

10.2.2.2 Current transducers

Hall effect closed loop (compensated) multi-range current transducers (LTS 15NP) are used to measure the currents. These current transducers can measure DC, AC, pulsed currents and equipped with a galvanic isolation between the primary circuit (high power) and the secondary circuit (electronic circuit). Because of its compact design it can be easily mounted on a PCB. This current transducer has an extended measuring range. In the present case, we set the range at -15 to +15 A. The measuring currents have a linear relation with the output voltage with linearity $< 0.1\%$. The current transducers were calibrated to measure between -5.5 to +5.5 A. The output voltage is fed to a data acquisition system for further processing.

10.2.2.3 Voltage transducers

Hall effect Closed loop (compensated) voltage transducers (LV 25NP) are used to measure the voltages. This voltage transducer can measure DC, AC, pulsed voltages and equipped with a galvanic isolation between the primary circuit (high power) and the secondary circuit (electronic circuit). The measuring range is configurable. We have set the range at -100 to +100 V. The measured voltage has a linear relation with the output voltage with linearity $< 0.2\%$. The voltage transducers were calibrated to measure between -74 to +74 V. The output voltage is fed to a data acquisition for further processing.

10.2.3 Mechanical design of the system

For an eccentric rotor a significant UMP force is produced in the airgap usually tending to pull the rotor even further away from the concentric position. Thus for a

stable operation the mechanical stiffness of the shaft must be greater than the negative stiffness introduced by the UMP.

The mean airgap for the induction machine used in this experimental rig is 0.4 mm. The negative stiffness is the slope of the curve of magnetic force in the airgap versus displacement of the rotor. Magnetic forces are calculated by solving the magnetic field when the rotor is shifted from centre along positive x -direction as well as negative x -direction. Figure (3.17) of Chapter 3 shows the magnetic forces per unit of axial length versus eccentricity of the rotor when 3-phase currents with a peak of 200 A (per slot) is applied. The slope of this curve is 2×10^6 N/m per meter of the axial length. From this negative stiffness the total load is calculated for a travel of the airgap and this is ≈ 800 N. The shaft is designed for up to a loading capacity of 1000 N. This force is regarded as a concentrated load on a simply supported beam. The diameter of the shaft is calculated based on the assumption that the deflection of the beam in the motor position is 30% of the airgap. Figure (10.3) shows a simply supported beam with a concentrated load. The deflection of the beam under the load is

$$\delta_w = \frac{Wa^2(l-a)^2}{3EI} \quad (10.4)$$

where W is the concentrated load, R_1 and R_2 are the reaction forces, a is the distance of W from reaction force, R_1 , l is the length of the beam. In our case: $W = 1000$ N, $a = 156.5$ mm, and $l = 1020$ mm. It is found that for a 50 mm diameter shaft the deflection under the load is nearly equal to 25% of the airgap. Thus a shaft with diameter of 50 mm is chosen for the rig.

10.2.4 Other transducers

The impact hammer method is a convenient and economical excitation method for injecting known inputs into a vibrating system. The impact hammer consists of a hammer with a piezoelectric force transducer at its tip. The impact hammer is highly portable for fieldwork and provides no unwanted mass loading to the structure under test. The impact hammer produces an impulse force at one hit, which excites the

structure with a constant force over a frequency range of interest. The waveform produced by an impact hammer is an impulse. The test setup for impact hammer excitation experimental is shown in Figure (10.4). An impact hammer with an output of 0.01 Volts/g is used to supply an impulse force signal. A signal conditioner is used for conditioning the input force signal. The input signal is measured using a multi-channel signal analyser.

Aluminium foil strain gauges are mounted in the bearing housing at one end of the shaft. Figure (10.5) shows the strain gauges along with the bearing in the rig. Figures (10.6) and (10.7) show the strain gauge calibration curves for forces along x and y directions. The test setup is shown in Figure (10.1). Horizontal and vertical forces are measured separately and fed into the oscilloscope. The vertical force signal is measured using a multi-channel signal analyser.

10.2.5 Data acquisition

The sensor or transducer signals are often incompatible with the data acquisition interface and these signals must be conditioned before they are fed to a data acquisition interface. The analog signals are converted to digital signals via the analog to digital converter of the data acquisition interface. The data acquisition card used is a dSPACE DS1104 R&D Controller Board. The whole unit is used in conjunction with Matlab, Simulink and Real time workshop software package. The data acquisition card has 8-channels where 4 multiplexed channels equipped with one sample and hold A/D converters, another 4 parallel channels each equipped with one sample and hold converters.

10.3 Numerical model verification with experimental results

Figure (10.8) shows a schematic diagram of the experimental rig. The rig consists of a 4-pole 2 kW induction motor with a long and flexible shaft. This motor is wound with fractional pitch double-layered bridge-configured windings. The stator of the machine with the winding connections and the bridge configured winding scheme are shown in Figures (4.2) and (4.7) of Section 4 respectively. The shaft is supported by preloaded

angular contact ball bearings at each end. This whole assembly is fixed on the top of a steel plate. Strain gauges are mounted in the bearing #1 which is situated in the left hand side of the shaft. The right end of the shaft is attached to another shaft via a flexible bellows coupling and this second shaft is coupled to another induction motor via a belt drive. The second induction motor is used as a brake by applying DC currents across the terminals (plug braking). This section compares the results from the numerical model with that of experiments.

10.3.1 Mechanical model

The development of the mechanical model can be found in Section (7.3) of Chapter 7. We can write the equation of motion of the mechanical model as

$$[M]\{\ddot{q}\} + ([D] + \Omega [G])\{\dot{q}\} + ([K_{\text{mech}}] + \Omega [F])\{q\} = \{f\} \quad (10.5)$$

where $\{[M], [D], [K]\}$ denote mass, damping and stiffness matrices. The mean rotational speed of the rotor is denoted by Ω .

In Chapter 8 we have solved the mechanical model numerically using FEM without considering the effect of the base plate.

Tests using an impact hammer test are used to investigate the mode shapes of the rig. The experimental setup for the impact hammer test is shown in Figure (10.8). The hammer produces an impulse force at a single hit and this excites the structure with a fairly flat force spectrum over a given range of frequency. The response signals are captured with the strain gauges and these signals are amplified and conveyed to a signal analyser. We have chosen 12 locations for excitation on the rig i.e. 5 points on the shaft and 7 points on the base plate. The frequency range is selected as 0-160 Hz. Frequency response functions were obtained taking 16 averages at each location in order to reduce the effects of the noise. The shaft was rotating while the FRFs were being obtained. We get a total of 12 FRFs. Figure (10.10) shows a FRF at when the impulse is applied at point 3 on the shaft. Mode shapes can be calculated once the FRF at 12 points is obtained by solving the following equation

$$h_{ij}(\omega) = \sum_{k=1}^n \frac{\phi_{R,ik} \phi_{L,jk}}{(\lambda_{kk} + j\omega\gamma_{kk} - \omega^2)} \quad (10.6)$$

where $h_{ij}(\omega)$ is one entry of the frequency response matrix, λ_{kk} is the k -th eigenvalue, ω is the excitation frequency, $\phi_{L,ik}$ represents the amount by which one unit of excitation at input degree of freedom $\#j$ excites mode $\#k$ and $\phi_{R,ik}$ represents the amount of output at output degree of freedom $\#i$ is contributed by each mode $\#k$. The derivation of frequency response matrix for a second order system is explained in Appendix B.

Figures (10.11), (10.12), (10.13) and (10.14) show the modes shapes of the rig at 1.35 Hz, 58.61 Hz, 65.78 Hz and 72.39 Hz respectively. The deflected and un-deflected rotor and base are shown separately and they are distinguished by different colours. Mode shapes obtained from the numerical model are shown in Chapter 8. Since the effect of the base plate is not considered in the numerical model explained in Chapter 8, therefore there is a slight difference in the results. The numerical model can be improved by incorporating the effect of the base plate.

10.3.2 Electrical model

The development of electrical dynamics coupling circuit equation with the field equation is explained in Chapter 5. For a constant mechanical speed, Ω_{mech} the electro-magneto-mechanical equation can be written as

$$\{V\} = \left([R] + \Omega_{\text{mech}} \frac{d[L(\{I_{RS}\}, \theta)]}{d\theta} \right) \{I_{RS}\} + [L_{\text{mar}}(\{I_{RS}\}, \theta)] \frac{d\{I_{RS}\}}{dt} \quad (10.7)$$

where $\{V\}$ is the vector of externally-applied voltages, $[R]$ is the resistance matrix of the machine including the effects of the end-windings, $\{I_{RS}\}$ is the vector of independent machine currents, θ is the angular position of the rotor and $[L_{\text{mar}}(\{I_{RS}\}, \theta)]$ is the marginal inductance matrix which is a function of machine

currents and angular position of the rotor. Chapter 6 discusses different methods of calculating marginal inductance of an induction machine. The results of this numerical model are compared with the experimental results of a rig with the same parameters.

To solve the numerical model, the circuit equation [Equation (10.7)] is solved for no-load and locked-rotor conditions using ode45 integration routine of MATLAB. Marginal inductance $[L_{\text{mar}}(\{I_{\text{RS}}\}, \theta)]$ is calculated by solving the field equation using MagFEA, the 2D FEA code developed in the MATLAB environment. Material non-linearity is not considered for this calculation. End winding effects are also not included in the resistance and inductance matrix. The applied voltages at the stator windings terminals are:

$$\left. \begin{aligned} v_A &= V_m \cos(\omega t) \\ v_B &= V_m \cos\left(\omega t - \frac{2\pi}{3}\right) \\ v_C &= V_m \cos\left(\omega t - \frac{4\pi}{3}\right) \end{aligned} \right\} \quad (10.8)$$

The stator and rotor currents are obtained for no-load and locked-rotor conditions for $V_m = 1$ V. These numerical results are compared with the experimental results by scaling the stator and rotor currents according to the voltage obtained from experiments.

The supply voltage and stator terminal currents of the experimental rig are measured using voltage transducers and current transducers respectively for no-load and locked-rotor conditions. The following section compares the experimental results with the numerical results.

10.3.2.1 No-load test

The no-load test of an induction motor measures the rotational losses of the motor and provides information about its magnetization current. The only load on the motor is

the friction and windage losses. Experiments are carried out for the no-load test by spinning the rotor at synchronous speed for different supply frequencies. The supply frequencies are chosen as 20, 25, 30, 35, 40, 45, and 50 Hz. Figures (10.15) and (10.16) show the no-load supply voltages and stator phase currents from numerical model as well as from the experiments when the supply frequency is 20 Hz. The experimental results show a very good agreement with the numerical results. Figures (10.17) and (10.18) show the no-load supply voltages and stator phase currents from both numerical model and experiments when supply frequency is 25 Hz.

10.3.2.2 Locked rotor test

When voltage is applied to the stator windings of an induction motor, EMFs are induced in the rotor circuits of the machine. Generally, the greater the relative motion between the rotor and the stator magnetic fields, the greater the resulting rotor EMFs and rotor frequency. The largest relative motion occurs when the rotor is stationary and this situation is called the locked-rotor or blocked rotor condition, so the largest voltage and rotor frequency are induced in the rotor at that condition. A voltage is then applied to the motor and the resulting voltages and currents are measured with the help of voltage and current transducers respectively. Figures (10.19) and (10.20) show the locked-rotor supply voltages and stator phase currents from numerical model as well as from the experiments. The machine is saturated in the locked-rotor test. As mentioned earlier magnetic saturation is not considered in the numerical model, therefore currents from the experiments are higher than the numerical one.

10.4 Results for the modified motor

As mentioned in Section (10.2.1.1), the induction machine under test is wound with bridge configured windings. This unique winding scheme can be used for torque generation as well as for passive or active modification of UMP. The arrangement of the bridge configured windings shown in Figure (9.2) has two parallel paths with one equalising connection in each phase. Because of the inevitable manufacturing and assembling tolerances, there will be always, to some degree, a non-uniform airgap in an electrical machine. This problem is particularly significant for small and medium

sized induction machines with a nominal airgap of a fraction of 1 mm (Ellison *et al.*, 1971). We expect some degree of non-uniform airgap in our machine.

If the rotor happens to be concentric and if the stator is electromagnetically symmetric, there will be no equalising currents even if the equalising links are short circuited. In case of an eccentric rotor obviously there will be no net equalising currents flowing when the equalising links are not short circuited. Once the equalising links have been short circuited, any unbalance of field present will induce an EMF tending to drive currents in the closed circuit such that a MMF comes to exist opposing the rate of change of this field. Hereafter the short circuited and open circuited links are known as CLOSED bridge and OPEN bridge respectively. This section presents a comparison between measured induced voltages and equalising currents in the bridge and the results obtained experimentally.

10.4.1 Bridge currents and voltages

The induced voltages and currents in the three bridges are measured for CLOSED bridge using voltage and current transducers respectively. Figures (10.21) and (10.22) show the measured equalising voltages and currents respectively for a supply voltage of 20 Hz. Figures (10.23) and (10.24) show the measured equalising voltages and currents respectively for a supply frequency of 25 Hz. An average voltage of 1V is induced in the bridge. The main frequency components of equalising currents are $\frac{1}{2}f_s$, f_s and $\frac{3}{2}f_s$, where f_s is the frequency of the supply voltage. Appendix B provides more results of measured equalising voltages and currents for different supply frequencies.

Section (8.7) of Chapter 8 presents a case study of an induction machine. The electromagnetic parameters of the machine used for this numerical study are the same as the machine used in the experimental rig. The rotor of the machine is shifted from the centre by a known percentage of airgap thickness along x -direction. The eccentricity obtained in this way static. This eccentricity produces harmonics into the airgap field and these harmonics induces currents in the rotor cage as well as in the equalising connections in the bridge configured windings. The steady state currents

are calculated by solving the electro-magneto-mechanical equation of the machine at this eccentric position. As explained in Chapter 4, there are six terminal currents associated with the bridge configured windings. Three of these six currents are the phase currents and the other three currents are bridge currents. The bridge currents are also referred to as equalising currents in this thesis.

Since we do not have knowledge about the eccentricity of the machine in the experimental rig, we can not compare these experimental results with the numerical results presents in Chapter 8 [refer Figures (8.5) to (8.10)]. However, it is noted that the patterns of the equalising currents from experiments are similar to the pattern of equalising currents from numerical simulations. It can be concluded that the magnitude of the equalising currents are a measure of eccentricity present in the machine.

Ellison and Yang (1971) investigated noise reduction using similar types of winding with 2 parallel paths and one equaliser in case of a cage induction motor. They also found that equalising currents vary linearly with the relative eccentricity of the machine.

10.4.2 Reduction of UMP

When we short-circuit the bridge we create paths for equalising currents. The forces on the bearings are calculated for OPEN and CLOSED bridges using strain gauges. The forces acting along horizontal and vertical directions are plotted and the reduction of UMP is investigated for OPEN and CLOSED bridges. Figures (10.25) and (10.26) show the frequency response function and force orbit when the supply frequency is 25 Hz for OPEN and CLOSED bridge. From Figure (10.26) it is seen that by closing the bridge we can reduce UMP by about 75%.

Similar results of reducing UMP using parallel connections are reported by Berman (1993). His experimental findings have shown that using equalising connections in the stator the UMP of an induction machine can be reduced by 25 times.

10.5 Conclusions

An experimental setup has been commissioned to investigate the electromechanical interaction of an induction machine. The design procedure for the electrical and mechanical system is described. The bench mark results of the electrical model as well as the mechanical model of this experiment have been presented. These results are used to verify the coupled model (numerical) described in Chapter 7. The bench mark results of the mechanical model give good agreement. The bench mark results of the electrical model also give good agreement except the locked rotor test. There is some difference in the case of the locked-rotor test of the machine. The effectiveness of bridge configured windings to reduce UMP is clearly demonstrated.

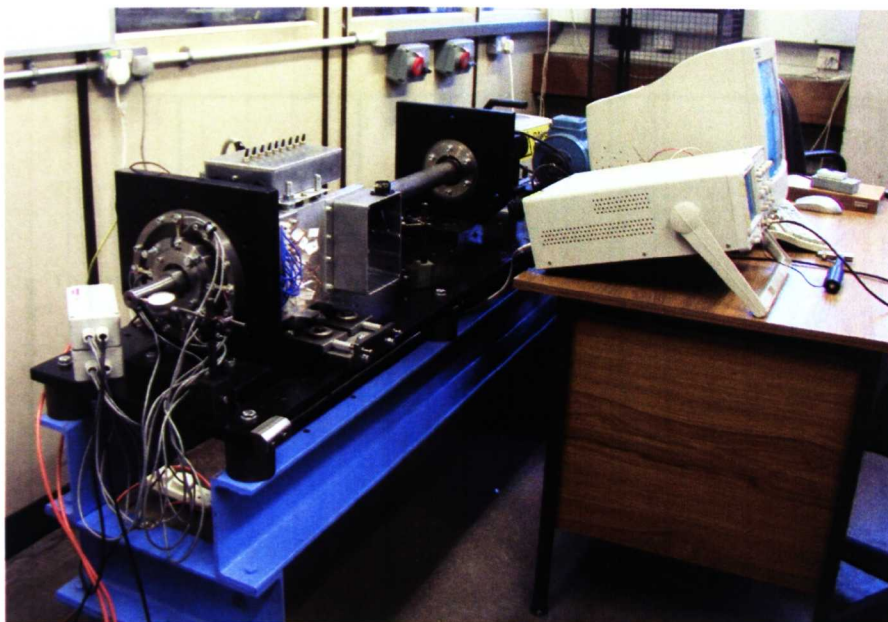


Figure (10.1): Experimental setup

Table (10.1): MMF harmonics with different slot combinations

Harm onics	Full pitch	Fractional - $\frac{8}{9}$	Fractional - $\frac{7}{9}$	Fractional - $\frac{6}{9}$
0	0.001953125000	0	0.001953125000	0
1	3.668218869325	3.609653303498	3.447480634178	3.172590876457
2	0.001953125000	0	0.001953125000	0
3	0.854074066085	0.733379054737	0.428913563056	0.002599583840
4	0.001953125000	0	0.001953125000	0
5	0.172187715542	0.105528021612	0.026702945104	0.142885832007
6	0.001953125000	0	0.001953125000	0
7	0.092907467687	0.033265064671	0.073962024974	0.084433609203
8	0.001953125000	0	0.001953125000	0
9	0.141491198647	0.000434065909	0.141464569607	0.001302181386

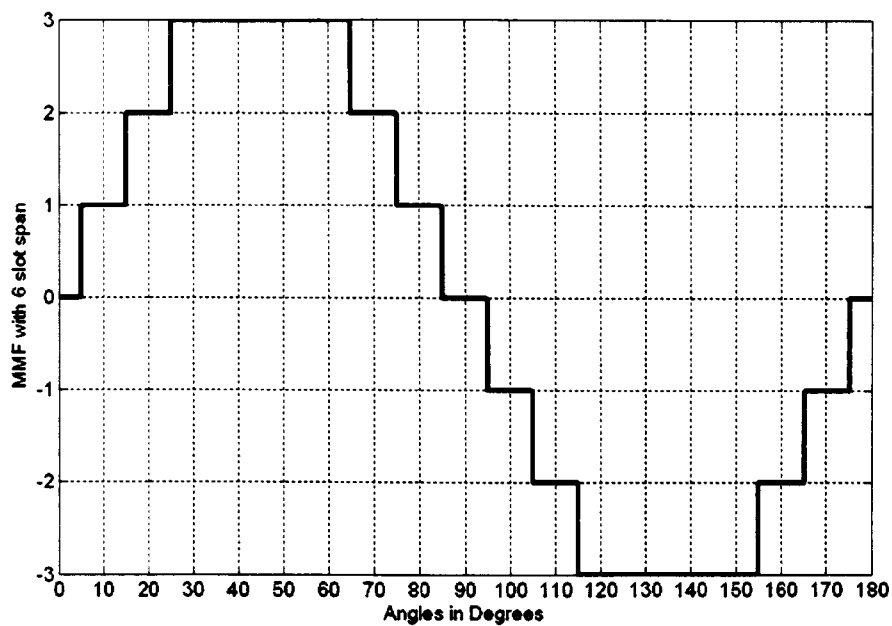


Figure (10.2): MMF harmonics with fractional pitch - $\frac{6}{9}$ of the stator windings

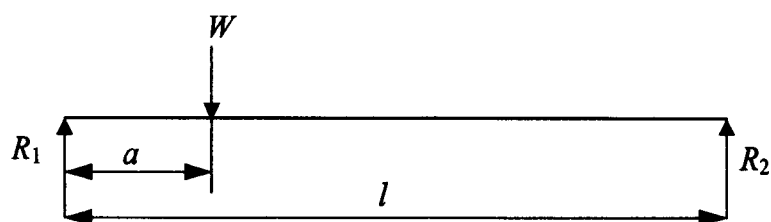
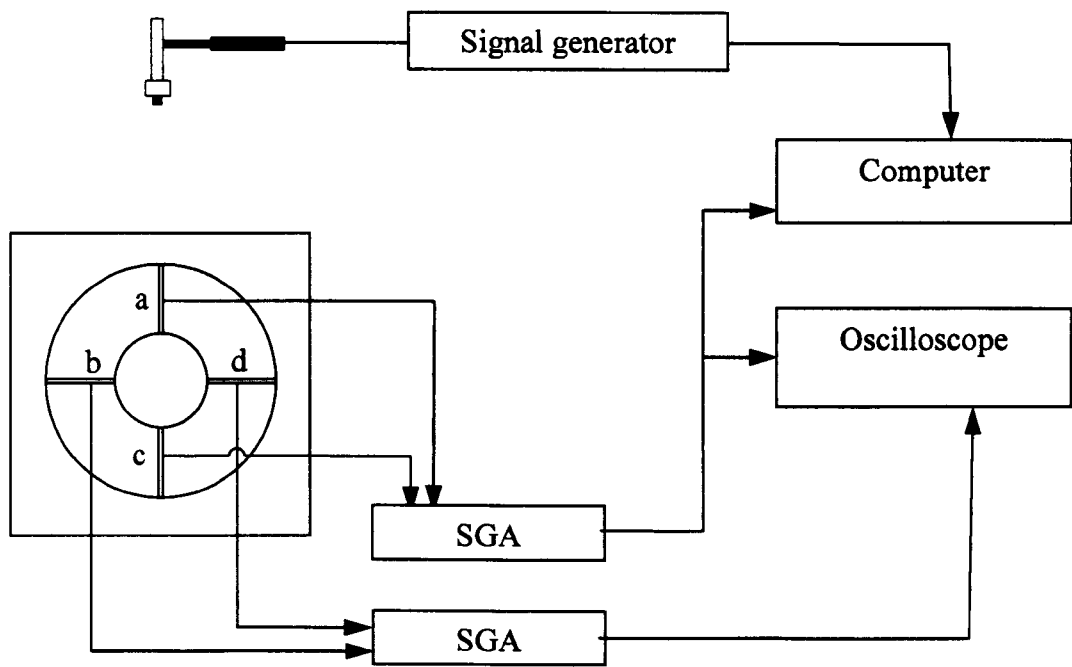


Figure (10.3): A simply supported beam with a concentrated load



a, b, c, and d are the strain gauges

SGA – Strain Gauge Amplifier

Figure (10.4): Test setup of impact hammer excitation experiment

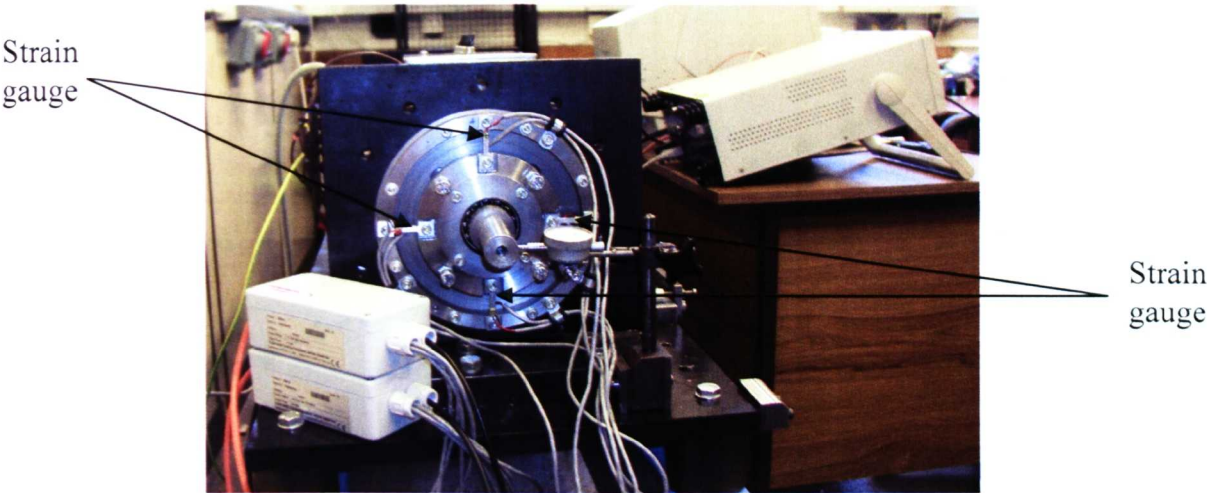


Figure (10.5): Experimental setup showing the stator with the strain gauges

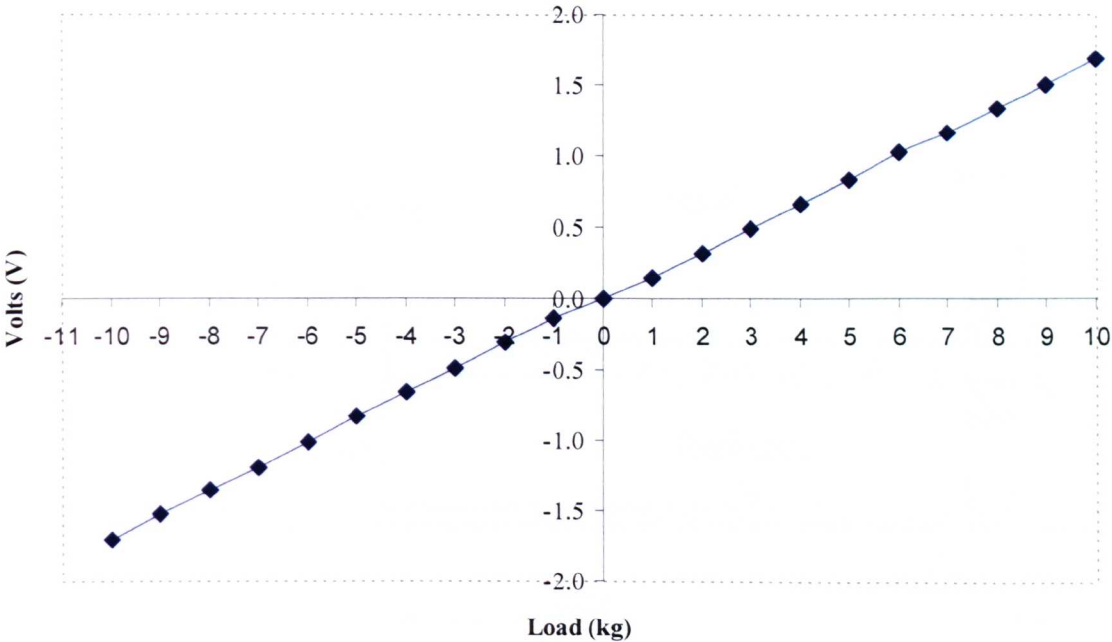


Figure (10.6): Output voltage of the strain gauge amplifier when the load is applied along x-direction

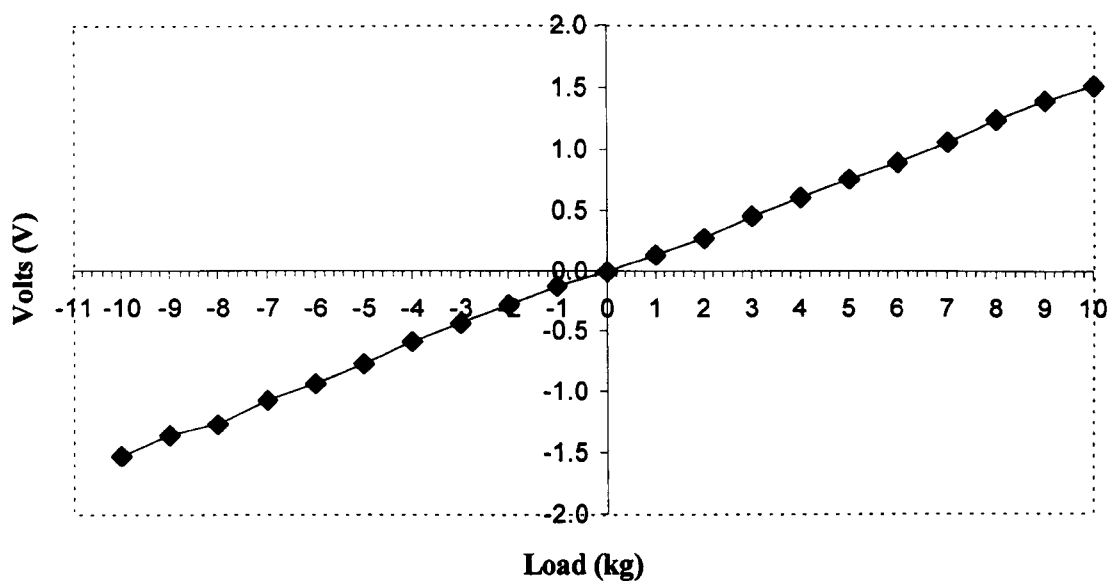


Figure (10.7): Output voltage of the strain gauge amplifier when the load is applied along y -direction

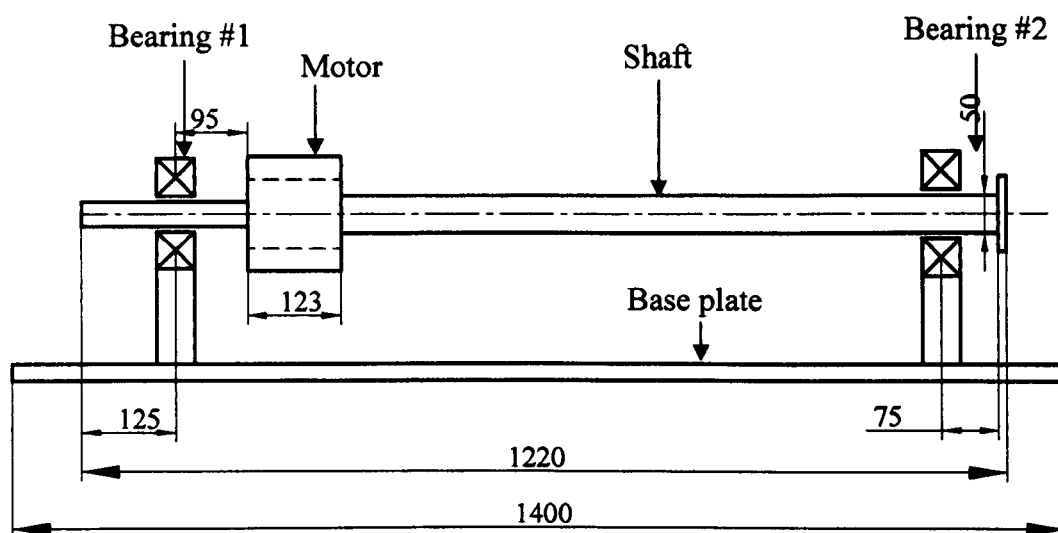


Figure (10.8): A schematic diagram of the experimental rig (all dimensions are in mm)

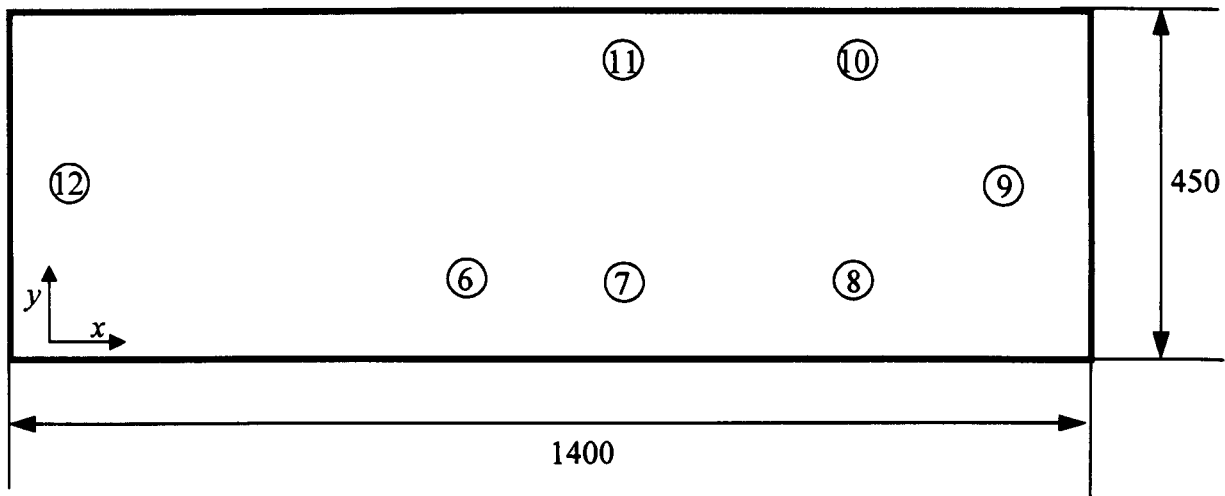


Figure (10.9a): Excitation points on the base of the experimental rig

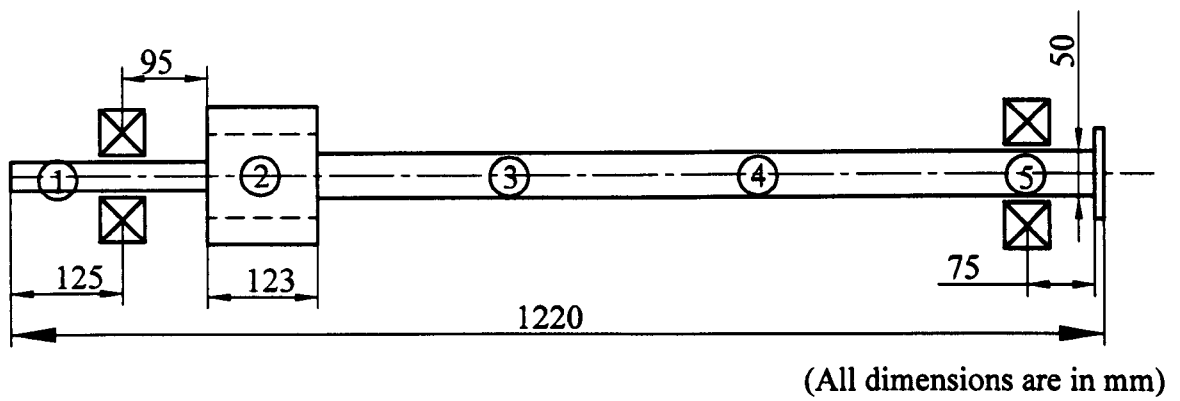


Figure (10.9b): Excitation points on the shaft of the experimental rig

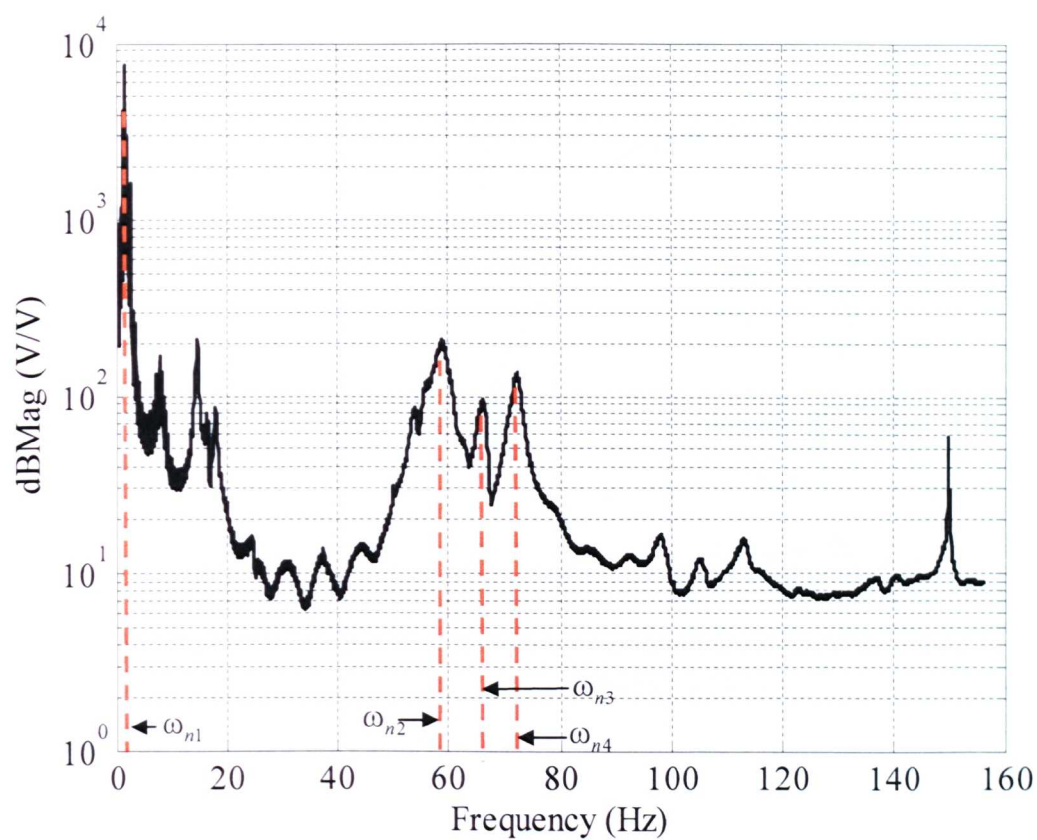


Figure (10.10): Frequency responses from the strain gauge in dB (V/V) for non-rotating shaft.

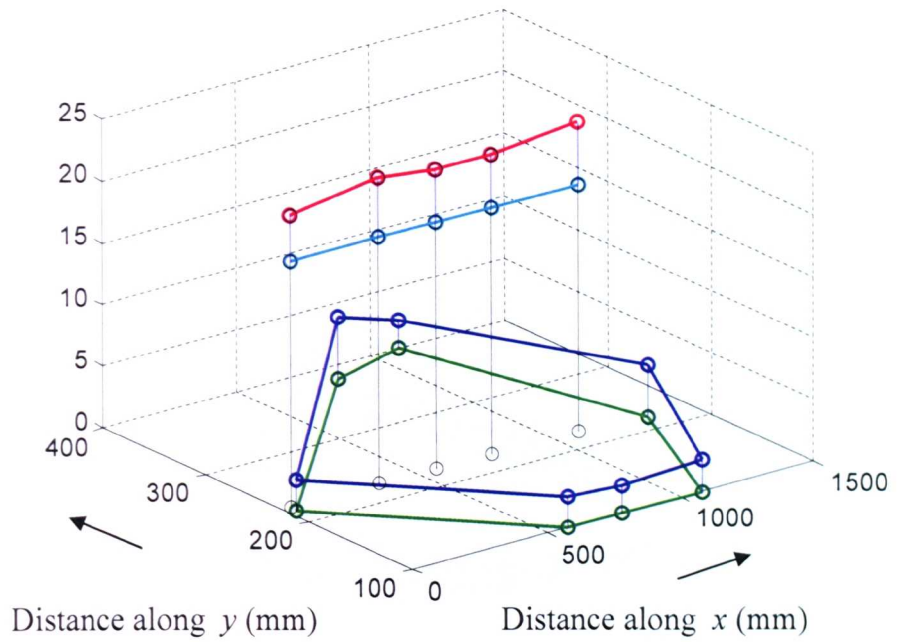


Figure (10.11): Mode shape at 1.35 Hz. ‘Cyan’ and ‘red’ colours show the un-deflected and deflected rotor respectively. ‘Green’ and ‘blue’ colours show the un-deflected and deflected base respectively.

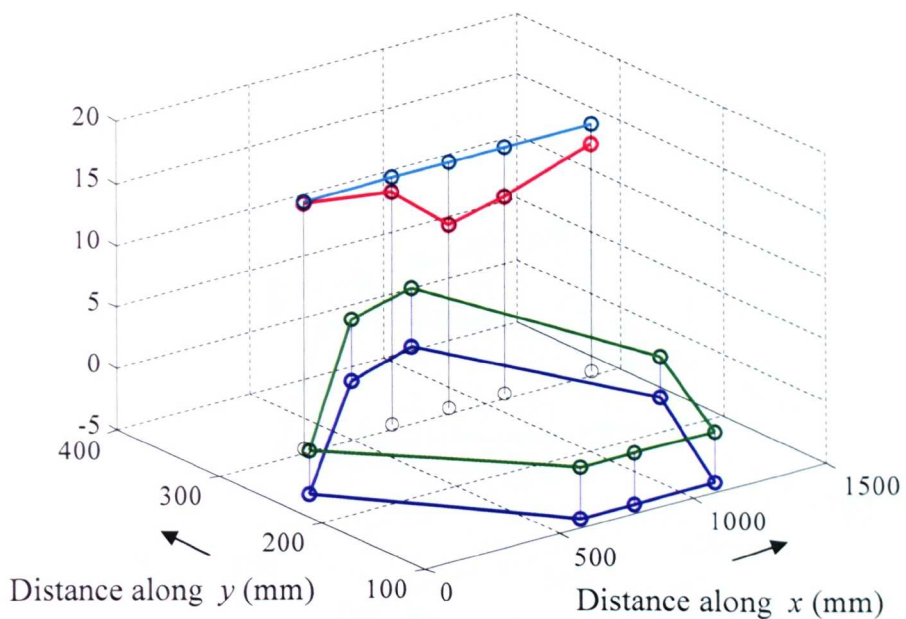


Figure (10.12): Mode shape at 58.61 Hz. ‘Cyan’ and ‘red’ colours show the un-deflected and deflected rotor respectively. ‘Green’ and ‘blue’ colours show the un-deflected and deflected base respectively.

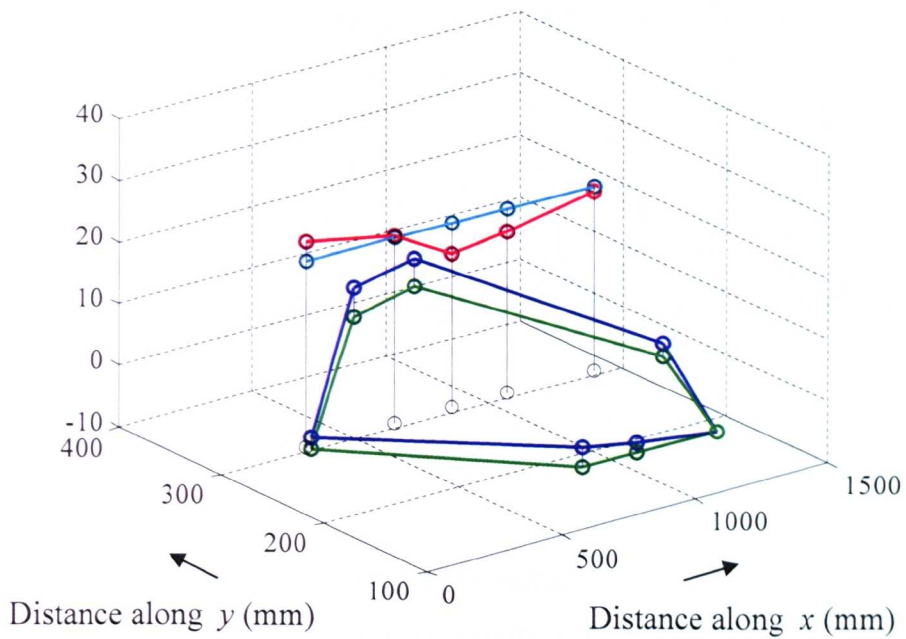


Figure (10.13): Mode shape at 65.78 Hz. ‘Cyan’ and ‘red’ colours show the undeformed and deflected rotor respectively. ‘Green’ and ‘blue’ colours show the undeformed and deflected base respectively.

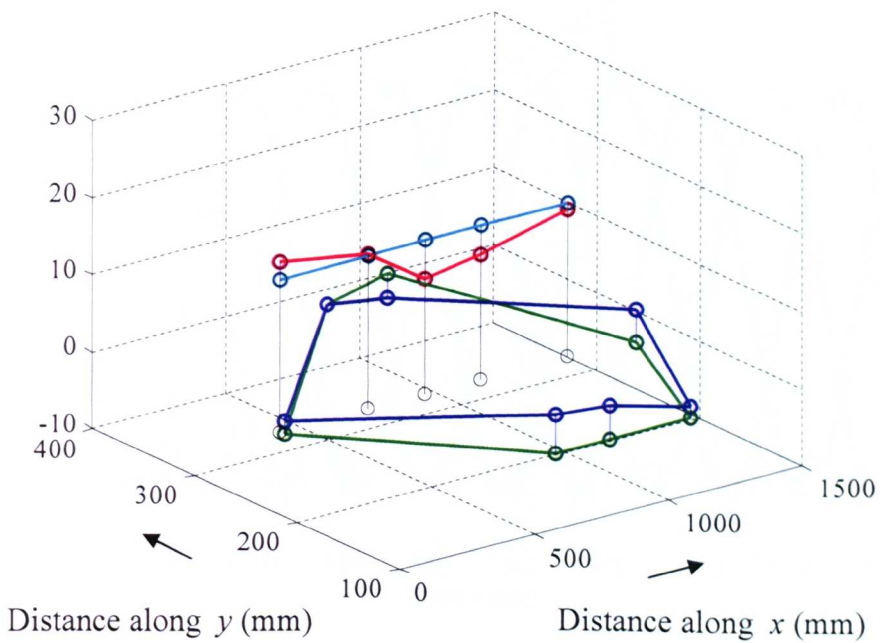


Figure (10.14): Mode shape at 72.39 Hz. ‘Cyan’ and ‘red’ colours show the undeformed and deflected rotor respectively. ‘Green’ and ‘blue’ colours show the undeformed and deflected base respectively.

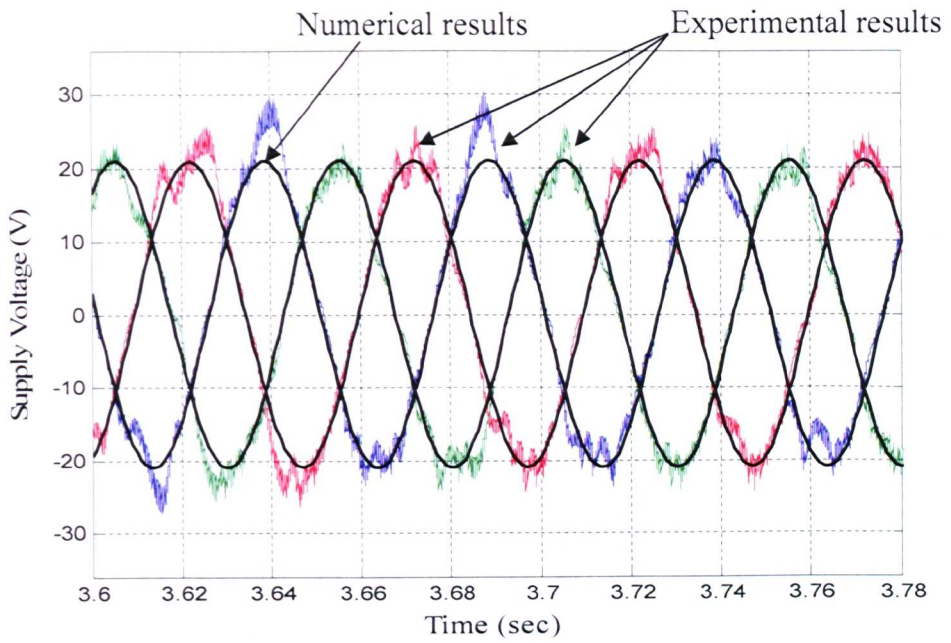


Figure (10.15): No-load supply voltages from numerical model as well experiments when supply frequency is 20 Hz

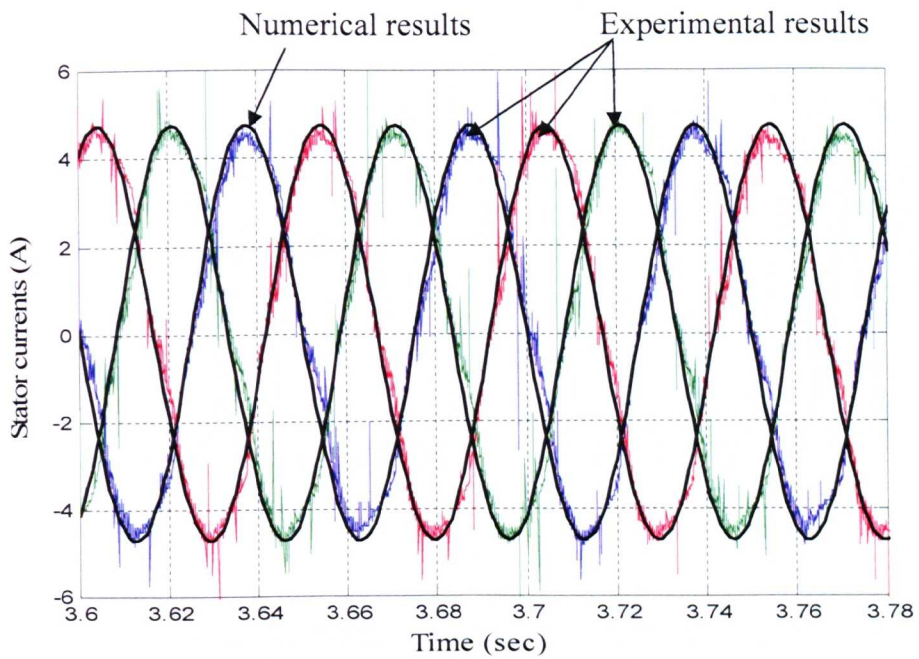


Figure (10.16): No-load stator currents from numerical model as well experiments when supply frequency is 20 Hz

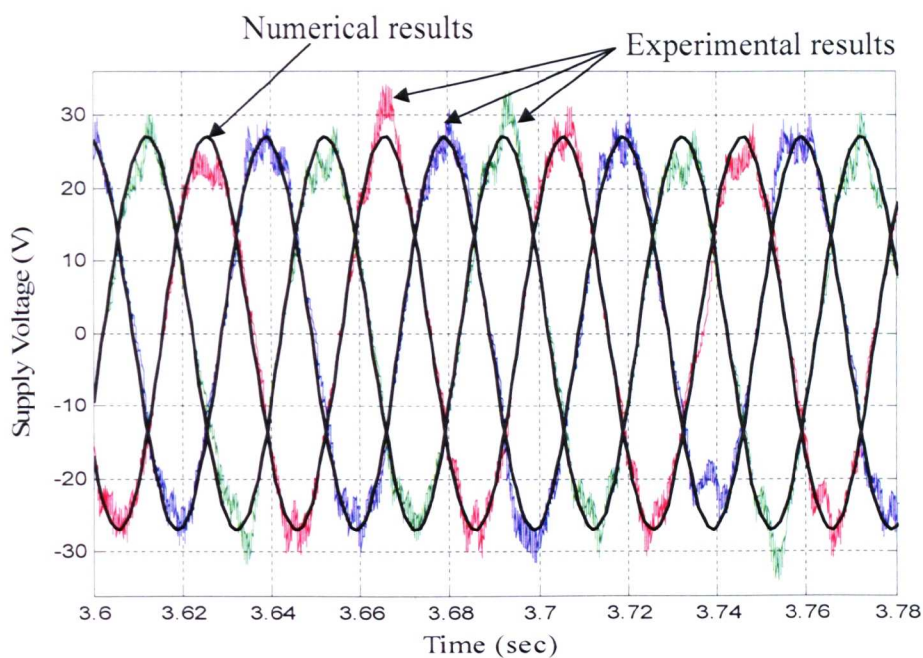


Figure (10.17): Noload supply voltages from numerical model as well experiments when supply frequency is 25 Hz

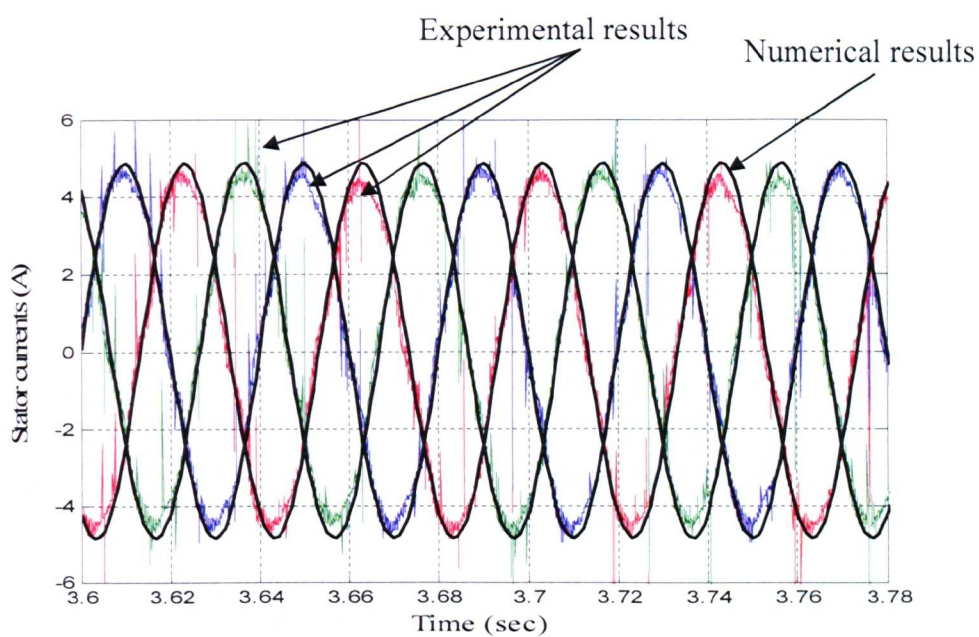


Figure (10.18): Noload stator currents from numerical model as well experiments when supply frequency is 25 Hz

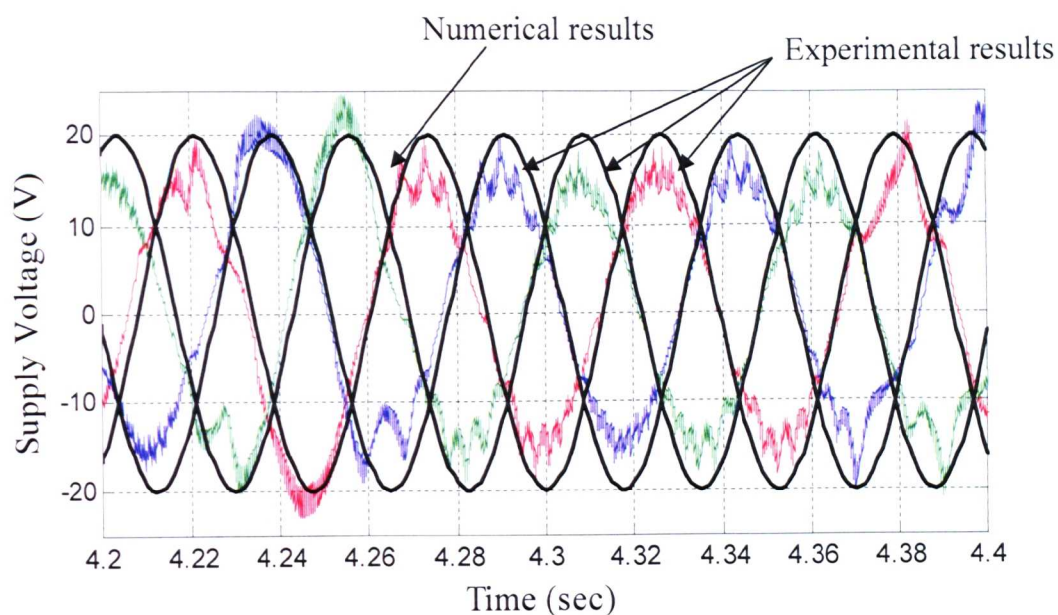


Figure (10.19): Supply voltages for locked rotor test from numerical model and experiments

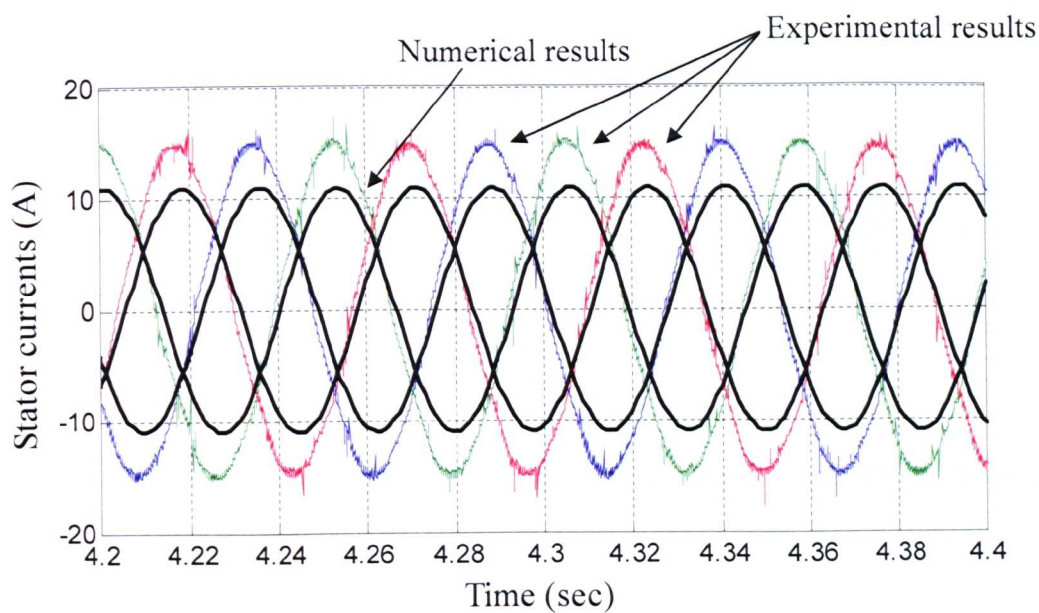


Figure (10.20): Stator currents from numerical and experiments for locked rotor test

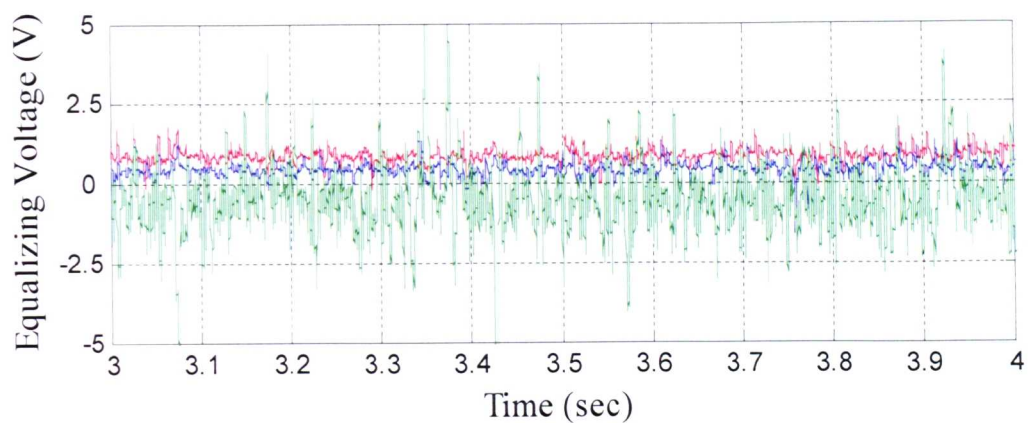


Figure (10.21): Equalising voltages from experiments when supply frequency is 20 Hz

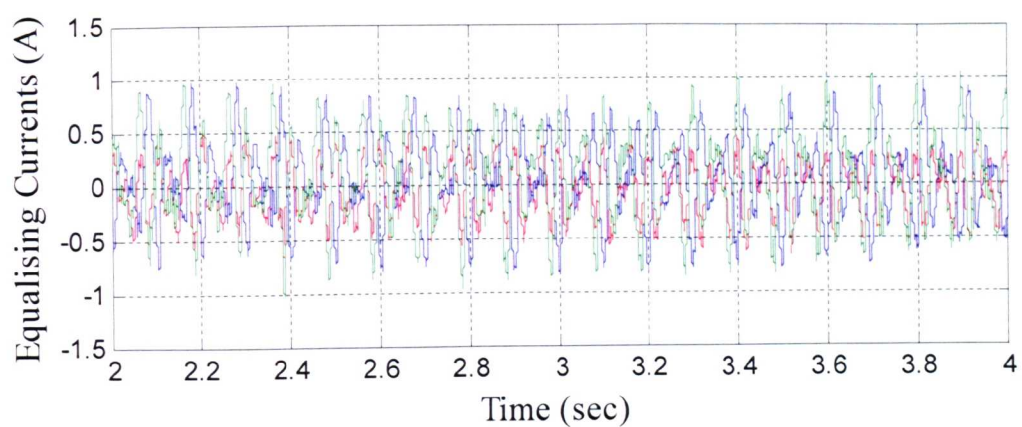


Figure (10.22): Equalising currents from experiments when supply frequency is 20 Hz

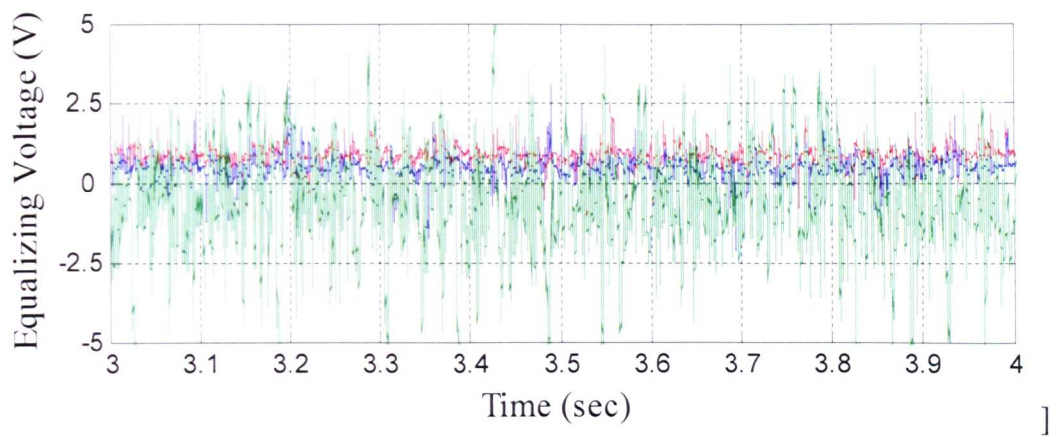


Figure (10.23): Equalising voltages from experiments when supply frequency is 25 Hz

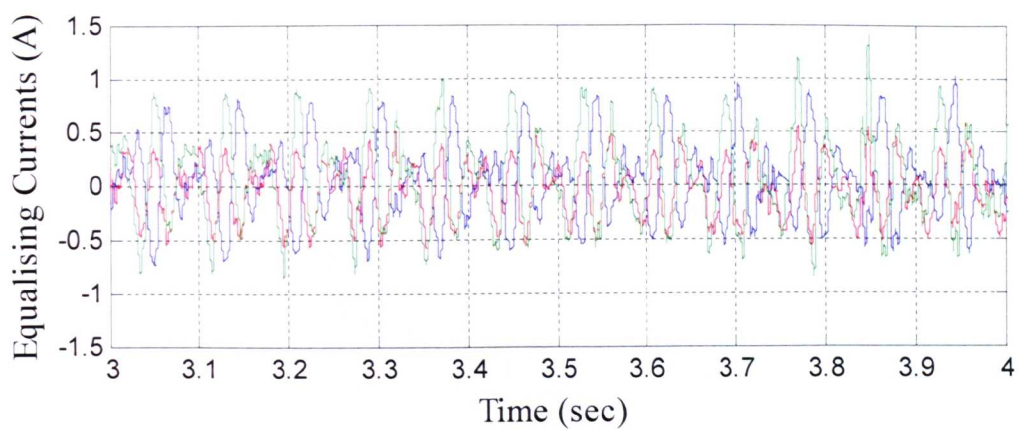


Figure (10.24): Equalising currents from experiments when supply frequency is 25 Hz

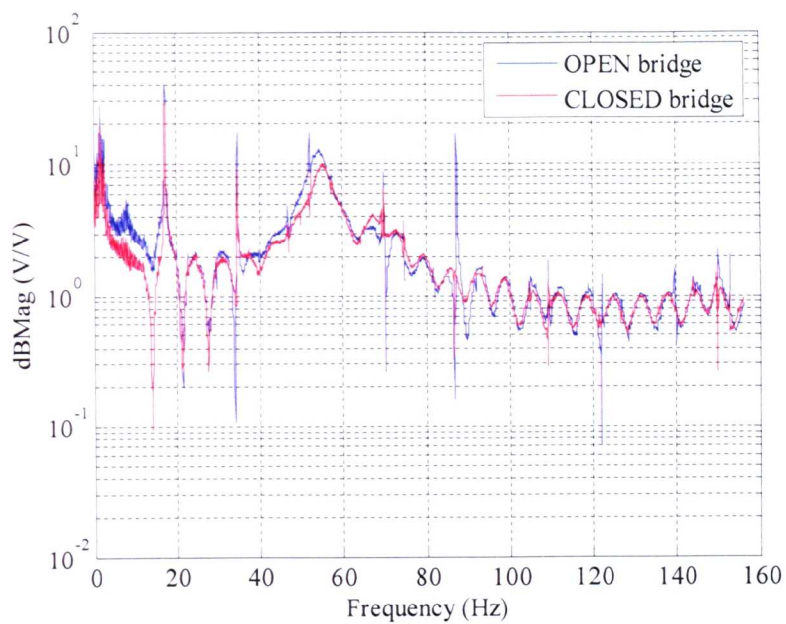


Figure (10.25): Frequency response when the supply frequency is 25 Hz with OPEN bridge (blue) and CLOSED bridge (red)

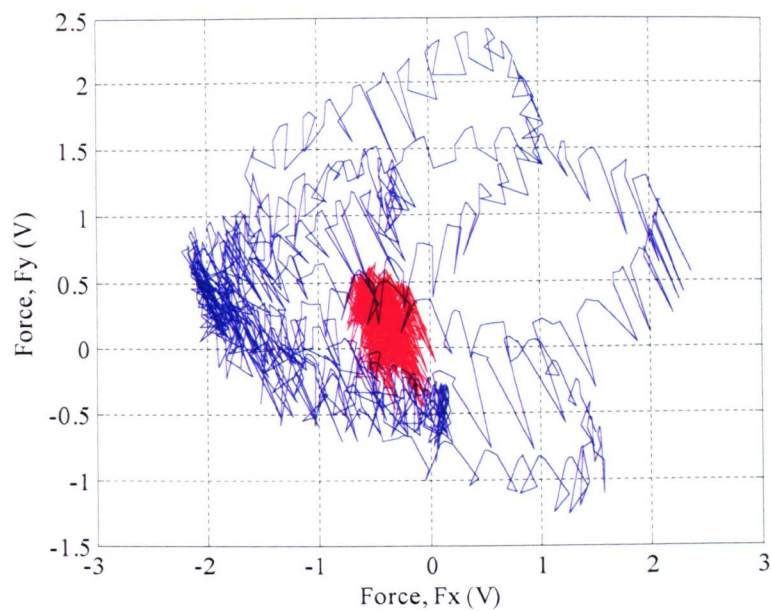


Figure (10.26): Rotor centre orbit with OPEN and CLOSED bridge when the supply frequency is 25 Hz

Chapter Eleven

Conclusions and Future work

11.1 Conclusions

The objectives of this thesis can be divided into two, (1) development of a unified model combining electrical dynamics and mechanical dynamics (2) commissioning an experimental setup to investigate the electromechanical interactions in an electrical machine and also to investigate the effectiveness of the bridge configured windings as a passive method of reducing UMP.

This study starts with the development of 2D finite element models of a prismatic electromagnetic device. A single representation is applied to every cross section over the entire length of the 3D object which is the actual model. The three dimensional effects such as stator end-windings and rotor end-rings are added separately. Initially the formulation is developed for linear problems and subsequently extended to non-linear problems. The 2D finite element model represents the instantaneous relationship between the nodal magnetic potentials and the nodal currents starting from the Maxwell's equation. The excitations are given in terms of current density and permanent magnet regions. The idea is that, if the excitations are known, the magnetic potentials can be calculated from the relation between the magnetic potentials and the currents through a magneto-static analysis. The procedures for developing this 2D FE model are described in Chapter 3 in a systematic way. In fact Chapter 3 is the back-bone of the thesis.

A generic 2D Finite element (FE) code has been developed in MATLABTM using these procedures. This general procedure is called MagFEA and this code is thoroughly validated. This code has a linear solver as well as a non-linear solver and can solve any electromagnetic device including rotating electrical machines. Using

this code three electrical machines have been investigated. It is shown that overhung machines are more prone to unbalanced magnetic pull and that the actual critical speed can be very different from the critical speed computed without including UMP. Another investigation has revealed that magnetic slot wedges in an electrical machine reduce the tooth passing frequency component of the magnetic normal stress in the airgap.

The FE model of an electromagnetic device has a few independent currents. There can be two sets of nodes in the model based on the conducting and non-conducting regions. Only those nodes correspond to the conducting regions can carry currents and those nodes are called current carrying nodes. These currents are also not independent because constraint exists on these currents as a result of the way that the machine is wound. Chapter 4 discusses different transformations employed to reduce the vector of nodal currents to a smaller number of independent currents. It is well known that the density of current in the rotor bars of a cage induction machine and also in damper bars in a synchronous machine varies with the radial position in the bar due to skin effect. Transformations are also developed to reduce this vector of nodal currents to a lower-dimensional vector. If we know the independent currents for the stator as well as for the rotor we can calculate the full set of nodal currents and hence we can calculate the magnetic potentials. Transformations are also applied to the magnetic potentials. In an electric machine model we usually enforce a tangential-flux condition at the outside diameter of the stator and this is achieved by imposing constraints. Chapter 4 discusses all transformations applied to the currents as well as magnetic potentials.

Most of the electromagnetic devices can be considered to be voltage-driven. The circuit equation has to be coupled with field equation. A model for electro-magneto-mechanical device has been developed. The presented model can be applied to any EMM devices including induction machines. The effects of end-windings are incorporated in the 2D model by writing the end-winding currents in terms of rotor bar currents. For variable current densities this transformation is obtained from the minimisation of resistive losses.

The steady state characteristic is one of the most fundamental requirements in the design of electrical machines. There is a requirement for these steady state currents in

the proposed coupled dynamic model. General methods for calculating steady state currents are discussed. The airgap stitching method and the central circle method are discussed in detail. A main advantage of the airgap stitching method is that it can cope with the case of an eccentric rotor. It suffers from two disadvantages - (1) in reality, it is obvious that the machine inductance matrix should be a continuous function of rotor angle. With the airgap stitching method, at instants where the connectivity of rotor and stator nodes has to be changed, discontinuities will appear in the inductance, (2) even for analyses which are magnetically linear, the element matrices must be derived afresh for the stitching elements at each instant in time. The central circle method overcomes these two disadvantages. It has also two major disadvantages (1) when constraints are applied the sparsity of the stiffness matrix is reduced, (2) it can not cope with the case of an eccentric rotor and stator. Different variants of the central circle method are exploited. One of the interesting outcomes is that the stiffness matrix which is used to calculate the inductance matrix can be approximated using a non-linear function.

Once the steady state currents of the electrical machine are known, a unified model is developed combining the electrical dynamics and the mechanical dynamics. The variables are electric charge and point displacements. The coupled system is a time-varying linear system with periodic coefficient matrices. One of the main points of interest of this study is the effective mechanical damping provided by the closure of the parallel-path circuits in the three different phases. The parallel paths do not stabilise any of the unstable conditions (which appear to be dominated by negative magnetic stiffness) but they do reduce the real parts of eigenvalues in all cases. Effective electrical damping has been assessed by forcing the rotor centre to take a positive circular synchronous orbit of 1% of the air-gap and examining the energy transferred into the electrical circuits from the mechanical motion over the period of time.

An experimental rig has been commissioned for two distinct reasons; (1) to verify the results of the coupled model (numerical) combining the electrical and the mechanical dynamics as proposed, (2) to investigate the effectiveness of the bridge configured windings as a passive method for reducing UMP. The numerical results of mechanical and electrical model are separately verified using the experimental results. The

parallel paths in the stator windings can reduce the UMP. This has been clearly demonstrated by experimental results. It is seen that by employing bridge configured winding the UMP can be reduced by about 75%.

11.2 Future work

The present study presents some interesting possibilities for further investigations. Some recommendations for future work are presented here

11.2.1 Application to other electrical machine

The models developed in this study have been applied to only on a particular class of machine. These models can be applied to other electrical machines such as axial flux machines, linear induction machines and cylindrical machines with double airgap.

11.2.2 Three dimensional analysis

The models developed in this study are two dimensional. Three dimensional effects are either ignored or approximated in this study. For example, inductances due to end-windings are ignored and resistances of the end-windings of stator coils and the resistances of the end-rings of the rotor bars are approximated. It will be interesting to see the effect of these parameters by developing a complete three-dimensional model.

11.2.3 Detailed study of the approximate method

Chapter 6 discusses different methods by which we can calculate steady state characteristics of an induction machine. These methods can easily be used to calculate the steady state characteristics of other electrical machines such as synchronous machines. Separate methods are discussed for different conditions of a particular machine which include geometry change and magnetic saturation. When magnetic saturation of the iron cores is not considered in the calculation then there is no issue with the computational time. When material non-linearity is incorporated in the calculation, a full FE solution demands substantial computational time. This work has

proposed a new and interesting idea whereby instead of regarding the materials as having a separate permeability at every Gauss point dependent on the flux density there, we approximate the complete inductance matrix of the device as a continuous function of a small number of variables. The method is applied to a simple electromagnetic problem in which there are only two independent current variables. Electric machines are complex devices where, in addition to magnetic non-linearity, there is also relative movement between the stationary and rotating parts. There is scope to adapt this method for use in electrical machines.

A feature of this method which is proposed in this work is that separate approximations are created for both rotor and the stator and the problem of accommodating movement is removed.

11.2.4 Optimum scaling in the approximate function

For the approximate method, the ultimate measure of success is how closely the steady state currents can be found from the approximate method which will match that of full non-linear solution. Recalling the approximate functions for the rotor and the stator mentioned in Equations (7.32) and (7.32) respectively

$$[K_R]\{B_{RC}\} = [K_R](0) + \sum_{i=1}^{2h} [M_{A-i}] \left(\frac{\{B_{RC}\}(i) - \alpha \{I_R\}(i)}{B_{ref}} \right)^2 + \sum_{i=1}^{2h} [M_{B-i}] \left(\frac{\{B_{RC}\}(i) + \alpha \{I_R\}(i)}{B_{ref}} \right)^2 \quad (10.1)$$

where α is reference parameter and $\alpha = \frac{B_{ref}}{I_{Rref}}$, I_{Rref} is the reference value of the rotor bar currents.

$$[K_S]\{B_{SC}\} = [K_S](0) + \sum_{i=1}^{2h} [M_{S-i}] \left(\frac{\{B_{SC}\}(i)}{B_{ref}} \right)^2 \quad (10.2)$$

The parameters which determine this measure are the Fourier coefficients of the magnetic potentials in the central circle ($\{A_{RC}\}$ and $\{A_{SC}\}$), the rotor bar currents $\{I_R\}$, the reference values of the Fourier coefficients of the magnetic potentials B_{ref} and the reference values of the rotor bar currents I_{Rref} .

It is possible to investigate the optimum number of harmonics of the magnetic potentials and the optimum number of independent currents per rotor bar. Investigation can also be extended to find a better way to choose the optimum value of these reference parameters.

11.2.5 Extending the central circle method so that it can accommodate eccentricity

Our approximate method is used only to find the reference solution when rotor remains concentric. It is possible to accommodate some small displacement from the central circle by incorporating additional parameters in the approximate function.

11.2.6 Automatic differentiation of the stiffness matrix with respect to position

In this study two methods are introduced for accommodating the relative movement between the stationary and the rotating parts. These two methods are (1) the airgap stitching method and (2) the central circle method. In the central circle method, there is no element derivation is required while accommodating the relative movement. In this method the differentiation of the stiffness matrix with respect to angular position (θ) is achieved analytically. In the airgap stitching method the layer (band) combining the outer diameter of the rotor and the inner diameter of the stator has to be derived afresh. In case of the airgap stitching method the rates of change of stiffness with respect to the geometry (x , y position and θ) are calculated separately using the central difference method. It is possible to calculate these rates of change during the element derivation of the layer whose elements have to be derived afresh to accommodate the relative movement. .

11.2.7 Time dependent transformations

The analysis of time-dependent linear second-order systems is of high generic interest. A time-dependent linear second-order system is shown in Equation (7.12) of Chapter 7. Equation (7.12) can be written as

$$[M'(t)]\{\ddot{q}'(t)\} + [D'(t)]\{\dot{q}'(t)\} + [K'(t)]\{q'(t)\} = 0 \quad (10.3)$$

where $[M'(t)]$, $[D'(t)]$ and $[K'(t)]$ are the time-dependent mass, damping and stiffness matrices respectively and $\{q'(t)\}$ is the vector of generalised displacements. There are several possible approaches to dealing with the time-dependency of this system. One approach would be to employ time-dependent transformation matrices $[T_L(t)]$ and $[T_R(t)]$ to Equation (10.3) starting with

$$\{q'(t)\} = [T_R(t)]\{p'(t)\} \quad (10.4)$$

where $\{p'(t)\}$ is a new vector representation of the generalized deflections of the system. The first and second derivatives of $\{q'(t)\}$ are then

$$\{\dot{q}'(t)\} = [T_R(t)]\{\dot{p}'(t)\} + [\dot{T}_R(t)]\{p'(t)\} \quad (10.5)$$

$$\{\ddot{q}'(t)\} = [T_R(t)]\{\ddot{p}'(t)\} + 2[\dot{T}_R(t)]\{\dot{p}'(t)\} + [\ddot{T}_R(t)]\{p'(t)\} \quad (10.6)$$

Making the obvious substitutions into Equation (10.3) and pre-multiplying the result by the transpose of $[T_L(t)]$ leads to a new equation. With appropriate choice of $[T_L(t)]$ and $[T_R(t)]$ it is evident that at least two out of the three system matrices can be made constant. In essence, the analytical approaches to UMP modeling do precisely this. In the fully general case, all three matrices cannot be made constant using this limited transformation. Further investigations can be made for a general class of transformations where the system matrices will be constant with respect to time.

11.2.8 Passive components in the parallel paths

It is possible to include additional components such as capacitance, inductances and resistances. By adjusting the values of these components, the mechanical dynamics of the machine can be modified. Note that with no capacitances or inductances present, the MMF resulting in the parallel paths from induced currents caused by changing flux imbalance in the machine will lag behind the original flux imbalance by 90%. Introducing capacitance will obviously increase the impedance of the circuit but will also reduce the lag at any given frequency. Inductances will do the opposite. Considerable “tuning” of the mechanical dynamics is possible by using different combinations of capacitances and inductance.

11.2.9 Inclusion of torsional dynamics in the coupled model

In our proposed coupled model lateral dynamics is considered to investigate the electromechanical interactions. In the present model the displacement vector contains electrical charge and point lateral displacements (x, y) . The torsional dynamics can be included in our mechanical model by introducing more degrees of freedom. This model will facilitate to investigate the coupling between the torsional and lateral dynamics through the electrical interactions.

11.2.10 Incorporation of the effect of base plate in the mechanical model

The dynamic modes of the rig obtained from experiments are slightly different from the results obtained from numerical model. One reason for this difference is that the effects of the base plate of the rig are ignored in the mechanical model. In the future study on the electromechanical interaction of a real machine the effects of the base plate should be incorporated.

References

- 1 Abdel-Razek, A.A., Coulmn, J. L., Feliachi, M., and Sabonnadiere, J. C., *Conception of an air-gap element for the dynamic analysis of the electromagnetic field in electric machines*. IEEE Transactions on Magnetics, 1982. **18**(2): p. 655-659.
- 2 Amirulddin, U.A.U., Asher, G. M., Sewell, P., and Bradley, K. J., *Dynamic field modelling of torque and radial forces in vector-controlled induction machines with bearing relief*. IEE Proceedings on Electric Power Applications, 2005. **152**(4): p. 894-904.
- 3 Antila, M., Lantto, E., and Arkkio, A., *Determination of forces and linearized parameters of radial active magnetic bearings by finite element technique*. IEEE Transactions on Magnetics, 1998. **34**(3): p. 684-694.
- 4 Arkkio, A., *Analysis of induction motors based on the numerical solution of the magnetic field and circuit equations*, in *Department of Electrical and Communication Engineering*. 1987, Helsinki University of Technology: Helsinki. p. 97.
- 5 Arkkio, A., Antila, M., Pokki, K., Simon, A., and Lantto, E., *Electromagnetic force on a whirling cage rotor*. IEE Proceedings of Electric Power Application, 2000. **147**(5): p. 353-360.
- 6 Bangura, J.F., Isaac. F. N., Demerdash, N. A., and Arkadan, A. A., *A time-stepping coupled finite element-state space model for induction motor drives - Part 2: machine performance computation and verification*. IEEE Transactions on Energy Conversion, 1999. **14**(4): p. 1472-1478.
- 7 Bastos, J.P.A., and Sadowski, N., *Electromagnetic modelling by finite element*

methods. Founding ed. 2003, New York, USA: Marcel Dekker, Inc. 490.

- 8 Bathe, K., *Finite element procedures*. Vol. 1037. 1996: Prentice-Hall, Inc.
- 9 Belahcen, A., *Magnetoelastic coupling in rotating electrical machines*. IEEE Transactions on Magnetics, 2005. **41**(5): p. 1624-1627.
- 10 Belkhatat, D., Romary, R., Adnani, M. El., Corton, R., and Brudny, J. F., *Fault diagnosis in induction motors using radial magnetic field measurement with an antenna*. Measurement Science and Technology, Institute of Physics, 2003. **14**: p. 1695-1700.
- 11 Belmans, R., Geysen, W., Jordan. H. and Vendenput, A., *Unbalanced magnetic pull in three phase two pole induction motors with eccentric rotors*. IEE Conference Publication, 1982: p. 65-69.
- 12 Belmans, R., Heylen, W., Vendenput, A. and Geysen, W., *Influence of rotor-bar stiffness on the critical speed of an induction motor with an aluminium cage*. IEE Proceedings, 1984. **131B**(5): p. 203-208.
- 13 Belmans, R., Vendenput, A., and Geysen, W., *Calculation of the flux density and the unbalanced pull in two pole induction machines*. Archives of Electrotechnik, 1987. **70**: p. 151-161.
- 14 Belmans, R., Vendenput, A. and Geysen, W., *Influence of unbalanced magnetic pull on the radial stability of flexible-shaft induction machines*. IEE Proceedings, 1987. **134B**(2): p. 101-109.
- 15 Benaragama, D.S., Ward, D. M. and Tavner, P. J. *Unbalanced magnetic pull on the eccentric rotor of a turbo-generator; International conference on Electrical Machines*. 1982. Hungary.
- 16 Berman, M. *On the reduction of magnetic pull in induction motors with off-centre*. in *Industry Applications Society Annual Meeting, 1993., Conference*

- 17 Binns, K.J., and Dye, M., *Identification of principal factors causing unbalanced magnetic pull in cage induction motors*. Proceedings of the IEE, 1973. **120**(3): p. 349-354.
- 18 Bottauscio, O., Chiampi, M., and Manzin, A., *Different finite-element approaches for electromechanical dynamics*. IEEE Transactions on Magnetics, 2004. **40**(2): p. 541-544.
- 19 Boualem, B., and Piriou, F., *Numerical models for cage induction machines using finite element method*. IEEE Transactions on Magnetics, 1998. **34**(5): p. 3202-3205.
- 20 Bradford, M., *Unbalanced magnetic pull in a 6-pole, 10 kW, induction motors with a series-connected stator windings*, in *The Electrical Research Association*. 1968.
- 21 Chapman, S.J., *Electric machinery fundamentals*. Third ed. McGraw-Hill series in electrical and computer engineering. 1998, Singapore: McGraw-Hill.
- 22 Coulomb, J.L., *A methodology for the determination of global electromechanical quantities from a finite element analysis and its application to the evaluation of magnetic forces, torques and stiffness*. IEEE Transactions on Magnetics, 1983. **19**(6): p. 2514-2519.
- 23 Cundev, D., and Petkovska, L., *Computation of electromechanical characteristic of salient poles synchronous motor with damper based on FEM*. Journal of Materials Processing Technology, 2005. **161**: p. 241-246.
- 24 Cunha, C.C.M., Lyra, Renato O. C., and Filho, Braz cardoso, *Simulation and analysis of induction machines with rotor asymmetries*. IEEE Transactions on Industry Applications, 2005. **41**(1): p. 18-24.

- 25 D'Angelo, H., *Linear time-varying systems: analysis and synthesis*. Allyn and Bacon Series in Electrical Engineering, ed. S.U. Norman Balabanian. 1970. 346.
- 26 DeBortoli, M.J., Salon, S. J., Burow, D. W. and Slavik, C. J., *Effects of rotor eccentricity and parallel windings on induction machine behaviour: A study using finite element analysis*. IEEE Transactions on Magnetics, 1993. **29**(2): p. 1676-1682.
- 27 Demerdash, N.A., and Nehl, T. W., *Electric machinery parameters and torques by current and energy perturbations from field computations - part I: theory and formulations*. IEEE Transactions on Energy Conversion, 1999. **14**(4): p. 1507-1513.
- 28 Devanneaux, V., Dagues, B., Faucher, J. and Barakat, G., *An accurate model of squirrel cage induction machines under stator faults*. Mathematics and Computers in Simulation, 2003. **63**: p. 377-391.
- 29 Dorell, D.G., Smith, A. C., *Calculation of UMP in induction motors with series or parallel winding connections*. IEEE Transactions on Energy Conversion, 1994. **9**(2): p. 304-310.
- 30 Dorell, D.G., *Calculation of unbalanced magnetic pull in small cage induction motors with skewed rotors and dynamic rotor eccentricity*. IEEE Transactions on Energy Conversion, 1996. **11**(3): p. 483-488.
- 31 Dorell, D.G., *Experimental behavior of unbalanced magnetic pull in 3-phase induction motors with eccentric rotors and the relationship with tooth saturation*. IEEE Transactions on Energy Conversion, 1999. **14**(3): p. 304-309.
- 32 Dorrell, D.G., Thomson, W. T., and Roach, S., *Analysis of airgap flux, current, and vibration signals as a function of the combination of static and dynamic airgap eccentricity in 3-phase induction motors*. IEEE Transactions

- on Industry Applications, 1997. **33**(1): p. 24-34.
- 33 Ellison, A.J., and Yang, S. J. , *Effects of rotor eccentricity on acoustic noise from induction machines*. Proceeding of IEE, 1971. **118**(1): p. 174-184.
 - 34 Faiz, J., Tabatabaei, I., and Sherifi-Ghazvini, E., *A precise electromagnetic modeling and performance analysis of a three-phase squirrel-cage induction motor under mixed eccentricity condition*. Electromagnetic, 2004. **24**: p. 471-489.
 - 35 Fitzgerald, A.E., Kingsley, Charles Jr., and Umans, S. D. , *Electric machinery*. 1992, Singapore: McGraw-Hill
 - 36 Freise, W., and Jordan, H., *Unbalanced magnetic pull in 3 Phase a. c. machines*. ETZ, 1962. **A83**(9): p. 299-303.
 - 37 Frohne, M., *The practical importance of unbalanced magnetic pull, possibilities of calculating and damping it*. Conti Electro Brichte, 1967. **13**: p. 81-92.
 - 38 Fruchtenicht, J., Jordan, H. and Seinsch, H. O., *Running instability of cage induction motors caused by harmonic fields due to eccentricity. part 1: electromagnetic spring constant and electromagnetic damping coefficient, part 2: self excited transverse vibration of rotors*. Archives of Electrotech, 1982. **65**: p. 271-292.
 - 39 Fu, W.N., Zheng Zhang, Zhou, P., Lin, D., Stanton, S., and Cendes, Z.J. *Curvilinear finite elements for modeling the sliding surface in rotating electrical machines and its applications*. in *IEEE International Conference on Electric Machines and Drives*. 2005.
 - 40 Garvey, S.D., Penny, J. E., Friswell, M. I., and Lees, A. W. . *The stiffening effect of laminated cores on the rotors of electrical machines*. in *IMEchE. 8th International Conference on Vibrations of Rotating Machines*. 2004. Swansea.

- 41 Garvey, S.D., and Watson, J., *Improvements in UMP performance of rotatory electrical machine*. 2004.
- 42 Gersem, H.D., Vandewalle, S., Clemens, M. and Weiland, T. *Interface preconditioners for splitting interface conditions in air gaps of electrical machine models*. in *Fourteen International Conference on Domain Decomposition Methods*. 2003.
- 43 Gersem, H.D., and Weiland, T., *A computationally efficient air-gap element for 2-D FE machine tools*. IEEE Transactions on Magnetics, 2005. **41**(5): p. 1844-1847.
- 44 Guo, D., Chu, F. and Chen, D., *The unbalanced magnetic pull and its effects on vibration in a three-phase generator with eccentric rotor*. Journal of Sound and Vibration, 2002. **254**(2): p. 297-312.
- 45 Haase, H., Jordan, H. and Kovacs, K. P., *Vibratory forces as a result of shaft fluxes with two pole induction machines*. Electrotech (ETZ), 1972. **93**(485-486).
- 46 Hameyer, K., and Belmans, R., *Numerical modeling and design of electrical machines and devices*. 1999, Southampton, UK: WIT Press.
- 47 Ho, S.L., Li, H. L., Fu, W. N., and Wong, H. C., *A novel approach to circuit-field-torque coupled time stepping finite element modeling of electric machines*. IEEE Transactions on Magnetics. Vol. 36. 2000. 1886-1889.
- 48 Holopainen, T., Tenhunen, A. and Arkkio, A. *Electromechanical interaction in rotor vibrations of electric machines*. in *Fifth World Congress on Computational Mechanics (WCCM V)*. 2002. Vienna, Austria: Vienna University of Technology, Austria.
- 49 Holopainen, T., Tenhunen, A., Lantto, E. and Arkkio, A., *Numerical*

- identification of electromagnetic force parameters for linearized rotordynamic model of cage induction motors*. Transaction of ASME: Journal of Vibration and Acoustics, 2004. **126**(3): p. 384-390.
- 50 Holopainen, T., Tenhunen, A. and Arkkio, A., *Electromechanical interaction in rotordynamics of cage induction motors*. Journal of Sound and Vibration, 2005. **284**: p. 733-755.
 - 51 Holopainen, T., Tenhunen, A., Lantto, E. and Arkkio, A., *Unbalanced magnetic pull induced by arbitrary eccentric motion of cage rotor in transient operation. Part 1: analytical model*. Electrical Engineering, 2005. **88**(1): p. 12-24.
 - 52 Holopainen, T., Tenhunen, A., Lantto, E. and Arkkio, A., *Unbalanced magnetic pull induced by arbitrary eccentric motion of cage rotor in transient operation. Part 2: Verification and numerical parameter estimation*. Electrical Engineering, 2005. **88**(1): p. 25-34.
 - 53 Holopainen, T.P., Tenhunen, A., and Arkkio, A. *Electromagnetic circulatory forces and rotordynamic instability in electrical machines*. in *IFTOMM Conference on Rotordynamics*. 2002. Sydney, Australia.
 - 54 Holopainen, T.P., Tenhunen, A., Lantto, E., and Arkkio, A. *Numerical identification of electromagnetic force parameters for linearized rotordynamic model of cage induction motors*. in *Proceedings of ASME International 19th Biennial Conference on Mechanical Vibration and Noise*. 2003. Chicago, Illionis, USA: ASME.
 - 55 Ishibashi, F., Noda, S., and Mochizuki, M., *Numerical simulation of electromagnetic vibration of small induction motors*. IEE Proceedings of Electric Power Application, 2000. **145**(6): p. 528-534.
 - 56 Joksimovic, G.M., Durovic, Momir D., Penman, J., and Arthur, N., *Dynamic simulation of dynamic eccentricity in induction machines - winding function approach*. IEEE Transactions on Energy Conversion, 2000. **15**(2): p. 143-148.

- 57 Joksimovic, G.M., *Dynamic simulation of cage induction machine with air gap eccentricity*. IEE Proceedings of Electric Power Applications, 2005. **152**(4): p. 803-811.
- 58 Jordan, H., Roder, G. and Weis, M, *Under what circumstances may mechanical vibrations of the stator core be expected at supply frequency in four pole three phase asynchronous machines?* Electric, 1967. **21**(3): p. 91-95.
- 59 Jordan, H., Schroder, R. D., and Seinsch, H. O., *Zur Berechnung einseitig magnetischer Zugkrafte in Drehfeld-Maschinen*. Archives of Electrotech, 1981. **63**: p. 117-124.
- 60 Kanerva, S., Seman, S., and Akrrio A., *Inductance model for coupling finite element analysis with circuit simulation*. IEEE Transactions on Magnetics 2005. **41**(5): p. 1620-1623.
- 61 Kasmieh, T., Lefevre, Y. Roboam, X., and Faucher, J., *Establishment of a two-phase non-linear simulation model of the dynamic operation of the induction machine*. The European Physical Journal Applied Physics, 1998.
- 62 Kasmieh, T., Lefevre, Y., and J. C. Hapiot, *Modelling and experimental characterization of saturation effect of an induction machine*. The European Physical Journal Applied Physics, 2000. **10**: p. 123 -130.
- 63 Khoo, W.K.S., Fittro, R. L., and Garvey, S. D. *AC polyphase self-bearing motors with a bridge configured winding*. in *Proc. 8th Int. Symp Magnetic Bearings*. 2002. Mito, Japan.
- 64 Khoo, W.K.S., Garvey, S. D., Kalita, K., and Houlston, P. R. *Vibration control with lateral force produced in electrical machines*. in *IMEchE Proceedings of 8th International Conference Vibrations in Rotating Machinery*. 2004. Swansea, UK.

- 65 Khoo, W.K.S., *Bridge configured winding for polyphase self-bearing machines*. IEEE Transactions on Magnetics, 2005. **41**(4): p. 1289-1295.
- 66 Khoo, W.K.S., Garvey, S.D., and Kalita, K. *Controlled UMP in electrical machines can stabilize otherwise unstable machines*. in *ISCORMA-3*. 2005. Cleveland, Ohio, USA.
- 67 Kovacs, K.P., *Two-pole induction motor vibrations caused by homopolar alternating fluxes*. IEEE Transactions on Power Apparatus and Systems, 1977. **PAS-96**(4): p. 1105-1108.
- 68 Kozisek, D.-I.J., *Elektrische Maschine mit Kommutatortrommelwicklung*, S. AG, Editor. 1935.
- 69 Lai, H.C., Rodger, D., and Leonard, P. J., *Coupling meshes in 3D problems involving movements*. IEEE Transactions on Magnetics, 1994. **28**(2): p. 1732-1734.
- 70 Lalanne, M., and Ferraris, G., *Rotordynamics predictions in engineering*. 1990, Chichester, England: John Wiley & Sons Ltd.
- 71 Lemaire-Semail, B., Louis, J. P., and Bouillault, F., *Computation of induction machine inductances for extended analytical modeling accounting for saturation*. The European Physical Journal Applied Physics, 1999. **5**: p. 257-267.
- 72 Leplat, P.M., Lemaire-Semail, B., Clenet, S. and Piriou, F., *Comparison between finite element method and magnetic equivalent scheme to model an induction machine*. COMPEL-The International Journal for Computation and Mathematics for Electrical and Electronic Engineering, 1996. **15**(4): p. 82-87.
- 73 Marghitu, D.B., *Quantitative measure of vehicle stability*. Comput. Model. Simul. Eng., 1997. **2**(2): p. pp. 163–176.

- 74 McDermott., T.E., Zhou., P. and Gilmore, J., *Electromechanical system simulation with models generated from finite element solutions*. IEEE Transactions on Magnetics, 1997. **33**(2): p. 1682-1685.
- 75 Melgoza, E., Guwardado, J. L. and Venegas, V. *A method for coupling electromagnetic transients programs with finite element magnetic field solvers*. in *International Conference on Power Systems Transients (IPST, 05)*. 2005. Montreal, Canada.
- 76 Moreira, J.C., and Lipo, T., *Modeling of saturated ac machines including air gap flux harmonic components*. IEEE Transactions on Industry Applications, 1992. **28**(2): p. 343-349.
- 77 Mori, D., and Ishikawa, T., *Force and vibration analysis of induction motors*. IEEE Transactions on Magnetics, 2005. **41**(5): p. 1948-1951.
- 78 Nakata, T., Takahashi, N., Fujiwara, K., Okamoto, Muramatsu, K., *Improvements of convergence characteristics of Newton-Raphson method for nonlinear magnetic field analysis*. IEEE Transactions on Magnetics, 1992. **28**(2): p. 1048-1051.
- 79 Nandi, S., *A detailed model of induction machines with saturation extendable for fault analysis*. IEEE Transactions on Industry Applications, 2004. **40**(5): p. 1302-1309.
- 80 Neves, C.G.C., Carlson, R., Sadowski, N., and Bastos, J. P. A., *Experimental and numerical analysis of induction motor vibrations*. IEEE Transactions on Magnetics, 1999. **35**(3): p. 1314-1317.
- 81 Newmark, N., *A method of computation for structural dynamics*. Journal of Engineering and Mechanical Division of American Society of Civil Engineers, 1959. **85**: p. 67-94.
- 82 Oapos, D., J., and Oapos, D., T., *Choosing the relaxation parameter for the*

- solution of nonlinear magnetic field problems by the Newton-Raphson method.* IEEE Transactions on Magnetics, 1995. **31**(3): p. 1484-1487.
- 83 Okoro, O.I., *Computer simulation of a squirrel-cage induction machine with non-linear effects.* The Greenwich Journal of Science and Technology (GJST), 2003. **4**(1): p. 56-64.
 - 84 Pennacchi, P., and Frosini, L, *Dynamical behaviour of a three-phase generator due to unbalanced magnetic pull.* IEE Proceedings of Electric Power Applications, 2005. **152**(6): p. 1389-1400.
 - 85 Pham, T.H., Wendling, P. F., Salon, S. J., and Acikgoz, H., *Transient finite element analysis of an induction motor with external circuit connections and electromechanical coupling.* IEEE Transactions on Energy Conversion, 1999. **14**(4): p. 1407-1412.
 - 86 Piriou, F., and Razek, A., *Finite element analysis in electromagnetic systems accounting for electric circuits.* IEEE Transactions on Magnetics, 1993. **29**(2): p. 1669-1675.
 - 87 Rodger, D., Lai, H. C., and Leonard, P. J., *Coupled elements for problem involving movement.* IEEE Transactions on Magnetics, 1990. **27**(5): p. 3955-3957.
 - 88 Rodger, D., Lai, H. C., Hill-Cottingham, R. J., and Coles, P. C., *Some tricks for modelling rotating electrical machines using finite elements.* IEEE Transactions on Magnetics, 2004. **40**(2): p. 802-805.
 - 89 Salon, S.J., DeBortoli, M. J. and Palma, R, *Coupling of transient fields, circuits and motion using finite element analysis.* Journal of Electromagnetic Waves and Applications, 1990. **4**(11): p. 1077-1106.
 - 90 Salon, S.J., Burow, D. W., Ashley III, R. E., Ovacik, L. and DeBortoli, M. J., *Finite element analysis of induction machines in the frequency domain.* IEEE Transactions on Magnetics, 1993. **29**(2): p. 1438-1441.

- 91 Schuisky, V.W., *Magnetic pull in electrical machines due to eccentricity of the rotor*. Electrotech Masch.ball, 1971. **88**: p. 391-399.
- 92 Schweitzer, G., Bleuler, H., and Traxler, A., *Active magnetic bearings: basics, properties and applications of active magnetic bearings*. 2003: Mechatronics Consulting Inc., Lindenbergstr. 18A. 244.
- 93 Silvester, P.P., and Ferrari, R. L., *Finite elements for electrical engineers*. Third ed. 1996: University Press, Cambridge. 494.
- 94 Sinha, S.C., Pandiyan, R., and Bibb, J. S., *Liapunov-Floquet transformation: computation and application to periodic systems*. Transaction of ASME: Journal of Vibration and Acoustics 1996. **118**: p. 209-219.
- 95 Smith, A.C., and Dorell D. G., *Calculation and measurement of unbalanced magnetic pull in cage induction motors with eccentric rotors. Part 1: Analytic model*. IEE Proc.-Electric Power Application, 1996. **143**(3): p. 193-201.
- 96 Smith, A.C., and Dorell, D. G., *Calculation and measurement of unbalanced magnetic pull in cage induction motors with eccentric rotors. Part 2: Experimental Investigation*. IEE Proceedings of Electric Power Application, 1996. **143**(3): p. 202-210.
- 97 Sprysl, H., Vogele, H., and Ebi, G. *The influence of magnetic forces on the stability behaviour of large electrical machines*. 2004 [cited; Available from: www.sensoplan.com/download/publication/VDI-Nr1285-eng].
- 98 Stoll, R.L., *Simple computational model for calculating the unbalanced magnetic pull on a two-pole turbogenerator rotor due to eccentricity*. IEE Proceedings of Electric Power Application, 1997. **144**(4): p. 263-270.
- 99 Strangas, E.G., *Coupling the circuit equations to the non-linear time dependent field solution in inverter driven induction motors*. IEEE

Transactions on Magnetics, 1985. **21**(6): p. 2408-2411.

- 100 Swann, S.A., *Effect of rotor eccentricity on the magnetic field in the air gap of a non-salient pole machine*. Proceeding of IEE, 1963. **110**(5): p. 903-915.
- 101 Sylvester, P.P., and Ferrari, R. L., *Finite elements for electrical engineers*, ed. 3rd. 1996: Cambridge University Press.
- 102 Tenhunen, A., and Arkkio, A., *Modelling of induction machines with skewed rotor slots*. IEE Proceedings - Electric Power Application, 2001. **148**(1): p. 45-50.
- 103 Tenhunen, A., *Electromagnetic forces acting between the stator and eccentric cage rotor*, in *Laboratory of Electromechanics, Department of Electrical and Communication Engineering*. 2003, Helsinki University of Technology: Helsinki.
- 104 Tenhunen, A., Holopainen T. P. and Arkkio, A., *Impulse method to calculate the frequency response of the electromagnetic forces on whirling cage rotors*. IEE Proceedings - Electric Power Application, 2003. **150**(6): p. 752-756.
- 105 Tenhunen, A., Holopainen, T. P. and Arkkio, A. *Effects of equalizing currents on electromagnetic forces of whirling cage rotor*. in *Proceedings of IEMDC'03*. 2003. Madison, WI, USA.
- 106 Tenhunen, A., Holopainen, T. P. and Arkkio, A. *Effects of saturation on the forces in induction motors with whirling cage rotor*. in *Proceedings of Compumag'03*. 2003. Saratoga Springs, NY, USA.
- 107 Toliyat, H.A., and Lipo, T. A., *Transient analysis of cage induction machines under stator, rotorbar and end ring faults*. IEEE Transactions on Energy Conversion, 1995. **10**(2): p. 241-247.
- 108 von Kaene, P., *Unbalanced magnetic pull in rotating electric machines:*

- 109 Wang, R., Mohellebi, H., Flack, T. J., Kamper, M. J., Buys, J. D., and Feliachi, M., *Two-dimensional cartesian air-gap element (CAGE) for dynamic finite-element modeling of electrical machines with a flat air gap.* IEEE Transactions on Magnetics, 2002. **38**(2): p. 1357-1359.
- 110 Williamson, S., and Smith, A. C., *Field analysis for rotating induction machines and its relationship to the equivalent-circuit method.* IEE Proceedings, 1980. **127B**(2): p. 83-90.
- 111 Williamson, S., and Smith, A. C., *Steady-state analysis of 3-phase cage motors with rotor-bar and end-rings faults.* IEE Proceedings, 1982. **129B**(3): p. 93-100.
- 112 Williamson, S., Lim, L. H., and Robinson, M., *Finite-element models for cage induction motor analysis.* IEEE Transactions on Industry Applications, 1990. **26**(6): p. 1007-1017.
- 113 Williamson, S. *Induction motor modelling using finite elements.* in *Proceedings of ICEM.* 1994. Paris.
- 114 Williamson, S., Healey, R. C., Lloyd, J. D., and Tevaarwerk, J. L., *Rotor cage anomalies and unbalanced magnetic pull in single-phase induction motors.* IEEE Transactions on Industry Applications, 1997. **33**(6): p. 1553-1562.
- 115 Wonk, V., *Machinery vibration: measurement and analysis.* 1991: McGraw-Hill, Inc.
- 116 Yan, D., and Hu, M. *The finite element method of computing exact inductance in squirrel cage induction motor.* in *ICEM 2000.* 2000. Helsinki University of Technology, Espoo, Finland.
- 117 Yang, B.S., Kim, Y. H., Son, B. G., *Instability and imbalance response of*

large induction motor by unbalanced magnetic pull. Journal of Vibration and Control, 2004. **10**(3): p. 447-560.

- 118 Zadrozny., J., Wiak., S., Zadrozny., J. (jr) and Welfle., H. *Field/inductance computation by means of FEM of induction motor dynamic states (for parametric resonance condition).* in *ICEM 2000*. 2000. Helsinki University of Technology, Espoo, Finland.
- 119 Zaim, M.E., *Non-linear models for the design of solid rotor induction machines.* IEEE Transactions on Magnetics, 1999. **35**(3): p. 1310-1313.
- 120 Zhou, P., Fu, W. N., Lin, D., Stanton, S., and Cendes, Z. J., *Numerical modeling of magnetic devices.* IEEE Transactions on Magnetics, 2004. **40**(4).
- 121 Zienkiewicz, O.C., and Taylor, R. L., *The finite element method volume 1: basic formulation and linear problems.* Vol. 1. 1989: McGraw-Hill Book Company.

APPENDIX A

A.1 Formulation for directional permeability for two dimensional magneto-static problem

The magnetic flux density is derived as the curl of another vector field:

$$\mathbf{B}(x, y) = \nabla \times \mathbf{A}(x, y) \quad (\text{A.1})$$

A static magnetic problem is described by

$$\nabla \times \mathbf{H}(x, y) = \mathbf{J}_0(x, y) \quad (\text{A.2})$$

$$\nabla \cdot \mathbf{B}(x, y) = 0 \quad (\text{A.3})$$

And also

$$\mathbf{H}(x, y) = \nu \mathbf{B}(x, y) \quad (\text{A.4})$$

$$\nabla \times ([\nu] \mathbf{B}(x, y)) = \mathbf{J}_0(x, y) \quad (\text{A.5})$$

where $[\nu]$ is the inverse of permeability and can be written for an orthotropic material as

$$[\nu] = \begin{bmatrix} \frac{1}{\mu_{xx}} & 0 \\ 0 & \frac{1}{\mu_{yy}} \end{bmatrix} \quad (\text{A.6})$$

where $\mu_{xx} \neq \mu_{yy}$

Equation (A.4) can be written as

$$\nabla \times [\mathbf{v}](\nabla \times \mathbf{A}(x, y)) = \mathbf{J}_0(x, y) \quad (\text{A.7})$$

$$\nabla \times \mathbf{A}(x, y) = \begin{bmatrix} i & j & k \\ \frac{\partial}{\partial x} & \frac{\partial}{\partial y} & \frac{\partial}{\partial z} \\ 0 & 0 & \mathbf{A}(x, y) \end{bmatrix} = \frac{\partial \mathbf{A}(x, y)}{\partial y} i - \frac{\partial \mathbf{A}(x, y)}{\partial x} j \quad (\text{A.8})$$

$$[\mathbf{v}](\nabla \times \mathbf{A}(x, y)) = \left(\frac{1}{\mu_{xx}} \right) \frac{\partial \mathbf{A}(x, y)}{\partial y} i - \left(\frac{1}{\mu_{yy}} \right) \frac{\partial \mathbf{A}(x, y)}{\partial x} j \quad (\text{A.9})$$

$$\begin{bmatrix} i & j & k \\ \frac{\partial}{\partial x} & \frac{\partial}{\partial y} & \frac{\partial}{\partial z} \\ \frac{1}{\mu_{xx}} \frac{\partial \mathbf{A}(x, y)}{\partial y} & -\frac{1}{\mu_{yy}} \frac{\partial \mathbf{A}(x, y)}{\partial x} & 0 \end{bmatrix} = \mathbf{J}_0(x, y) \quad (\text{A.10})$$

$$\left(\frac{1}{\mu_{yy}} \right) \frac{\partial^2 \mathbf{A}(x, y)}{\partial x^2} + \left(\frac{1}{\mu_{xx}} \right) \frac{\partial^2 \mathbf{A}(x, y)}{\partial y^2} = -\mathbf{J}_0(x, y) \quad (\text{A.11})$$

A.2 Approximation for B(H) curve

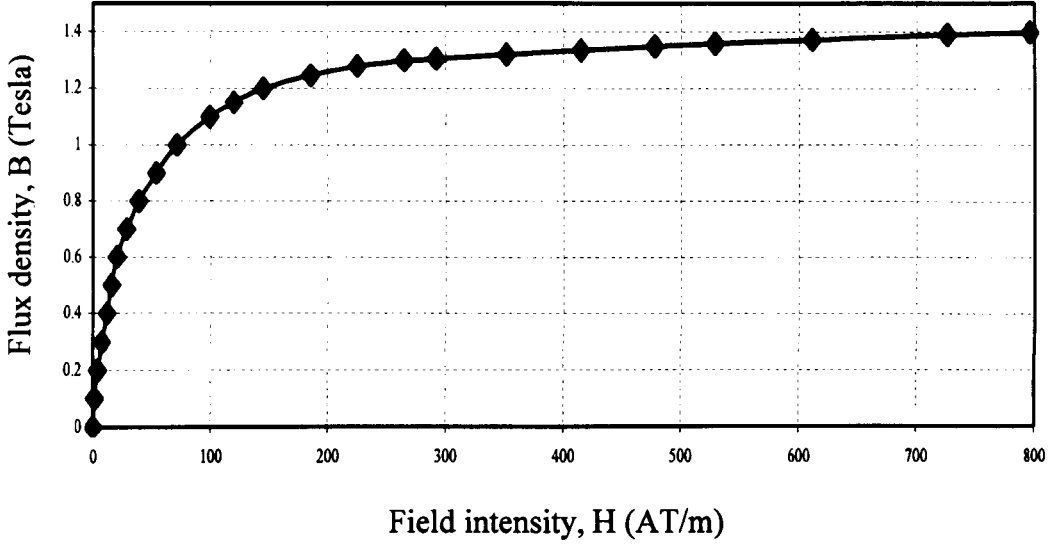


Figure (A.1): A $B(H)$ curve of a standard electrical steel

Figure (A.1) shows $B(H)$ curve for a standard electrical steel which is obtained experimentally. It is better to have an analytical function when we solve nonlinear finite element as the field intensity has to be calculated at every iterations for all elements. For the above reason the $B(H)$ curve shown in Figure (A.1) is divided into four regions and is fitted with four different polynomial functions maintaining C^1 continuity. Equation (A.12) shows the polynomial functions for different regions.

$$H = \begin{cases} a_1 B - b_1 B^2 & \text{for } 0.0 \leq B \leq 0.1 \text{ Tesla} \\ \frac{a_2}{(1 + b_2 e^{-c_2 B})} & \text{for } 0.1 \leq B \leq 1.4 \text{ Tesla} \\ a_3 + b_3 B + c_3 B^2 & \text{for } 1.4 \leq B \leq 2.0 \text{ Tesla} \\ \frac{1}{\mu_0} (B - 2.0) + a_3 + 2b_3 + 4c_3 & \text{for } 2.0 \leq B \text{ Tesla} \end{cases} \quad (\text{A.12})$$

where a_1 , b_1 , a_2 , b_2 , c_2 , a_3 , b_3 , and c_3 are constants and values of these constants are

a_1	69.80926049616697
b_1	291.2027377442727
a_2	-179.599730
b_2	-59.6075740
c_2	2.7802181
a_3	$1.261085222177513 \times 10^6$
b_3	$-1.813387839003966 \times 10^6$
c_3	$6.522906386158606e \times 10^5$

A.3 Approximating the stiffness matrix: what is important and what is not

Equation (3.59) in Chapter 3 appears as

$$[K]\{A\} \approx [U]\{I_{RS}\} + \{b\} \quad (A.13)$$

where $[U]$ is the transformation matrix which determines the transformation of nodal currents to the terminal currents. Generally $[U]$ is a tall thin matrix.

Assert that $[K]$ can be written in the following way

$$[K] = [H_U][H_U]^T + [H_V][H_V]^T \quad (A.14)$$

where

$$([H_U]([H_U]^T[H_U])^{-1}[H_U]^T)[U] = [U] \quad (A.15)$$

i.e. $[H_U]$ spans the same space as $[U]$.

Also,

$$([U]([U]^T[U])^{-1}[U]^T)[H_U] = [H_U] \quad (A.16)$$

And further more

$$[H_v]^T[U] = [H_v]^T[H_U] = 0 \quad (A.17)$$

To find $[H_U]$ the procedure is adopted. It is speculated that

$$[H_U] = [U][X] \quad (A.18)$$

$[X]$ can be calculated as

$$[U]^T[K]U = ([U]^T[U])([X]X^T)([U]^T[U]) \quad (A.19)$$

$$[X]X^T = ([U]^T[U])([U]^T[K]U)([U]^T[U])^{-1} \quad (A.20)$$

The Cholesky decomposition can be used to evaluate the matrix $[X]$. The matrix $[X]$ can also be calculated by solving the eigenvalue problem. Once $[H_U]$ is calculated $[H_v]$ is calculated as

$$[H_v][H_v] = [K] - [H_U][H_U]^T \quad (A.21)$$

Again assert that

$$[K]^{-1} = [H_U][X_U][H_U]^T + [H_v][X_v][H_v]^T \quad (A.22)$$

The following procedure is adopted to calculate $[X_U]$ and $[X_v]$.

$$[K][K]^{-1} = [I] \quad (A.23)$$

$$[H_U][H_U]^T[H_U][X_U][H_U]^T + [H_V][H_V]^T[H_V][X_V][H_V]^T = [I] \quad (A.24)$$

Pre-multiplying by $[H_U]^T$ and post-multiplying by $[H_U]$ we can write Equation (A.24) as

$$[H_U]^T[H_U][H_U]^T[H_U][X_U][H_U]^T[H_U] = [H_U]^T[H_U] \quad (A.25)$$

$$[X_U] = ([H_U]^T[H_U])^{-1}([H_U]^T[H_U])^{-1} \quad (A.26)$$

Similarly $[X_V]$ can be calculated as

$$[X_V] = ([H_V]^T[H_V])^{-1}([H_V]^T[H_V])^{-1} \quad (A.27)$$

The main purpose of the calculation of $[K]^{-1}$ is to evaluate inductance matrix, $[L]$, which is calculated using the formula

$$[L] = [U]^T[K]^{-1}[U] \quad (A.28)$$

It is clear from Equation (A.28) that not all the entries of $[K]^{-1}$ are relevant while calculating the inductance matrix.

A.4 Lagrange's equation of motion for coupled electrical and mechanical dynamics

In this coupled system a mechanical process and an electromagnetic process are coupled. The mechanical system is described by a generalised displacement vector, $\{q\}$ and electrical dynamics part of a R-L system is described by generalised electrical quantity (charge), $\{Q\}$.

The Magnetic Field Energy, MFE can be written

$$MFE = \frac{1}{2} \{\dot{Q}\}^T [L_0(q, \theta)] \{\dot{Q}\} \quad (A.29)$$

Here $\{\dot{Q}\}$ is the electric current and $[L_0(q, \theta)]$ is the inductance of the system which is a function of displacement and rotational position of the rotor.

Similarly, the Kinetic Energy, KE of the system can be written as

$$KE = \frac{1}{2} \{\dot{q}\}^T [M] \{\dot{q}\} \quad (A.30)$$

where $[M]$ and $\{\dot{q}\}$ are the mass matrix and generalised velocity respectively.

Potential energy of the system, PE is

$$PE = \frac{1}{2} \{q\}^T [K] \{q\} \quad (A.31)$$

Here $[K]$ and $\{q\}$ are the stiffness matrix and generalised displacement vector respectively. Dissipation function, F^* is expressed as

$$F^* = \frac{1}{2} \{\dot{Q}\}^T [R] \{\dot{Q}\} + \frac{1}{2} \{\dot{q}\}^T [C] \{\dot{q}\} \quad (A.32)$$

Here $[R]$ is the resistance and $[C]$ is the damping of the system. In the mechanical dynamics $\{q\}$ is the displacement vector and in electrical dynamics $\{Q\}$ is the electric charge vector. The Lagrangian of the electrical and mechanical coupled system is

$$L = KE(\{q\}, \{\dot{q}\}) + MFE(\{\dot{q}\}, \{Q\}) - PE(\{q\}) \quad (A.33)$$

Motion of the system is governed by the Lagrange equation

$$\frac{d}{dt} \left(\frac{\partial L}{\partial \dot{Q}} \right) - \frac{\partial L}{\partial Q} + \frac{\partial F}{\partial \dot{Q}} = \{F_1\} \quad (A.34)$$

and

$$\frac{d}{dt} \left(\frac{\partial L}{\partial \dot{q}} \right) - \frac{\partial L}{\partial q} + \frac{\partial F}{\partial \dot{q}} = \{F_2\} \quad (A.35)$$

where $\{F_1\}$ and $\{F_2\}$ are vectors the generalised forces. For the electrical system $\{F_1\}$ is the vector generalised electric potentials and for the mechanical system $\{F_2\}$ is the vector generalised mechanical forces.

Again from Equation (A.34) we get

$$\frac{d}{dt} ([L_o] \{\dot{Q}\}) + [R] \{\dot{Q}\} = \{F_1\} \quad (A.36)$$

$$[L_o] \{\ddot{Q}\} + \left(\Omega \frac{\partial [L_o]}{\partial \theta} + [R] \right) \{\dot{Q}\} + \frac{\partial [L_o]}{\partial \{q\}} \{\dot{q}\} \{\dot{Q}\} = \{F_1\} \quad (A.37)$$

$$[L_o] \{\ddot{Q}\} + \left(\Omega \frac{\partial [L_o]}{\partial \theta} + [R] \right) \{\dot{Q}\} + \frac{\partial [L_o]}{\partial \{q\}} \{\dot{Q}\} \{\dot{q}\} = \{F_1\} \quad (A.38)$$

From Equation (A.35) we get

$$\frac{d}{dt}([M]\{\dot{q}\}) + [K]\{q\} - \frac{1}{2}\{\dot{Q}\}^T \frac{\partial[L_0]}{\partial\{q\}}\{\dot{Q}\} + [C]\{\dot{q}\} = \{F_2\} \quad (A.39)$$

$$[M]\{\ddot{q}\} + [K]\{q\} - \frac{1}{2}\{\dot{Q}\}^T \frac{\partial[L_0]}{\partial\{q\}}\{\dot{Q}\} + [C]\{\dot{q}\} = \{F_2\} \quad (A.40)$$

Combining Equations (A.38) and (A.40)

$$\begin{bmatrix} \frac{1}{2}L_0 & 0 \\ 0 & M \end{bmatrix} \begin{bmatrix} \ddot{Q} \\ \ddot{q} \end{bmatrix} + \begin{bmatrix} \frac{1}{2}\left(\Omega \frac{\partial L_0}{\partial \theta} + R\right) & \frac{1}{2}\frac{\partial L_0}{\partial q}\dot{Q} \\ -\frac{1}{2}\dot{Q}^T \frac{\partial L_0}{\partial q} & C \end{bmatrix} \begin{bmatrix} \dot{Q} \\ \dot{q} \end{bmatrix} + \begin{bmatrix} 0 & 0 \\ 0 & K \end{bmatrix} \begin{bmatrix} Q \\ q \end{bmatrix} = \begin{bmatrix} \frac{1}{2}F_1 \\ F_2 \end{bmatrix} \quad (A.41)$$

A.5 Calculation of $[F_0]$ based on the minimization of total resistive losses

$$\frac{d}{d[F_0]} \{I_{B0}\}^T \left([G_0]^T [R_E] [G_0] \right) \{I_{B0}\} = 0 \quad (A.42)$$

$$\frac{d}{d[F_0]} \{I_{B0}\}^T \left(\left([H_0^+]^T + [H_0^\perp] [F_0] \right)^T [R_E] \left([H_0^+]^T + [H_0^\perp] [F_0] \right) \right) \{I_{B0}\} = 0 \quad (A.43)$$

$$\frac{d}{d[F_0]} \{I_{B0}\}^T \left(\left([H_0^+] + [F_0]^T [H_0^\perp]^T \right)^T [R_E] \left([H_0^+]^T + [H_0^\perp] [F_0] \right) \right) \{I_{B0}\} = 0 \quad (A.44)$$

$$\frac{d}{d[F_0]} \{I_{B0}\}^T \left(\begin{aligned} & [H_0^+] [R_E] [H_0^+]^T + [H_0^+] [R_E] [H_0^\perp] [F_0] \\ & + [F_0]^T [H_0^\perp]^T [R_E] [H_0^+]^T + [F_0]^T [H_0^\perp]^T [R_E] [H_0^\perp] [F_0] \end{aligned} \right) \{I_{B0}\} = 0 \quad (A.45)$$

$$2 [H_0^+] [R_E] [H_0^\perp] + 2 [F_0]^T [H_0^\perp]^T [R_E] [H_0^\perp] = 0 \quad (A.46)$$

$$[F_0] = - \left([H_0^\perp]^T [R_E] [H_0^\perp] \right)^{-1} \left([H_0^\perp] [R_E] [H_0^+] \right) \quad (A.47)$$

A.6 Effects of different number of modes of conductance in a rotor bar

The machine considered is a 4-pole, 3-phase induction motor wound with double layered windings. The stator of this machine has three independent currents. The number of rotor bars is 32. This study provides the effects of different number of modes of conductance in a rotor bar.

If two modes of conductance are considered for the rotor bar and the number of harmonics for the Fourier approximation of the rotor bar is also five, the transformations in Chapter 4 leads to a total of 20 independent rotor currents. The stator and rotor currents can be written as

$$\{I_{RS2}\} = \left\{ \begin{array}{cccccc} \text{Stator currents} & \text{Rotor currents (DC components)} & \text{Rotor currents (1st harmonics, cos)} & \text{Rotor currents (1st harmonics, sin)} & \text{Rotor currents (2nd harmonics, cos)} & \text{Rotor currents (2nd harmonics, sin)} \\ i_1 & \dots & i_3 & i_4 & i_5 & \dots & i_6 & i_7 & \dots & i_8 & i_9 & \dots & i_{10} & i_{11} & \dots & i_{12} & \dots & i_{20} \end{array} \right\}^T \quad (A.48)$$

here i_1, \dots, i_3 are the three stator currents, i_4 is the DC components of the rotor currents, i_5, \dots, i_6 are the cosine components of the first harmonics of the rotor currents and so on.

Similarly the stator and rotor currents for three, four and five modes of conductance can be written as Equations (A.49), (A.50) and (A.51) respectively.

$$\{I_{RS3}\} = \left\{ \begin{array}{cccccc} \text{Stator currents} & \text{Rotor currents (DC components)} & \text{Rotor currents (1st harmonics, cos)} & \text{Rotor currents (1st harmonics, sin)} & \text{Rotor currents (2nd harmonics, cos)} & \text{Rotor currents (2nd harmonics, sin)} \\ i_1 & \dots & i_3 & i_4 & i_5 & i_6 & \dots & i_8 & i_9 & \dots & i_{11} & i_{12} & \dots & i_{14} & i_{15} & \dots & i_{17} & \dots & i_{29} \end{array} \right\}^T \quad (A.49)$$

$$\{I_{RS4}\} = \left\{ \overbrace{i_1 \cdots i_3}^{\text{Stator currents}} \overbrace{i_4 \cdots i_6}^{\text{Rotor currents (DC components)}} \overbrace{i_7 \cdots i_{10}}^{\text{Rotor currents (1st harmonics, cos)}} \overbrace{i_{11} \cdots i_{14}}^{\text{Rotor currents (1st harmonics, sin)}} \overbrace{i_{15} \cdots i_{18}}^{\text{Rotor currents (2nd harmonics, cos)}} \overbrace{i_{19} \cdots i_{22} \cdots i_{38}}^{\text{Rotor currents (2nd harmonics, sin)}} \right\}^T \quad (\text{A.50})$$

$$\{I_{RS5}\} = \left\{ \overbrace{i_1 \cdots i_3}^{\text{Stator currents}} \overbrace{i_4 \cdots i_7}^{\text{Rotor currents (DC components)}} \overbrace{i_8 \cdots i_{12}}^{\text{Rotor currents (1st harmonics, cos)}} \overbrace{i_{13} \cdots i_{17}}^{\text{Rotor currents (1st harmonics, sin)}} \overbrace{i_{18} \cdots i_{23}}^{\text{Rotor currents (2nd harmonics, cos)}} \overbrace{i_{23} \cdots i_{27} \cdots i_{47}}^{\text{Rotor currents (2nd harmonics, sin)}} \right\}^T \quad (\text{A.51})$$

Figure (A.2) shows the rotor currents for different modes of conductance corresponds to the first modes of the cosine component of the 2nd harmonics and Figure (A.3) shows the rotor currents for different modes of conductance corresponds to the first modes of the sine component of the 2nd harmonics. It can be concluded that four modes of conductance are enough to represent the currents in a rotor bar for this machine.

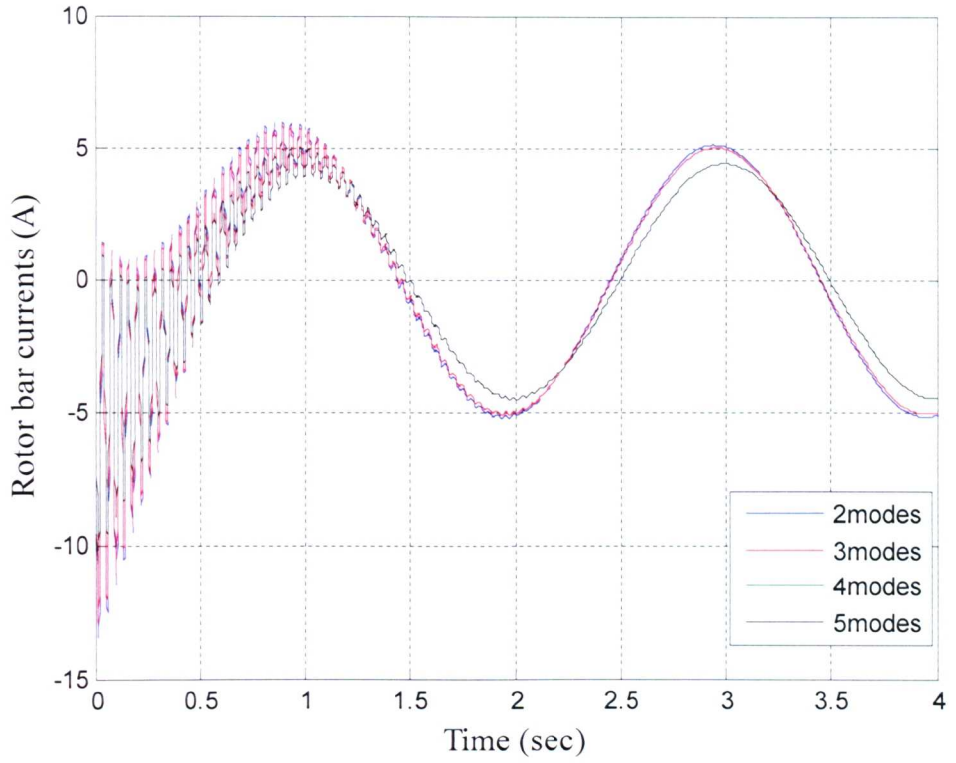


Figure (A.2) shows the rotor currents for different modes of conductance corresponds to the first modes of the cosine component of the 2nd harmonics

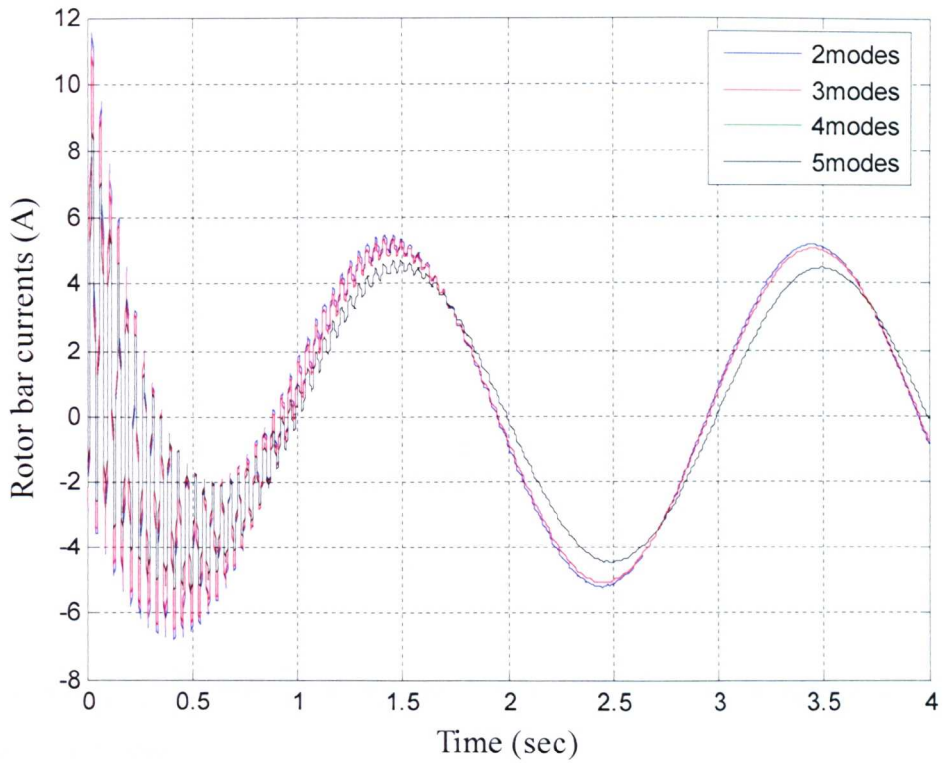


Figure (A.3) shows the rotor currents for different modes of conductance corresponds to the first modes of the cosine component of the 2nd harmonics

APPENDIX B

B.1 Frequency response matrix

Consider a second-order system described by the three equations:

$$\{f\} = [S_L] \{u\} \quad (B.1)$$

$$[K_{\text{mech}}] \{q\} + [D] \{\dot{q}\} + [M] \{\ddot{q}\} = \{f\} \quad (B.2)$$

$$\{y\} = [S_R]^T \{q\} \quad (B.3)$$

If this system is classically-damped, then it is possible to define a coordinate transformation in the form

$$\{q\} = [S_R] \{q'\} \text{ and } \{f'\} = [S_L]^T \{f\} \quad (B.4)$$

with the effect that the equations of motion can be written as

$$\{f'\} = [\Phi_L]^T \{u\} \quad (B.5)$$

$$[\Lambda] \{q'\} + [\Gamma] \{\dot{q}'\} + [I] \{\ddot{q}'\} = \{f'\} \quad (B.6)$$

$$\{y\} = [\Phi_R]^T \{q'\} \quad (B.7)$$

with matrices $[\Lambda]$, $[\Gamma]$ and $[I]$ all diagonal. It is obvious from Equations (B.1), (B.2), (B.3) and (B.4) that

$$\begin{aligned}
[\Phi_L]^T &= [T_L]^T [S_L], [\Phi_R]^T = [T_R]^T [S_R] \\
[\Lambda]^T &= [T_L]^T [K_{\text{mech}}] [T_R], [\Gamma]^T = [T_L]^T [D] [T_R] \text{ and } [I]^T = [T_L]^T [M] [T_R]
\end{aligned} \tag{B.8}$$

All of the matrices here are real-valued. The frequency-response matrix, $[H(\omega)]$, is $(n_o \times n_i)$ where n_o represents the number of outputs (the dimension of $\{y\}$) and where n_i represents the number of inputs (the dimension of $\{u\}$). $[H(\omega)]$ can be expressed in terms of either the original representation of Equations (B.1), (B.2) and (B.3) or the transformed (modal) representation of Equations (B.5), (B.6) and (B.7) thus

$$\begin{aligned}
[H(\omega)] &= [S_R]^T ([K_{\text{mech}}] + j\omega[D] - \omega^2[M])^{-1} [S_L] \\
&= [\Phi_R] ([\Lambda] + j\omega[\Gamma] - \omega^2[I])^{-1} [\Phi_L]^T
\end{aligned} \tag{B.9}$$

A single entry of the frequency response matrix can be constructed as:

$$h_{ij}(\omega) = \sum_{k=1}^n \frac{\phi_{R,ik}^T \phi_{L,jk}}{(\lambda_{kk} + j\omega\gamma_{kk} - \omega^2)} \tag{B.10}$$

where $\phi_{L,jk}$ represents the amount by which one unit of excitation at input degree of freedom $\#j$ excites mode $\#k$ and $\phi_{R,ik}$ represents the amount of output at output degree of freedom $\#i$ is contributed by each mode $\#k$.

B.2 Supply Voltages and Stator Currents for No-Load conditions from experimental rig

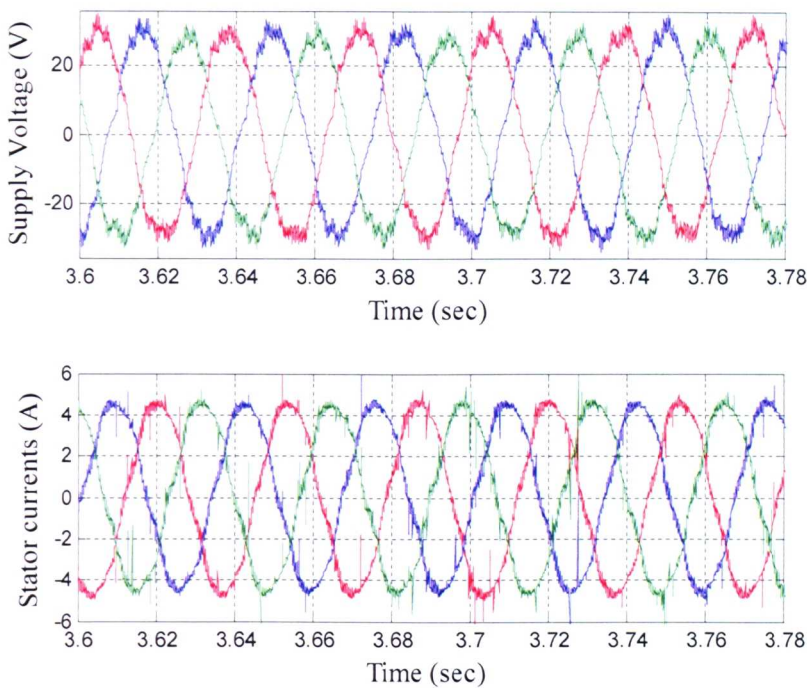


Figure (B.2): Supply voltages and stator currents at no load condition for supply frequency of 30 Hz

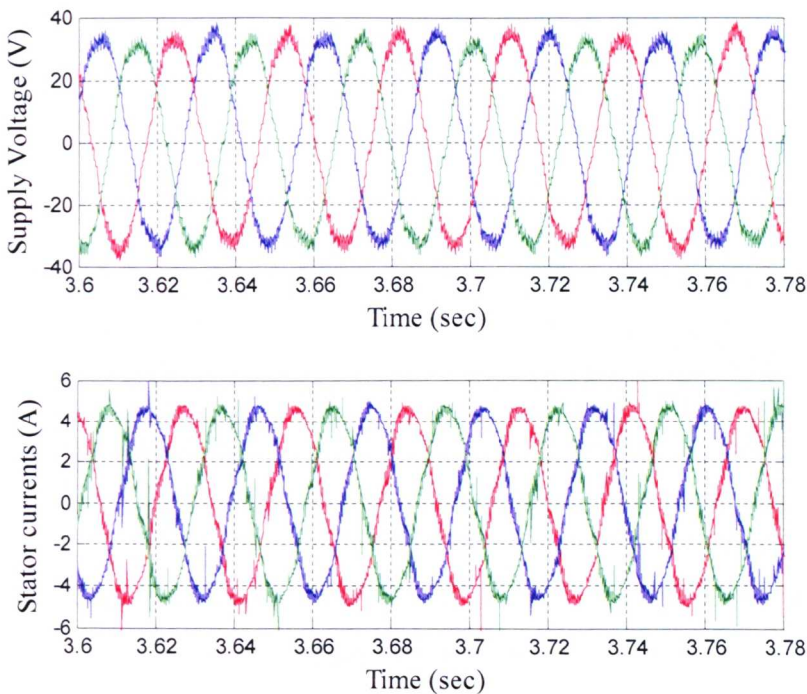


Figure (B.3): Supply voltages and stator currents at no load condition for supply frequency of 35 Hz

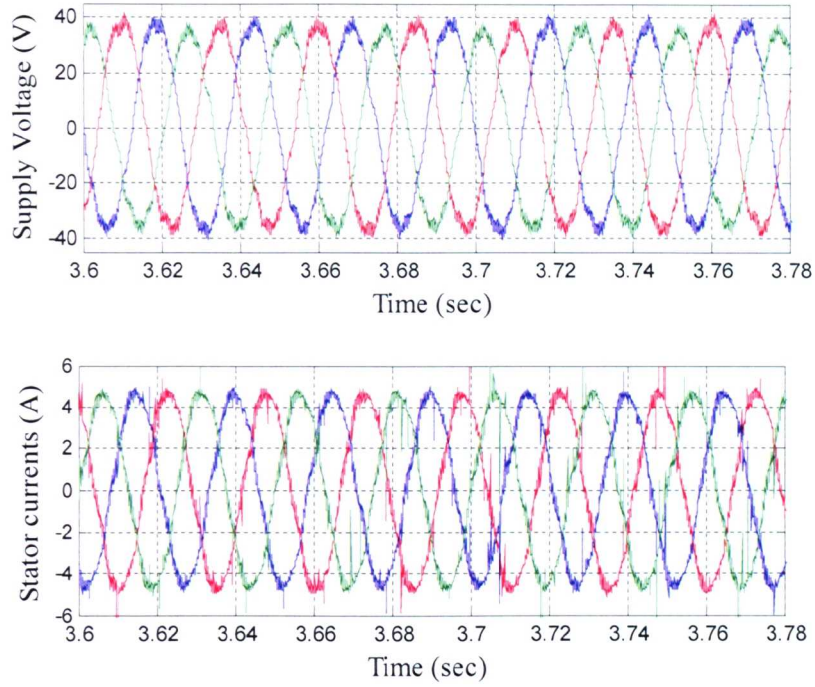


Figure (B.4): Supply voltages and stator currents at no load condition for supply frequency of 40 Hz

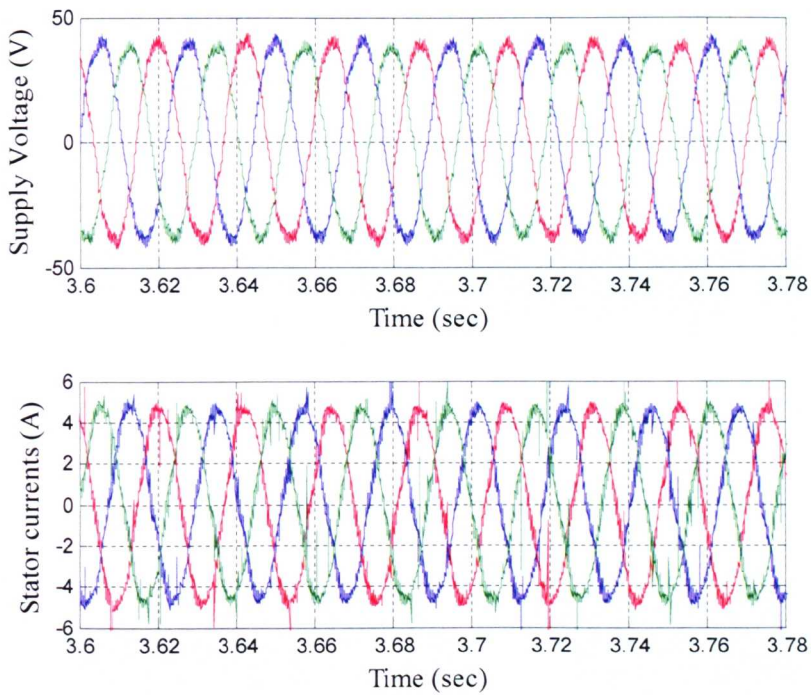


Figure (B.5): Supply voltages and stator currents at no load condition for supply frequency of 45 Hz

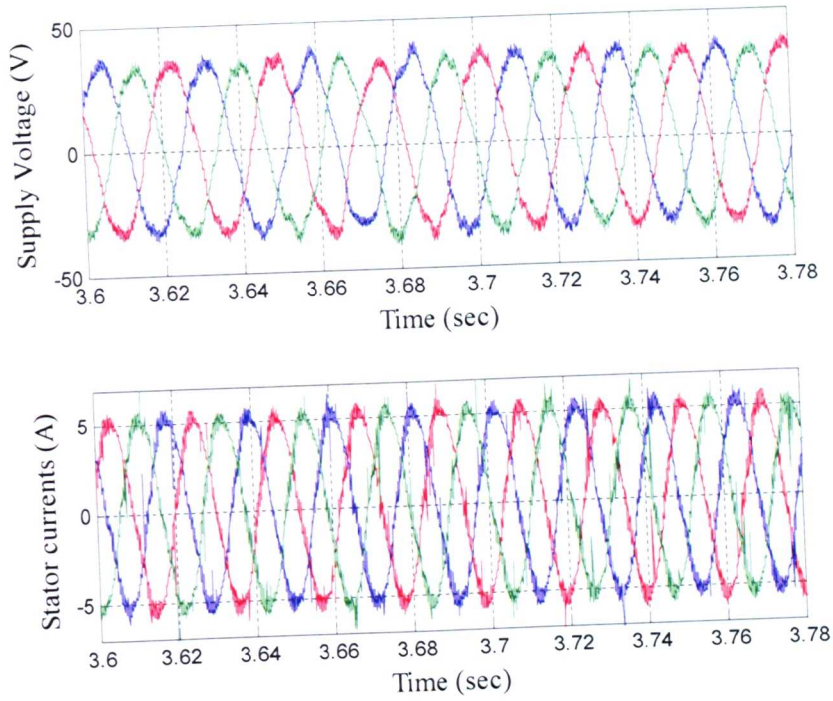


Figure (B.6): Supply voltages and stator currents at no load condition for supply frequency of 50 Hz

B.3 Equalizing Voltages and Currents for No-Load conditions from experimental rig

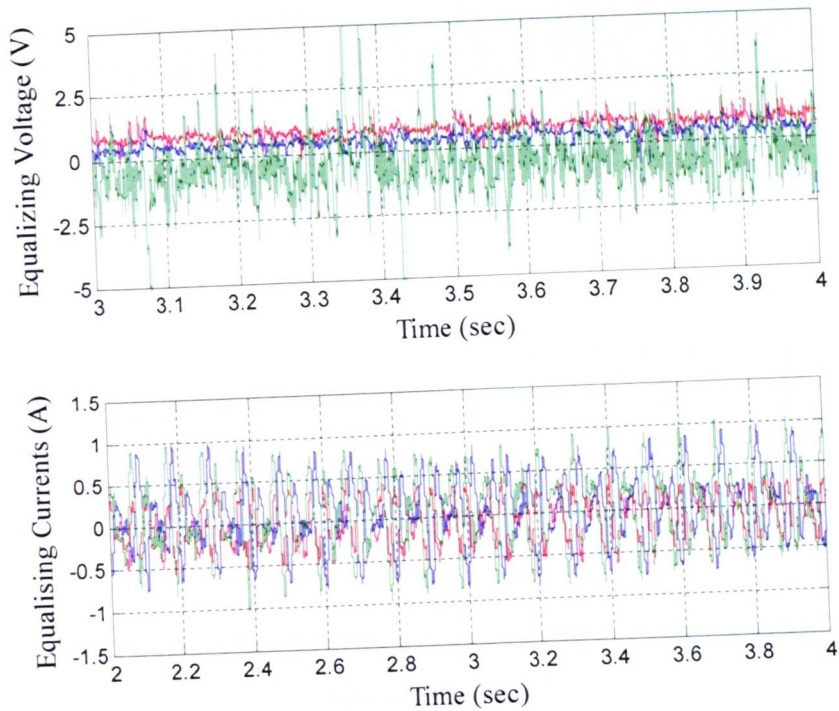


Figure (B.7): Equalizing voltages and currents at no load condition for supply frequency of 20 Hz

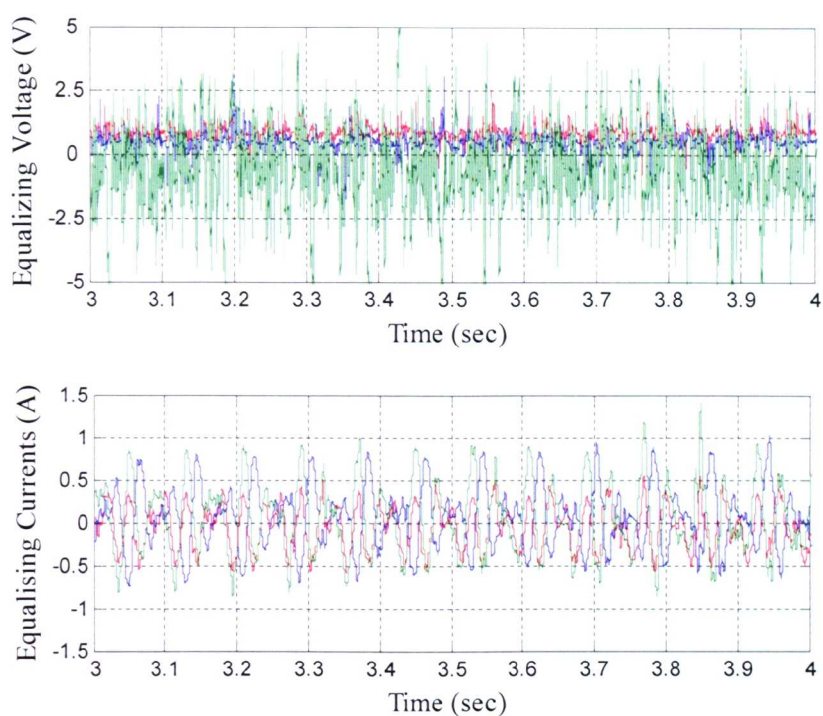


Figure (B.8): Equalizing voltages and currents at no load condition for supply frequency of 25 Hz

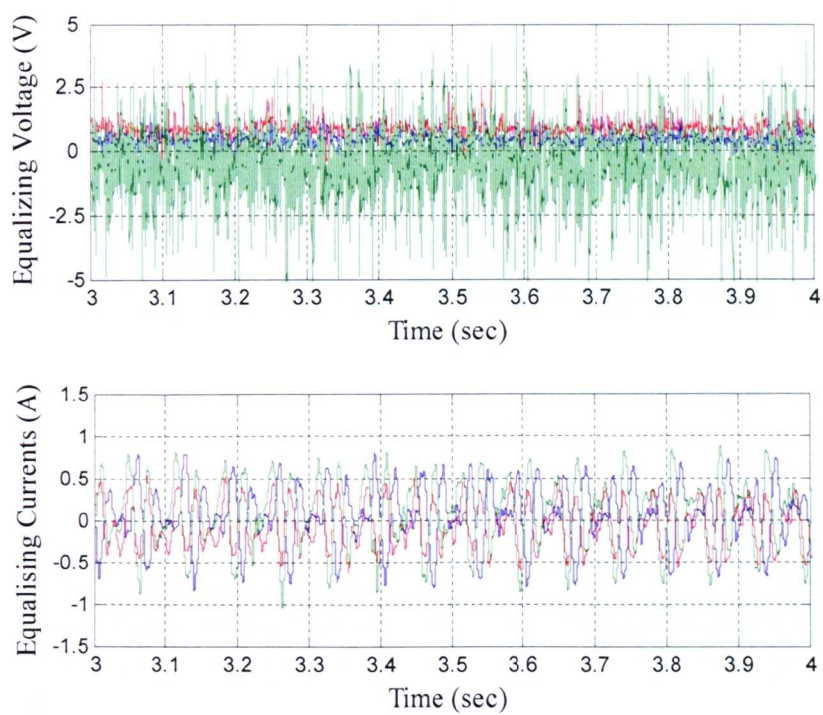


Figure (B.9): Equalizing voltages and currents at no load condition for supply frequency of 30 Hz

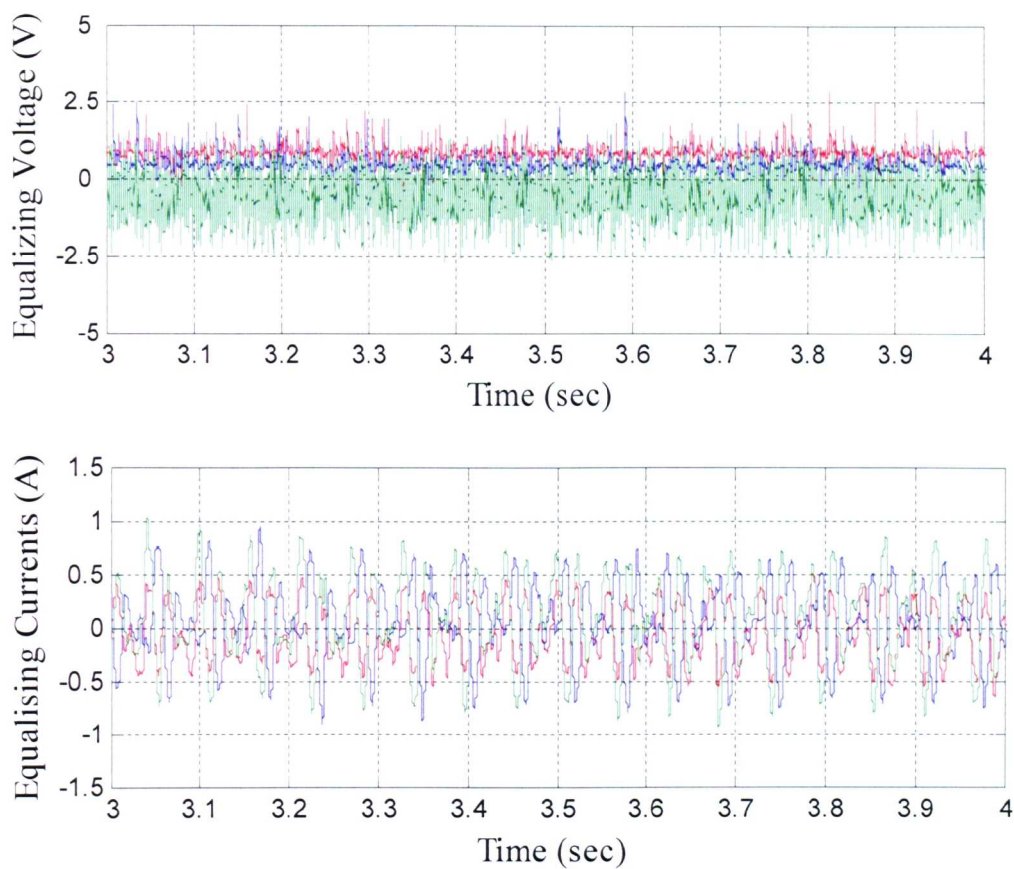


Figure (B.10): Equalizing voltages and currents at no load condition for supply frequency of 35 Hz

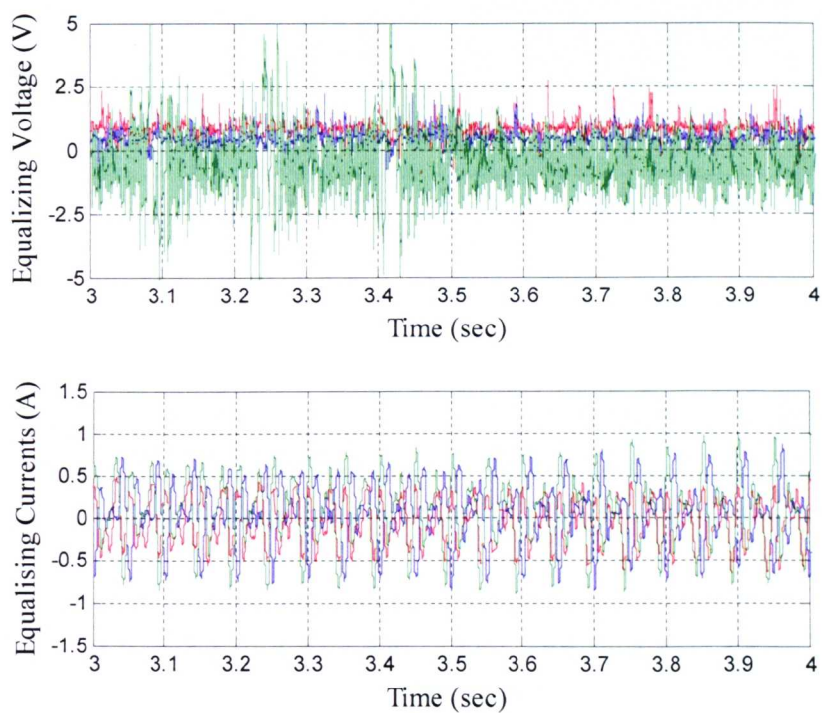


Figure (B.11): Equalizing voltages and currents at no load condition for supply frequency of 40 Hz

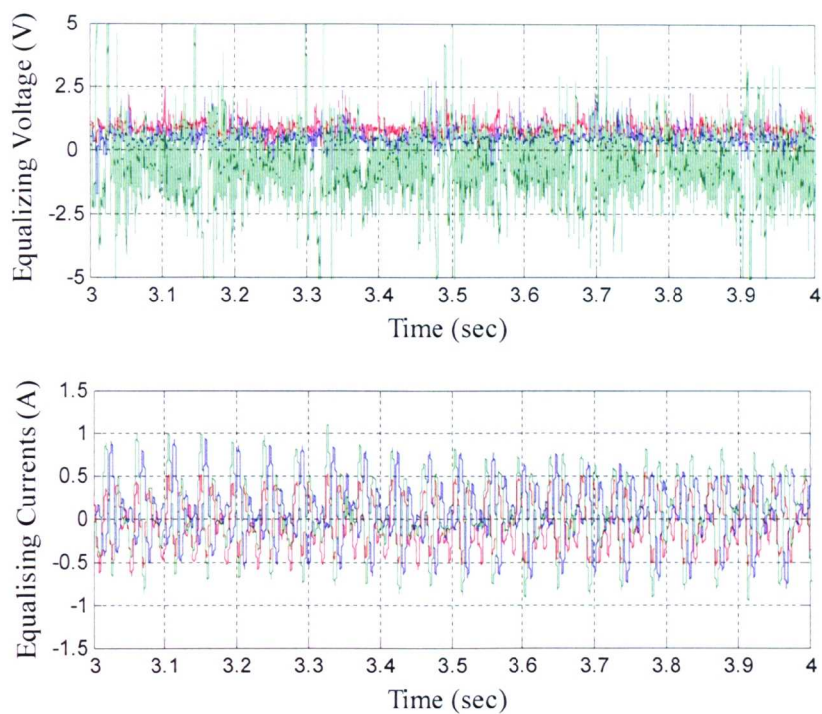


Figure (B.12): Equalizing voltages and currents at no load condition for supply frequency of 45 Hz

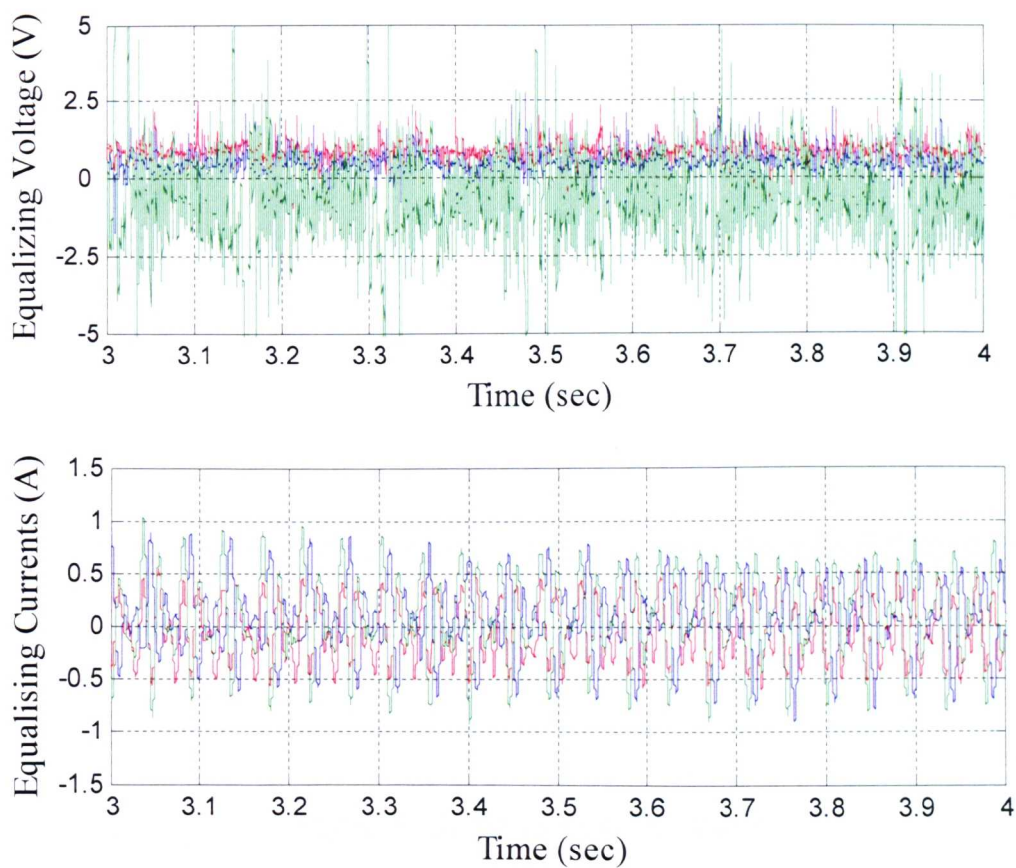


Figure (B.13): Equalizing voltages and currents at no load condition for supply frequency of 50 Hz

C.1 Comparison of results from MagFEA and MEGA

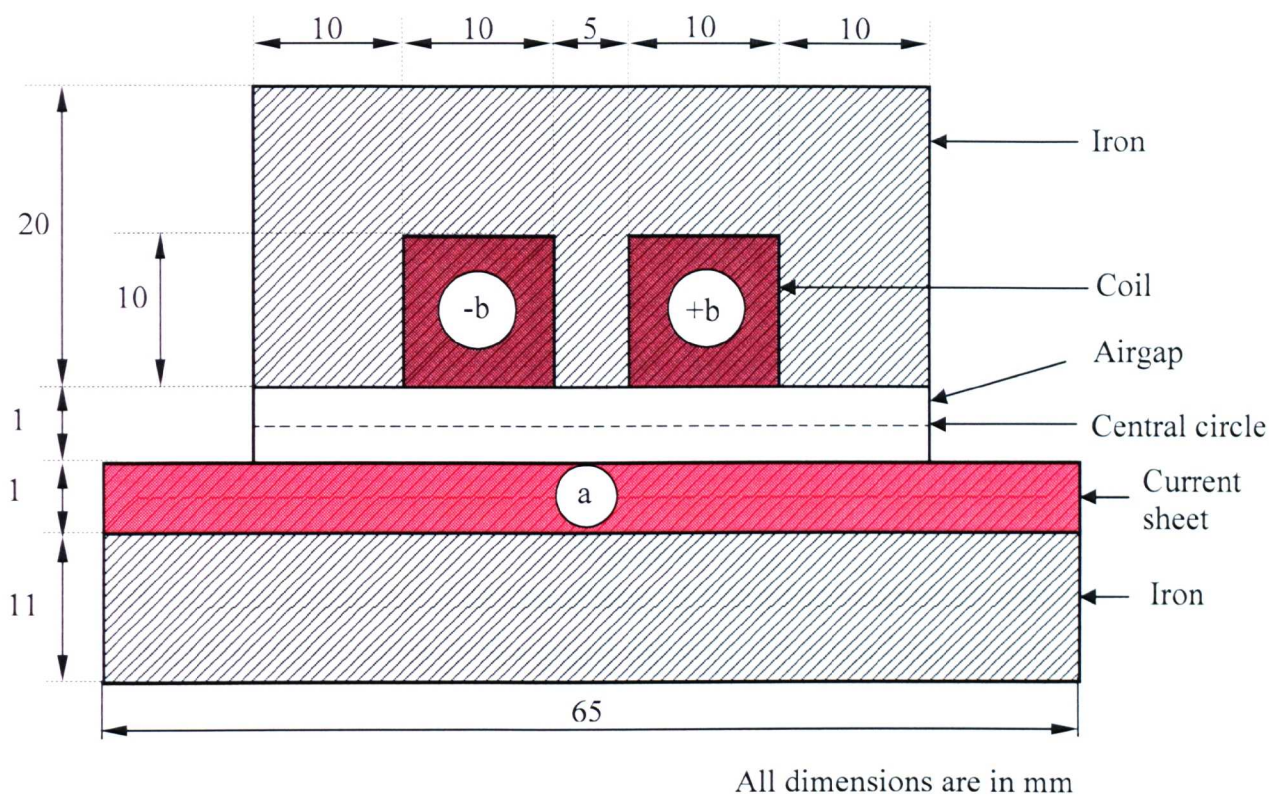


Figure (C.1): A simple electromagnetic device

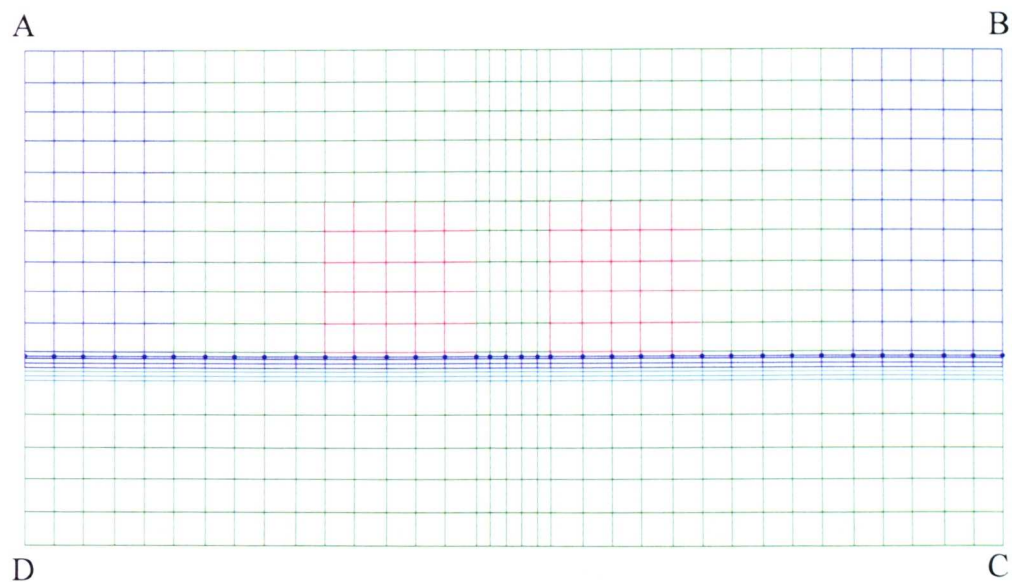


Figure (C.2): FE mesh of the model

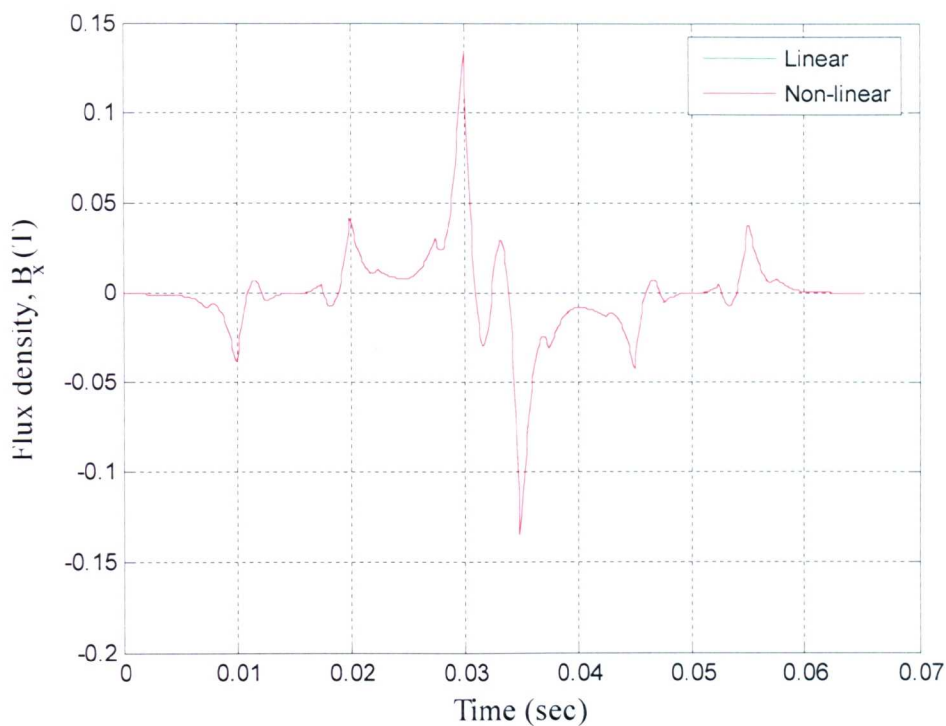


Figure (C.3): x-component of the flux density for linear and non-linear case from MagFEA in the middle of the airgap when $C1 = 5 \text{ A/mm}^2$ and $C2 = 0$

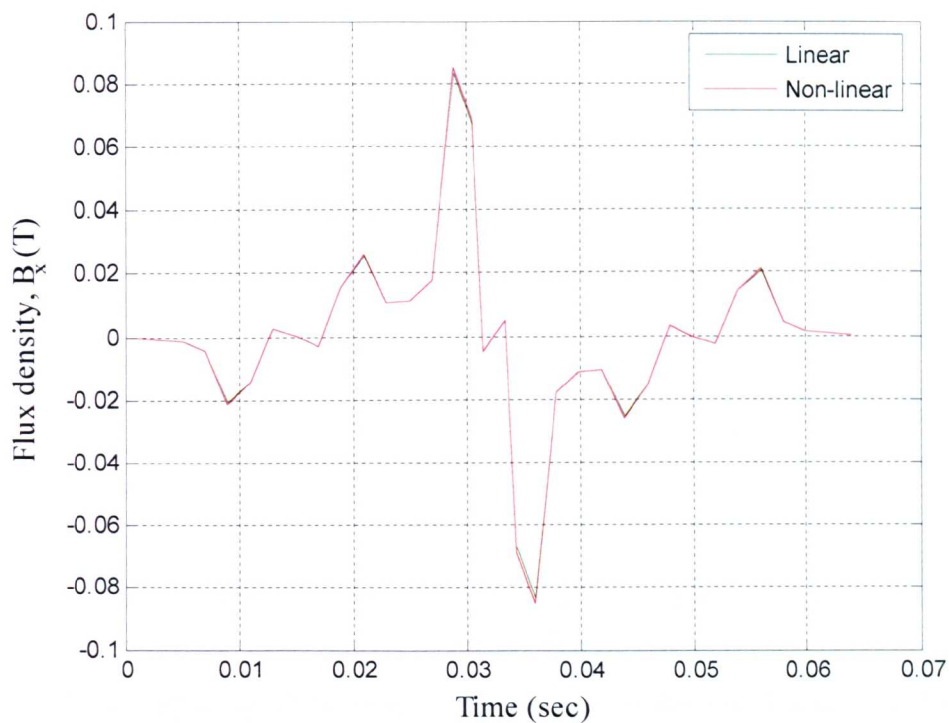


Figure (C.4): x-component of the flux density for linear and non-linear case from MEGA in the middle of the airgap when $C1 = 5 \text{ A/mm}^2$ and $C2 = 0$

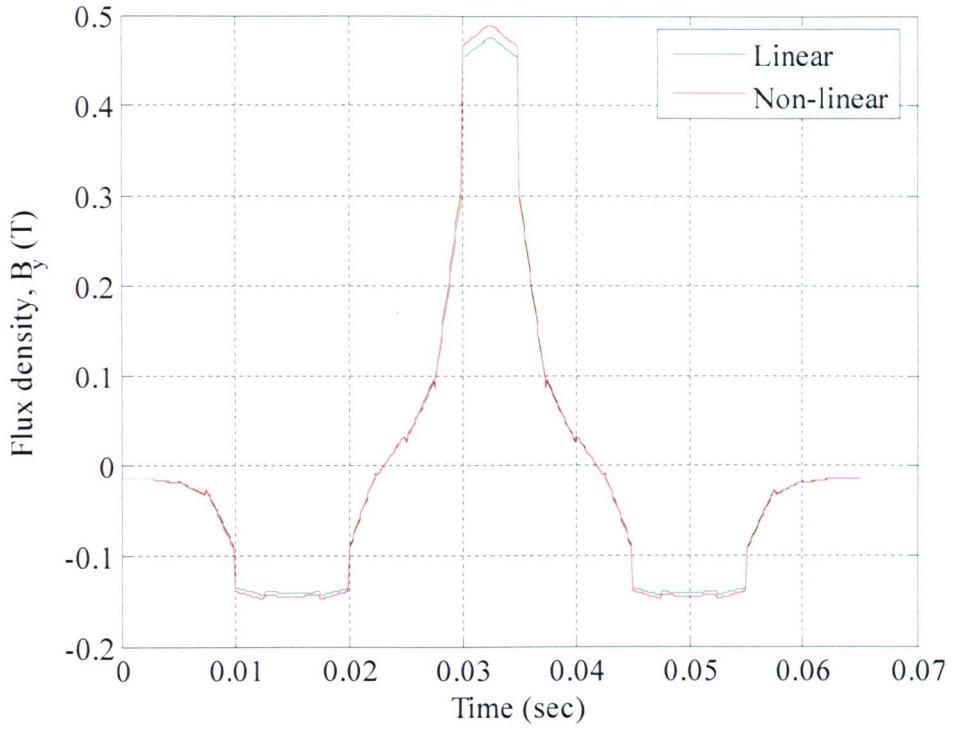


Figure (C.5): y-component of the flux density for linear and non-linear case from MagFEA in the middle of the airgap when $C1 = 5 \text{ A/mm}^2$ and $C2 = 0$

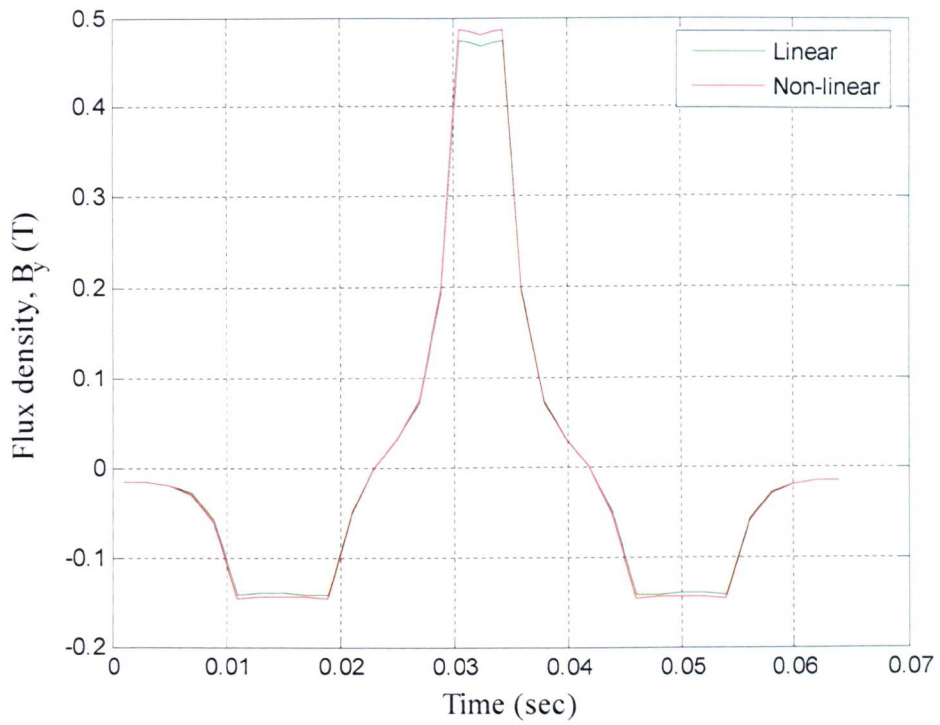


Figure (C.6): y-component of the flux density for linear and non-linear case from MEGA in the middle of the airgap when $C1 = 5 \text{ A/mm}^2$ and $C2 = 0$

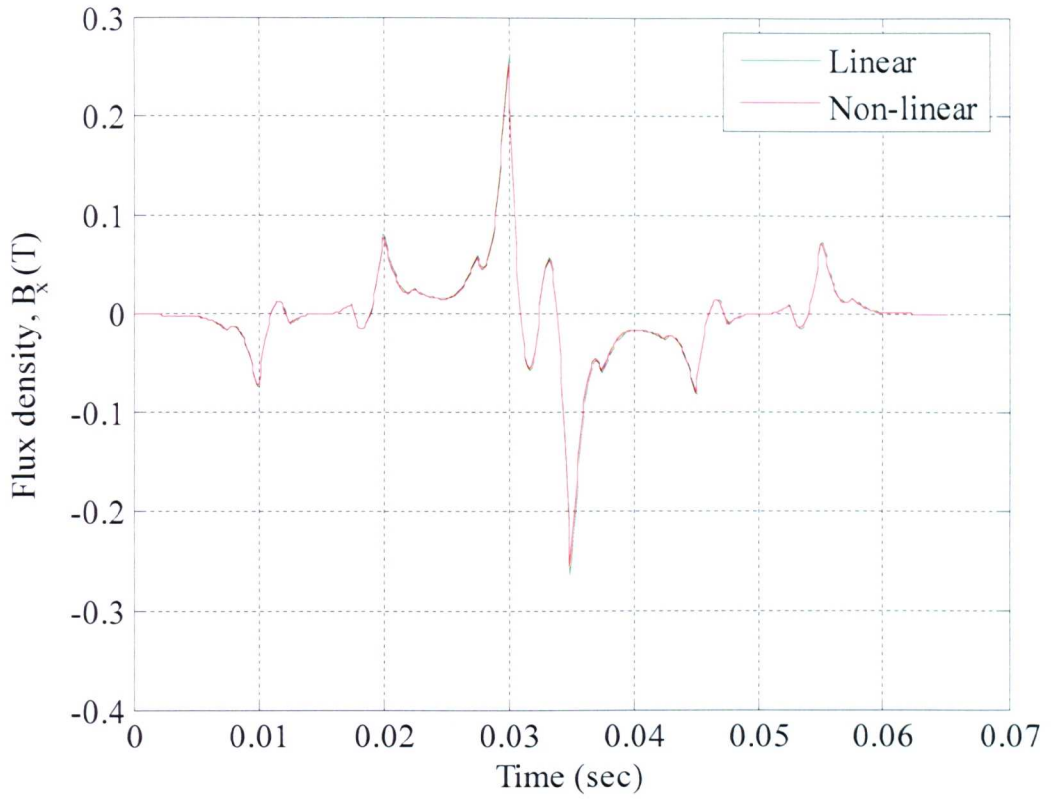


Figure (C.7): x-component of the flux density for linear and non-linear case from MagFEA in the middle of the airgap when $C1 = 10 \text{ A/mm}^2$ and $C2 = 0$

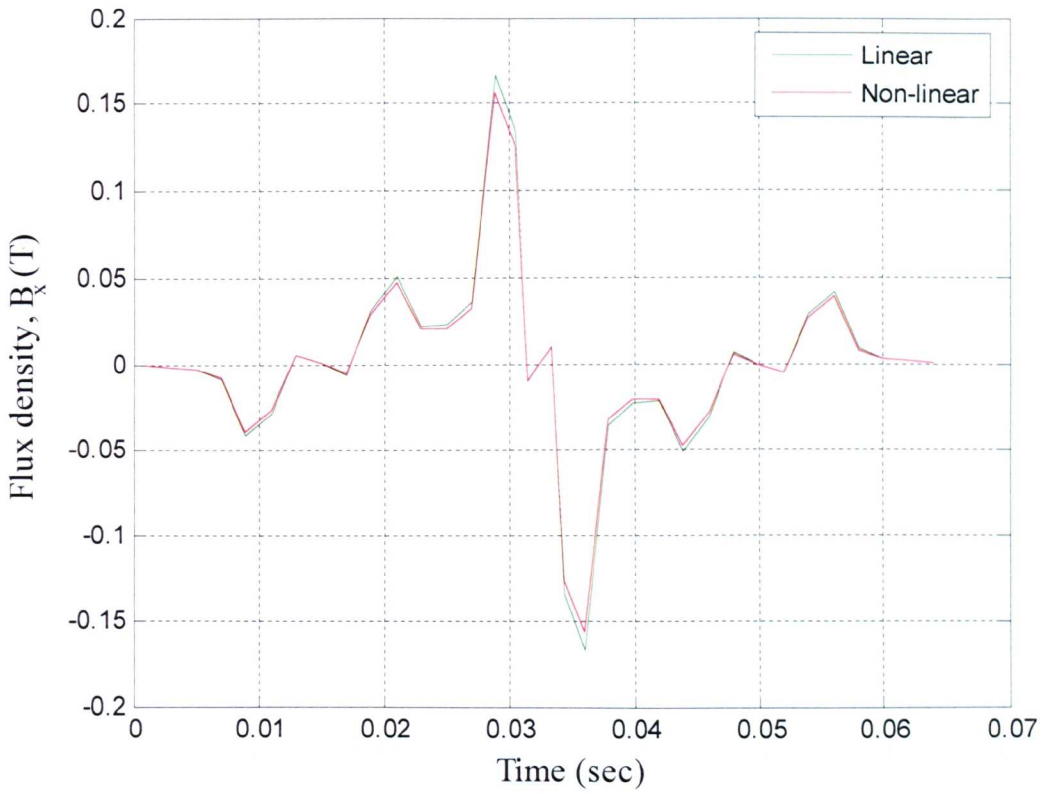


Figure (C.8): x-component of the flux density for linear and non-linear case from MEGA in the middle of the airgap when $C1 = 10 \text{ A/mm}^2$ and $C2 = 0$

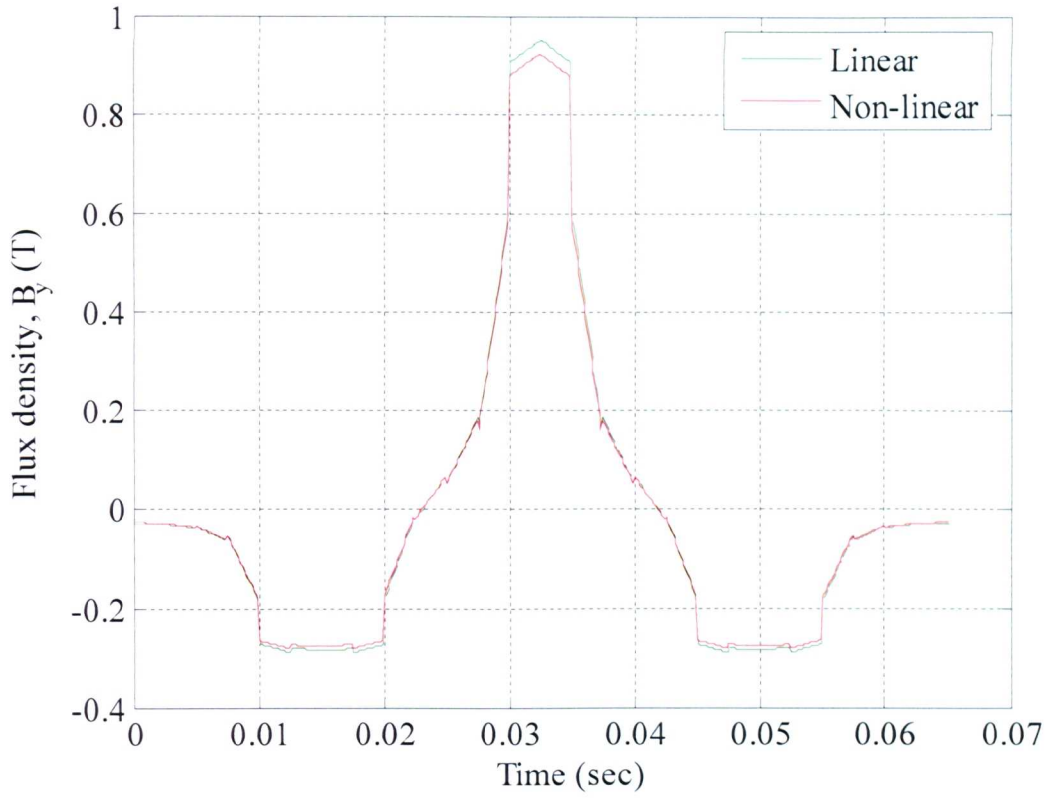


Figure (C.9): y-component of the flux density for linear and non-linear case from MagFEA in the middle of the airgap when $C1 = 10 \text{ A/mm}^2$ and $C2 = 0$

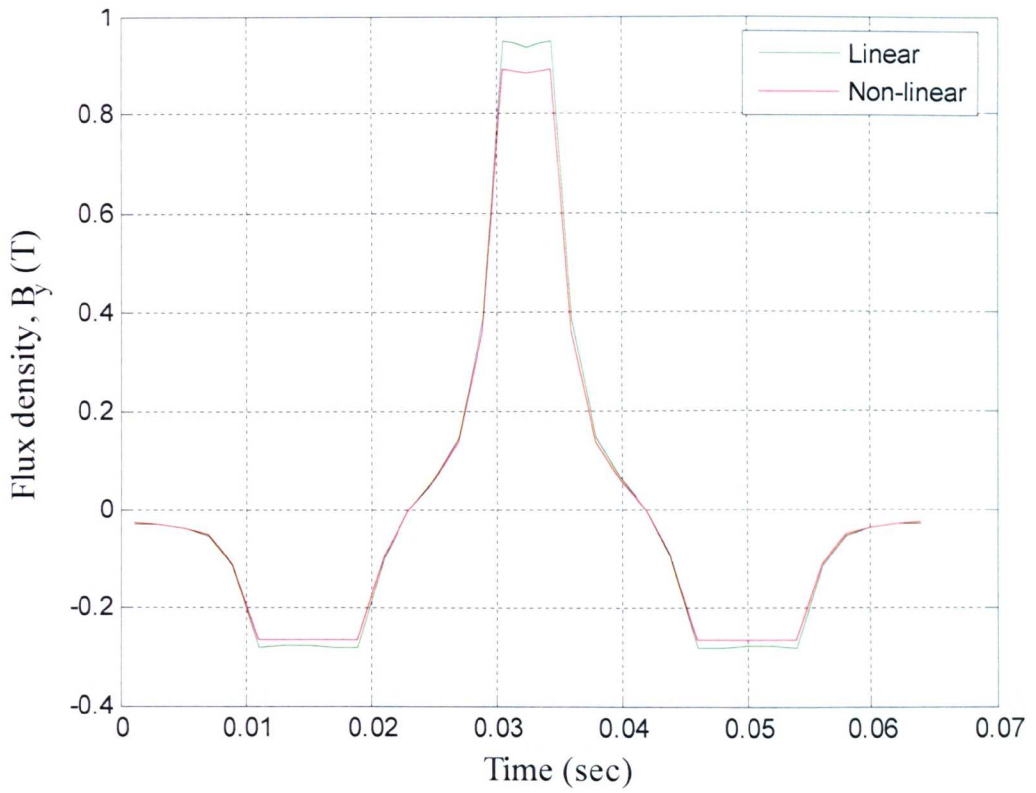


Figure (C.10): y-component of the flux density for linear and non-linear case from MEGA in the middle of the airgap when $C1 = 10 \text{ A/mm}^2$ and $C2 = 0$

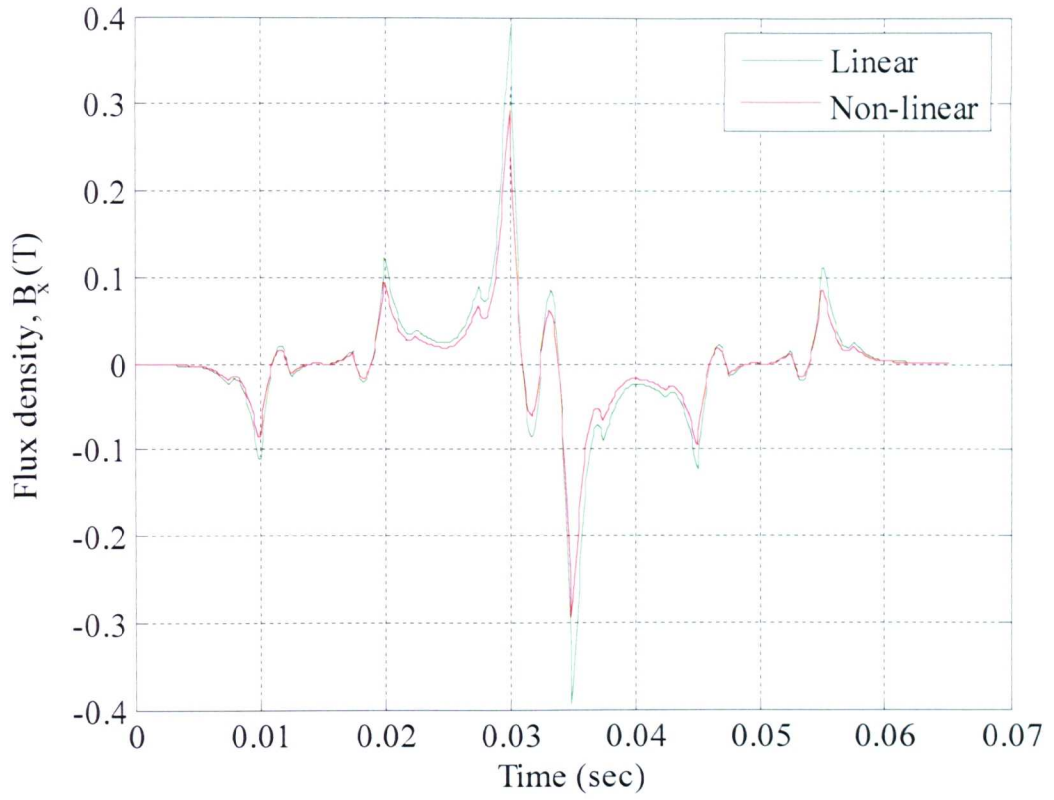


Figure (C.11): x-component of the flux density for linear and non-linear case from MagFEA in the middle of the airgap when $C1 = 15 \text{ A/mm}^2$ and $C2 = 0$

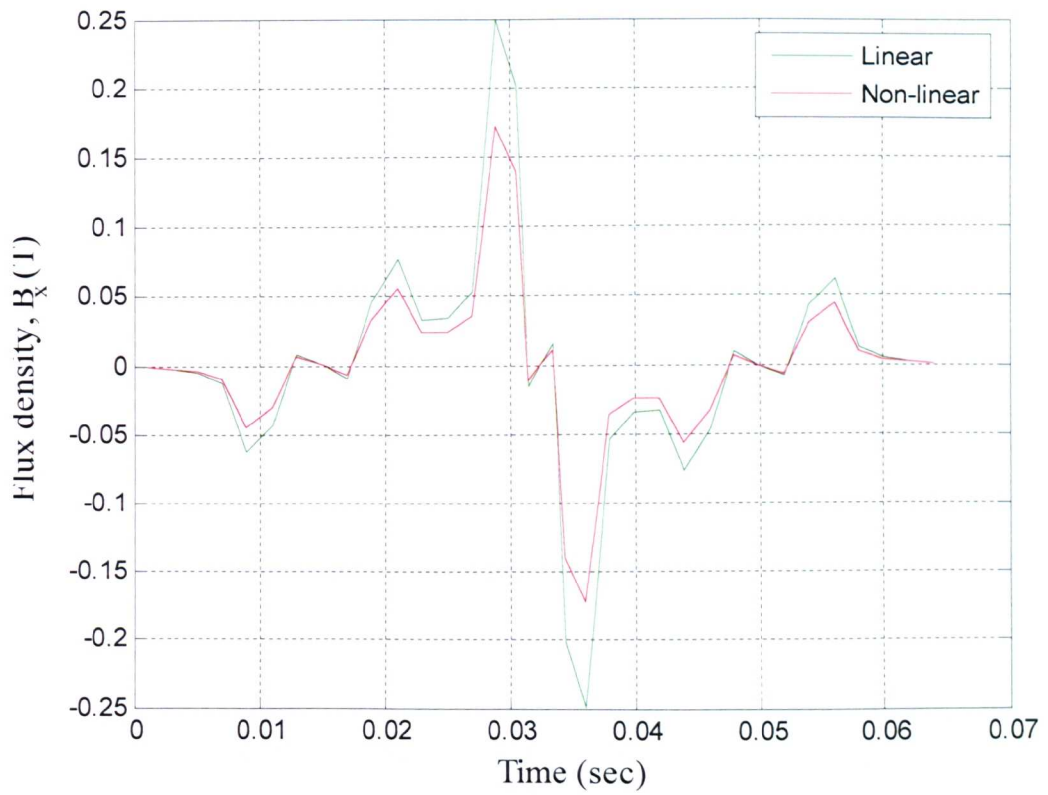


Figure (C.12): x-component of the flux density for linear and non-linear case from MEGA in the middle of the airgap when $C1 = 15 \text{ A/mm}^2$ and $C2 = 0$

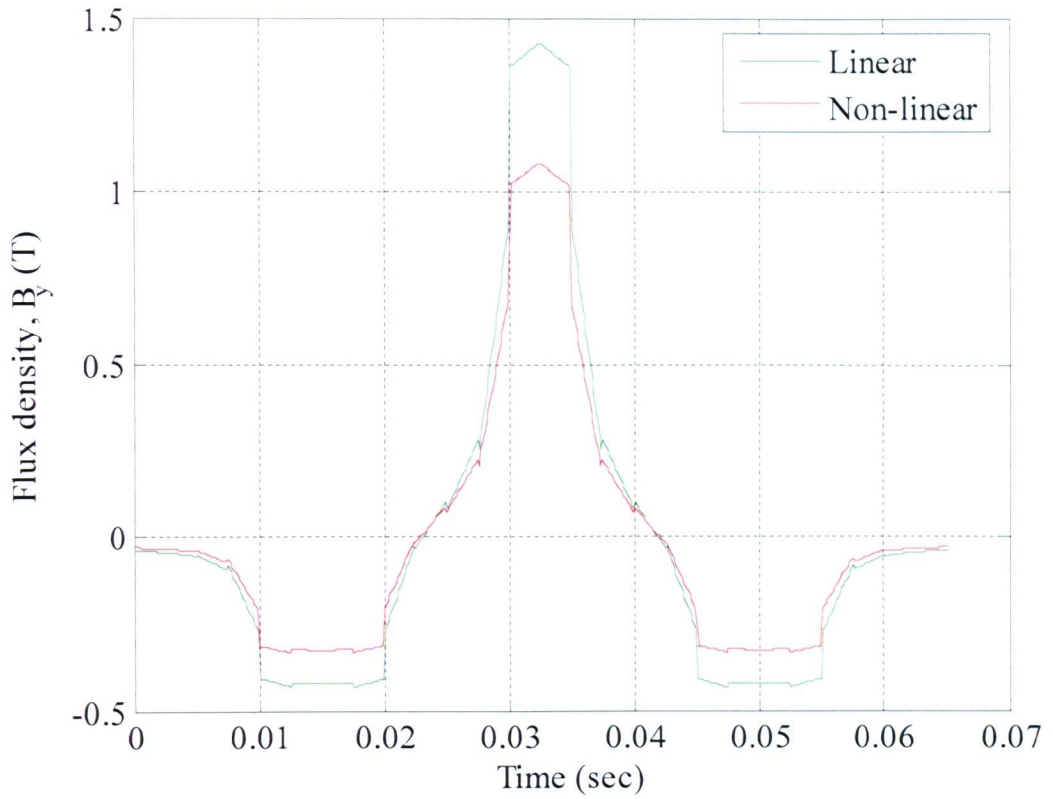


Figure (C.13): y-component of the flux density for linear and non-linear case from MagFEA in the middle of the airgap when $C1 = 15 \text{ A/mm}^2$ and $C2 = 0$

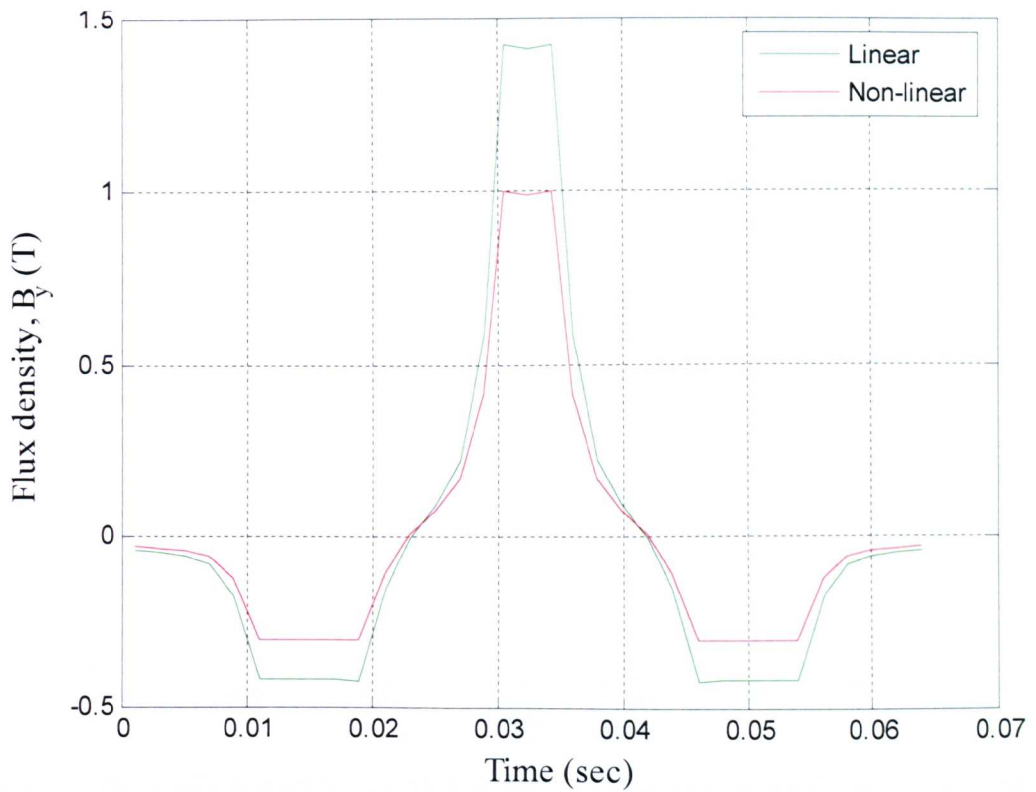


Figure (C.14): y-component of the flux density for linear and non-linear case from MEGA in the middle of the airgap when $C1 = 15 \text{ A/mm}^2$ and $C2 = 0$

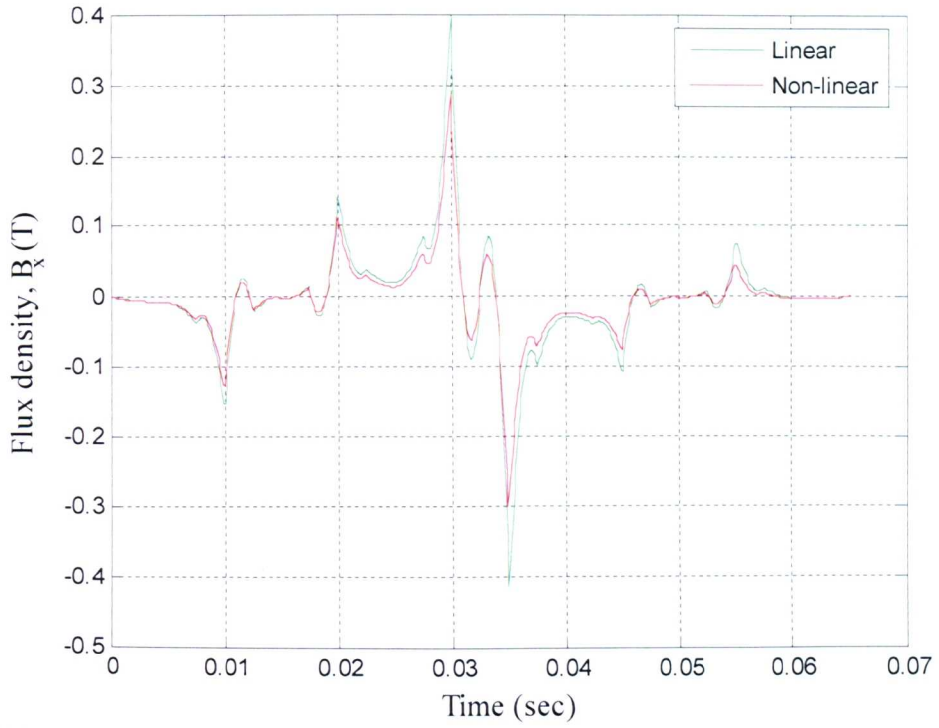


Figure (C.15): x-component of the flux density for linear and non-linear case from MagFEA in the middle of the airgap when $C1 = 15 \text{ A/mm}^2$ and $C2 = 5 \text{ A/mm}^2$

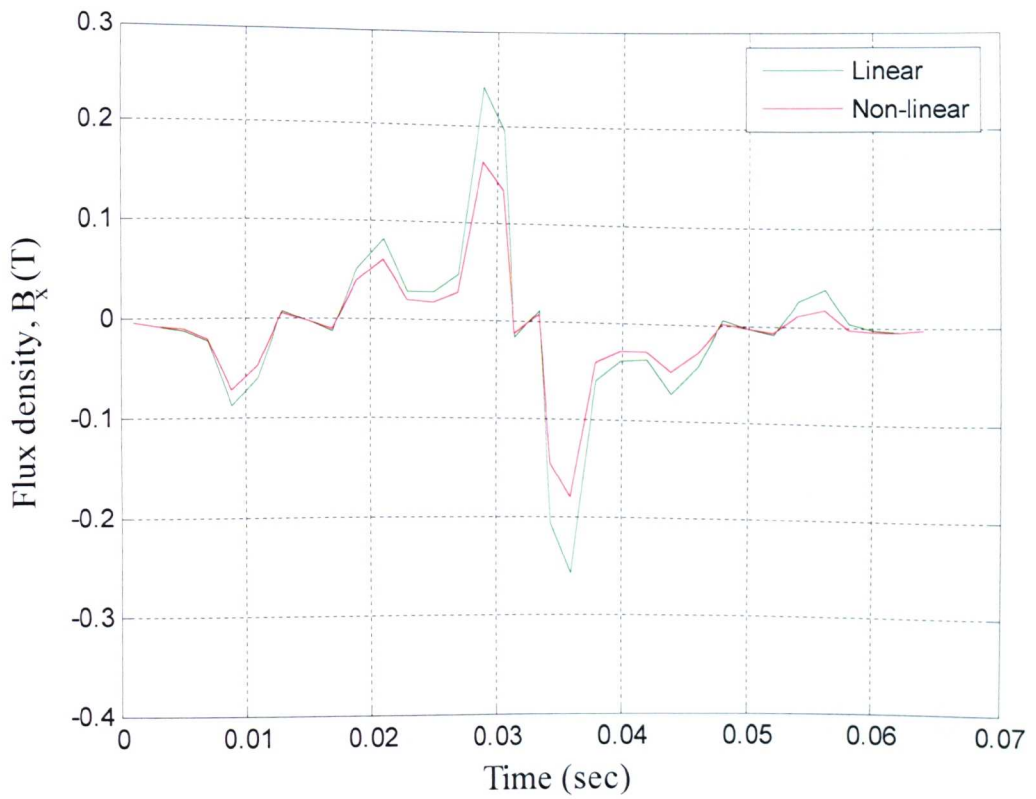


Figure (C.16): x-component of the flux density for linear and non-linear case from MEGA in the middle of the airgap when $C1 = 15 \text{ A/mm}^2$ and $C2 = 5 \text{ A/mm}^2$

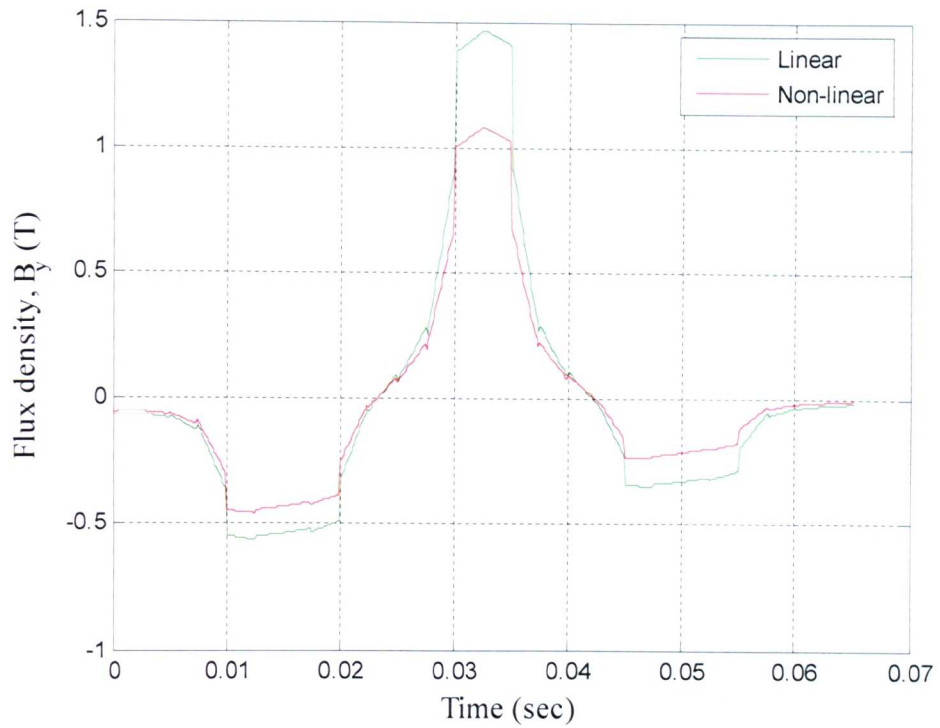


Figure (C.17): y-component of the flux density for linear and non-linear case from MagFEA in the middle of the airgap when $C2 = 15 \text{ A/mm}^2$ and $C2 = 5 \text{ A/mm}^2$

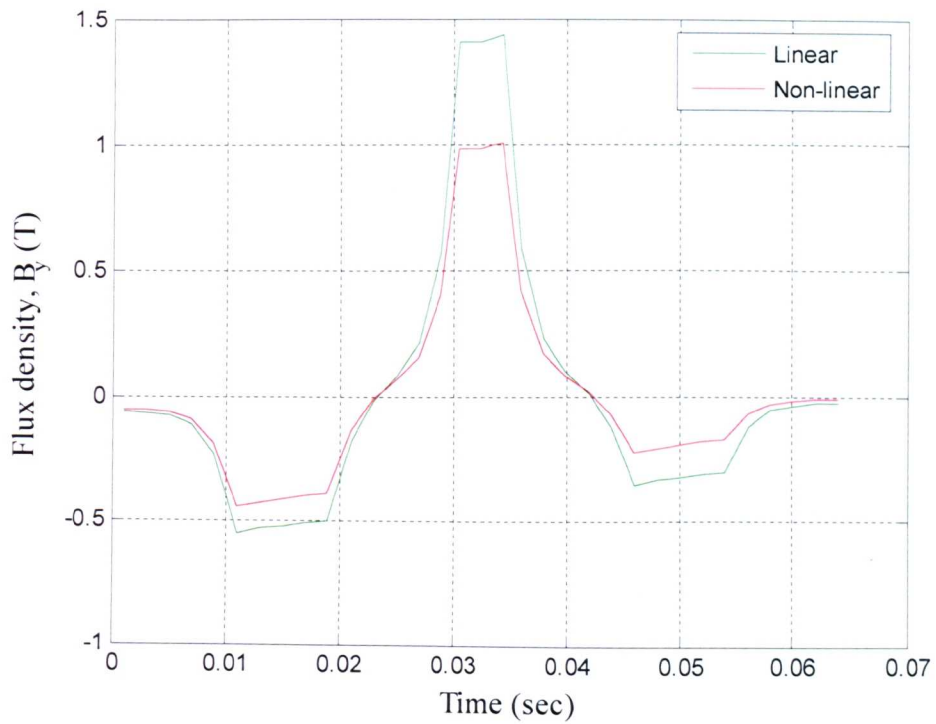


Figure (C.18): y-component of the flux density for linear and non-linear case from MEGA in the middle of the airgap when $C2 = 15 \text{ A/mm}^2$ and $C2 = 5 \text{ A/mm}^2$